UNIVERSIDADE FEDERAL DO RIO DE JANEIRO

INSTITUTO DE FÍSICA

Lattice Boltzmann method for semiclassical fluids and its application for electron hydrodynamics

Rodrigo Carlos Viana Coelho

Ph.D. Thesis presented to the Graduate Program in Physics of the Institute of Physics of the Federal University of Rio de Janeiro - UFRJ, as part of the requirements to the obtention of the title of Doctor in Sciences (Physics).

Advisor: Mauro Melchiades Doria

Co-advisor: Hans Jürgen Herrmann

Rio de Janeiro

December, 2017

Lattice Boltzmann method for semiclassical fluids and its application for electron hydrodynamics
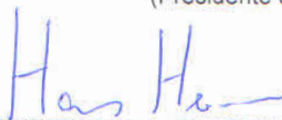
Rodrigo Carlos Viana Coelho

Mauro Melchiades Doria

Tese de Doutorado submetida ao Programa de Pós-Graduação em Física, Instituto de Física, da Universidade Federal do Rio de Janeiro – UFRJ, como parte dos requisitos necessários à obtenção do título de Doutor em Ciências (Física).
Aprovada por:

....
Mauro Melchiades Doria
(Presidente e Orientador)

....
Herrmann Hans Jürgen

....
Caio Henrique Lewenkopf

....
Welles Antonio Martinez Morgado

....
Felipe Arruda de Araujo Pinheiro

....
Luca Roberto Augusto Moriconi

Rio de Janeiro, RJ – Brasil
Dezembro de 2017

Resumo

Método lattice-Boltzmann para fluidos semi-clássicos e sua aplicação para hidrodinâmica de elétrons

Rodrigo Carlos Viana Coelho

Orientador: Mauro M. Doria

Coorientador: Hans J. Herrmann

Resumo da Tese de Doutorado apresentada ao Programa de Pós-Graduação em Física do Instituto de Física da Universidade Federal do Rio de Janeiro - UFRJ, como parte dos requisitos necessários à obtenção do título de Doutor em Ciências (Física).

Experimentos recentes apontaram que os portadores de carga em grafeno podem apresentar comportamento hidrodinâmico para uma ampla gama de temperaturas e densidades de portadores. Isto é devido à sua fraca interação elétron-fônon e às novas tecnologias para produzir amostras ultra-limpas, o que permite que o espalhamento entre elétrons domine sobre outros espalhamentos. Além disso, o comportamento hidrodinâmico pode ser observado em muitos outros materiais novos incluindo o paládio-cobalto metálico 2D, isolantes topológicos e semimetais de Weyl. Para investigar esses fenômenos, a equação de Navier-Stokes é resolvida, analiticamente ou numericamente, em geometrias simples e para fluxos estacionários. Neste contexto, o método lattice-Boltzmann (LBM) surge como um método computacional eficiente para simular fluxos de fluido eletrônico em geometrias complexas sem necessidade de malhas sofisticadas e ele permite também investigar estados transitórios do fluxo. O LBM teve um enorme sucesso para simular fluidos clássicos devido às suas muitas vantagens em relação a outros métodos de fluidodinâmica computacional como a fácil implementação dos algorítimos e sua fácil paralelização em placas de

vídeo. Nós ilustramos aqui o uso do LBM para fluidos clássicos ao investigar propriedades fluidodinâmicas de meios porosos, o que é uma aplicação comum do LBM na indística de óleo e gás.

Nesta tese, desenvolvemos LBMs para fluidos semiclássicos e aplicamos-os para simular elétrons em metais e em grafeno. Os polinômios de Hermite fornecem a base matemática para os LBMs clássicos porque sua função de peso é muito semelhante à distribuição Maxwell-Boltzmann. No entanto, esses polinômios não são adequados para expandir as distribuições de Bose-Einstein e Fermi-Dirac, que são usadas em nossos modelos semiclásicos. Para resolver este problema, desenvolvemos um novo conjunto de polinômios que nos permitem escolher pesos apropriados para nossa expansão. Assim, os LBMs desenvolvidos nesta tese são capazes de tratar fluidos de bósons e férmions longe do regime clássico. Como uma aplicação, nós construímos e testamos um LBM para elétrons em metais e o usamos para recuperar a lei de Ohm forçando o fluido eletrônico a passar por obstáculos alocados aleatoriamente de forma análoga a um meio poroso clássico, o que ilustra a aplicabilidade do novo método para geometrias complexas. Além disso, também construímos um LBM semiclásico para partículas ultra-relativísticas, que é o primeiro a recuperar a dissipação completa de um fluido relativístico. Este modelo é usado para calcular numericamente, com alta precisão, a viscosidade cinemática e a condutividade térmica para partículas ultra-relativísticas em duas dimensões, o que deve servir para futuras comparações com cálculos analíticos. Para incluir as propriedades pseudo-relativísticas dos elétrons no grafeno, como a relação de dispersão linear, utilizamos o nosso novo LBM relativístico para investigar a instabilidade fluidodinâmica de Kelvin-Helmholtz no fluido de Dirac de portadores de carga em grafeno. Propomos uma experiência baseada no fluxo de elétrons através de um obstáculo micrométrico para observar e detectar essa instabilidade. Esta aplicação em particular ilustra o uso de LBM para investigar estados transientes do fluxo de elétrons.

Palavras-chave: método lattice-Boltzmann, fluidos semi-clássicos, hidrodinâmica de elétrons, fluidodinâmica computacional.

Abstract

Lattice Boltzmann method for semiclassical fluids and its application for electron hydrodynamics

Rodrigo Carlos Viana Coelho

Advisor: Mauro M. Doria

Co-advisor: Hans J. Herrmann

Abstract da Tese de Doutorado apresentada ao Programa de Pós-Graduação em Física do Instituto de Física da Universidade Federal do Rio de Janeiro - UFRJ, como parte dos requisitos necessários à obtenção do título de Doutor em Ciências (Física).

Recent experiments have pointed out that the charge carriers in graphene can exhibit hydrodynamic behavior for a wide range of temperatures and carriers densities. This is due to its weak electron-phonon interaction and to the new technologies to produce ultra-clean samples, which allows the electron-electron scattering to dominates over the other scatterings. Furthermore, hydrodynamic behavior might be observable in many other novel materials including the 2D metal palladium cobaltate, topological insulators, and Weyl semimetals. To investigate these phenomena, the Navier-Stokes equation have been solved, analytically and numerically, in very simple geometries and for steady state flows. In this context, the lattice Boltzmann method (LBM) arises as an efficient computational method to simulate flows of electronic fluid in complex geometries without the need of sophisticated meshes and also to investigate transient states of the flow. The LBM have had an enormous success to simulate classical fluids due to its many advantages over other computational fluid dynamic methods as the easy implementation and parallelization. We

illustrate here the use of the LBM for classical fluids by investigating the fluid dynamic properties of porous media, which is a common application of LBM in the oil industry.

In this thesis, we develop LBMs for semiclassical fluids and apply them to simulate electrons in metals and in graphene. The Hermite polynomials provides the mathematical basis for the classical LBMs because its weight function is very similar to the Maxwell-Boltzmann distribution. Nevertheless, these polynomials are not suitable to expand the Bose-Einstein and the Fermi-Dirac distributions, which are used in our semiclassical models. To solve this problem, we develop a new set of polynomials that allow us to choose appropriate weights for our expansion. Thereby, the LBMs developed in this thesis are able to treat fluids of bosons and fermions far from the classical regime. As an application, we build and test a LBM for electrons in metals and use it recover the Ohm's law by forcing the electronic fluid to pass through randomly placed obstacles analogous to a porous medium, which illustrate the applicability of the new method for complex geometries. Besides that, we also construct a semiclassical LBM for ultra-relativistic particles, which is the first one to recover the full dissipation of a relativistic fluid. This model is used to calculate numerically, with high precision, the kinematic viscosity and the thermal conductivity for ultra-relativistic particles in two dimensions, which should serve for future comparisons with analytical calculations. In order to include the pseudo-relativistic properties of electrons in graphene, as the linear dispersion relation, we use our new relativistic LBM to investigate the fluid dynamic instability of Kelvin-Helmholtz on the Dirac fluid of charge carriers in graphene. We propose an experiment based on the flow of electrons through a micro-scale obstacle to observe an detect this instability. This application illustrates the use of LBM to investigate transient states of the electron flow.

Keywords: Lattice Boltzmann method, semiclassical fluids, electron hydrodynamics, computational fluid dynamics.

Acknowledgments

I thank all the people who helped me, directly or indirectly, to develop the work presented in this PhD thesis.

My deepest appreciation goes for Prof. Mauro Doria for his supervision and guidance during my PhD studies. Mauro offered me the chance to develop this multidisciplinary project, which amazed me during my PhD and made me greatly expand the horizons of my knowledge. I really admire his brilliant ideas, his ability to solve complex problems and his courage to face new challenges. Besides being always available to discuss project problems, Prof. Mauro has also shown care for my well-being and for the future of my professional career.

Special thanks to Prof. Hans Herrmann for giving me the opportunity to do my PhD sandwich in his prestigious research group at ETH Zürich, for the supervision during this period and for his valuable recommendations during the publication process. I highly appreciate his expertise, his broad knowledge and his talent to didactically present his ideas in conferences and lectures. I would also like to express my gratitude to Dr. Miller Mendoza for his guidance during my studies at ETH. His brilliant mind, his enthusiasm and his great sense of humor inspire everyone around him and make the work environment very pleasant. Besides, I thank to my friends from ETH for everything I learned with them and for the great time I had there: Robin, Jens-Daniel, Ilario, Ryuta, Oliver, Sergio, Lucas, Filippo, Pavel, Jan, Rilder, Dominik, Caio, Laurens, Kyriakos, Damian, Mirko.

I want to thank Dr. Rodrigo Neumann for his supervision during my internship at IBM Research. He presented me a new working environment for a physicist rather than academia and taught me many useful tools to become a computational physicist. I thank

Contents

List of Acronyms

Acronym	Description
BE	Bose-Einstein (distribution function)
BGK	Bhatnagar-Gross-Krook (collision operator)
CFD	Computational fluid dynamics
EDF	Equilibrium distribution function
EPD	Electric potential difference
FD	Fermi-Dirac (distribution function)
GPU	Graphics processing unit
KHI	Kelvin-Helmholtz instability
LBM	Lattice Boltzmann method
MB	Maxwell-Boltzmann (distribution function)
MJ	Maxwell-Jüttner (distribution function)
RLBM	Relativistic lattice Boltzmann method
SSA	Specific surface area

List of Figures

List of Tables

List of Publications

- R. C. V. Coelho; M. J. Mendoza; M. M. Doria; H. J. Herrmann, *"Kelvin-Helmholtz instability of the Dirac fluid of charge carriers on graphene"*, Phys. Rev. B **96**, 184307 (2017), `https://journals.aps.org/prb/abstract/10.1103/PhysRevB.96.184307`, `https://arxiv.org/abs/1706.00801v2`.

- R. C. V. Coelho, A. S. Ilha, and M. M. Doria, *"A lattice Boltzmann method based on generalized polynomials and its application for electrons in metals"*, EPL (Europhysics Letters) **116**, 20001 (2016). `https://epljournal.edpsciences.org/articles/epl/abs/2016/20/epl18215/epl18215.html`, `https://arxiv.org/abs/1510.07328v2`.

- R. C. V. Coelho and R. F. Neumann, *"Fluid Dynamics in Porous Media with Sailfish"*, European Journal of Physics **37**, 055102 (2016), `http://iopscience.iop.org/article/10.1088/0143-0807/37/5/055102`, `https://arxiv.org/abs/1601.05361`

- M. M. Doria; R. C. V. Coelho, *"Chebyshev, Legendre, Hermite and other orthonormal polynomials in D-dimensions "*, Reports on Mathematical Physics, Volume 81, Issue 2, April 2018, Pages 243-271, `https://www.sciencedirect.com/science/article/pii/S0034487718300405?via%3Dihub`, `https://arxiv.org/abs/1703.08670`.

- R. C. V. Coelho; M. J. Mendoza; M. M. Doria; H. J. Herrmann, *"Fully dissipative relativistic lattice Boltzmann method in two dimensions "*, Computers & Fluids, Available online 16 April 2018, `https://www.sciencedirect.com/science/article/pii/S0045793018302196?via%3Dihub`, `https://arxiv.org/abs/1709.09073`.

- R. C. V. Coelho; M. M. Doria, *"Lattice Boltzmann method for semiclassical fluids"*, Computers & Fluids, Volume 165, 30 March 2018, Pages 144-159 `https://www.sciencedirect.com/science/article/pii/S0045793018300276`, `https://arxiv.org/abs/1710.09472`.

Chapter 1

Introduction

In this chapter, we briefly review the main concepts related to this thesis and explain our motivations based on the state of the art of this field. First, we review the literature about semiclassical fluids and the possibility of modeling them using the lattice Boltzmann method (LBM). Then, we describe some recent experiments which were able to detect the hydrodynamic effects of electrons in graphene. Next, we use the classical LBM (standard) as an example to explain how the method works and we comment about the relativistic models. Finally, we conclude and make a summary of the next chapters.

1.1   Semiclassical fluids

In 1900, Paul Drude explained the transport properties of electrons in materials by treating them like particles in a rarefied gas whose microscopic velocities satisfy the Maxwell-Boltzmann (MB) equilibrium distribution function (EDF) [7,65]. However, electrons are fermions whose microscopic velocities are distributed according to the Fermi-Dirac (FD) distribution instead of the MB one. Indeed, in 1927, Arnold Sommerfeld showed that even at room temperature the quantum mechanical properties of the electron gas are relevant. The gas is essentially governed by their zero temperature properties, where they are piled in energy according to the Pauli exclusion principle. Only the electrons with the highest energy (Fermi energy) are available for conduction. Thus, the

conduction electrons move with the Fermi speed instead of the thermal microscopic velocity. Interestingly, the Boltzmann equation with the Bhatnagar-Gross-Krook (BGK) collision operator provides the standard framework to understand the Drude-Sommerfeld model that describes the electrons in metals [65]. In the 1930's E. A. Uheling and G. E. Uhlenbeck [149] were the first ones to generalize the Boltzmann equation to account for particles obeying either Bose-Einstein (BE) and FD statistics.

In the 1950's Bhatnagar, Gross and Krook proposed to describe collisions among particles in the Boltzmann equation through relaxation of the distribution function to an EDF within a typical time τ. This collision term became fundamental for the development of computationally efficient algorithms to solve the Boltzmann equation. Nevertheless, only in the 1980's this goal was fully reached by the development of the LBM, which numerical solution of the Boltzmann-BGK equation relies on a discretization of space and time. The ability to simulate flows in complex geometries had been finally reached and, since then, it has been extensively used to tackle many problems of classical fluid dynamics ranging from biology to material science [82]. It features an elegant solution for the quadrature problem, by means of the D-dimensional Hermite polynomials, which is the exact calculation of an integral in a discrete lattice. The expanded EDF in terms of the ratio between the macroscopic velocity and a reference velocity (Mach velocity) still respects the conservation laws of hydrodynamics [85] in the time evolution process. However the proposal of such a LBM for semiclassical fluids remained as an open problem, although the existing interest to solve the Boltzmann equation in arbitrary geometries and in presence of granular non-conducting grains (defects or impurities).

The Hermite polynomials are well fitted to describe classical particles, that is, those obeying the MB statistics, since they are orthonormal under the Hermite weight function which is essentially the MB EDF. Previous attempts [30, 34, 67, 130, 157] to build a semiclassical LBM were based on the expansion of the BE-FD distributions in Hermite polynomials, but they were limited to a nearly classical regime since the weight function of

the Hermite polynomials differs greatly from the BE-FD distributions on the semiclassical or quantum regimes (low temperatures and high densities). Recently, Coelho, Ilha and Doria have proposed a semiclassical LBM to reach this goal, based on new D-dimensional polynomials [31] (Chap. 4). The point of view of Ref. [31] is that a new polynomial set must be used for semiclassical fluids where the weight function is similar or equal to the EDF.

The three fundamental EDFs of statistical mechanics are the MB for classical distinguishable particles, the FD for fermions and the BE for bosons, the last two ones are indistinguishable semiclassical particles. The quantum statistics takes into account that particles have an intrinsic wavelength, which if larger than their average separation, makes them overlap and turn them indistinguishable from each other. Oppositely in case of low densities the BE-FD statistics reduce to the MB statistics where particles are distinguishable since this overlap is sufficently small to be neglected. However for a large range of density and temperature quantum effects are still present and for this reason the BE-FD statistics are known as semiclassical statistics whereas MB is a classical statistics.

1.2   Electron hydrodynamics in graphene

Graphene [22, 111, 112] has caught a lot of attention due to its excellent electrical, mechanical and thermal properties, which open many possibilities for technological applications. Close to the charge neutrality point, the charge carriers in graphene show a relativistic dispersion relation making them behave effectively as a Dirac fluid of massless quasi-particles moving with the Fermi speed ($v_F \sim 10^6$ m/s), with a very low viscosity-entropy ratio [106] and very high thermal conductivity [8]. It also shows an extremely high electrical mobility, reaching saturation velocities above 3×10^5 m/s for low carrier densities even at room temperature [41].

Recently there has been a great interest in the hydrodynamic regime of charge carriers in conductors [5, 110]. To achieve this regime, the electron-electron scattering must
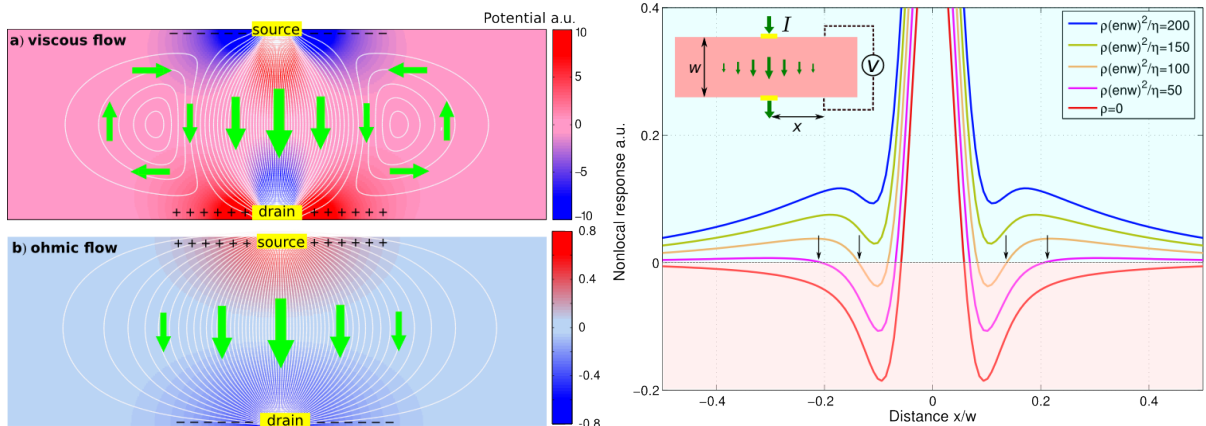
Figure 1.1: (Left) Comparison between viscous and ohmic flow of electron in graphene calculated from Navier-Stokes equation. The colors represents the electrical potential in arbitrary units and the streamlines and the arrows indicates the electrical current. In the viscous flow, we see the formation of the whirlpools, which explain the negative nonlocal resistance. (Right) Voltage at a distance x from the contacts (see the inset) for different resistivity-to-viscosity ratios (ρ/η). The arrows indicate where the voltage changes its sign, which provides a way to measure the ratio ρ/η in experiments. Reprint from Ref. [86].

dominate over the electron-impurities and the electron-phonon scattering, which is difficult to obtain for most metals and semi-conductors. Before graphene, one of the few observations of such hydrodynamic effects in solids was an analogue of Poiseuille flow in two-dimensional high mobility wires of (Al,Ga)As heterostructures [38] theoretically predicted by Gurzhi [58]. Recent experiments have shown that electrons in graphene exhibit hydrodynamic behavior for a wide range of temperatures and carrier densities [9], due to weak electron-phonon scattering [142] and to new technologies to produce ultra-clean samples [133]. Remarkably, the formation of whirlpools (vortices) in graphene was predicted and subsequently observed [9, 86, 119, 145] providing unambiguous detection of the viscous regime (See Figs. 1.1 and 1.2). Those whirlpools are able to explain the observed negative resistance close to contacts. Another evidence for the hydrodynamic regime in graphene was found for electrons passing through a constriction Refs. [57, 83]. In this experiment, the measured electrical mobility exceeds the maximum limit predicted for the ballistic regime, but can be explained by the hydrodynamic model. In addition, a

signature of the Dirac fluid was pointed out in Ref. [36] by the observation of a breakdown of the Wiedemann-Franz law close to the charge neutrality point.
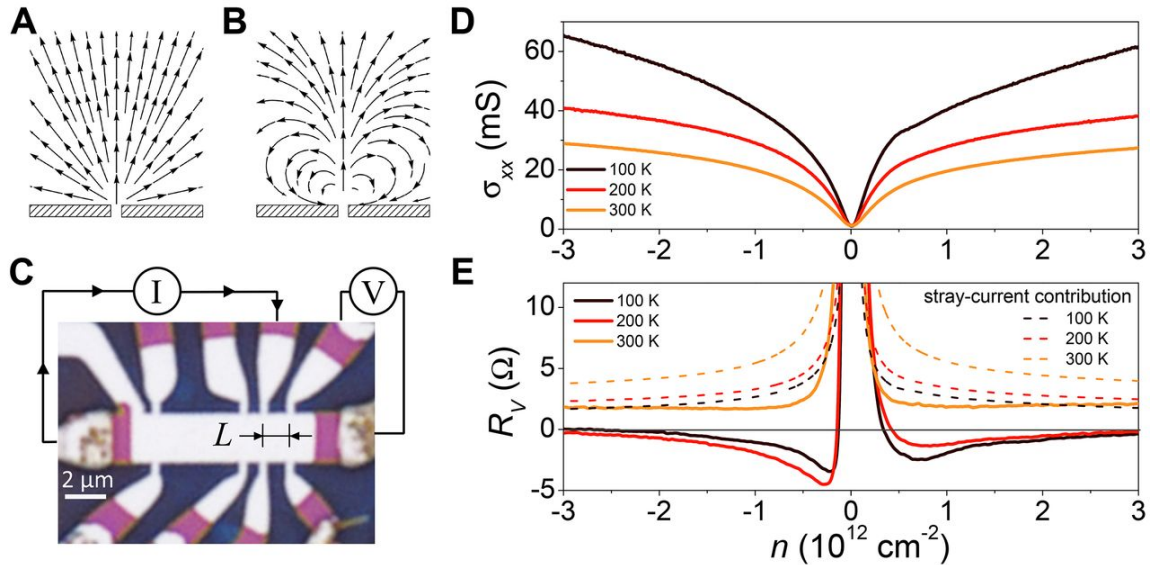
Figure 1.2: Experimental detection of viscous flow of electrons in doped graphene. Calculated steady-state current injected through a narrow slit for A) a inviscid fluid and B) for a viscous fluid. C) Optical micrography of the device with single layer graphene used in the experiments. D and E) Longitudinal conductivity σ_{xx} and vicinity resistance $R_v = V_v/I$ as a function of the carrier density n for three different temperatures. Reprint from Ref. [9].

The Boltzmann equation [23, 81] is widely used to derive hydrodynamic equations for graphene, since the macroscopic collective behavior of charge carriers, not always recovered by standard hydrodynamics, can be calculated from first principles [20, 46, 53, 105, 108–110, 123]. In Ref. [20], the generalized Navier-Stokes for electronic flow in graphene is derived with a procedure similar to the Chapman-Enskog expansion [26]. Interestingly, the resulting hydrodynamic equations are not Lorentz or Galilean invariant due to nonlinear terms, which are specially relevant in the high velocity regime. The Boltzmann equation is not valid at the quantum critical point where charge density and temperature are equal to zero. Nevertheless in experiments performed at finite carrier density, controlled by an external gate voltage, the Boltzmann equation is expected to give reliable results [22].

1.3 The lattice Boltzmann method

1.3.1 Classical LBM

The LBM [82,136] is a computational fluid dynamics technique based on the space-time discretization of the Boltzmann equation that has been successfully applied to simulate classical, semi-classical [30, 31, 157], quantum [115, 116, 135] and relativistic fluids. It has many advantages over other numerical methods as the facility to simulate flows through complex geometries and the easy implementation and parallelization of computational codes. Here we describe the basics about the standard LBM (classical fluids), which was used in Chap. 2 to simulate flows in porous media. Due to its simplicity, it serves as an introduction to understand the more sophisticated LBM's developed in this thesis for non-relativistic and relativistic semiclassical fluids.

The Boltzmann equation [80] in its finite-difference form, is given by

$$f(\mathbf{x} + \boldsymbol{\xi}\Delta t, \boldsymbol{\xi} + \frac{\mathbf{F}}{m}\Delta t, t + \Delta t) - f(\mathbf{x}, \boldsymbol{\xi}, t) = \Delta t \left(\frac{\partial f}{\partial t}\right)_{\text{coll}}, \tag{1.1}$$

where $\mathbf{x}$ is the position, $\boldsymbol{\xi}$ is the microscopic velocity, t is the time, $\mathbf{F}$ is the external force and m is mass of the particles. Expanding (1.1) up to first order in Δt, we obtain the Boltzmann equation in its continuous form,

$$\frac{\partial f}{\partial t} + \frac{\partial f}{\partial x^i}\xi^i + \frac{\partial f}{\partial \xi^i}F^i = \left(\frac{\partial f}{\partial t}\right)_{\text{coll}}. \tag{1.2}$$

The above equation gives the time evolution of the distribution function, $f(\mathbf{x}, \boldsymbol{\xi}, t)$, by knowing the collision operator, $(\partial f/\partial t)_{\text{coll}}$, which includes all information about atomic aspects of scattering process of the particles in the gas. The BGK collision term [14],

$$\left(\frac{\partial f}{\partial t}\right)_{\text{coll}} = -\frac{f(\mathbf{x}, \boldsymbol{\xi}, t) - f^{\text{eq}}(\mathbf{x}, \boldsymbol{\xi}, t)}{\tau},$$

is the simplest and commonly used in LBM. It assumes that the non-equilibrium function $f(\mathbf{x}, \boldsymbol{\xi}, t)$ tends to the EDF $f^{\text{eq}}(\mathbf{x}, \boldsymbol{\xi}, t)$ with a characteristic time τ, called "relaxation time". To illustrate this, note that when the external force is zero and the fields are

homogeneous, the integration of Boltzmann-BGK equation in its continuous form becomes $f = f^{\text{eq}} + (f^{\text{init}} - f^{\text{eq}})e^{-t/\tau}$, where f^{init} is the distribution function at $t = 0$. Despite its simplicity, the BGK collision term leads to the correct equations of mass and momentum conservation (Navier-Stokes equations) [101]. As a consequence of using a single relaxation time, the macroscopic moments, i.e., density and velocity, change at the same rate. The choice of relaxation time in the simulation has an impact on fluid flow, since the kinematic viscosity depends on τ [101]. In LBM the position and velocity spaces are discretized [121] as illustrated in Figure 1.3. The time step Δt, used in (1.1), is the time for a particle to move from its site to one of the first neighbors sites and this time step, together with the lattice parameter (a) form a system of unities called *lattice units* [101], which can be converted for any other system of units.
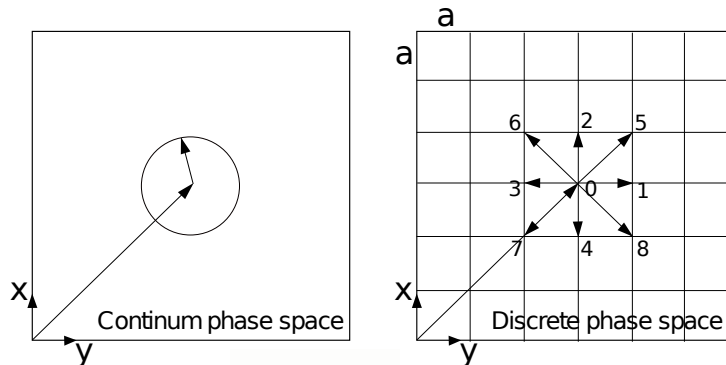
Figure 1.3: Discretization of position and velocity spaces using the D2V9 lattice (two dimensions and nine velocity vectors). Reprint from Ref. [33]

We conveniently write the discrete Boltzmann equation (1.1) in two steps,

$$f_\alpha^{aux}(\boldsymbol{x}, t + \Delta t) = f_\alpha(\boldsymbol{x}, t) - \frac{1}{\tau}[f_\alpha(\boldsymbol{x}, t) - f_\alpha^{eq}(\boldsymbol{x}, t)], \qquad (1.3)$$

$$f_\alpha(\boldsymbol{x} + \boldsymbol{\xi_\alpha}\Delta t, t + \Delta t) = f_\alpha^{aux}(\boldsymbol{x}, t + \Delta t) \qquad (1.4)$$

by introducing a *auxiliary* distribution function $f_\alpha^{aux}(\boldsymbol{x}, t)$. These two steps can be interpreted as collision and streaming of fictitious particles, respectively. In the standard LBM, the EDF is given by the MB distribution expanded up to second order in Hermite

Polynomials:

$$f_\alpha^{eq} = \rho w_\alpha \left[1 + \frac{(\boldsymbol{\xi}_\alpha \cdot \boldsymbol{u})}{c_s^2} - \frac{\boldsymbol{u}^2}{2c_s^2} + \frac{(\boldsymbol{\xi}_\alpha \cdot \boldsymbol{u})^2}{2c_s^4} \right].$$ (1.5)

The discrete weights w_α are calculated through the Gauss-Hermite quadrature [1]. For the D2V9 lattice, they are $w_0 = 4/9$ for $\alpha = 0$, $w_s = 1/9$ for $\alpha = 1, 2, 3, 4$ and $w_l = 1/36$ for $\alpha = 5, 6, 7, 8$, while $c_s = 1/\sqrt{3}$ is the sound speed.
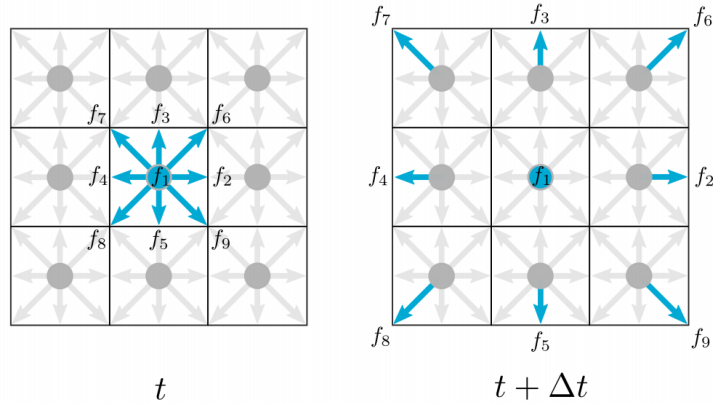
Figure 1.4: Streaming step for the D2V9 lattice. Reprint from Ref. [40]

The basic algorithm can be summarized as follows (see Fig. 1.5):

a) **Initial conditions**: The macroscopic variables ρ, $\boldsymbol{u}$ are initialized to given values in $f_\alpha^{eq}(\boldsymbol{x}, t)$.

b) **Collision**: The Eq.(1.3) describes how the distribution function changes at each node, as if it had undergone a collision.

c) **Streaming**: The Eq.(1.4) gives the evolution of the distribution function for a time step Δt, as if it had undergone a propagation. So, in the streaming step we move the direction-specific function f_α to the nearest neighbor lattice nodes, as shown in figure 1.4 for the D2V9 lattice.

d) **Macroscopic quantities**: Using the weights of the lattice we can calculate the moments of the distribution function

$$\rho = \sum_\alpha f_\alpha, \quad \boldsymbol{u} = \frac{1}{\rho} \sum_\alpha \boldsymbol{\xi_\alpha} f_\alpha.$$ (1.6)

e) EDF: Once in power of these three moments, we go introduce them in the EDF of Eq.(1.5)

f) Repeat from **b** to **e** for each step time until you want (for instance, until the steady state is reached).

The steps from **b** to **e** can be cyclically permuted. The boundary conditions can be implemented together with the streaming step just by replacing the distributions at the obstacles surface by the ones given by the specific boundary condition. See Fig. 1.5 for an illustration of the bounce-back boundary condition, which is very used in LBM. The bounce-back condition implies that the velocity at the obstacle's surface is zero. It is very easy to be implemented and automatized computationally, allowing us to simulate flows in arbitrarily complex geometries such as porous media [33].
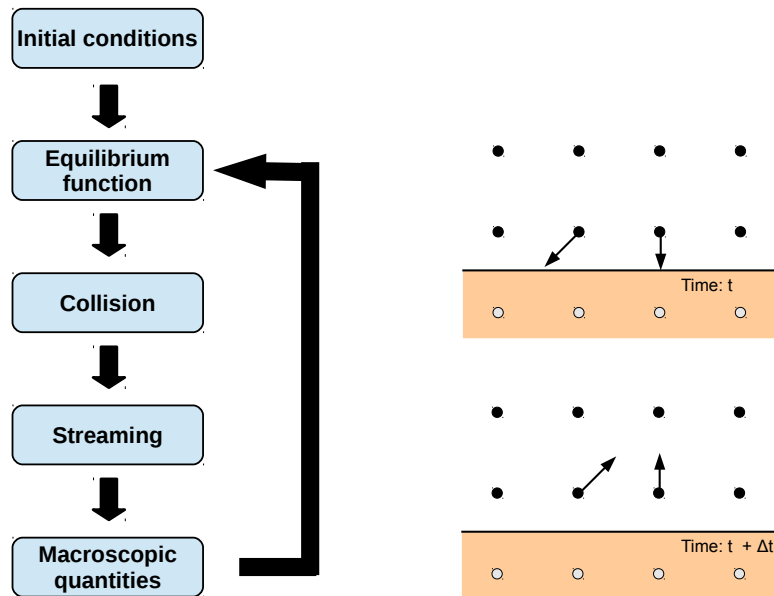
Figure 1.5: (Left) Basic cycle of LBM. (Right) Bounce-back boundary condition.

1.3.2 Relativistic LBM

In 2010, the first relativistic lattice Boltzmann method (RLBM) was proposed by Mendoza et. al. [96] and subsequently improved in numerical stability [63]. The theoret-

ical background for the RLBM and the extension to ultra-relativistic gases was done by Romatschke et. al. [125], where the authors used a model with interpolated streaming since the velocity vectors disposed along a sphere do not match with the square lattice. In Ref. [99], an improved dissipation model based on a third order expansion of the Maxwell-Jüttner (MJ) distribution was proposed, which does not recover the dissipation completely because a fifth order expansion is required. This model relies on a new Gaussian quadrature with exact streaming on a square lattice, recovering one of the main advantages of LBM, but costing a loss of resolution. Very recently, a new RLBM, also based on a third order expansion of the MJ distribution, can implement exact streaming on a square lattice without loosing spatial resolution allowing also to treat the regime of massive particles [49]. Meanwhile, other RLBMs with exact streaming have been used for graphene, where the grid points are disposed on a hexagonal lattice [47, 113] such as in the molecular structure of graphene. Nevertheless, for these quadratures, the polynomial expansion of the EDF is limited to second order, which might be enough for practical purposes, but gives a poor description if the velocities and/or the temperature fluctuations are moderately high, as shown in chapter 5. In 2017, Coelho et. al. [32, 35] proposed the first model based on a fifth order expansion of the FD distribution and used it to study the Kelvin-Helmholtz instability on graphene (Chaps. 5 and 6). Since this is a viscous fluid dynamical effect, a fully dissipative method is desirable to achieve better accuracy of the results.

The relativistic version of LBM [49, 96] has been extensively used in the literature to simulate the Dirac fluid in graphene [47, 52, 97, 98, 113]. This approach naturally includes the linear dispersion relation and the relativistic equation of states by treating the quasi-particles in graphene as ultra-relativistic particles, analogously to models for the Quark-Gluon plasma [63, 64, 99, 125, 140], which is a truly relativistic fluid. The speed of light in this approach is played by the Fermi speed and a low macroscopic velocity regime is always adopted, making the relativistic corrections disappear. The relativistic formalism is used

for convenience since, the hydrodynamic equations effectively solved by these models are the standard ones [85].

1.4   Outline of the thesis

The semiclassical version of the LBM developed in this thesis can be used to model many fluids made of bosons or fermions. It is specially useful for the study of electron hydrodynamics, which is a renewed research area due to recent experiments showing hydrodynamic behavior of electrons in graphene. The LBM for electrons allows us to describe non-steady-states of the flow such as fluid dynamic instabilities and flows in arbitrarily complex geometries.

This thesis is organized as follows. In Chap. 2, we demonstrate the use of the classical LBM to study fluid dynamic properties of porous media. We calculate the permeability of a fluid passing through artificial samples of porous media and relate it with the geometrical properties of the samples, as the porosity, the tortuosity and the specific surface area. In Chap. 3, we orthogonalize the generalized polynomials, used in the semiclassical LBM, up to fourth order. It is also shown that they recover the well known Chebyshev, Hermite and Legendre polynomials when their respective weight functions are introduced in the coefficients equations. In Chap. 4, we establish the theoretical basis for the new semiclassical LBM's. We expand the BE-FD EDFs up to fourth order, study the forcing term and calculate the quadratures for simulations in one, two and three dimensions. Besides, we construct and study a simple model for electron in metals, which is validated by means of three numerical tests: the Riemann problem, the Poiseuille flow and the Ohm's law. In Chap. 5, we build the relativistic LBM with full dissipation. This is possible thanks to the expansion up to fifth order of the distribution functions in relativistic polynomials, which are inspired by the generalized polynomials of Chap. 3. We validate the new model using the Riemann problem. We also measure numerically the kinematic viscosity and the thermal conductivity, which are calculated by the first time for relativistic fluids in

two dimensions. Interestingly, they are not the ones predicted by the Grad's method. They will serve as a reference for future analytic calculations with the Chapman-Enskog method, which give the correct transport coefficients in three dimensions. In addition, we analyze the differences between models based on EDFs expanded from second to fifth orders. In Chap. 6, we use the relativistic LBM to simulate the Dirac fluid in graphene and we investigate the fluid dynamic instability of Kelvin-Helmholtz. An experiment is proposed to observe it through the electrical current and the electrical potential difference. In Chap. 7, we summarize the main results and conclude.

Chapter 2

Fluid dynamics in porous media

In this chapter we show the application of Sailfish to the study of fluid dynamics in porous media. Sailfish is an open-source software based on the lattice-Boltzmann method. This application of computational fluid dynamics is of particular interest to the oil and gas industry and the subject could be a starting point of a research project for an undergraduate or graduate student in physics or engineering. We built artificial samples of porous media with different porosities and used Sailfish to simulate the fluid flow through them in order to calculate their permeability and tortuosity. We also present a simple way to obtain the specific superficial area of porous media using `Python` libraries. To contextualize these concepts, we analyze the applicability of Kozeny–Carman equation, which is a well-known permeability-porosity relation, to our artificial samples.

2.1 Introduction

A porous medium is characterized by containing pores, i.e. void space, in its interior. These pores can be all connected, as in a sand pack, or not, as in Styrofoam. If the goal is to study the fluid flow in porous media, only those with connected pores must be considered. The understanding of fluid dynamic properties of porous media is particularly relevant to the oil and gas industry, since oil is found in underground porous rocks (reser-

voirs). It is crucial to estimate the permeability of a rock reservoir to hydrocarbons in order to assist decision-making and oil recovery strategies. Permeability can be measured experimentally or calculated as a function of other porous rock properties such as porosity, tortuosity and specific surface area. The most popular empirical relationship used to calculate the permeability from those quantities is the Kozeny–Carman equation [21, 78], but there are many other formulas for more specific purposes [71, 156].

In this context, computational fluid dynamics (CFD) plays an important role and the LBM has many advantages over other methods making it a good choice to address systems with complex geometries. LBM was first derived in 1988 by McNamara and Zanetti [94] and, since then, it has emerged as an alternative powerful method for solving CFD problems. It was very successful in simulating complex flows, such as fluids with immiscible components, interfacial problems and flows in complex geometries (e.g., in porous media). In recent years, LBM has been extended even to semiclassical [30] and relativistic fluids [96]. The advantage over other methods lies in the simplicity of its dynamics, easy handling of complex geometries and, especially, its flexibility for implementation in parallel computing. Sailfish [66] is an open-source LBM/CFD solver that comes with many examples ready to use. It has a simple `Python` interface, which is relatively simple to learn and is already optimized for graphic processing units (GPUs). Its advantages make it an appropriate choice for the study of flow in porous media, even for beginners in this subject.

`Python` as a programming language is often deemed unsuitable for high-end HPC applications for its relatively low performance when compared to compiled languages such as `Fortran` and `C/C++`. But with the advent of libraries like `PyCUDA` and `PyOpenCL` [73], one can offload the computationally-intensive calculations to the GPU while keeping the user-friendly `Python` interface. Performance in LBM is usually measured in terms of *lattice updates per second* (LUPS). CPU-only LBM codes typically achieve 10^7 LUPS in desktop computers and 10^8 LUPS in HPC clusters [39,51,59,92]. GPU-enabled LBM codes, on the

other hand, typically achieve $10^8 \sim 10^9$ LUPS on a single GPU [59, 66, 143], for a fraction of the space and energy required by a cluster. This considerable gain in performance permits the concurrent computation and visualization of results at a reasonable frame-rate for on-the-fly simulations. Although current laptop CPUs are still limited to 4 or 8 cores, it has become commonplace to find mobile GPUs with hundreds or thousands of cores, which represents a substantial increase in computing power without compromising portability. This enables the use of GPU-equipped portable computers for classroom *live* demonstrations of virtual CFD experiments.

In this chapter we propose a simple and efficient way to study fluid dynamics in porous media by using Sailfish. We show how to calculate the most important fluid dynamics properties of porous media, in order to analyze the applicability of Kozeny–Carman equation to samples of porous media we built artificially. These samples were generated by placing obstacles in random positions allowing them to overlap, which is more realistic than some other models in literature. For instance, many authors adopt a porous medium made of identical spheres placed in a regular lattice [71, 117] or used a two-dimensional porous media composed by identical squares placed in random positions [75, 76]. We also present an original and simple method to measure the specific surface area (SSA) from a digital rock tomography based on `Python` image-processing libraries.

This chapter is organized as follows. In Sec. 2.2 an introduction to Sailfish is presented. In Sec. 2.3.1 the algorithm used to build artificial samples is explained. In Sec. 2.3.2 we demonstrate how the permeability was calculated using the output from simulation. In Sec. 2.3.3 we apply the Kozeny–Carman equation to our samples and calculate its Kozeny's constant. In Sec. 2.3.4 our method to calculate the SSA is presented and tested for a simple case and, in Sec. 2.3.5, a simple way to calculate the tortuosity from the output data is shown. Finally, in Sec. 2.4 a discussion about the results and our concluding remarks are provided.

2.2   Sailfish

This section contains a brief introduction to Sailfish [66], the software we used to simulate fluid flow in our artificially-created porous media. We do not intend to provide a tutorial, for a very detailed one can be found at the developer's website [1], where you can download and follow the instructions to start using it. Sailfish requires no actual installation step, since the code is written in an interpreted programming language: `Python`. The required packages are all enumerated in Sailfish's website. A graphics card or GPU is also needed to run the calculations.

The main advantages of Sailfish are its ease of use and high performance. It comes with many strategic examples that can be run and easily adapted to the needs of the user. As all routines and examples are written in `Python`, they are easy to read and write – as compared to compiled languages like `Fortran` and `C/C++` – without compromising the computational performance, for all the time-consuming calculations run in the massively-parallel GPU. Sailfish offers a high-level programming interface with several built-in functionalities, so that the user only needs to provide simple instructions like the boundary and initial conditions, physical parameters of the fluid and select the LBM relaxation dynamics. Programming general-purpose GPUs is usually a difficult task, but Sailfish hides this complexity away and makes all parallelization behind the scenes [66]. Simulations in Sailfish can be made interactive which, combined to its high performance, makes it a powerful tool to illustrate hydrodynamic principles in the classroom in real-time. While a simulation is running in visualization mode, one can add new (solid) obstacles by freehand drawing them with a cursor.

---

[1]Download Sailfish and see the tutorial at `http://sailfish.us.edu.pl`

2.3 Fluid flow in porous media

The most relevant quantities related to fluid dynamics in porous media are porosity, tortuosity, surface area and permeability. In this section we define these concepts and relate them using the Kozeny–Carman equation.

We start with the porosity, that is defined as the fraction $\phi = V_{\mathrm{pores}}/V_{\mathrm{total}}$ of the total volume that is occupied by connected pores. Media with non-connected pores, as in Styrofoam, do not allow flow and, therefore, need not be considered for our purposes. In case the medium has both connected and non-connected pores, the volume occupied by the latter must be disregarded.
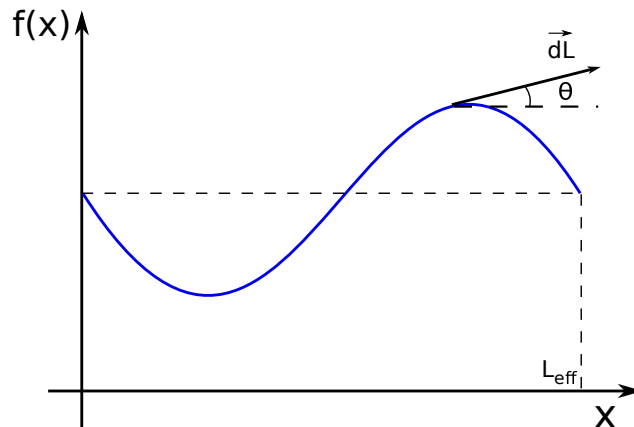
Figure 2.1: Example of a fluid streamline for tortuosity calculations.

Tortuosity [28, 129] is a geometrical figure-of-merit that indicates how much the fluid flow streamlines deviate from straight paths. It is defined as the ratio between the total length along the streamline and its effective length (the length of the straight line connecting final and initial positions), as depicted in Figure 2.1. Note that $\tau \geq 1$. If the streamline is given by a function $f(x)$, as exemplified in Figure 2.1, the tortuosity can be calculated as

$$\tau = \frac{\int dL}{L_{\mathrm{eff}}} = \frac{\int_0^{L_{\mathrm{eff}}} \sqrt{1 + \left(\frac{\partial f}{\partial x}\right)^2}\, dx}{L_{\mathrm{eff}}}. \tag{2.1}$$

The internal area of obstacles in contact with the fluid greatly influences the fluid dynamics. Ultimately, the SSA (or "surface-to-volume ratio") is responsible for the strength of surface interaction effects. This figure-of-merit is defined as $s = A_{\text{obs}}/V_{\text{obs}}$, where A_{obs} is the surface area of obstacles and V_{obs} is their total volume.

In general, permeability is the quantity of greatest interest in the study of flow through porous media. It quantifies how easily a specific fluid passes through the media, i.e, the inverse of a "flow resistance". In its simplest formulation, it depends only on the geometry of the medium and the viscosity of the fluid, μ, and can be calculated using Darcy's law [37, 151],

$$\kappa_{ij} = \frac{\mu \langle u^i \rangle}{\frac{dP}{dx^j}}, \qquad (2.2)$$

where $\frac{dP}{dx^j}$ is the pressure gradient along direction x^j and $\langle u^i \rangle$ is the average velocity of the fluid in the direction x^i. Note that, in general, permeability is a 3×3 tensor, but in practical cases we are usually interested only in the diagonal components $\{\kappa_{xx}, \kappa_{yy}, \kappa_{zz}\}$. The SI unit for permeability is m^2, however, the "darcy" ($1\,\text{darcy} = 10^{-12}\,m^2$) is the most used.

The four concepts presented previously are related by the Kozeny–Carman equation

$$\kappa = \frac{1}{Cs^2} \frac{\phi^3}{(1-\phi)^2}, \qquad (2.3)$$

where C is an empirical and dimensionless constant, known as Kozeny's constant, that depends only on the geometry of the media. In this model, the porous medium is assumed to be equivalent to a conduit, in which the pore space is reproduced by an array of cylindrical channels. The fluid flow inside these channels is described by the Hagen–Poiseuille equation [151]. Consider, for instance, a medium composed of identical spheres with diameter d, equally distributed in a bed packed [70]. In this case, the SSA is $s = A_{\text{sphere}}/V_{\text{sphere}} = 6/d$. So (2.3) becomes

$$\kappa = \frac{d^2}{36C} \frac{\phi^3}{(1-\phi)^2}. \qquad (2.4)$$

Note that the dimensionality is entirely contained within d^2, which agrees with the fact that the dimension of κ is *length-squared*. The Kozeny–Carman is not the only existing permeability-porosity relationship [156], but it works fairly well for granular beds as in our case.

2.3.1 Artificial porous media

In this section we describe the algorithm we developed to build artificial samples. An object-oriented implementation example for such algorithm, written in `Python`, is available as a Supplementary Material. Our intention was to produce a more realistic porous medium than the usual bed packed, but with more controllable parameters than the real samples digitized from rock tomography. In this way, we can, for instance, relate the geometry of the obstacles to permeability.

The input parameters for the algorithm are: the length of obstacles, the length of the sample and the target porosity. The obstacle's shape is determined by the equation of a ellipsoid with radii $\{r_x, r_y, r_z\}$ centered at (x_c, y_c, z_c). The samples are rectangular parallelepipeds, for which three lengths $\{L_x, L_y, L_z\}$ are required as inputs. The last input is the target porosity (ϕ_t), that is the desired porosity for the sample within a tolerance ε.

Given these input parameters, the algorithm builds a sample by placing obstacles in random positions, one at a time. After creating an obstacle, the algorithm checks if the target porosity has been reached. If not, another obstacle is added. The algorithm stops when $|\phi - \phi_\mathrm{t}| \leq \varepsilon$, as depicted in Figure 2.2.
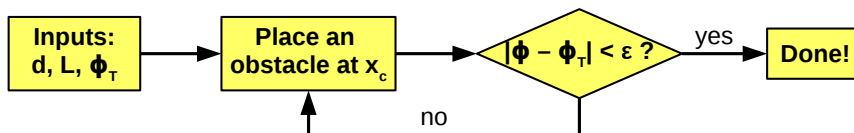
Figure 2.2: Flowchart of the algorithm used to generate artificial porous media samples.

For our simulations, we used samples with 208^3 nodes, spherical obstacles with di-

ameters between $d = 12$ and $d = 30$ and porosities in the range $0.2 \leq \phi \leq 0.4$. The number of nodes ($\sim 9 \times 10^6$) was limited by the available GPU memory. In Figure 2.3, we show some slices of artificial samples generated by our algorithm side-by-side with slices of real digitized rock tomography samples for comparison. The agreement is good for highly homogeneous rocks such as sand packs and most sandstones, but our algorithm may not be as suitable for more inhomogeneous rocks such as carbonates and shales, for they exhibit porosity at multiple scales. These artificial samples have the same obstacle diameter ($d = 20$) but different porosities: 0.2, 0.3 and 0.4. Since the spheres are allowed to overlap, they form more complex structures that are very close to those observed in real porous media. This leads to more realistic simulations of fluid flow.
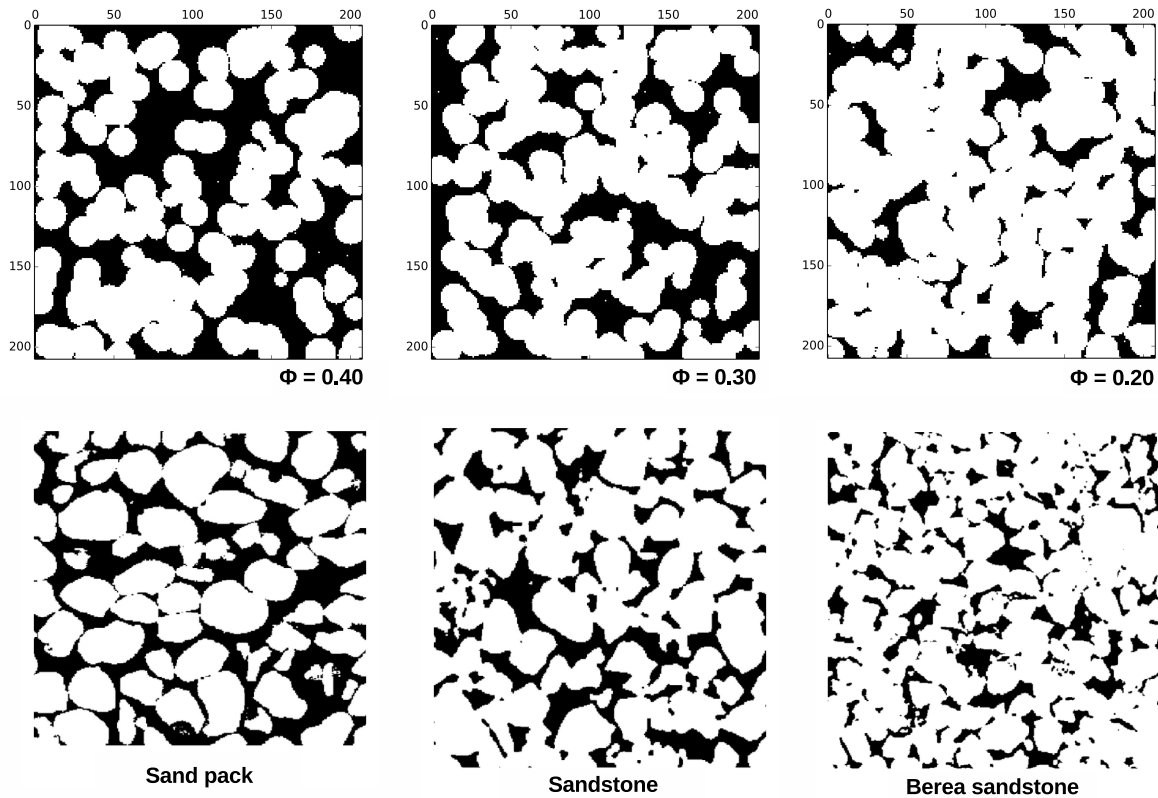
Figure 2.3: Comparison between slices of our artificial samples and of real rocks taken from the literature [6]. The artificial media were built using spherical obstacles with diameter of 20 nodes and with target porosity as indicated in each figure.

2.3.2 Permeability

The two main methods for inducing fluid flow in a porous medium using Sailfish are: by setting a pressure difference across the sample or a body force acting on every fluid node. Although the pressure method is closer to what is done in experiments, we observed that the steady-state flow is reached much faster with the force method. This happens because all points of the fluid feel the driving force at the same time when using the force method, instead of by propagation of shock waves as in the pressure method. In order to detect when the steady-state is achieved in our simulations, we calculate $||\boldsymbol{u}_{\text{new}}| - |\boldsymbol{u}_{\text{old}}|| / |\boldsymbol{u}_{\text{new}}|$ at every time step for every point of the fluid and, when the maximum value of this quantity is less than a given threshold, the simulation stops. We found 5×10^{-7} to be sufficient for our purposes.

The permeability is calculated using Darcy's law but, as it assumes a pressure gradient instead of a body force, we modify it using the relation $\frac{dP}{dx^j}dx^j = F_j/A_j$, where F_j is the body force along direction x^j and A_j is the cross-sectional area of the fluid at the boundary where the pressure is applied. The cross-sectional area of the fluid is ϕ times the total area. Therefore, given a force density $\mathbf{f} = f_x\mathbf{i}$, Darcy's law becomes

$$\kappa = \frac{\mu v_x \phi}{f_x},$$ (2.5)

which is the equation used to calculate permeability.

Since permeability, porosity and viscosity are not velocity-dependent, we expect the applied force f_x and the mean velocity $v_x = \langle u^x \rangle$ to be proportional to each other in the steady state. We tested this by taking an artificial sample with porosity $\phi = 0.3$, obstacles with diameters $d = 16$ nodes and using it as input for fluid flow simulations with different driving forces. The fluid had viscosity $\mu = 0.01$ in lattice units. The result is shown is Figure 2.4. We fit the data points with the function $v_x = \alpha f_x$, obtaining the proportionality constant $\alpha = (26.67 \pm 0.02)$ in lattice units. Using (2.5), we can determine the permeability of the sample to be $\kappa = (8.001 \pm 0.006) \times 10^{-2}$ in lattice units.
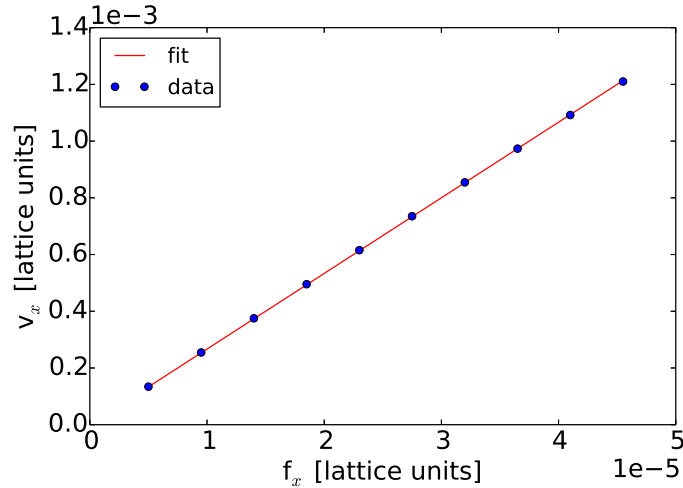
Figure 2.4: Proportionality between the mean velocity and the applied force for a given artificial sample with $\phi = 0.30$ and $d = 16$.

2.3.3 The Kozeny–Carman equation

We calculated the permeability using (2.5) and estimated the Kozeny's constant of the artificial porous media samples created using the method described in Section 2.3.1. In order to determine the individual contributions from porosity and obstacle dimension to the permeability, we built 210 samples with 208^3 nodes: 10 obstacle diameters $d \in [12, 30]$ and 21 porosities $\phi \in [0.2, 0.4]$, for each diameter. The fluid viscosity was 0.01 and the external force, $f_x = 10^{-5}$. The results are shown in Figure 2.5. One sees that permeability increases with porosity for a given obstacle diameter. Analogously, for a given porosity, permeability also increases with obstacle diameter. Next, we investigate the suitability of the Kozeny–Carman equation to describe our data.

Equation (2.4) tells us that permeability is proportional to d^2 or, in other words, that there is a scale-law involving obstacle dimensions and permeability. In order to turn permeability into a scale-free non-dimensional quantity, we calculate κ/d^2, and confirm that all points fall (despite fluctuations) within the same curve (see Figure 2.5). We fit

the function

$$\frac{\kappa}{d^2} = \frac{1}{36C} \frac{\phi^3}{(1-\phi)^2} \tag{2.6}$$

to the data points, with C (Kozeny's constant) as the free parameter. Its value was determined to be $C = 3.18 \pm 0.02$. As the fit uncertainty represents less than 1% of the main value, we consider (2.6) to be in good agreement with our simulated data points.

For simplicity, some approximations were made while fitting (2.6) to the data points. The obstacle diameter d is taken as the *theoretical* diameter but the *effective* one might be slightly different due to the "digital" nature of the spheres, i.e., being composed of cubic pixels (see Figure 2.6). Also, we used the SSA of non-overlapping spheres, $s = 6/d$, although we allow the spheres to overlap. In the next sections we present an analysis of the impact of such approximations.

Despite those simplifications, the value we obtained for Kozeny's constant is consistent with previously published values in the literature [104]. For instance, $C = 5$ for a bed packed of non-overlapping spheres [156] and, typically, between 2.2 and 8.9 for a fibrous media [158].
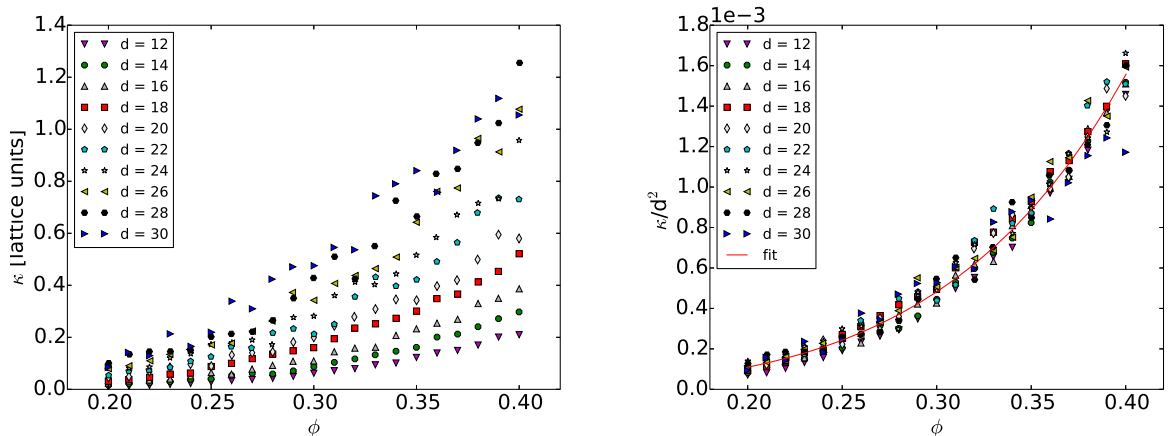
Figure 2.5: Permeability dependence on porosity and obstacle diameter. (Left) Permeability as a function of porosity for several obstacle diameters. (Right) Non-dimensional permeability as a function of porosity for several obstacle diameters. The curve fit is given by (2.6) with $C = 3.18 \pm 0.02$.

2.3.4 Specific superficial area

With the increasing popularization of Digital Rock Physics [3,4], some recent works proposed new techniques to calculate the SSA [6,68], but they are still quite complex and indirect. Measuring the SSA of porous rocks experimentally is a hard task [88] but it is important to understand the rock's properties [138]. We propose a methodology to calculate the SSA using widely-available `Python` libraries for image-processing. The advantage of our method is that it provides a visual interpretation of what is being calculated, making it simple enough to be understood and applied by beginners.

To calculate the SSA of a digital rock sample, we use the `binary_erosion` method of the `SciPy` library [2]. This operation *erodes* the image by removing a layer of pixels at the rock/pore boundary. When the eroded image is subtracted from the original, what remains are the pixels at the surface, which allows us to calculate the SSA using its basic definition. A `Python` implementation example is provided in the Supplementary Material section.

The first application of this method is a simple problem with analytical solution that consists in calculating the SSA of a single sphere for different radii. In Figure 2.6, we see the results for radii ranging from 5 to 70 compared to the analytical solution, $s = 3/R$. We see that the data follows the same behavior of the analytical curve, but with a small discrepancy that decreases as the radius increases. For instance, the relative difference between measured and analytical SSA for $R = 5$ is 28% and for $R = 70$ it decreases to 18%. This difference is due to a limitation in the spatial resolution that all digital images are subjected to. In Figure 2.6 we see three slices of spheres with different radii. The sphere with $R = 5$ is far from a spheroidal shape, while that with $R = 70$ is much closer. The better the spatial resolution, the more accurate is the proposed methodology. However, since the available GPU memory is limited, we cannot use arbitrarily large sample sizes to achieve higher resolutions.

---

[2]See `http://www.scipy-lectures.org/advanced/image_processing/`
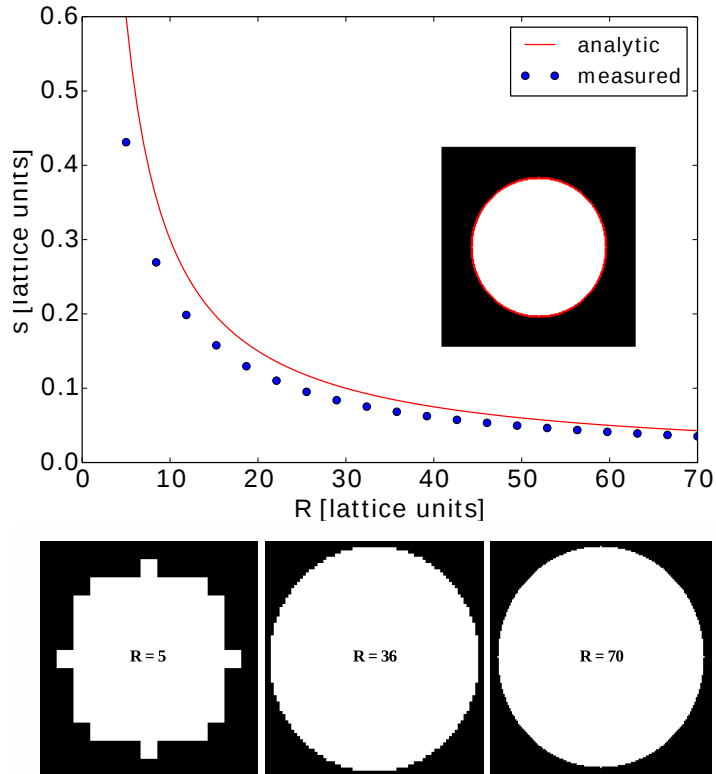
Figure 2.6: Specific surface area calculated according to the method in Sec. 2.3.4. (Top) Specific surface area for a single sphere as a function of radius, compared to the analytical expression. The inset shows a slice of a sphere with $R = 70$ and its surface area in red. (Bottom) Slices at the equator of digital spheres with different radii. The larger the radii, the closer the figure gets to a spherical shape.

After this simple, but revealing, example we calculated the SSA for our porous media samples. Figure 2.7 shows the surface of the obstacles, that is, the outermost layer isolated using the erosion operation. We clearly see the contour of the overlapped spheres and some partially filled circles, due to the finite resolution issue. In Figure 2.7 we show the SSA obtained as a result of our method for 21 samples with $d = 20$ and different porosities. The SSA clearly depends on porosity, which was not considered in our previous calculation of the Kozeny's constant. This dependence occurs due to obstacles being able to overlap [76], which changes their shape to non-spherical. If the spheres were isolated from each other, as in a close-packed structure, the SSA would be $s = 3/R$ as for a single sphere.
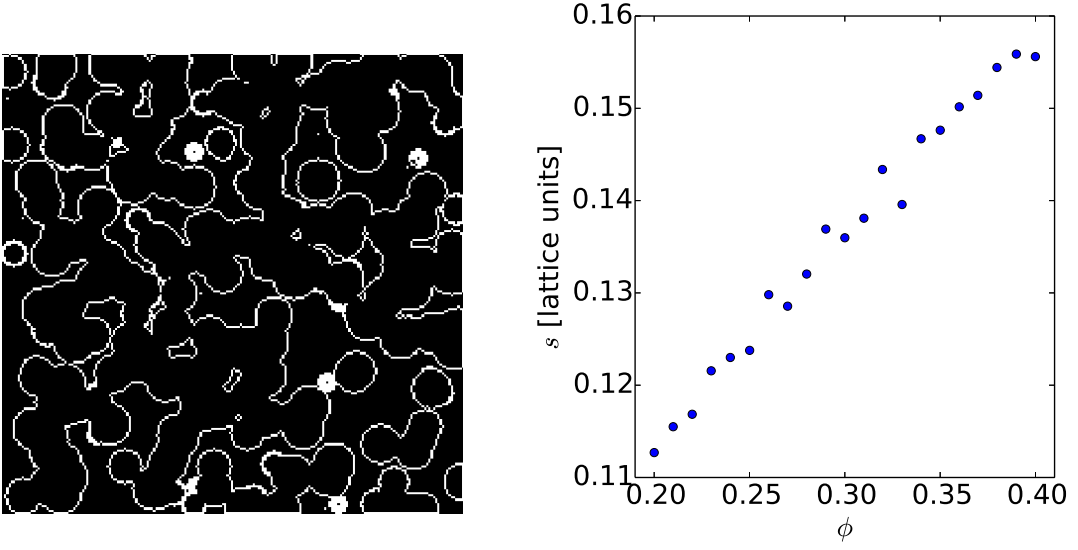
Figure 2.7: Specific surface are for porous media built using $d = 20$ nodes as obstacle diameter. (Left) A slice showing the SSA of an artificial porous media sample with $\phi = 0.3$. (Right) Specific surface area as a function of porosity for a given obstacle diameter.

2.3.5 Tortuosity

In general, it is difficult to calculate tortuosity using its basic definition, (2.1), for one would have to know exactly the central streamline. However, if one knows the velocity field, there is an easier way to perform this calculation. It has been shown [75] that (2.1) is equivalent to

$$\tau = \frac{\langle |\boldsymbol{u}| \rangle}{\langle u^j \rangle}, \tag{2.7}$$

where $|\boldsymbol{u}|$ is the magnitude of local velocity, u^j is the component of local velocity along the direction of flow x^j and $\langle \cdot \rangle$ represents the average over the entire system volume. This method has been extensively tested [93] and its results agree with theoretical predictions. For instance, for the trivial case of flow in a straight channel, $|\boldsymbol{u}| = u^j$ for every point in the fluid, which gives $\tau = 1$. This is the same result predicted by (2.1) since all streamlines are straight in this case [93]. If the streamlines in a particular flow are not straight, $|\boldsymbol{u}| \geq u^j$ for each point and $\tau > 1$ as in (2.1).

The tortuosity was calculated using the aforementioned method for samples with $d =$

20, as in Figure 2.8. We found a linear relationship between τ and ϕ in this range of porosities, despite all the noise, similar to previous reports in the literature [75, 76]. We adjusted a linear function to the data points and obtained $\tau(\phi) = 1.79 - 1.08\phi$.
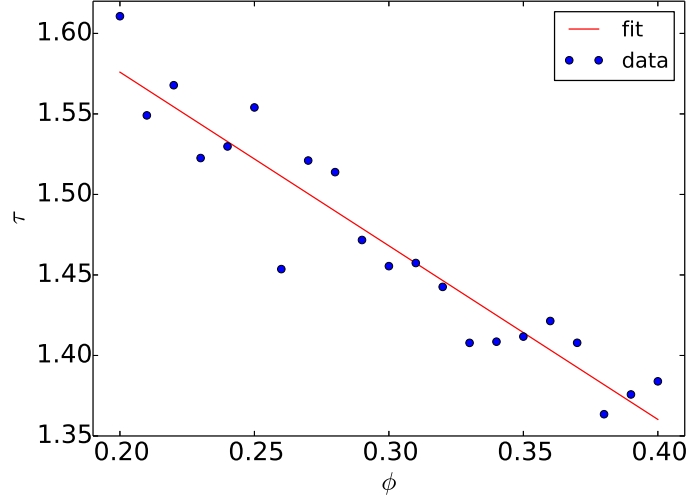
Figure 2.8: Relationship between tortuosity and porosity for samples with obstacle diameter $d = 20$.

2.4 Conclusion

This present chapter had two goals: (i) constructing an algorithm to build artificial porous media samples and (ii) presenting how the main properties of porous media are calculated using the output from LBM simulations. The first goal was addressed in Sec. 2.3.1. Identical spheroidal obstacles were placed in random positions (allowing overlap), creating structures similar to those observed in real rock samples, as exemplified in Figure 2.3.1.

To achieve the second goal, we developed the following analysis. In Sec. 2.3.2 we calculated the permeability of a particular sample using Darcy's law and verified that the drift velocity is linear to the external force. In Sec. 2.3.3 we investigated whether the Kozeny–Carman equation applies to the permeability-porosity relationship of our samples, obtaining a good agreement as seen in Figure 2.5. Although we allowed obstacles

to overlap in our artificial samples, destroying their otherwise spherical shape, Figure 2.5 shows that permeability still depends on the obstacle diameter, which allowed us to use a scale-law leading to Figure 2.5. In Sec. 2.3.4, we developed our technique for calculating the specific surface area in digital samples, tested it on a single sphere for different radii and obtained good agreement to the analytic solution for big radii. In Sec. 2.3.5 we presented a simple method to calculate tortuosity from the velocity field of the fluid.

Sailfish is a powerful LBM solver with many features that are out of the scope of this chapter. More complex flows can be simulated in porous media using Sailfish, such as multiphase [62] and turbulent flows [124]. One can also use Sailfish and the techniques described here to perform fluid dynamics studies inside fractures, which is another interesting subject for the oil and gas industry. The relationship between SSA and porosity in porous media is yet another interesting subject for future works [76].

Chapter 3

Generalized polynomials

In this chapter, we propose a set of orthonormal polynomials under a general weight in D-dimensional Euclidean space. They are symmetric tensors and the well known D-dimensional Hermite polynomials are shown to be a particular case of the present ones for the case of a gaussian weight. We explicitly determine the parameters of the first five polynomials (N from 0 to 4) and conjecture that the parameters can be obtained in any N^{th} order because of the remarkable match found between the orthonormality condition and the symmetrical tensors in the D-dimensional Euclidean space. In this way, we obtain generalizations of the Legendre and of the Chebyshev polynomials in D dimensions that reduce to the respective well-known orthonormal polynomials in D=1 dimensions. We also obtain new orthonormal D-dimensional polynomials under weights of interest to Physics, such as the Fermi-Dirac, Bose-Einstein, Graphene equilibrium distribution functions and the Yukawa potential.

3.1 Introduction

The theory of orthonormal polynomials is a branch of Mathematics and Physics [27, 56, 132, 139] that started in the nineteenth century and is still unfolding. It has provided the key ingredients to understand the Hilbert space in Quantum Mechanics, and also properties of Statistical Mechanics and Electromagnetism. Charles Hermite was the first

to introduce tensorial properties to the D-dimensional orthonormal polynomials but he has only considered the gaussian weight. They reduce to the well-known previously found one-dimensional Hermite polynomials (D=1). The properties of the D-dimensional Hermite polynomials have been investigated under several aspects, such as the obtainment of recurrence formulas [11]. The remarkably rich tensorial structure of the D-dimensional Euclidean space is the key element that allows for the existence of D-dimensional polynomials orthonormal under an arbitrary weight satisfying general properties. This rich tensorial structure is not present in D=1 since there is no Kronecker's delta function. However for higher $(D > 1)$ dimensions many tensors can be built as products and sums of the Kronecker's delta function. Harold Grad was the first one to notice the general properties of the D-dimensional tensors built from the Kronecker's delta function [54]. However he never extended his study to derive the D-dimensional polynomials orthonormal under a general weight. We carry on this task left by him and obtain these D-dimensional orthonormal polynomials.

Here we give the general form of the new D-dimensional tensorial polynomials and determine the parameters of the first five polynomials (N=0 to 4) by explicitly orthonormalizing them. The D-dimensional Hermite polynomials are retrieved as the particular case of the gaussian weight. We obtain D-dimensional generalizations of the Legendre and Chebyshev of first and second kind polynomials. By taking (D=1) the well-known one-dimensional Legendre and Chebyshev of first and second kind polynomials are retrieved. We construct new D-dimensional tensorial polynomials of interest for Physics, which are orthonormal under the BE, the FD and also the Graphene EDFs. They are of direct interest for the search of solutions of the Boltzmann equation describing semi-classical fluids [30, 31]. In such cases the corresponding D-dimensional Euclidean space is that of the microscopic velocity. As a last example we construct the D-dimensional polynomials for the Yukawa weight, which are useful in position space to derive the concept of an orthonormal multipole series expansion.

The D-dimensional Hermite polynomials have been applied in Quantum Optics [74] and Statistical Mechanics [33, 55, 81, 121]. In the latter case they offer fundamental aid to solve the Boltzmann equation for classical particles. Indeed it was H. Grad who first used the D-dimensional Hermite polynomials to describe the microscopic velocity space of the Boltzmann equation [54, 55, 81]. The Boltzmann equation aims a statistical description of an ensemble of particles and so describes the motion of a set of particles at a scale between the microscopic and the macroscopic levels. While the microscopic level has a deterministic description of motion, since Newton's law is applied to the individual particles, at the macroscopic level the only laws available are those of conservation of mass and momentum for many particles. For fluids and gases the macroscopic level corresponds to the continuity and to the Navier-Stokes equation, respectively, and it can be shown that both follow from the Boltzmann equation [30, 81, 121]. A few decades ago the study of the Boltzmann equation experienced a revival because of a new method developed to solve it on a lattice version of position space. Because of its simplicity this method revolutionized the way to numerically tackle problems in fluid dynamics. It became known as the LBM [82, 136] and uses the D-dimensional Hermite polynomials to span the distribution function, which essentially gives the number of particles in a point in phase space. The Gauss-Hermite quadrature is also used in this method to perform integration in the D-dimensional space. Thus D-dimensional polynomials are useful to understand the physical properties of many systems. In particular D=2 Laguerre polynomials [154] were developed to study Quantum Optics [74, 153]. Recently it was found that to render the LBM applicable to semi-classical fluids the weight that render the D-dimensional polynomials must be the EDF itself [31]. Therefore the gaussian weight is not appropriate because it is associated to the MB EDF whereas for semi-classical fluids the particles obey the BE or the FD EDFs [31]. Therefore there is a need to go beyond the D-dimensional Hermite polynomials in case of many problems treated by Boltzmann theory, such as for electrons in metals [31], the Kelvin-Helmholtz instability

on graphene [32] and for relativistic fluids [35, 96].

This chapter is organized as follows. In section 3.2 we propose the general form of the D-dimensional tensorial polynomials and explicitly write the first five ones. In section 3.3 the rich tensorial properties of D-dimensional space. The explicit construction of the first five (N=0 to 4) orthonormal polynomials is carried in section 3.4, which means that all their coefficients are obtained as functions of some integrals over the weight (I_N). Next we apply this general theory to specific weights in section 3.5. The known D-dimensional Hermite polynomials are derived from the present ones and also new D-dimensional generalizations of the Legendre and Chebyshev polynomials of the first and second kinds are proposed here. The projection of such polynomials to D=1 dimensions does give the well-known Hermite in subsection 3.5.1, Legendre (subsection 3.5.2) and Chebyshev (subsections 3.5.3 and 3.5.4) which are projected to D=1 dimension (subsection 3.5.5). Next we consider D-dimensional polynomials orthonormal under new weights, such as FD (subsection 3.5.6), BE (subsection 3.5.7), graphene (subsection 3.5.8) and Yukawa potential (subsection 3.5.9). We reach conclusions in section 3.6. Some useful tensorial identities are discussed in appendix A.

3.2 General D-dimensional Polynomials

Consider the D-dimensional Euclidean space endowed with a weight function $\omega(\boldsymbol{\xi})$ where the vector $\boldsymbol{\xi} \equiv (\xi_1, \xi_2, \cdots, \xi_D)$ is defined. We claim here the existence of a set of orthonormal polynomials $\mathcal{P}_{i_1 \cdots i_N}(\boldsymbol{\xi})$ in this space.

$$\int d^D \boldsymbol{\xi}\, \omega(\boldsymbol{\xi}) \mathcal{P}_{i_1 \cdots i_N}(\boldsymbol{\xi}) \mathcal{P}_{j_1 \cdots j_M}(\boldsymbol{\xi}) = \delta_{NM} \delta_{i_1 \cdots i_N | j_1 \cdots j_M}. \tag{3.1}$$

The polynomials $\mathcal{P}_{i_1 \cdots i_N}(\boldsymbol{\xi})$ are expressed in terms of the vector components ξ_i and of δ_{ij}. The N$^{\text{th}}$ order polynomial is symmetrical in the indices $i_1 \cdots i_N$, and its parity is $(-1)^N$.

$$\mathcal{P}_{i_1 \cdots i_N}(-\xi_{i_1}, \ldots, -\xi_{i_k}, \ldots, -\xi_{i_N}) = (-1)^N \mathcal{P}_{i_1 \cdots i_N}(\xi_{i_1}, \ldots, \xi_{i_k}, \ldots \xi_{i_N}) \tag{3.2}$$

The following tensors, defined by Harold Grad [54], are expressed as sums of products of the Kronecker's delta function, ($\delta_{ij} = 1$ for $i = j$ and 0 for $i \neq j$).

$$\delta_{i_1 \cdots i_N | j_1 \cdots j_N} \equiv \delta_{i_1 j_1} \cdots \delta_{i_N j_N} + \text{ permutations of } i\text{'s}, \tag{3.3}$$

and,

$$\delta_{i_1 \cdots i_N \, j_1 \cdots j_N} \equiv \delta_{i_1 j_1} \cdots \delta_{i_N j_N} + \text{ all permutations}. \tag{3.4}$$

The knowledge of the number of terms in such tensors is useful and discussed in more details in section 3.3. The first five (N=0 to 4) polynomials are given by,

$$\mathcal{P}_0(\boldsymbol{\xi}) = c_0, \tag{3.5}$$

$$\mathcal{P}_{i_1}(\boldsymbol{\xi}) = c_1 \, \xi_{i_1}, \tag{3.6}$$

$$\mathcal{P}_{i_1 i_2}(\boldsymbol{\xi}) = c_2 \, \xi_{i_1} \xi_{i_2} + f_2(\xi) \, \delta_{i_1 i_2}, \text{where } f_2(\xi) \equiv \bar{c}_2 \xi^2 + c'_2, \tag{3.7}$$

$$\mathcal{P}_{i_1 i_2 i_3}(\boldsymbol{\xi}) = c_3 \, \xi_{i_1} \xi_{i_2} \xi_{i_3} + f_3(\xi) \big(\xi_{i_1} \delta_{i_2 i_3} + \xi_{i_2} \delta_{i_1 i_3} + \xi_{i_3} \delta_{i_1 i_2} \big),$$

$$\text{where } f_3(\xi) \equiv \bar{c}_3 \xi^2 + c'_3, \tag{3.8}$$

$$\mathcal{P}_{i_1 i_2 i_3 i_4}(\boldsymbol{\xi}) = c_4 \, \xi_{i_1} \xi_{i_2} \xi_{i_3} \xi_{i_4} + f_4(\xi) \, \big(\xi_{i_1} \xi_{i_2} \delta_{i_3 i_4} + \xi_{i_1} \xi_{i_3} \delta_{i_2 i_4} + \xi_{i_1} \xi_{i_4} \delta_{i_2 i_3}$$

$$+ \xi_{i_2} \xi_{i_3} \delta_{i_1 i_4} + \xi_{i_2} \xi_{i_4} \delta_{i_1 i_3} + \xi_{i_3} \xi_{i_4} \delta_{i_1 i_2} \big) + g_4(\xi) \, \delta_{i_1 i_2 i_3 i_4},$$

$$\text{where } f_4(\xi) \equiv \big(\bar{c}_4 \xi^2 + c'_4 \big), \text{ and } g_4(\xi) \equiv \big(\bar{d}_4 \xi^4 + d'_4 \xi^2 + d_4 \big). \tag{3.9}$$

Therefore the Nth order polynomial is the sum of all possible symmetric tensors built from products of ξ_i and of δ_{ij} times coefficients which are themselves polynomials in ξ^2 to maximum allowed power. This proposal yields a unique expression for the Nth order polynomial. There is a deep tensorial structure behind the orthonormal condition of Eq.(3.1). Notice that the first five polynomials sum to a total of 14 coefficients to be determined (1 for N=0, 1 for N=1, 3 for N=2, 3 for N=3 and 6 for N=4). The orthonormality condition of Eq.(3.1) produces exactly the 14 equations needed to determine these coefficients. This remarkable matching between the orthonormality condition and the D-dimensional

Euclidean space symmetry group makes us conjecture that the present method of determining the coefficients can be extended to the Nth order.

We define integrals I_N which are central to the present study. They are assumed to exist and to have well defined properties.

$$I_N \, \delta_{i_1 \cdots i_N} \equiv \int d^D \boldsymbol{\xi} \, \omega(\boldsymbol{\xi}) \, \xi_{i_1} \cdots \xi_{i_N} \tag{3.10}$$

Hereafter the weight function is assumed to only depend on the modulus of the vector: $\omega(\boldsymbol{\xi}) = \omega(\xi)$, $\xi \equiv |\boldsymbol{\xi}|$. By symmetry it holds that $I_{2N+1} = 0$ since the integral vanishes. Using the spherical integration volume, $\int d^D \boldsymbol{\xi} \, \omega(\boldsymbol{\xi}) = D\pi^{D/2}/\Gamma(D/2+1) \int d\xi \, \xi^{D-1} \omega(\xi)$, the I_{2N} integrals become,

$$I_{2N} = \frac{\pi^{\frac{D}{2}}}{2^{N-1}\Gamma\left(N + \frac{D}{2}\right)} \int_0^{\xi_{max}} d\xi \, \omega(\xi) \, \xi^{2N+D-1}. \tag{3.11}$$

In case that $\xi_{max} = \infty$ the weight function must have the property $\omega(\boldsymbol{\xi}) \to 0$ for $\xi \to \infty$ faster than any power of ξ. Next we shall explicitly prove the orthonormality of the first five polynomials.

3.3 D-dimensional tensors based on the Kronecker's delta

The orthonormality condition of Eq.(3.1) shows a rich tensorial structure in D dimensions revealed by the following two important tensors, $\delta_{i_1 \cdots i_N | j_1 \cdots j_N}$ and $\delta_{i_1 \cdots i_N j_1 \cdots j_N}$, defined in Eqs.(3.3) and (3.4), respectively. The former is associated with the orthonormality condition while the latter is the totally symmetric tensor introduced in the definition of the functions I_N given by Eq.(3.10). Both tensors are expressed as sums over several terms each one expressed as a product of Kronecker's delta functions. We determine the number of terms in these two tensors. The tensor $\delta_{i_1 \cdots i_N | j_1 \cdots j_N}$ has N! terms since this tensor is a sum over all possible permutations of the i's under a fixed set of j's. The tensor $\delta_{i_1 \cdots i_N j_1 \cdots j_N}$

has $(2N-1)!/2^{N-1}(N-1)!=(2N-1)(2N-3)(2N-5)...1$ terms according to the arguments below. Firstly notice that the tensor $\delta_{i_1\cdots i_N j_1\cdots j_N}$ has more terms than $\delta_{i_1\cdots i_N|j_1\cdots j_N}$ and here we seek to find these remaining tensors.

$$\delta_{i_1\cdots i_N j_1\cdots j_N} = \delta_{i_1\cdots i_N|j_1\cdots j_N} + \text{ other tensors} \tag{3.12}$$

Next we determine the remaining "other tensors" in case N=0 to 4 and determine the number of components of the above tensor by induction. For this we introduce a short notation that only distinguishes indices i from j indices. In this notation the previous expression becomes equal to,

$$\delta_{ii\cdots i jj\cdots j} = \delta_{ii\cdots i|jj\cdots j} + \text{ other tensors.} \tag{3.13}$$

For N=1 we have that,

$$\delta_{ij} = \delta_{i|j}, \tag{3.14}$$

and we express this identity with respect to the number of terms simply as $1 = 1$. For N=2 notice that, $\delta_{i_1 i_2 j_1 j_2} = \delta_{i_1 j_1}\delta_{i_2 j_2} + \delta_{i_1 j_2}\delta_{i_2 j_1} + \delta_{i_1 i_2}\delta_{j_1 j_2}$. Since $\delta_{i_1 i_2|j_1 j_2} = \delta_{i_1 j_1}\delta_{i_2 j_2} + \delta_{i_1 j_2}\delta_{i_2 j_1}$ the above relation becomes, $\delta_{i_1 i_2 j_1 j_2} = \delta_{i_1 i_2|j_1 j_2} + \delta_{i_1 i_2}\delta_{j_1 j_2}$. Therefore it holds that $\delta_{i_1 i_2 j_1 j_2} = \delta_{i_1 i_2|j_1 j_2} + \delta_{i_1 i_2}\delta_{j_1 j_2}$. While $\delta_{i_1 i_2 j_1 j_2}$ contains 3 components, $\delta_{i_1 i_2|j_1 j_2}$ has only 2, such that it holds for this decomposition that $3 = 2 \oplus 1$. In the short notation the above relation becomes,

$$\delta_{ii|jj} = \delta_{ij}\delta_{ij} \tag{3.15}$$

$$\delta_{iijj} = \delta_{ij}\delta_{ij} + \delta_{ii}\delta_{jj}. \tag{3.16}$$

The tensors $\delta_{ij}\delta_{ij}$ and $\delta_{ii}\delta_{jj}$ contain 2 and 1 components, respectively. Thus the short notation gives that $\delta_{ii\cdots i|jj\cdots j} \equiv \delta_{ij}\delta_{ij}\cdots\delta_{ij}$ where the products of δ_{ij} takes into account all possible permutations. The tensor $\delta_{ii\cdots ijj\cdots j}$ cannot be expressed similarly because not all combinations of δ_{ij}'s are included. Therefore the need to decompose it into $\delta_{ii\cdots i|jj\cdots j}$

plus other tensors. For N=3 according to the short tensorial notation,

$$\delta_{iiijjj} = \delta_{ij}\delta_{ij}\delta_{ij} + \delta_{ii}\delta_{jj}\delta_{ij}. \tag{3.17}$$

To determine the number of components of this tensor, notice that for $\delta_{i_1 i_2 i_3 j_1 j_2 j_3}$ once a pair is chosen, say $\delta_{i_1 j_1}$, the previous N=2 is retrieved concerning the number of components. Since there are 5 ways to construct this first pair, the total number of components is 5 times 3, that is, 15 terms. The tensor $\delta_{ij}\delta_{ij}\delta_{ij}$ has 3! components, thus to know the number of terms in the tensor $\delta_{ii}\delta_{ij}\delta_{jj}$ we use the following argument. There are 3 components in δ_{ii}, namely, $\delta_{i_1 i_2}$, $\delta_{i_1 i_3}$ and $\delta_{i_2 i_3}$ and similarly, 3 components in δ_{jj}. Once fixed δ_{ii}, and δ_{jj} the tensor δ_{ij} has only one possible component left. Therefore $\delta_{ii}\delta_{ij}\delta_{jj}$ has a total of 3 times 1 times 3, that is 9 components, and the tensorial decomposition is expressed as $15 = 6 \oplus 9$.

Finally for N=4 the i and j short tensorial notation gives that,

$$\delta_{iiiijjjj} = \delta_{ij}\delta_{ij}\delta_{ij}\delta_{ij} + \delta_{ii}\delta_{jj}\delta_{ij}\delta_{ij} + \delta_{ii}\delta_{ii}\delta_{jj}\delta_{jj} \tag{3.18}$$

The same reasoning of the previous cases is used here, namely, once a pair is fixed, say $\delta_{i_1 j_1}$, the number of terms of the remaining indices is provided by the previous N=3 case. There are 7 ways to construct this first pair, thus the total number of terms is 7 times 15, that is, 105 terms. The tensor $\delta_{ij}\delta_{ij}\delta_{ij}\delta_{ij}$ has 4! terms, The tensor $\delta_{ii}\delta_{jj}\delta_{ij}\delta_{ij}$ has 6 possible terms for δ_{ii}, $\delta_{i_1 i_2}$, $\delta_{i_1 i_3}$, $\delta_{i_1 i_4}$, $\delta_{i_2 i_3}$, $\delta_{i_2 i_4}$ and $\delta_{i_3 i_4}$, and the same applies for δ_{jj}. Thus only 2 choices are left for $\delta_{ij}\delta_{ij}$, once the indices of δ_{ii} and δ_{jj} are fixed. Hence the total number of terms is 6 times 6 times 2, namely, 72 terms. For the tensor $\delta_{ii}\delta_{ii}\delta_{jj}\delta_{jj}$ the pairs $\delta_{ii}\delta_{ii}$ have only three terms each and so is for $\delta_{jj}\delta_{jj}$, such that the total is 3 times 3, namely, 9 terms. The tensorial decomposition is expressed as $105 = 24 \oplus 72 \oplus 9$.

3.4 Orthonormalization of polynomials to order N=4

The coefficients of the polynomials are determined here in terms of the integrals I_N. This is done for the first five polynomials by explicitly computing their inner products. We refer to Eq.(3.1) by the short notation,

$$\left(\mathcal{P}_{(M)}, \mathcal{P}_{(N)}\right) \equiv \int d^D \boldsymbol{\xi}\, \omega(\boldsymbol{\xi}) \mathcal{P}_{(M)}(\boldsymbol{\xi}) \mathcal{P}_{(N)}(\boldsymbol{\xi}),$$

used here for $M, N = 0, \cdots 4$. The Nth order polynomial is shortly referred as $\mathcal{P}_{(N)}$ such that the polynomials of Eqs.(3.5), (3.6), (3.7), (3.8), (3.9) are called $\mathcal{P}_{(0)}$, $\mathcal{P}_{(1)}$, $\mathcal{P}_{(2)}$, $\mathcal{P}_{(3)}$ and $\mathcal{P}_{(4)}$, respectively. The inner product between polynomials with distinct parity vanishes, $\left(\mathcal{P}_{(even)}, \mathcal{P}_{(odd)}\right) = 0$. Thus the only relevant orthonormality relations are among polynomials with the same parity (odd with odd and even with even).

The number of equations given by orthonormalization conditions must be equal to the number of free coefficients. Indeed this is the case, according to Eqs.(3.5), (3.6), (3.7), (3.8), (3.9). The total number of coefficients is 14 (c_K for $K = 0, 1, 2, 3, 4$, c'_K for $K = 2, 3, 4$, $\bar{c}_K$ for $K = 2, 3, 4$, d_4, d'_4 and $\bar{d}_4$). Remarkably 14 equations arise from the 9 orthonormalization conditions $\left(\mathcal{P}_{(M)}, \mathcal{P}_{(N)}\right)$, as seen below.

- $\left(\mathcal{P}_{(0)}, \mathcal{P}_{(0)}\right)$

The normalization of the N=0 polynomial is,

$$c_0^2 \int d^D \boldsymbol{\xi}\, \omega(\xi) = 1, \tag{3.19}$$

which gives that,

$$c_0 = \pm \frac{1}{\sqrt{I_0}}, \tag{3.20}$$

where Eq. (3.5) and the definition of I_0 in Eq.(3.10) have been used.

- $\left(\mathcal{P}_{(1)}, \mathcal{P}_{(1)}\right)$

$$c_1^2 \int d^D \boldsymbol{\xi} \; \omega(\xi) \xi_{i_1} \xi_{j_1} = \delta_{i_1 j_1} \tag{3.21}$$

The definition of I_2 in Eq.(3.10) is invoked to obtain that,

$$c_1 = \pm \frac{1}{\sqrt{I_2}}. \tag{3.22}$$

The N=0 and N=1 polynomials are naturally orthogonal because they have distinct parity and to make them orthonormal is enough to normalize them which has been done above by determining the coefficients c_0 and c_1. The polynomial $\mathcal{P}_{(2)}$ has three coefficients, according to Eq.(3.7), and so, three equations are needed to determine them. These equations must arise from the tensorial structure of the D dimensional space.

- $\left(\mathcal{P}_{(0)}, \mathcal{P}_{(2)}\right)$

This conditions is equivalent to $c_0 \left(1, \mathcal{P}_{(2)}\right) = 0$ since $\mathcal{P}_{(0)}$ is a constant.

$$c_0 \int d^D \boldsymbol{\xi} \omega(\xi) \left[c_2 \, \xi_{i_1} \xi_{i_2} + f_2(\xi) \, \delta_{i_1 i_2} \right] = 0. \tag{3.23}$$

Using the tensorial formulas of appendix A and Eq.(3.10), it follows that,

$$I_2 c_2 + D I_2 \bar{c}_2 + I_0 c_2' = 0. \tag{3.24}$$

- $\left(\mathcal{P}_{(2)}, \mathcal{P}_{(2)}\right)$

Remarkably the normalization of the N=2 polynomial leads to multiple equations, in

this case the following two equations.

$$\int d^D \boldsymbol{\xi}\, \omega(\xi)\, [c_2\, \xi_{i_1}\xi_{i_2} + f_2(\xi)\, \delta_{i_1 i_2}]\, [c_2\, \xi_{j_1}\xi_{j_2} + f_2(\xi)\, \delta_{j_1 j_2}] = \delta_{i_1 j_1}\delta_{i_2 j_2} + \delta_{i_1 j_2}\delta_{i_2 j_1}. \quad (3.25)$$

This is because while the orthonormalization is associated to the tensor $\delta_{i_1 j_1}\delta_{i_2 j_2} + \delta_{i_1 j_2}\delta_{i_2 j_1}$ the integration over $\xi_{i_1}\xi_{i_2}\xi_{j_1}\xi_{j_2}$ leads to the tensor $\delta_{i_1 j_1}\delta_{i_2 j_2} + \delta_{i_1 j_2}\delta_{i_2 j_1} + \delta_{i_1 i_2}\delta_{j_1 j_2}$. This difference is responsible for the onset of more than one condition. Using the tensorial formulas of appendix A, one obtains that:

$$c_2^2 I_4 \big(\delta_{i_1 j_1}\delta_{i_2 j_2} + \delta_{i_1 j_2}\delta_{i_2 j_1} + \delta_{i_1 i_2}\delta_{j_1 j_2} \big) + \Big[2(D+2)I_4 c_2 \bar{c}_2 + 2I_2 c_2 c_2' + \bar{c}_2^2 D(D+2)I_4$$

$$+2DI_2 \bar{c}_2 c_2' + c_2'^2 I_0 \Big] \delta_{i_1 i_2}\delta_{j_1 j_2} = \delta_{i_1 j_1}\delta_{i_2 j_2} + \delta_{i_1 j_2}\delta_{i_2 j_1}. \quad (3.26)$$

The independence of the two tensors leads to two independent equations, given by,

$$c_2^2 I_4 = 1, \quad c_2^2 I_4 + 2(D+2)I_4 c_2 \bar{c}_2 + 2I_2 c_2 c_2' + \bar{c}_2^2 D(D+2)I_4 + 2DI_2 \bar{c}_2 c_2' + c_2'^2 I_0 = 0. (3.27)$$

The three equations are promptly solved and the coefficients c_2, $\bar{c}_2$ and c'_2 are determined below.

$$c_2 = \pm \frac{1}{\sqrt{I_4}}. \quad (3.28)$$

Using Eq.(3.23) to write c'_2, we have

$$c_2' = -\frac{I_2}{I_0} c_2 - D\frac{I_2}{I_0}\bar{c}_2. \quad (3.29)$$

Substituting c'_1 in Eq.(3.27),

$$\bar{c}_2^2 \Big[D(D+2)I_4 - D^2\frac{I_2^2}{I_0} \Big] + \bar{c}_2 c_2 \Big[2(D+2)I_4 - 2D\frac{I_2^2}{I_0} \Big] + c_2^2 \Big(I_4 - \frac{I_2^2}{I_0} \Big) = 0, \quad (3.30)$$

which is a equation for $\bar{c}_2$. The solutions, are:

$$\bar{c}_2 = \frac{c_2}{D}(-1 + \Delta_2), \text{ where } \Delta_2 \equiv \pm\sqrt{\frac{2}{(D+2) - DJ_2}}, \quad J_2 \equiv \frac{I_2^2}{I_0 I_4} \quad (3.31)$$

The coefficient $\bar{c}_2$ must be a real number, and this is the case provided that $(D+2) - DJ_2 \geq 0$. From Eq.(3.23), we calculate c'_2, to obtain that,

$$c_2' = -c_2 \frac{I_2}{I_0}\Delta_2. \quad (3.32)$$

The orthogonalization of the first three polynomials has been concluded here. We proceed to the next order (N=3), and because of the increasing difficulty introduce a short notation for tensors, which is discussed in section 3.3. The N=3 polynomial has three coefficients, similarly to the N=2 case, and so, three equations are needed to determine them.

- $\left(\mathcal{P}_{(1)}, \mathcal{P}_{(3)}\right)$

$$c_1 \int d^D \boldsymbol{\xi}\, \omega(\xi)\, \xi_{i_1} \left[c_3\, \xi_{j_1} \xi_{j_2} \xi_{j_3} + f_3(\xi) \left(\xi_{j_1} \delta_{j_2 j_3} + \xi_{j_2} \delta_{j_1 j_3} + \xi_{j_3} \delta_{j_1 j_2} \right) \right] = 0. \qquad (3.33)$$

The integrals are calculated with the help of the tensorial formulas of appendix A, such that the above expression becomes $\left[c_3 I_4 + \bar{c}_3 I_4 (D+2) + c_3' I_2 \right] \delta_{ijjj} = 0$. The tensor δ_{ijjj} is short for $\delta_{i_1 j_1 j_2 j_3}$, according to the notation of section 3.3. Thus we obtain that,

$$c_3 I_4 + \bar{c}_3 I_4 (D+2) + c_3' I_2 = 0. \qquad (3.34)$$

- $\left(\mathcal{P}_{(3)}, \mathcal{P}_{(3)}\right)$

This normalization condition gives the two other equations necessary to calculate the coefficients.

$$\int d^D \boldsymbol{\xi}\, \omega(\xi) \left[c_3\, \xi_{i_1} \xi_{i_2} \xi_{i_3} + f_3(\xi) \left(\xi_{i_1} \delta_{i_2 i_3} + \xi_{i_2} \delta_{i_1 i_3} + \xi_{i_3} \delta_{i_1 i_2} \right) \right] \left[c_3\, \xi_{j_1} \xi_{j_2} \xi_{j_3} \right.$$
$$\left. + f_3(\xi) \left(\xi_{j_1} \delta_{j_2 j_3} + \xi_{j_2} \delta_{j_1 j_3} + \xi_{j_3} \delta_{j_1 j_2} \right) \right] = \delta_{i_1 i_2 i_3 | j_1 j_2 j_3} \qquad (3.35)$$

We stress the difference between the tensors δ_{iiijjj} and $\delta_{iii|jjj}$ as the reason for multiple equations from a single normalization condition. Using the short notation of section 3.3 the integral over the six vector components becomes, $\int d^D \boldsymbol{\xi}\, \omega(\xi)\, \xi_i \xi_i \xi_i \xi_j \xi_j \xi_j = I_6 \delta_{iiijjj}$,

where all permutations of i's and j's are taken into account. From the other side in this short notation, $\delta_{iii|jjj} = \delta_{ij}\delta_{ij}\delta_{ij}$, as explained in section 3.3, and, as shown there, $\delta_{iiijjj} = \delta_{ij}\delta_{ij}\delta_{ij} + \delta_{ii}\delta_{ij}\delta_{jj}$. Thus the above integrals are computed with the aid of appendix A. Using this notation, Eq.(3.35) becomes,

$$
c_3^2 I_6 \left(\delta_{ij}\delta_{ij}\delta_{ij} + \delta_{ii}\delta_{ij}\delta_{jj} \right) + \left[2I_6(D+4)c_3\bar{c}_3 + 2I_4 c_3 c_3' + I_2 {c_3'}^2 + 2I_4(D+2)\bar{c}_3 c_3' \right.
$$
$$
\left. + I_6(D+2)(D+4)\bar{c}_3^2 \right] \delta_{ii}\delta_{ij}\delta_{jj} = \delta_{ij}\delta_{ij}\delta_{ij}, \tag{3.36}
$$

which gives two equations:

$$
c_3^2 I_6 = 1 \ \text{ and, } \ c_3^2 I_6 + 2I_6(D+4)c_3\bar{c}_3 + 2I_4 c_3 c_3' + I_2 {c_3'}^2 + 2I_4(D+2)\bar{c}_3 c_3'
$$
$$
+ I_6(D+2)(D+4)\bar{c}_3^2 = 0. \tag{3.37}
$$

The solution of the first equation is,

$$
c_3 = \pm \frac{1}{\sqrt{I_6}}. \tag{3.38}
$$

Eq.(3.34) is used to eliminate c_3' from Eq.(3.37),

$$
\bar{c}_3^2(D+2) \left[\left(I_6 - \frac{I_4^2}{I_2} \right)(D+2) + 2I_6 \right] + 2 \left[\left(I_6 - \frac{I_4^2}{I_2} \right)(D+2) + 2I_6 \right] c_3\bar{c}_3
$$
$$
+ \left(I_6 - \frac{I_4^2}{I_2} \right) c_3^2 = 0. \tag{3.39}
$$

This equation can be solved for $\bar{c}_3$.

$$
\bar{c}_3 = \frac{c_3}{D+2}(-1 + \Delta_4), \tag{3.40}
$$

and c_3' is calculated by Eq.(3.34):

$$
c_3' = -\frac{I_4}{I_2}\Delta_4 c_3 \ \text{ where } \ \Delta_4 = \pm \sqrt{\frac{2}{(D+4) - J_4(D+2)}}, \ J_4 = \frac{I_4^2}{I_6 I_2}. \tag{3.41}
$$

The N=4 polynomial of Eq.(3.9) sets a new level of difficulty as six equations must be obtained to calculate the six coefficients.

- $\left(\mathcal{P}_{(0)}, \mathcal{P}_{(4)}\right)$

The orthonormalization with the N=0 polynomial means that $c_0\left(1, \mathcal{P}_{(4)}\right)=0$.

$$c_0 \int d^D \boldsymbol{\xi} \omega(\xi)\left[c_4\, \xi_{j_1}\xi_{j_2}\xi_{j_3}\xi_{j_4} + f_4(\xi)\left(\xi_{j_1}\xi_{j_2}\delta_{j_3 j_4} + \xi_{j_1}\xi_{j_3}\delta_{j_2 j_4} + \xi_{j_1}\xi_{j_4}\delta_{j_2 j_3}\right.\right.$$
$$\left.\left.+\xi_{j_2}\xi_{j_3}\delta_{j_1 j_4} + \xi_{j_2}\xi_{j_4}\delta_{j_1 j_3} + \xi_{j_3}\xi_{j_4}\delta_{j_1 j_2}\right) + g_4(\xi)\,\delta_{j_1 j_2 j_3 i j_4}\right] = 0 \tag{3.42}$$

A single equation results from this integral since it can only be proportional to the tensor δ_{iiii}.

$$c_4 I_4 + 2\left[c_4' I_2 + \bar{c}_4 I_4(D+2)\right] + d_4 I_0 + d_4' I_2 D + \bar{d}_4 I_4(D+2)D = 0.$$

- $\left(\mathcal{P}_{(2)}, \mathcal{P}_{(4)}\right)$

The integration of the N=2 with the N=4 polynomial gives that,

$$\int d^D \boldsymbol{\xi} \omega(\xi)\left[c_2\, \xi_{i_1}\xi_{i_2} + f_2(\xi)\,\delta_{i_1 i_2}\right]\left[c_4\, \xi_{j_1}\xi_{j_2}\xi_{j_3}\xi_{j_4} + f_4(\xi)\left(\xi_{j_1}\xi_{j_2}\delta_{j_3 j_4} + \xi_{j_1}\xi_{j_3}\delta_{j_2 j_4}\right.\right.$$
$$\left.\left.+\xi_{j_1}\xi_{j_4}\delta_{j_2 j_3} + \xi_{j_2}\xi_{j_3}\delta_{j_1 j_4} + \xi_{j_2}\xi_{j_4}\delta_{j_1 j_3} + \xi_{j_3}\xi_{j_4}\delta_{j_1 j_2}\right) + g_4(\xi)\,\delta_{j_1 j_2 j_3 j_4}\right] = 0. \tag{3.43}$$

The sixth order tensorial integral, $\int d^D \boldsymbol{\xi} \omega(\xi)\xi_i\xi_i\xi_j\xi_j\xi_j\xi_j = I_6 \delta_{iijjjj}$ has 15 terms. This tensor can be decomposed as $\delta_{iijjjj} = \delta_{ii}\delta_{jjjj} + \delta_{ij}\delta_{ijjj}$, namely, as a sum of two other tensors, which have 3 and 12 terms, respectively. This decomposition can be formally expressed as $15 = 3 \oplus 12$, as discussed in section 3.3. We notice the presence of the tensor $\delta_{i_1 i_2 j_1 j_2}\delta_{j_3 j_4} + \delta_{i_1 i_2 j_1 j_3}\delta_{j_2 j_4} + \delta_{i_1 i_2 j_1 j_4}\delta_{j_2 j_3} + \delta_{i_1 i_2 j_2 j_3}\delta_{j_1 j_4} + \delta_{i_1 i_2 j_2 j_4}\delta_{j_1 j_3} + \delta_{i_1 i_2 j_3 j_4}\delta_{j_1 j_2}$, which has 18 terms, and is equal to $2\delta_{jjjj}\delta_{ii} + \delta_{iiij}\delta_{ij}$ (2 times 3 plus 12). Therefore Eq.(3.43)

becomes,

$$c_4 c_2 I_6 \big(\delta_{ii}\delta_{jjjj} + \delta_{ij}\delta_{ijjj} \big) + c_4 \big[c'_2 I_4 + \bar{c}_2 I_6(D+4) \big] \delta_{ii}\delta_{jjjj} + c_2 \big[c'_4 I_4 + \bar{c}_4 I_6(D+4) \big]$$

$$\big(2\delta_{ii}\delta_{jjjj} + \delta_{ij}\delta_{ijjj} \big) + 2\big[c'_4 c'_2 I_2 + \big(\bar{c}_4 c'_2 + c'_4 \bar{c}_2 \big) I_4(D+2) + \bar{c}_4 \bar{c}_2 I_6(D+4)(D+2) \big] \delta_{ii}\delta_{jjjj}$$

$$+ c_2 \big[d_4 I_2 + d'_4 I_4(D+2) + I_6 \bar{d}_4 (D+4)(D+2) \big] \delta_{ii}\delta_{jjjj} + \big[d_4 c'_2 I_0 + \big(d_4 \bar{c}_2 + d'_4 c'_2 \big) I_2 D$$

$$+ \big(d'_4 \bar{c}_2 + \bar{d}_4 c'_2 \big) I_4(D+2)D + \bar{d}_4 \bar{c}_2 I_6(D+4)(D+2)D \big] \delta_{ii}\delta_{jjjj} = 0. \tag{3.44}$$

This lead to two equations, one proportional to $\delta_{ij}\delta_{ijjj}$,

$$c_4 I_6 + [c'_4 I_4 + \bar{c}_4 I_6(D+4)] = 0, \tag{3.45}$$

and the other proportional to $\delta_{ii}\delta_{jjjj}$,

$$c_4 c_2 I_6 + c_4 \big[c'_2 I_4 + \bar{c}_2 I_6(D+4) \big] + 2c_2 \big[c'_4 I_4 + \bar{c}_4 I_6(D+4) \big] + 2\big[c'_4 c'_2 I_2$$

$$+ \big(\bar{c}_4 c'_2 + c'_4 \bar{c}_2 \big) I_4(D+2) + \bar{c}_4 \bar{c}_2 I_6(D+4)(D+2) \big] + c_2 \big[d_4 I_2 + d'_4 I_4(D+2)$$

$$+ \bar{d}_4 I_6(D+4)(D+2) \big] + \big[d_4 c'_2 I_0 + \big(d_4 \bar{c}_2 + d'_4 c'_2 \big) I_2 D + \big(d'_4 \bar{c}_2 + \bar{d}_4 c'_2 \big) I_4(D$$

$$+2)D + \bar{d}_4 \bar{c}_2 I_6(D+4)(D+2)D \big] = 0, \tag{3.46}$$

respectively.

- $\big(\mathcal{P}_{(4)}, \mathcal{P}_{(4)} \big)$

The normalization of the N=4 polynomial is given by,

$$\int d^D \boldsymbol{\xi}\, \omega(\xi) \Big[c_4\, \xi_{i_1}\xi_{i_2}\xi_{i_3}\xi_{i_4} + f_4(\xi) \big(\xi_{i_1}\xi_{i_2}\delta_{i_3 i_4} + \xi_{i_1}\xi_{i_3}\delta_{i_2 i_4} + \xi_{i_1}\xi_{i_4}\delta_{i_2 i_3} + \xi_{i_2}\xi_{i_3}\delta_{i_1 i_4}$$

$$+ \xi_{i_2}\xi_{i_4}\delta_{i_1 i_3} + \xi_{i_3}\xi_{i_4}\delta_{i_1 i_2} \big) + g_4(\xi)\,\delta_{i_1 i_2 i_3 i_4} \Big] \Big[c_4\, \xi_{j_1}\xi_{j_2}\xi_{j_3}\xi_{j_4} + f_4(\xi) \big(\xi_{j_1}\xi_{j_2}\delta_{j_3 j_4} + \xi_{j_1}\xi_{j_3}\delta_{j_2 j_4}$$

$$+ \xi_{j_1}\xi_{j_4}\delta_{j_2 j_3} + \xi_{j_2}\xi_{j_3}\delta_{j_1 j_4} + \xi_{j_2}\xi_{j_4}\delta_{j_1 j_3} + \xi_{j_3}\xi_{j_4}\delta_{j_1 j_2} \big) + g_4(\xi)\,\delta_{j_1 j_2 j_3 j_4} \Big] = \delta_{i_1 i_2 i_3 i_4 | j_1 j_2 j_3 j_4}.$$

$$\tag{3.47}$$

Here we extensively use the short notation of section 3.3, where $\delta_{iiii|jjjj} = \delta_{ij}\delta_{ij}\delta_{ij}\delta_{ij}$. There is the integral $\int d^D \boldsymbol{\xi}\, \omega(\xi)\ \xi_i\xi_i\xi_i\xi_i\xi_j\xi_j\xi_j\xi_j = I_8 \delta_{iiiijjjj}$. It holds that $\delta_{iiii|jjjj} =$

$\delta_{ij}\delta_{ij}\delta_{ij}\delta_{ij} + \delta_{ii}\delta_{jj}\delta_{ij}\delta_{ij} + \delta_{ii}\delta_{ii}\delta_{jj}\delta_{jj}$. There are 105 terms in $\delta_{iiiijjjj}$, 24 in $\delta_{ij}\delta_{ij}\delta_{ij}\delta_{ij}$, 72 in $\delta_{ii}\delta_{jj}\delta_{ij}\delta_{ij}$, and 9 in $\delta_{ii}\delta_{ii}\delta_{jj}\delta_{jj}$. We computed each of the integrals individually and identify them by the following notation that uses the product of their coefficients c_4, f_4 and g_4. For instance the first one is

$$\int d^D\boldsymbol{\xi}\,\omega(\xi)\,c_4^2[\cdots] = I_8 c_4^2(\delta_{ij}\delta_{ij}\delta_{ij}\delta_{ij} + \delta_{ii}\delta_{jj}\delta_{ij}\delta_{ij} + \delta_{ii}\delta_{ii}\delta_{jj}\delta_{jj}) \tag{3.48}$$

The second term is,

$$\int d^D\boldsymbol{\xi}\,\omega(\xi)\,c_4 f_4[\cdots] = 2[c_4' I_6 + \bar{c}_4 I_8(D+6)]c_4(\delta_{ii}\delta_{jj}\delta_{ij}\delta_{ij} + 2\delta_{ii}\delta_{ii}\delta_{jj}\delta_{jj}), \tag{3.49}$$

where we have used that $\delta_{iiiijj}\delta_{jj} = \delta_{ii}\delta_{jj}\delta_{ij}\delta_{ij} + 2\delta_{ii}\delta_{ii}\delta_{jj}\delta_{jj}$.

$$\int d^D\boldsymbol{\xi}\,\omega(\xi)\,c_4 g_4[\cdots] = 2[d_4 I_4 + d_4' I_6(D+4) + \bar{d}_4 I_8(D+6)(D+4)]c_4(\delta_{ii}\delta_{ii}\delta_{jj}\delta_{jj}), \tag{3.50}$$

$$\int d^D\boldsymbol{\xi}\,\omega(\xi)\,f_4 g_4[\cdots] = 4[c_4' d_4 I_2 + (c_4' d_4' + \bar{c}_4 d_4)I_4(D+2) + (\bar{c}_4 d_4'$$
$$+c_4'\bar{d}_4)I_6(D+4)(D+2) + \bar{c}_4\bar{d}_4 I_8(D+6)(D+4)(D+2)](\delta_{ii}\delta_{ii}\delta_{jj}\delta_{jj}) \tag{3.51}$$

$$\int d^D\boldsymbol{\xi}\,\omega(\xi)\,f_4^2[\cdots] = [c_4'^2 I_4 + 2c_4'\bar{c}_4 I_6(D+4)$$
$$+\bar{c}_4^2 I_8(D+6)(D+4)](4\delta_{ii}\delta_{ii}\delta_{jj}\delta_{jj} + \delta_{ii}\delta_{jj}\delta_{ij}\delta_{ij}) \tag{3.52}$$

$$\int d^D\boldsymbol{\xi}\,\omega(\xi)\,g_4^2[\cdots] = [d_4^2 I_0 + 2d_4 d_4' I_2 D + (d_4'^2 + 2d_4\bar{d}_4)I_4(D+2)D$$
$$+2d_4'\bar{d}_4 I_6(D+4)(D+2)D + \bar{d}_4^2 I_8(D+6)(D+4)(D+2)D](\delta_{ii}\delta_{ii}\delta_{jj}\delta_{jj}) \tag{3.53}$$

Next these integrals are introduced into Eq.(3.47) to obtain that,

$$I_8(\delta_{ij}\delta_{ij}\delta_{ij}\delta_{ij} + \delta_{ii}\delta_{jj}\delta_{ij}\delta_{ij} + \delta_{ii}\delta_{ii}\delta_{jj}\delta_{jj})c_4^2 + 2[c_4' I_6 + \bar{c}_4 I_8(D+6)]c_4(2\delta_{ii}\delta_{ii}\delta_{jj}\delta_{jj}$$
$$+\delta_{ii}\delta_{jj}\delta_{ij}\delta_{ij}) + 2[d_4 I_4 + d_4' I_6(D+4) + \bar{d}_4 I_8(D+6)(D+4)]\delta_{ii}\delta_{ii}\delta_{jj}\delta_{jj} + 4[c_4' d_4 I_2$$
$$+(c_4' d_4' + \bar{c}_4 d_4)I_4(D+2) + (\bar{c}_4 d_4' + c_4'\bar{d}_4)I_6(D+4)(D+2) + \bar{c}_4\bar{d}_4 I_8(D+6)(D+4)$$
$$\cdot(D+2)]\delta_{ii}\delta_{ii}\delta_{jj}\delta_{jj} + [c_4'^2 I_4 + 2c_4'\bar{c}_4 I_6(D+4) + \bar{c}_4^2 I_8(D+6)(D+4)](4\delta_{ii}\delta_{ii}\delta_{jj}\delta_{jj}$$
$$+\delta_{ii}\delta_{jj}\delta_{ij}\delta_{ij}) + [d_4^2 I_0 + 2d_4 d_4' I_2 D + (d_4'^2 + 2d_4\bar{d}_4)I_4(D+2)D + 2d_4'\bar{d}_4 I_6(D+4)$$
$$\cdot(D+2)D + \bar{d}_4^2 I_8(D+6)(D+4)(D+2)D]\delta_{ii}\delta_{ii}\delta_{jj}\delta_{jj} = \delta_{ij}\delta_{ij}\delta_{ij}\delta_{ij}. \tag{3.54}$$

The three remaining equations are the coefficients of the three independent tensors in the above equation.

$$I_8 c_4^2 = 1, \tag{3.55}$$

$$I_8 c_4^2 + 2[c_4' I_6 + \bar{c}_4 I_8(D+6)]c_4 + [c_4'^2 I_4 + 2c_4' \bar{c}_4 I_6(D+4) + \bar{c}_4^2 I_8(D+6)(D+4)] = 0, \tag{3.56}$$

$$
\begin{aligned}
I_8 c_4^2 &+ 4c_4[c_4' I_6 + \bar{c}_4 I_8(D+6)] + 2c_4[d_4 I_4 + d_4' I_6(D+4) + \bar{d}_4 I_8(D+6)(D+4)] \\
&+ 4[c_4' d_4 I_2 + (c_4' d_4' + \bar{c}_4 d_4)I_4(D+2) + (\bar{c}_4 d_4' + c_4' \bar{d}_4)I_6(D+4)(D+2) \\
&+ \bar{c}_4 \bar{d}_4 I_8(D+6)(D+4)(D+2)] + 4[c_4'^2 I_4 + 2c_4' \bar{c}_4 I_6(D+4) + \bar{c}_4^2 I_8(D+6) \\
&\cdot(D+4)] + [d_4^2 I_0 + 2d_4 d_4' I_2 D + (d_4''^2 + 2d_4 \bar{d}_4)I_4(D+2)D + 2d_4' \bar{d}_4 I_6(D+4) \\
&\cdot(D+2)D + \bar{d}_4^2 I_8(D+6)(D+4)(D+2)D] = 0. \tag{3.57}
\end{aligned}
$$

The six equations given by the Eqs.(3.43), (3.45), (3.46), (3.55), (3.56) and (3.57) can be solved to obtain the six coefficients. Nevertheless notice that coefficients c_4, $\bar{c}_4$ and c_4' are determined from a sub set of equations, namely, Eqs.(3.45), (3.55), and (3.56). From them it follows that,

$$c_4 = \pm\frac{1}{\sqrt{I_8}}, \text{ and,} \tag{3.58}$$

$$\bar{c}_4^2(D+4)\Big[I_8(D+6) - \frac{I_6^2}{I_4}(D+4)\Big] + 2\Big[I_8((D+6)$$
$$-\frac{I_6^2}{I_4}(D+4) +\Big]c_4\bar{c}_4 + \Big(I_8 - \frac{I_6^2}{I_4}\Big)c_4^2 = 0. \tag{3.59}$$

Hence one obtains that,

$$\bar{c}_4 = c_4\frac{(-1+\Delta_6)}{D+4}, \text{ and} \tag{3.60}$$

$$c_4' = -\frac{I_6}{I_4}\Delta_6 c_4. \tag{3.61}$$

The remaining coefficients are given by,

$$\bar{d}_4 = \frac{\delta_2}{\delta_4 D(D+2)}d_4 + \frac{c_4[D - 2(D+2)\Delta_6]}{D(D+2)(D+4)}, \tag{3.62}$$

$$d'_4 = -\frac{d_4}{D}\left(\frac{I_0}{I_2} + \frac{I_4}{I_2}\frac{\delta_2}{\delta_4}\right) + \frac{2I_6\Delta_6 c_4}{I_4 D}, \tag{3.63}$$

and,

$$d_4 = \pm\sqrt{\frac{8\delta_4^2 I_4}{\delta_2}}\frac{1}{\sqrt{\delta_2\delta_6(D+4) - \delta_4^2 D}}, \tag{3.64}$$

where

$$\Delta_6 = \pm\sqrt{\frac{2}{(D+6) - J_6(D+4)}}, \quad J_6 = \frac{I_6^2}{I_8 I_4}, \tag{3.65}$$

$$\delta_2 = I_0 I_4(D+2) - I_2^2 D, \tag{3.66}$$

$$\delta_4 = I_2 I_6(D+4) - I_4^2(D+2), \tag{3.67}$$

$$\delta_6 = I_4 I_8(D+6) - I_6^2(D+4). \tag{3.68}$$

Notice that $\delta_{2K} = 2I_{2K+2}I_{2K-2}/\Delta_{2K}^2$.

Hence we have determined all the coefficients in Eqs.(3.20), (3.22), (3.28), (3.29), (3.31), (3.38), (3.40), (3.41), (3.58), (3.60), (3.61), (3.62), (3.63), and (3.64). Some of the coefficients can be summarized in simple formulas for all polynomials, using a general notation:

$$c_K = \frac{1}{\sqrt{I_{2K}}}, \text{ for } K = 0, 1, 2, 3, 4,$$

$$c'_K = -c_K \frac{I_{2K-2}}{I_{2K-4}}\Delta_{2K-2}, \text{ for } K = 2, 3, 4,$$

$$\bar{c}_K = c_K \frac{(-1 + \Delta_{2K-2})}{D + 2K - 4}, \text{ for } K = 2, 3, 4,$$

$$\Delta_{2K} = \sqrt{\frac{2}{(D+2K) - J_{2K}(D+2K-2)}}$$

$$J_{2K} = \frac{I_{2K}^2}{I_{2K+2}I_{2K-2}}$$

Notice that we have chosen the positive solutions for the square roots, but the negative ones would also lead to orthogonal polynomials. We have completed the orthonormalization of the first five polynomials (N=0,1,2,3,4). The procedure can be applied for higher polynomials, although it becomes increasingly laborious.

3.5   D-dimensional polynomials for specific weights

In this section we obtain the D-dimensional polynomials for some specific weights and from them retrieve some well known D=1 polynomials. We also obtain the I_N functions associated to some new weights.

3.5.1   D-dimensional Hermite polynomials

We show that the D-dimensional Hermite polynomials are straightforwardly retrieved from the above polynomials for the gaussian weight,

$$\omega(\xi) = \frac{1}{(2\pi)^{D/2}} e^{-\frac{\xi^2}{2}}, \text{ and } \xi_{max} = \infty. \tag{3.69}$$

To obtain the integrals I_{2N} of Eq.(3.11), we note that,

$$\int_0^\infty d\xi \, \omega(\xi) \, \xi^{2N+D-1} = \frac{2^{N-1}}{\pi^{\frac{D}{2}}} \Gamma\left(N + \frac{D}{2}\right). \tag{3.70}$$

Then it follows from Eq.(3.70) that,

$$I_{2N} = 1. \tag{3.71}$$

In this limit $c_K = 1$, $\bar{c}_K = 0$ $c'_K = -1$, $d_4 = 1$, $\bar{d}_4 = 0$ and $d'_4 = 0$, and the polynomials of Eqs.(3.5), (3.6), (3.7), (3.8), (3.9) become,

$$\mathcal{P}_0(\boldsymbol{\xi}) = 1, \tag{3.72}$$

$$\mathcal{P}_{i_1}(\boldsymbol{\xi}) = \xi_{i_1}, \tag{3.73}$$

$$\mathcal{P}_{i_1 i_2}(\boldsymbol{\xi}) = \xi_{i_1}\xi_{i_2} - \delta_{i_1 i_2} \tag{3.74}$$

$$\mathcal{P}_{i_1 i_2 i_3}(\boldsymbol{\xi}) = \xi_{i_1}\xi_{i_2}\xi_{i_3} - \left(\xi_{i_1}\delta_{i_2 i_3} + \xi_{i_2}\delta_{i_1 i_3} + \xi_{i_3}\delta_{i_1 i_2}\right) \tag{3.75}$$

and,

$$\mathcal{P}_{i_1 i_2 i_3 i_4}(\boldsymbol{\xi}) = \xi_{i_1}\xi_{i_2}\xi_{i_3}\xi_{i_4} - \left(\xi_{i_1}\xi_{i_2}\delta_{i_3 i_4} + \xi_{i_1}\xi_{i_3}\delta_{i_2 i_4}\right.$$
$$\left. +\xi_{i_1}\xi_{i_4}\delta_{i_2 i_3} + \xi_{i_2}\xi_{i_3}\delta_{i_1 i_4} + \xi_{i_2}\xi_{i_4}\delta_{i_1 i_3} + \xi_{i_3}\xi_{i_4}\delta_{i_1 i_2}\right) + \delta_{i_1 i_2 i_3 i_4} \tag{3.76}$$

We notice that the tensorial basis that spans the new generalized polynomials contains the basis that spans the Hermite polynomials but not vice-versa. The D-dimensional Hermite polynomials $\mathcal{P}_{i_1 \cdots i_N}$ are symmetric tensors in the indices $i_1 \cdots i_N$ spanned over the basis formed by the tensors,

$$T_{i_1 \cdots i_N} \equiv \xi_{i_1} \cdot \xi_{i_2} \cdots \xi_{i_P} \cdot \delta_{i_{P+1}, i_{P+2}} \cdot \delta_{i_{P+3}, i_{P+4}} \cdots \delta_{i_{N-1}, i_N}.$$

This basis is not large enough to span the new generalized polynomials, $\mathcal{P}_{i_1 \cdots i_N}$, which demand a larger basis formed by the tensors

$$T_{i_1 \cdots i_N} \equiv F(\xi) \xi_{i_1} \cdot \xi_{i_2} \cdots \xi_{i_P} \cdot \delta_{i_{P+1}, i_{P+2}} \cdot \delta_{i_{P+3}, i_{P+4}} \cdots \delta_{i_{N-1}, i_N},$$

whose scalar functions $F(\xi)$ are polynomials in powers of the vector modulus, 1, ξ^2, ξ^4, ..., ξ^{2k}.

3.5.2 D-dimensional Legendre polynomials

We define D-dimensional Legendre polynomials satisfying the general orthonormal relation of Eq.(3.1) with $\xi_{max} = 1$ and the following weight:

$$\omega(\xi) = 1, \text{ and } \xi_{max} = 1. \tag{3.77}$$

From this it follows that,

$$I_{2N} = \frac{\pi^{D/2}}{2^{N-1} \Gamma(N + D/2)} \int_0^1 d\xi \, \xi^{2N+D-1} = \frac{2^{1-N} \pi^{D/2}}{(D + 2N) \Gamma \left[\frac{D+2N}{2} \right]}, \tag{3.78}$$

Using the expressions corresponding coefficients up to fourth order

$$c_N = \frac{1}{\sqrt{\frac{2^{-N} \pi^{D/2}}{\Gamma \left[1 + \frac{D}{2} + N \right]}}}, \tag{3.79}$$

$$\bar{c}_2 = \frac{-2 + \sqrt{2(2+D)}}{D \sqrt{\frac{\pi^{D/2}}{\Gamma \left[3 + \frac{D}{2} \right]}}}, \quad \bar{c}_3 = \frac{-2\sqrt{2} + 2\sqrt{4+D}}{(2+D) \sqrt{\frac{\pi^{D/2}}{\Gamma \left[4 + \frac{D}{2} \right]}}}, \quad \bar{c}_4 = \frac{-4 + 2\sqrt{2(6+D)}}{(4+D) \sqrt{\frac{\pi^{D/2}}{\Gamma \left[5 + \frac{D}{2} \right]}}}, \tag{3.80}$$

$$c_2' = -\sqrt{\frac{2}{(2+D)\frac{\pi^{D/2}}{\Gamma[3+\frac{D}{2}]}}}, \quad c_3' = -\sqrt{\frac{4}{(4+D)\frac{\pi^{D/2}}{\Gamma[4+\frac{D}{2}]}}}, \quad c_4' = -\sqrt{\frac{8}{(6+D)\frac{\pi^{D/2}}{\Gamma[5+\frac{D}{2}]}}}, \quad (3.81)$$

$$d_4 = \sqrt{\frac{\frac{16(6+D)\pi^{3D/2}}{(4+D)\Gamma[3+\frac{D}{2}]\Gamma[4+\frac{D}{2}]^2}}{\pi^{2D}\left(\frac{(2+D)(96+D(8+D)(24+D(8+D)))}{(8+D)\Gamma[3+\frac{D}{2}]^4} - \frac{2(4+D)(4+D(8+D))}{\Gamma[2+\frac{D}{2}]^3\Gamma[5+\frac{D}{2}]}\right)}}, \quad (3.82)$$

$$d_4' = \frac{\left(2D(6+D)^{3/2}\Gamma\left[1+\frac{D}{2}\right]\Gamma\left[3+\frac{D}{2}\right]^2 - 8\sqrt{6+D}\Gamma\left[3+\frac{D}{2}\right]^3\right)d_4}{D(4+D)\sqrt{6+D}\left(-(6+D)\Gamma\left[2+\frac{D}{2}\right]^3 + 2\Gamma\left[1+\frac{D}{2}\right]\Gamma\left[3+\frac{D}{2}\right]^2\right)}$$

$$+ \frac{\left(\frac{8\sqrt{2}\Gamma[3+\frac{D}{2}]^3}{D+2} - 4\sqrt{2}\Gamma\left[2+\frac{D}{2}\right]^2\Gamma\left[4+\frac{D}{2}\right]\right)c_4}{D(4+D)\sqrt{6+D}\left(-(6+D)\Gamma\left[2+\frac{D}{2}\right]^3 + 2\Gamma\left[1+\frac{D}{2}\right]\Gamma\left[3+\frac{D}{2}\right]^2\right)}, \quad (3.83)$$

$$\bar{d}_4 = \frac{c_4\left(D - 2\sqrt{2(6+D)} - D\sqrt{2(6+D)}\right) + (4+D)^2(6+D)d_4}{D(2+D)(4+D)}. \quad (3.84)$$

These coefficients provides orthogonal polynomials for any dimension and, as we will see in subsection 3.5.5, they give the well known D=1 Legendre polynomials for the particular case with $D = 1$.

3.5.3   D-dimensional Chebyshev polynomials of first kind

Following the same procedure used for the Legendre polynomials, we define the D-dimensional Chebyshev polynomials of first kind with the weight $\omega(\xi)$ below and integrated under a sphere of radius ξ_{max},

$$\omega(\xi) = \frac{1}{1-\xi^2}, \text{ and } \xi_{max} = 1, \quad (3.85)$$

with the corresponding integral

$$I_{2N} = \frac{\pi^{D/2}}{2^{N-1}\Gamma(N+D/2)}\int_0^1 d\xi \frac{1}{1-\xi^2}\xi^{2N+D-1} = \frac{2^{-N}\pi^{\frac{1+D}{2}}}{\Gamma\left[\frac{1}{2}(1+D+2N)\right]}, \quad (3.86)$$

and coefficients up to fourth order

$$c_N = \frac{1}{\sqrt{\frac{2^{-N}\pi^{\frac{1+D}{2}}}{\Gamma\left[\frac{1+D}{2}+N\right]}}}, \tag{3.87}$$

$$\bar{c}_2 = \frac{2\left(-1+\sqrt{1+D}\right)}{D\sqrt{\frac{\pi^{\frac{1+D}{2}}}{\Gamma\left[\frac{5+D}{2}\right]}}}, \quad \bar{c}_3 = \frac{2\sqrt{2}\left(-1+\sqrt{3+D}\right)}{(2+D)\sqrt{\frac{\pi^{\frac{1+D}{2}}}{\Gamma\left[\frac{7+D}{2}\right]}}}, \quad \bar{c}_4 = \frac{4\left(-1+\sqrt{5+D}\right)}{(4+D)\sqrt{\frac{\pi^{\frac{1+D}{2}}}{\Gamma\left[\frac{9+D}{2}\right]}}}, \tag{3.88}$$

$$c_2' = -\frac{2}{\sqrt{\frac{(1+D)\pi^{\frac{1+D}{2}}}{\Gamma\left[\frac{5+D}{2}\right]}}}, \quad c_3' = -\frac{2\sqrt{2}}{\sqrt{\frac{(3+D)\pi^{\frac{1+D}{2}}}{\Gamma\left[\frac{7+D}{2}\right]}}}, \quad c_4' = -\frac{4}{\sqrt{\frac{(5+D)\pi^{\frac{1+D}{2}}}{\Gamma\left[\frac{9+D}{2}\right]}}} \tag{3.89}$$

$$d_4 = \frac{8\sqrt{\frac{\pi^{\frac{3(1+D)}{2}}}{(3+D)(5+D)^2\Gamma\left[\frac{5+D}{2}\right]^3}}}{\sqrt{\pi^{2+2D}\left(-\frac{D(2+D)^2}{\Gamma\left[\frac{5+D}{2}\right]^4} + \frac{(4+D)(7+D)(4+D(7+D)(8+D(7+D)))}{4(3+D)\Gamma\left[\frac{3+D}{2}\right]^2\Gamma\left[\frac{9+D}{2}\right]^2}\right)}}, \tag{3.90}$$

$$d_4' = \frac{2\left(c_4\sqrt{5+D} - d_4(3+D)(5+D)\right)\Gamma\left[\frac{3+D}{2}\right]\Gamma\left[\frac{5+D}{2}\right]^2}{D(4+D)(5+D)\Gamma\left[\frac{5+D}{2}\right]^3 - 2D(2+D)\Gamma\left[\frac{3+D}{2}\right]\Gamma\left[\frac{7+D}{2}\right]^2}, \tag{3.91}$$

$$\bar{d}_4 = \frac{1}{4(2+D)}\left(\frac{4c_4\left(D - 4\sqrt{5+D} - 2D\sqrt{5+D}\right)}{D(4+D)}\right.$$
$$\left. + \frac{8d_4(5+D)\Gamma\left[\frac{5+D}{2}\right]^2}{D(4+D)\Gamma\left[\frac{5+D}{2}\right]^2 - D(2+D)\Gamma\left[\frac{3+D}{2}\right]\Gamma\left[\frac{7+D}{2}\right]}\right). \tag{3.92}$$

The polynomials with the coefficients above are orthogonal for any dimensions and, as we will see in subsection 3.5.5 for $D = 1$ they give the well known D=1 Chebyshev polynomials of first kind.

3.5.4 D-dimensional Chebyshev polynomials of second kind

For the D-dimensional Chebyshev polynomials of second kind, we define the following weight function and maximum radius

$$\omega(\xi) = \sqrt{1-\xi^2}, \text{ and } \xi_{max} = 1 \tag{3.93}$$

which give the integral and coefficients below

$$I_{2N} = \frac{\pi^{D/2}}{2^{N-1}\Gamma(N+D/2)} \int_0^1 d\xi \sqrt{1-\xi^2}\xi^{2N+D-1} = \frac{2^{-1-N}\pi^{\frac{1+D}{2}}}{\Gamma\left[\frac{1}{2}(3+D+2N)\right]}, \qquad (3.94)$$

$$c_N = \frac{1}{\sqrt{\frac{2^{-1-N}\pi^{\frac{1+D}{2}}}{\Gamma\left[\frac{3+D}{2}+N\right]}}}, \qquad (3.95)$$

$$\bar{c}_2 = \frac{2\sqrt{2}\left(-3+\sqrt{3(3+D)}\right)}{3D\sqrt{\frac{\pi^{\frac{1+D}{2}}}{\Gamma\left[\frac{7+D}{2}\right]}}}, \quad \bar{c}_3 = \frac{-4+4\sqrt{5+D}/\sqrt{3}}{(2+D)\sqrt{\frac{\pi^{\frac{1+D}{2}}}{\Gamma\left[\frac{9+D}{2}\right]}}}, \quad \bar{c}_4 = \frac{4\sqrt{2}\left(-3+\sqrt{3(7+D)}\right)}{3(4+D)\sqrt{\frac{\pi^{\frac{1+D}{2}}}{\Gamma\left[\frac{11+D}{2}\right]}}},$$

$$(3.96)$$

$$c_2' = -\sqrt{\frac{8}{\frac{3(3+D)\pi^{\frac{1+D}{2}}}{\Gamma\left[\frac{7+D}{2}\right]}}}, \quad c_3' = -\sqrt{\frac{16}{\frac{3(5+D)\pi^{\frac{1+D}{2}}}{\Gamma\left[\frac{9+D}{2}\right]}}}, \quad c_4' = -\sqrt{\frac{32}{\frac{3(7+D)\pi^{\frac{1+D}{2}}}{\Gamma\left[\frac{11+D}{2}\right]}}} \qquad (3.97)$$

$$d_4 = \frac{4\sqrt{\frac{3(7+D)\pi^{\frac{3(1+D)}{2}}}{(5+D)\Gamma\left[\frac{9+D}{2}\right]^3}}}{\sqrt{\pi^{2+2D}\left(-\frac{D(2+D)^2}{\Gamma\left[\frac{7+D}{2}\right]^4} + \frac{(4+D)(9+D)(36+D(1+D)(8+D)(9+D))}{4(5+D)\Gamma\left[\frac{5+D}{2}\right]^2\Gamma\left[\frac{11+D}{2}\right]^2}\right)}} \qquad (3.98)$$

$$d_4' = \frac{2\left(c_4\sqrt{3(7+D)}-3d_4(5+D)(7+D)\right)\Gamma\left[\frac{5+D}{2}\right]\Gamma\left[\frac{7+D}{2}\right]^2}{D(4+D)(7+D)\Gamma\left[\frac{7+D}{2}\right]^3 - 2D(2+D)\Gamma\left[\frac{5+D}{2}\right]\Gamma\left[\frac{9+D}{2}\right]^2} \qquad (3.99)$$

$$\bar{d}_4 = \frac{1}{4(2+D)}\left(-\frac{4c_4\left(4\sqrt{3(7+D)}+D\left(-3+2\sqrt{3(7+D)}\right)\right)}{3D(4+D)}\right.$$

$$\left. + \frac{24d_4(7+D)\Gamma\left[\frac{7+D}{2}\right]^2}{D(4+D)\Gamma\left[\frac{7+D}{2}\right]^2 - D(2+D)\Gamma\left[\frac{5+D}{2}\right]\Gamma\left[\frac{9+D}{2}\right]}\right) \qquad (3.100)$$

The corresponding polynomials are orthogonal for any dimension and, as we will see in subsection 3.5.5, give the well known D=1 Chebyshev polynomials of second kind.

3.5.5 Projection of Hermite, Legendre and Chebyshev polynomials into D=1 dimension

To obtain the projection of such polynomials in D=1 dimension, it suffices to drop the index of the vector, $\xi_{i_1} \to \xi$, and to take that $\delta_{i_1 i_2} \to 1$ since there is only one index, and so, $i_1 = i_2 = 1$. Thus the tensors based on the Kronecker's delta function have each of its terms equal to one, for instance, $\delta_{i_1 j_1} \cdots \delta_{i_N j_N} = 1$, and so, $\delta_{i_1 \cdots i_N | j_1 \cdots j_N} = N!$ and $\delta_{i_1 \cdots i_N j_1 \cdots j_N} = (2N-1)!/[2^{N-1}(N-1)!]$, according to section 3.3. Hence the orthonormality condition of Eq.(3.1) becomes,

$$\int d^D \boldsymbol{\xi}\, \omega(\boldsymbol{\xi}) \mathcal{P}_N(\boldsymbol{\xi}) \mathcal{P}_M(\boldsymbol{\xi}) = N! \delta_{NM} \tag{3.101}$$

Notice that this is not the standard normalization employed in the definition of most of D=1 orthonormal polynomials.

Hermite polynomials

The Hermite polynomials obtained via dimensional reduction from Eqs.(3.72), (3.73), (3.74), (3.75) and (3.76) are given by,

$$\mathcal{P}_0(\boldsymbol{\xi}) = 1,\ \ \mathcal{P}_1(\boldsymbol{\xi}) = \xi,\ \ \mathcal{P}_2(\boldsymbol{\xi}) = \xi^2 - 1,\ \ \mathcal{P}_3(\boldsymbol{\xi}) = \xi^3 - 3\xi,\ \ \text{and},\ \ \mathcal{P}_4(\boldsymbol{\xi}) = \xi^4 - 6\xi^2 + 3. \tag{3.102}$$

The known D=1 Hermite polynomials, defined with the normalization of probability theory [56], satisfy the following orthonormality condition,

$$\int_{-\infty}^{\infty} He_m(x) He_n(x)\, e^{-\frac{x^2}{2}}\, \mathrm{d}x = \sqrt{2\pi} n! \delta_{nm}.$$

The first five ones are $He_0(x) = 1$, $He_1(x) = x$, $He_2(x) = x^2 - 1$, $He_3(x) = x^3 - 3x$, and $He_4(x) = x^4 - 6x^2 + 3$ and they coincide exactly with the present polynomials.

Legendre polynomials

It follows by taking $D = 1$ that,

$$\mathcal{P}_0(\boldsymbol{\xi}) = \frac{1}{\sqrt{2}},\ \ \mathcal{P}_1(\boldsymbol{\xi}) = \frac{3}{2}\xi,\ \ \mathcal{P}_2(\boldsymbol{\xi}) = \frac{\sqrt{5}}{2}(3\xi^2 - 1), \tag{3.103}$$

$$\mathcal{P}_3(\boldsymbol{\xi}) = \frac{\sqrt{21}}{2}(5\xi^2 - 3), \text{ and } \mathcal{P}_4(\boldsymbol{\xi}) = \frac{3\sqrt{3}}{4}(35\xi^4 - 30\xi^2 + 3). \tag{3.104}$$

The Legendre polynomials [56] satisfy the following orthonormality condition,

$$\int_{-1}^{1} P_m(x) P_n(x) \, \mathrm{d}x = \frac{2}{2n+1}\delta_{nm}.$$

The first five ones are $P_0(x) = 1$, $P_1(x) = x$, $P_2(x) = (3x^2 - 1)/2$, $P_3(x) = (5x^3 - 3x)/2$, and $P_4(x) = (35x^4 - 30x^2 + 3)/8$. Thus apart from the normalization they coincide with the present polynomials.

Chebyshev polynomials of the first kind

$$\mathcal{P}_0(\boldsymbol{\xi}) = \frac{1}{\sqrt{\pi}}, \quad \mathcal{P}_1(\boldsymbol{\xi}) = \sqrt{\frac{2}{\pi}}\xi, \quad \mathcal{P}_2(\boldsymbol{\xi}) = \frac{2}{\sqrt{\pi}}(2\xi^2 - 1), \tag{3.105}$$

$$\mathcal{P}_3(\boldsymbol{\xi}) = 2\sqrt{\frac{3}{\pi}}(4\xi^3 - 3\xi), \text{ and } \mathcal{P}_4(\boldsymbol{\xi}) = 4\sqrt{\frac{3}{\pi}}\left(8\xi^4 - 8\xi^2 + 1\right). \tag{3.106}$$

The Chebyshev polynomials of the first kind [56] satisfy the following orthonormality condition,

$$\int_{-1}^{1} T_n(x) T_m(x) \frac{dx}{\sqrt{1-x^2}} = \begin{cases} 0 & n \neq m \\ \pi & n = m = 0 \\ \frac{\pi}{2} & n = m \neq 0 \end{cases}.$$

The first five ones are $T_0(x) = 1$, $T_1(x) = x$, $T_2(x) = 2x^2 - 1$, $T_3(x) = 4x^3 - 3x$, and $T_4(x) = 8x^4 - 8x^2 + 1$. Thus apart from the normalization they coincide with the present polynomials.

Chebyshev polynomials of the second kind

$$\mathcal{P}_0(\boldsymbol{\xi}) = \sqrt{\frac{2}{\pi}}, \quad \mathcal{P}_1(\boldsymbol{\xi}) = 2\sqrt{2}\pi\xi, \quad \mathcal{P}_2(\boldsymbol{\xi}) = \frac{2}{\sqrt{\pi}}(4\xi^2 - 1), \tag{3.107}$$

$$\mathcal{P}_3(\boldsymbol{\xi}) = 8\sqrt{\frac{3}{\pi}}(2\xi^3 - \xi), \text{ and, } \mathcal{P}_4(\boldsymbol{\xi}) = 4\sqrt{\frac{3}{\pi}}\left(16\xi^4 - 12\xi^2 + 1\right). \tag{3.108}$$

The Chebyshev polynomials of the second kind [56] satisfy the following orthonormality condition,

$$\int_{-1}^{1} U_n(x)\, U_m(x)\, \frac{dx}{\sqrt{1 - x^2}} = \begin{cases} 0 & n \neq m \\ \frac{\pi}{2} & n = m \end{cases}.$$

The first five ones are $U_0(x) = 1$, $U_1(x) = 2x$, $U_2(x) = 4x^2 - 1$, $U_3(x) = 8x^3 - 4x$, and $U_4(x) = 16x^4 - 12x^2 + 1$. Thus apart from the normalization they coincide with the present polynomials.

3.5.6 D-dimensional Fermi-Dirac polynomials

We seek the set of polynomials orthonormal under the weight defined by the FD statistical occupation number for $\boldsymbol{u} = 0$.

$$\omega(\boldsymbol{\xi}) = \frac{1}{z^{-1}e^{-\frac{\xi^2}{2\theta}} + 1} \text{ and } \xi_{max} = \infty. \tag{3.109}$$

The parameter $z \equiv e^{\mu/\theta}$ is called the fugacity, where μ is the chemical potential and θ is the temperature using the so-called reduced units ($m = k_B = c = \hbar = 1$). For the FD weight it holds that,

$$I_{2N} = (2\pi)^{D/2}\theta^{\nu} g_{\nu}(z)\,, \ \nu \equiv N + D/2, \text{ and } g_{\nu}(z) \equiv \int_0^{\infty} dx\, \frac{x^{\nu-1}}{z^{-1}e^x + 1}. \tag{3.110}$$

It is interesting to consider special limits where the integral $g_{\nu}(z)$ can be explicitly calculated and the I_{2N} obtained. One of such limits is when the quantum FD statistics becomes the classical MB statistics. This is the small fugacity limit,

$$g_{\nu}(z) = \Gamma(\nu)\left(z - \frac{z^2}{2^{\nu}} + \frac{z^3}{3^{\nu}} + \cdots\right). \tag{3.111}$$

The other interesting limit is the so-called Sommerfeld limit [118], used for the treatment of electrons in metals where the chemical potential (Fermi energy) is much larger than the room temperature. In this limit $\mu/\theta = \ln z \gg 1$, such that the terms of high order

in $(\theta/\mu)^{2k}$ can be disregarded.

$$g_\nu(z) = \frac{\Gamma(\nu)}{\Gamma(\nu+1)}(\ln z)^\nu \left\{ 1 + \nu(\nu-1)\frac{\pi^2}{6}\frac{1}{(\ln z)^2} \right.$$
$$\left. + \nu(\nu-1)(\nu-2)(\nu-3)\frac{7\pi^4}{360}\frac{1}{(\ln z)^4} + \cdots \right\} \tag{3.112}$$

3.5.7   D-dimensional Bose-Einstein polynomials

Similarly to the previous case, we seek the set of polynomials orthonormal under a weight which is the BE statistical occupation number.

$$\omega(\boldsymbol{\xi}) = \frac{1}{z^{-1}e^{-\frac{\xi^2}{2\theta}} - 1}, \text{ and } \xi_{max} = \infty. \tag{3.113}$$

It holds that,

$$I_{2N} = (2\pi)^{D/2}\theta^\nu h_\nu(z), \ \alpha \equiv N + D/2, \text{ and } h_\nu(z) \equiv \int_0^\infty dx \, \frac{x^{\nu-1}}{z^{-1}e^x - 1} \tag{3.114}$$

The are also special limits here, the first being when the quantum BE statistics becomes the classical MB one. This is the small fugacity limit,

$$h_\nu(z) = \Gamma(\nu)\left(z + \frac{z^2}{2^\nu} + \frac{z^3}{3^\nu} + \cdots \right). \tag{3.115}$$

Notice that in leading order in z, the FD and the BE polynomials become identical as they reduce to the MB polynomials at finite temperature. In fact at this limit these polynomials are just scaled versions of the D-dimensional Hermite polynomials. The other interesting limit is that of negative vanishing fugacity near to the onset of the BE condensate. For this we write $\alpha \equiv -\mu/\theta$, $\alpha \to 0$. Thus for $z \equiv e^{-\alpha}$, one obtains that,

$$h_\nu(z) = \frac{\Gamma(1-\nu)}{\alpha^{1-\nu}} + \sum_{i=0}^\infty \frac{(-1)^i}{i!}\zeta(\nu-i)\alpha^i, \tag{3.116}$$

where $\zeta(s)$ is the Riemann zeta function, which is defined for $\mathrm{Re}(s) > 1$. Thus for ν integer, the above expression must be replaced by,

$$h_m(z) = \frac{(-1)^{m-1}}{(m-1)!}\left(\sum_{i=1}^{m-1} \frac{1}{i} - \ln\alpha \right)\alpha^{m-1} + \sum_{\substack{i=0 \\ i \neq m-1}}^\infty \frac{(-1)^i}{i!}\zeta(m-i)\alpha^i. \tag{3.117}$$

3.5.8 D-dimensional Graphene polynomials

Graphene is a two-dimensional sheet of carbon atoms arranged in an hexagonal lattice where electrons move with a relativistic dispersion relation. To deal with this situation we seek a set of polynomials orthonormal under a weight which the following FD statistical occupation number for $\boldsymbol{u} = 0$ [113].

$$\omega(\boldsymbol{\xi}) = \frac{1}{z^{-1} e^{\frac{|\boldsymbol{\xi}|}{\theta}} + 1}, \text{ and } \xi_{max} = \infty. \tag{3.118}$$

It holds that,

$$I_{2N} = 2^{D+N} \pi^{\frac{1}{2}(-1+D)} \theta^{D+2N} \Gamma \left[\frac{1+D}{2} + N \right] g_{D+2N}(z) \tag{3.119}$$

$$\tag{3.120}$$

The limit of low doping in graphene corresponds to $\mu \to 0$ or, equivalently, $z \to 1$. The doping of graphene can be chemically adjusted for instance.

$$I_{2N} = 2^{-N} \left(-2 + 2^{D+2n} \right) \pi^{\frac{1}{2}(-1+D)} \theta^{D+2N} \Gamma \left[\frac{1+D}{2} + n \right] \zeta[D + 2N] \tag{3.121}$$

$$+ 2^{-N} \left(-4 + 2^{D+2N} \right) \pi^{\frac{1}{2}(-1+D)} \theta^{D+2N} \Gamma \left[\frac{1+D}{2} + N \right] \zeta[-1 + D + 2N](z - 1)$$

$$+ 2^{-1-N} \pi^{\frac{1}{2}(-1+D)} \theta^{D+2N} \Gamma \left[\frac{1+D}{2} + N \right] \left(\left(-8 + 2^{D+2N} \right) \zeta[-2 + D + 2N] \right.$$

$$\left. - \left(-4 + 2^{D+2N} \right) \zeta[-1 + D + 2N] \right) (z - 1)^2 + O[z - 1]^3$$

3.5.9 D-dimensional Yukawa polynomials

As an extra example (not applied to our models), consider the Yukawa potential of nuclear interactions that contains the parameter μ that renders it short ranged. Assume the Yukawa potential as a weight to obtain orthonormal polynomials.

$$\omega(\boldsymbol{\xi}) = \frac{e^{-\mu\xi}}{\xi} \text{ and } \xi_{max} = \infty. \tag{3.122}$$

To determine the coefficients that enter the polynomials, it is enough to have the integrals,

$$I_{2N} = \frac{\pi^{D/2}}{2^{N-1}} \frac{\Gamma(2N + D - 1)}{\Gamma(N + \frac{D}{2})} \frac{1}{\mu^{2N+D-3}}. \tag{3.123}$$

3.6   Conclusion

We propose here D-dimensional symmetric tensor polynomials orthonormal under a general weight. We show that the number of coefficients of the first five ones (N=0 to 4) matches exactly the number of equations that stem from their orthonormalization, which allows for their obtainment as functions of the integrals I_N's. In Statistical Mechanics it is well-known that the D-dimensional Hermite polynomials are a key element to solve the Boltzmann equation for classical particles, which satisfy the MB statistics [33,81,121]. The present generalized polynomials are applicable to semi-classical fluids where the particles obey the BE and FD statistics [30, 31]. The proposed generalized polynomials allows for the definition of orthonormal multipoles as shown in case of the Yukawa potential. We foresee many other applications because the proposed polynomials take into account the expanded function as the weight that render them orthonormal in the D-dimensional space.

Chapter 4

Lattice Boltzmann method for semiclassical fluids

In this chapter, we determine properties of the LBM for semiclassical fluids, which is based on the Boltzmann equation and on an equilibrium distribution function given either by the Bose-Einstein or the Fermi-Dirac distributions. New D-dimensional polynomials, developed in Chap. 3, are used and we find that the weight that renders the polynomials orthonormal has to be approximately equal, or equal, to the equilibrium distribution function itself for an efficient numerical implementation of the LBM. In light of the new polynomials we discuss the convergence of the series expansion of the equilibrium distribution function and the obtainment of the hydrodynamic equations. A discrete quadrature is proposed and some discrete lattices in one, two and three dimensions associated to weight functions other than the Hermite weight are obtained. We derive the forcing term for the LBM, given by the Lorentz force, which depends on the microscopic velocity, since the bosonic and fermionic particles can be charged. Motivated by the recent experimental observations of the hydrodynamic regime of electrons in graphene, we build an isothermal LBM for electrons in metals in two and three dimensions. This model is validated by means of the Riemann problem and of the Poiseuille flow. As expected for electron in metals, the Ohm's law is recovered for a system analogous to a porous medium.

4.1   Introduction

The Boltzmann equation [81] with a BGK collision term together with the MB EDF has found widespread use to describe the flow of classical particles. This is because it allows for an efficient numerical implementation, which is well fitted to perform simulations in complex geometries such as in porous media [31]. This is the LBM [82,136], based on a discretization of the phase space. The EDF is expanded in powers of the macroscopic velocity, under the assumption of a low Mach number, and yet, the hydrodynamical equations remain fully satisfied. This remarkable property follows from an underlying mathematical structure provided by the D-dimensional Hermite polynomials. In this chapter, we generalize the present framework to the semiclassical fluids whose constituents are either bosons or fermions.

Recently there has been a renewed interest in the study of the hydrodynamic regime for charge carriers in conductors [24,89,103,110]. Experiments have shown that electrons in graphene exhibit hydrodynamic behavior for a wide range of temperatures and carrier densities [9], due to its weak electron-phonon scattering [142] and to the new technologies to produce ultra-clean samples [133]. One of the clear signals of its hydrodynamical regime is the onset of whirlpools (vortices) that has been predicted and subsequently observed [9,86,119,145]. The Dirac fluid of electron has been simulated by a relativistic LBM many times [32,47,52,97,99,113] in order to unveil new properties of graphene. These authors expand the FD distribution in orthogonal polynomials, similarly as done here, but using a fully relativistic formalism for massless particles (see Ref. [32]). In this chapter we seek a general non-relativistic formalism for semiclassical fluids based on D-dimensional orthonormal polynomials. The Hermite polynomials are well fitted to describe classical particles, that is, those obeying the MB statistics, since they are orthonormal under the Hermite weight function which is essentially the MB EDF. Previous attempts [30,67,130,157] to build a semiclassical LBM were based on the expansion of the

BE-FD distributions in Hermite polynomials, but they were limited to a nearly classical regime since the weight function of the Hermite polynomials differs greatly from the BE-FD distributions on the semiclassical or quantum regimes (low temperatures and/or high densities). The point of view here is that a new polynomial set must be used for semiclassical fluids where the weight function is similar or equal to the EDF. We propose the general formalism to describe the flow of semiclassical particles based on a new set of D-dimensional polynomials that generalize the well-known D-dimensional Hermite polynomials (see Chap. 3). We obtain the expansion of the EDF under a general weight such that the cases of BE-FD EDFs can be immediately treated by the present formalism.

The description of electrons in metals with Boltzmann equation meets the following parameters [7]. The microscopic velocity of electrons is the Fermi speed, $v_F \sim 10^6$ m/s and the typical relaxation time is $\tau \sim 10^{-14}$ s. This renders a kinematic viscosity $\nu \approx v_F^2 \tau/3 \sim 10^{-3}$ m^2/s. The macroscopic velocity u is very low and can be computed by assuming that $u\,m_e/\tau = eE$, where m_e and e are the electron's mass and charge respectively. For a typical home appliance battery, the voltage is $V = 1.5$ Volts per $L = 1$ m, which gives an electric field of $E = V/L = 1.5$ Volts/m and so, $u \sim 3 \times 10^{-3}$ m/s. The typical electronic density is $\rho \sim 10^{-2}$ Kg/m^3. and the shear viscosity is $\eta = \rho\nu \sim 10^{-5}$ Kg/(ms). Thus one can get an estimative for the Reynolds number associated to a system of size L, $Re = uL/\nu \sim 3L$ where L is expressed in meters. Therefore electrons in metals behave similarly to Glycerin.

This chapter is organized as follows. In Sec. 6.2.2 we review the expansion of a EDF in terms of orthogonal polynomials (see Sec. 3.4). We also discuss the special case of a weight function equal to the EDF itself. In Sec. 4.3 the EDF is expanded up to fourth order in the set of new generalized polynomials orthonormal under a general weight. In Sec. 4.4 the EDF is expanded in polynomials orthonormal for the special case that the weight is equal to the EDF itself, $\omega(\xi) = f^{eq}(\xi)$. In Subsec. 4.4.1 we

directly derive the EDF to order N=2 without using the orthonormal polynomials just to confirm the rightness of our ideas. In Sec. 4.5, we derive the macroscopic equations for semiclassical fluids (i.e., mass, momentum and energy conservation equations) in the context of the generalized polynomials. A discussion is made about the minimum order that the EDF should be expanded in order to recover each macroscopic equation. In Sec. 4.6, we calculate the forcing term for a second order expansion of the semiclassical EDF and verify that it satisfies the moment constraints up to second order. In Sec. 4.7, we obtain the quadratures and calculate the discrete weights of the $D1V3$, $D2V9$, and $D3V15$ lattices (more quadratures can be found in B). They are calculated for a generic weight function similarly to the polynomials. In Sec. 4.8, we develop our LBM for electrons in metals in two (2D) and three (3D) dimensions and perform three numerical tests: the Riemann problem, the Poiseuille flow and the Ohm's law. In Sec. 4.9, we summarize our main results and conclude.

4.2 Expansion of the equilibrium distribution function

The EDF $f^{(eq)}(\boldsymbol{\xi})$ is a central quantity in the Boltzmann-BGK framework since the non-equilibrium distribution function f relaxes to the EDF, f^{eq}, within time τ, according to,

$$\frac{\partial f}{\partial t} + \boldsymbol{\xi} \cdot \boldsymbol{\nabla}_{\boldsymbol{x}} f + \boldsymbol{a} \cdot \boldsymbol{\nabla}_{\boldsymbol{\xi}} f = -\frac{f - f^{eq}}{\tau}. \tag{4.1}$$

where $\boldsymbol{\xi}$ and $\boldsymbol{a}$ are the microscopic velocity and acceleration, the latter defined by the external applied force. From this equation one obtains the hydrodynamical quantities under the Chapman-Enskog assumption, which says that expectation values over the microscopic velocity, $\boldsymbol{\xi}$, can be computed either from the non-equilibrium distribution function, $f(\boldsymbol{\xi})$, or from the equilibrium one, $f^{(eq)}(\boldsymbol{\xi})$. In this case the first three macroscopic moments

are given by,

$$\rho \equiv \int d^D \boldsymbol{\xi} f^{(eq)}(\boldsymbol{\xi} - \boldsymbol{u}), \tag{4.2}$$

$$\rho \boldsymbol{u} \equiv \int d^D \boldsymbol{\xi} f^{(eq)}(\boldsymbol{\xi} - \boldsymbol{u}) \boldsymbol{\xi}, \tag{4.3}$$

$$\rho \bar{\theta} \delta_{i_1 i_2} \equiv \int d^D \boldsymbol{\xi} f^{(eq)}(\boldsymbol{\xi} - \boldsymbol{u})(\xi - u)_{i_1}(\xi - u)_{i_2}. \tag{4.4}$$

They correspond to the mass density ρ, the macroscopic velocity $\boldsymbol{u}$, and the temperature related quantity $\bar{\theta}$, which gives a measure of the energy density $\varepsilon = D\bar{\theta}/2$ (for the classical case, it is the temperature itself: $\bar{\theta} = \theta$). Therefore the use of $f(\boldsymbol{\xi} - \boldsymbol{u})$ instead of $f^{(eq)}(\boldsymbol{\xi} - \boldsymbol{u})$ renders the same values at any position and time for ρ, $\boldsymbol{u}$, and $\bar{\theta}$ according to the Chapman-Enskog assumption. We also define for later purposes the quantity g associate to the fourth order expectation value,

$$\rho \bar{\theta}^2 g\, \delta_{i_1 i_2 i_3 i_4} \equiv \int d^D \boldsymbol{\xi} f^{(eq)}(\boldsymbol{\xi} - \boldsymbol{u})(\xi - u)_{i_1}(\xi - u)_{i_2}(\xi - u)_{i_3}(\xi - u)_{i_4}, \tag{4.5}$$

which is a function of the same parameters that define ρ and $\bar{\theta}$. Notice that the definition of the macroscopic velocity $\boldsymbol{u}$ is just the statement that at the local center of mass there is no net motion.

$$\int d^D \boldsymbol{\xi} f^{(eq)}(\boldsymbol{\xi} - \boldsymbol{u})(\boldsymbol{\xi} - \boldsymbol{u}) = 0$$

The D-dimensional Euclidean space is endowed with the following tensors, defined by Harold Grad [54], that can be expressed as sums of products of the Kronecker's delta function ($\delta_{ij} = 1$ for $i = j$ and 0 for $i \neq j$),

$$\delta_{i_1 \cdots i_N | j_1 \cdots j_N} \equiv \delta_{i_1 j_1} \cdots \delta_{i_N j_N} \,+\, \text{permutations of } i\text{'s}, \tag{4.6}$$

$$\delta_{i_1 \cdots i_N \, j_1 \cdots j_N} \equiv \delta_{i_1 j_1} \cdots \delta_{i_N j_N} \,+\, \text{all permutations.} \tag{4.7}$$

Properties of the above tensors, such as their number of terms, is discussed in more details Ref. [42].

Using the Chapman-Enskog expansion [26, 81], the macroscopic equations and the transport coefficients for a fluid governed by a given EDF f^{eq} can be calculated from the discrete Boltzmann equation,

$$f(\boldsymbol{x} + \boldsymbol{\xi}\Delta t, \boldsymbol{\xi} + \boldsymbol{a}\Delta t, t + \Delta t) - f(\boldsymbol{x}, \boldsymbol{\xi}, t) = -\Delta t\, \frac{f - f^{eq}}{\tau}, \qquad (4.8)$$

where Δt is the step time. The continuous form of this equation is obtained by expanding in powers of Δt and the first order term is the continuous Boltzmann equation, given Eq.(4.1).

We are interested in expanding the EDF in a polynomial power series in D-dimensional space, as such,

$$f^{(eq)}(\boldsymbol{\xi} - \boldsymbol{u}) = \omega(\boldsymbol{\xi}) \sum_{N=0}^{K} \frac{1}{N!} \mathcal{A}_{i_1 i_2 \cdots i_N}(\boldsymbol{u}) \mathcal{P}_{i_1 i_2 \cdots i_N}(\boldsymbol{\xi}). \qquad (4.9)$$

$\mathcal{A}_{i_1 i_2 \cdots i_N}$ are the projections of the EDF on the polynomials and $\mathcal{P}_{i_1 \cdots i_N}(\boldsymbol{\xi})$ are the polynomials themselves, which are orthonormal under a generic weight function $\omega(\boldsymbol{\xi})$. This weight function is assumed to only depend on the modulus of the microscopic velocity $\boldsymbol{\xi} \equiv (\xi_1, \xi_2, \cdots, \xi_D)$: $\omega(\boldsymbol{\xi}) = \omega(\xi)$, $\xi \equiv |\boldsymbol{\xi}|$, and to have the property that $\omega(\boldsymbol{\xi}) \to 0$ for $\xi \to \infty$ faster than any power of ξ.

Remarkably only a few terms in the above series expansion must be included to guarantee mass, momentum and energy conservation. The Chapman-Enskog analysis shows that in order to obtain the hydrodynamic equations of continuity and the Navier-Stokes equation the above series expansion can be cutoff at K=3 and to include the equation of energy conservation one must include only one more term, namely, go to order K=4. More details about the obtainment of the macroscopic equations can be found in Sec. 4.5. However the above cutoff procedure does not guarantee convergence of the cutoff series expansion to the orginal EDF. Hence it remains another very important requirement to

be fullfilled which is of convergence to the underlying physics. This is expected under the assumption that the macroscopic velocity is much smaller than the microscopic one, $u \ll \xi$. The point that we stress here is that clearly this convergence is intimately connected to the choice of the weight function $\omega(\xi)$, that must be close enough to $f^{(eq)}(\xi)$ such that the remaining multiplying series is just a small correction to it and so, only a few terms would be enough to describe the corrections in $\boldsymbol{\xi}$.

The three EDFs explicitly depend on the microscopic velocity, $\boldsymbol{\xi}$, and implicitly on the position, $\boldsymbol{x}$, through the local macroscopic parameters, such as the density $\rho(\boldsymbol{x})$, the chemical potential $\mu(\boldsymbol{x})$, the fugacity $z(\boldsymbol{x})$ the macroscopic velocity $\boldsymbol{u}(\boldsymbol{x})$, and the temperature $\theta(\boldsymbol{x})$. The FD $(+)$ and the BE $(-)$ EDFs are given by

$$f^{(eq)}_{FD/BE}(\boldsymbol{\xi}) = \frac{1}{z^{-1}\exp\left(\boldsymbol{\xi}^2/2\theta\right) \pm 1}, \quad z = \exp\left(\mu/\theta\right) \tag{4.10}$$

and the MB is,

$$f^{(eq)}_{MB}(\boldsymbol{\xi}) = \frac{\rho_0}{(2\pi\theta)^{D/2}} \exp\left(-\boldsymbol{\xi}^2/2\theta\right) \tag{4.11}$$

where ρ_0 is a dimensionless density. All variables are defined dimensionless ($m = k_B = c = \hbar = e = 1$) by means of appropriate temperature and velocity scales. We observe the remarkable property of the series expansion in terms of the new polynomials, which is to have the macroscopic velocity expressed always as a ratio to a reference velocity of the problem, not necessarily the thermal velocity. For instance, notice that, in case of electron's in metals, Mach's number diverges at $T = 0$ and cannot even be considered as a reference velocity. Indeed in this case the scale is set by the Fermi speed, v_F and, since the microscopic velocity U is very low in metals, for typical electric fields, $u/v_F \sim 0.4 \times 10^{-6}$, according to previously given values. Hence the new polynomials in case of electrons in metals render the series expansion of the EDF at $T = 0$ to be automatically in powers of the ratio u/v_F instead, as shown in Ref. [31].

The convergence problem is better understood in the limit of a vanishing macroscopic velocity at Eq.(4.9), which gives that,

$$f^{(eq)}(\boldsymbol{\xi}) = \omega(\xi) \sum_{N=0}^{K} \frac{1}{N!} \mathcal{A}_{i_1\,i_2\cdots i_N}(0) \mathcal{P}_{i_1\,i_2\cdots i_N}(\boldsymbol{\xi}). \tag{4.12}$$

$f^{(eq)}(\boldsymbol{\xi})$ for the MB EDF is a gaussian and so the choice of $\omega(\xi)$ equal to the Hermite weight function,

$$\omega(\boldsymbol{\xi}) = \frac{1}{(2\pi)^{D/2}} \exp\left(-\frac{\boldsymbol{\xi}^2}{2}\right), \tag{4.13}$$

is a good choice which implies the presence of the D-dimensional Hermite polynomials. However the Hermite weight is very different from the FD or MB EDFs rendering the need of many terms in the series expansion that multiplies $\omega(\xi)$. A striking example of such difficulty is provided by the FD EDF very near to zero temperature ($\theta \approx 0$) which becomes equal to a Heaviside step function ($f_{FD}^{(eq)} \approx 1$ for $\boldsymbol{\xi}^2/2 \leq \mu$ and $f_{FD}^{(eq)} \approx 0$ for $\boldsymbol{\xi}^2/2 \geq \mu$). Expressing the Heaviside function as the product of a gaussian times a series expansion implies that the latter must contain many terms. Hence this zero limit provides evidence of the inadequacy of the Hermite weight to describe electrons in metals for instance, since those behave at room temperature very similarly to the zero temperature limit [7]. Hence we reach the conclusion that for indistinguishable particles, namely BE or FD particles, the weight function must be chosen accordingly in order to reach convergence in the expanded EDF with a few terms. In this chapter we study separately two similar but distinguishable situations, namely, of the weight similar to the EDF itself, $\omega(\xi) \approx f^{(eq)}(\boldsymbol{\xi})$ and of the weight exactly equal to the EDF, $\omega(\xi) = f^{(eq)}(\boldsymbol{\xi})$. In order to treat these two cases we firstly obtain the D-dimensional polynomials orthonormal under a general weight $\omega(\xi)$.

4.3 Expansion in polynomials orthonormal under a general weight

In this section, we consider the series expansion in polynomials orthonormal under a general weight $\omega(\xi)$. Although we are ultimately interested in the situation that the weight is similar to the EDF itself, $\omega(\xi) \approx f^{(eq)}(\boldsymbol{\xi})$, because this makes convergence faster, we do no take this assumption here. For the special case that $\omega(\xi) = f^{eq}(\xi)$ some extra properties can be derived and this is done in the next section. The projections $\mathcal{A}_{i_1 i_2 \cdots i_N}$ are obtained from the general orthonormal relation of Eq.(3.1),

$$\mathcal{A}_{i_1 i_2 \cdots i_N}(\boldsymbol{u}) = \int d^D \boldsymbol{\xi}' \, f^{(eq)}(\boldsymbol{\xi}' - \boldsymbol{u}) \mathcal{P}_{i_1 i_2 \cdots i_N}(\boldsymbol{\xi}').$$

There is a completeness relation for these generalized tensorial polynomials, which is obtained from the above expression and Eq.(4.9):

$$f^{(eq)}(\boldsymbol{\xi} - \boldsymbol{u}) = \omega(\boldsymbol{\xi}) \cdot \sum_{N=0}^{\infty} \frac{1}{N!} \int d^D \boldsymbol{\xi}' \, f^{(eq)}(\boldsymbol{\xi}' - \boldsymbol{u}) \mathcal{P}_{i_1 i_2 \cdots i_N}(\boldsymbol{\xi}') \mathcal{P}_{i_1 i_2 \cdots i_N}(\boldsymbol{\xi}),$$

since $f(\boldsymbol{\xi} - \boldsymbol{u}) = \int d^D \boldsymbol{\xi}' \, \delta^D(\boldsymbol{\xi}' - \boldsymbol{\xi}) f(\boldsymbol{\xi}' - \boldsymbol{u})$. The completeness relation is given by,

$$\omega(\boldsymbol{\xi}) \sum_{N=0}^{\infty} \frac{1}{N!} \mathcal{P}_{i_1 i_2 \cdots i_N}(\boldsymbol{\xi}') \mathcal{P}_{i_1 i_2 \cdots i_N}(\boldsymbol{\xi}) = \delta^D(\boldsymbol{\xi}' - \boldsymbol{\xi}),$$

In terms of the relative (or peculiar) velocity $\boldsymbol{\eta} = \boldsymbol{\xi} - \boldsymbol{u}$ the quantities ρ, $\bar{\theta}$ and g become,

$$\rho \equiv \int d^D \boldsymbol{\eta} f^{(eq)}(\boldsymbol{\eta}), \tag{4.14}$$

$$\rho \bar{\theta} \delta_{i_1 i_2} \equiv \int d^D \boldsymbol{\eta} f^{(eq)}(\boldsymbol{\eta}) \eta_{i_1} \eta_{i_2}, \tag{4.15}$$

$$\rho \bar{\theta}^2 g \, \delta_{i_1 i_2 i_3 i_4} \equiv \int d^D \boldsymbol{\eta} f^{(eq)}(\boldsymbol{\eta}) \eta_{i_1} \eta_{i_2} \eta_{i_3} \eta_{i_4}. \tag{4.16}$$

For the case of the FD-BE EDF these quantities can be expressed in terms of the integrals defined as

$$g_\nu(z) = \frac{1}{\Gamma(\nu)} \int_0^\infty dx \frac{x^{\nu-1}}{z^{-1} \exp(x) \pm 1}, \tag{4.17}$$

which are functions of the fugacity z. One obtains that,

$$\rho(z,\theta) = (2\pi\theta)^{\frac{D}{2}} g_{\frac{D}{2}}(z), \tag{4.18}$$

$$\bar{\theta}(z,\theta) = \theta \frac{g_{\frac{D}{2}+1}(z)}{g_{\frac{D}{2}}(z)}, \tag{4.19}$$

$$g(z) = \frac{g_{\frac{D}{2}}(z) g_{\frac{D}{2}+2}(z)}{\left(g_{\frac{D}{2}+1}(z)\right)^2}. \tag{4.20}$$

Recall that the EDF is solely a function of the modulus of the relative velocity, namely, $f^{eq}(\eta)$, $\eta = |\boldsymbol{\eta}|$. Below the first five projections of the EDF are calculated by noticing that by taking that $d^D\boldsymbol{\xi} = d^D\boldsymbol{\eta}$ the limits of integration do not change since the integrand vanishes exponentially at infinity.

- **Zeroth order** – Since $\mathcal{P}_0(\boldsymbol{\xi}) = c_0$, one obtains that

$$\mathcal{A}_0 = \int d^D\boldsymbol{\eta} f^{(eq)}(\boldsymbol{\eta}) \mathcal{P}_0(\boldsymbol{\xi}) = c_0\rho \tag{4.21}$$

- **First order** – Since $\mathcal{P}_{i_1}(\boldsymbol{\xi}) = \mathcal{P}_{i_1}(\boldsymbol{\eta}) + c_1 u_{i_1}$, there are two terms to consider for the projection,

$$\mathcal{A}_{i_1} = \int d^D\boldsymbol{\eta} f^{(eq)}(\boldsymbol{\eta}) \mathcal{P}_{i_1}(\boldsymbol{\xi}),$$

The first term gives no contribution because the integration of an odd function vanishes. Hence only the second term contributes and gives that,

$$\mathcal{A}_{i_1} = c_1 u_{i_1} \int d^D\boldsymbol{\eta} f^{(eq)}(\boldsymbol{\eta}) = \rho c_1 u_{i_1}. \tag{4.22}$$

- **Second order** – In the projection,

$$\mathcal{A}_{i_1 i_2} = \int d^D\boldsymbol{\eta} f^{(eq)}(\boldsymbol{\eta}) \mathcal{P}_{i_1 i_2}(\boldsymbol{\xi}),$$

we introduce the expanded polynomial,

$$\mathcal{P}_{i_1 i_2}(\boldsymbol{\xi}) = \mathcal{P}_{i_1 i_2}(\boldsymbol{\eta}) + \frac{c_2}{c_1}[u_{i_1}\mathcal{P}_{i_2}(\boldsymbol{\eta}) + u_{i_2}\mathcal{P}_{i_1}(\boldsymbol{\eta})] + 2\frac{\bar{c}_2}{c_1}u_{i_3}\mathcal{P}_{i_3}(\boldsymbol{\eta})\delta_{i_1 i_2} + c_2 u_{i_1} u_{i_2} + \bar{c}_2 u^2 \delta_{i_1 i_2}.$$

The odd terms vanish and so,

$$\mathcal{A}_{i_1 i_2} = \rho \left[(c_2 \bar{\theta} + c_2') \delta_{i_1 i_2} + c_2 u_{i_1} u_{i_2} + \bar{c}_2 (D\bar{\theta} + \boldsymbol{u}^2) \delta_{i_1 i_2} \right] \tag{4.23}$$

• **Third order** – Similarly, the projection,

$$\mathcal{A}_{i_1 i_2 i_3} = \int d^D \boldsymbol{\eta} \, f^{(eq)}(\boldsymbol{\eta}) \mathcal{P}_{i_1 i_2 i_3}(\boldsymbol{\xi})$$

is calculated using the expanded polynomial.

$$\mathcal{P}_{i_1 i_2 i_3}(\boldsymbol{\xi}) = \mathcal{P}_{i_1 i_2 i_3}(\boldsymbol{\eta}) + c_3 u_{i_1} \eta_{i_2} \eta_{i_3} + c_3 u_{i_3} \eta_{i_1} \eta_{i_2} + c_3 u_{i_1} u_{i_3} \eta_{i_2} + c_3 u_{i_2} \eta_{i_1} \eta_{i_3} + c_3 u_{i_2} u_{i_3} \eta_{i_1}$$

$$+ c_3 u_{i_2} u_{i_3} u_{i_1} + c_3 u_{i_2} u_{i_1} \eta_{i_3} + (\bar{c}_3 \eta^2 + c_3')(u_{i_1} \delta_{i_2 i_3} + u_{i_2} \delta_{i_1 i_3} + u_{i_3} \delta_{i_1 i_2}) + \bar{c}_3 u^2 (\eta_{i_1} \delta_{i_2 i_3}$$

$$+ \eta_{i_2} \delta_{i_1 i_3} + \eta_{i_3} \delta_{i_1 i_2} + u_{i_1} \delta_{i_2 i_3} + u_{i_2} \delta_{i_1 i_3} + u_{i_3} \delta_{i_1 i_2}) + 2\bar{c}_3 u_{i_4} \eta_{i_4} (\eta_{i_1} \delta_{i_2 i_3} + \eta_{i_2} \delta_{i_1 i_3}$$

$$+ \eta_{i_3} \delta_{i_1 i_2} + u_{i_1} \delta_{i_2 i_3} + u_{i_2} \delta_{i_1 i_3} + u_{i_3} \delta_{i_1 i_2})$$

Using Eq.(4.16) we get that,

$$\mathcal{A}_{i_1 i_2 i_3} = \rho \left[\left(c_3 \bar{\theta} + \bar{c}_3 \bar{\theta}(D+2) + c_3' + \bar{c}_3 u^2 \right) (u_{i_1} \delta_{i_2 i_3} + u_{i_3} \delta_{i_1 i_2} + u_{i_2} \delta_{i_1 i_3}) + c_3 u_{i_1} u_{i_2} u_{i_3} \right]. \tag{4.24}$$

• **Fourth order** – The last projection obtained here is,

$$\mathcal{A}_{i_1 i_2 i_3 i_4} = \int d^D \boldsymbol{\eta} \, f^{(eq)}(\boldsymbol{\eta}) \mathcal{P}_{i_1 i_2 i_3 i_4}(\boldsymbol{\xi})$$

The expansion of the N=4 polynomial in the variable $\boldsymbol{\xi} = \boldsymbol{\eta} + \boldsymbol{u}$ renders a complex expression and for this reason we write below only its even terms, the only ones to contribute to the projection.

$$\mathcal{P}_{i_1 i_2 i_3 i_4}(\boldsymbol{\xi}) = c_4(\eta_{i_1} \eta_{i_2} \eta_{i_3} \eta_{i_4} + \eta_{i_1} \eta_{i_2} u_{i_3} u_{i_4} + \eta_{i_1} \eta_{i_3} u_{i_2} u_{i_4} + \eta_{i_1} \eta_{i_4} u_{i_2} u_{i_3} + \eta_{i_2} \eta_{i_3} u_{i_1} u_{i_4}$$

$$+ \eta_{i_2} \eta_{i_4} u_{i_1} u_{i_3} + \eta_{i_3} \eta_{i_4} u_{i_1} u_{i_2} + u_{i_1} u_{i_2} u_{i_3} u_{i_4}) + (c_4' + \bar{c}_4 \eta^2 + \bar{c}_4 u^2)[(\eta_{i_1} \eta_{i_2} + u_{i_1} u_{i_2}) \delta_{i_3 i_4}$$

$$+ (\eta_{i_1} \eta_{i_3} + u_{i_1} u_{i_3}) \delta_{i_2 i_4} + (\eta_{i_1} \eta_{i_4} + u_{i_1} u_{i_4}) \delta_{i_2 i_3} + (\eta_{i_3} \eta_{i_4} + u_{i_3} u_{i_4}) \delta_{i_1 i_2} + (\eta_{i_2} \eta_{i_4} + u_{i_2} u_{i_4}) \delta_{i_1 i_3}$$

$$+ (\eta_{i_2} \eta_{i_3} + u_{i_2} u_{i_3}) \delta_{i_1 i_4}] + 2\bar{c}_4(\boldsymbol{\eta} \cdot \boldsymbol{u})[(\eta_{i_1} u_{i_2} + \eta_{i_2} u_{i_1}) \delta_{i_3 i_4} + (\eta_{i_1} u_{i_3} + \eta_{i_3} u_{i_1}) \delta_{i_2 i_4} + (\eta_{i_1} u_{i_4}$$

$$+ \eta_{i_4} u_{i_1}) \delta_{i_2 i_3} + (\eta_{i_3} u_{i_4} + \eta_{i_4} u_{i_3}) \delta_{i_1 i_2} + (\eta_{i_2} u_{i_4} + \eta_{i_4} u_{i_2}) \delta_{i_1 i_3} + (\eta_{i_2} u_{i_3} + \eta_{i_3} u_{i_2}) \delta_{i_1 i_4}] + [d_4$$

$$+ d_4'(\eta^2 + u^2) + \bar{d}_4(\eta^4 + 2\eta^2 u^2 + 4(\boldsymbol{\eta} \cdot \boldsymbol{u})^2) + u^4](\delta_{i_1 i_2} \delta_{i_3 i_4} + \delta_{i_1 i_3} \delta_{i_2 i_4} + \delta_{i_1 i_4} \delta_{i_2 i_3})$$

$$+ \text{odd terms in } \eta.$$

we have finally the fourth order projection:

$$
\begin{aligned}
\mathcal{A}_{i_1 i_2 i_3 i_4} = \rho \Big\{ &\delta_{i_1 i_2 i_3 i_4} \big[c_4 \bar{\theta}^2 g + 2(c_4' + \bar{c}_4 u^2)\bar{\theta} + 2\bar{c}_4 \bar{\theta}^2 g(D+2) + d_4 + d_4'(D\bar{\theta} + u^2) \\
&+ \bar{d}_4 [\bar{\theta}^2 g D(D+2) + 2u^2 \bar{\theta} D + 4u^2 \bar{\theta} + u^4] \big] + (\delta_{i_1 i_2} u_{i_3} u_{i_4} + \delta_{i_1 i_3} u_{i_2} u_{i_4} + \delta_{i_1 i_4} u_{i_2} u_{i_3} \\
&+ \delta_{i_2 i_3} u_{i_1} u_{i_4} + \delta_{i_2 i_4} u_{i_1} u_{i_3} + \delta_{i_3 i_4} u_{i_1} u_{i_2})(c_4 \bar{\theta} + c_4' + \bar{c}_4 u^2 + \bar{c}_4 \bar{\theta} D + 4\bar{c}_4 \bar{\theta}) + c_4 u_{i_1} u_{i_2} u_{i_3} u_{i_4} \Big\}.
\end{aligned}
$$
(4.25)

From this we obtain the series expansion of the EDF until fourth order.

$$
f^{(eq)}(\boldsymbol{\xi} - \boldsymbol{u}) = \omega(\boldsymbol{\xi}) \Big\{ \mathcal{A}^0 \mathcal{P}_0 + \mathcal{A}_{i_1} \mathcal{P}_{i_1} + \frac{1}{2} \mathcal{A}_{i_1 i_2} \mathcal{P}_{i_1 i_2} + \frac{1}{6} \mathcal{A}_{i_1 i_2 i_3} \mathcal{P}_{i_1 i_2 i_3} + \frac{1}{24} \mathcal{A}_{i_1 i_2 i_3 i_4} \mathcal{P}_{i_1 i_2 i_3 i_4} \Big\}.
$$
(4.26)

where

$$
\mathcal{A}_0 \mathcal{P}_0 = \rho c_0^2, \quad \mathcal{A}_{i_1} \mathcal{P}_{i_1} = \rho c_1^2 (\boldsymbol{\xi} \cdot \boldsymbol{u}), \quad \mathcal{A}_{i_1 i_2} \mathcal{P}_{i_1 i_2} = \rho \{ c_2 (c_2 \bar{\theta} + c_2') \xi^2 + c_2^2 (\boldsymbol{\xi} \cdot \boldsymbol{u})^2
$$
$$
+ c_2 \bar{c}_2 (D\bar{\theta} + u^2) \xi^2 + (\bar{c}_2 \xi^2 + c_2')[D(c_2 \bar{\theta} + c_2') + c_2 u^2 + \bar{c}_2 D(D\bar{\theta} + u^2)] \},
$$
$$
\mathcal{A}_{i_1 i_2 i_3} \mathcal{P}_{i_1 i_2 i_3} = \rho \big\{ 3(c_3 \bar{\theta} + \bar{c}_3 \bar{\theta}(D+2) + c_3' + \bar{c}_3 u^2)(\boldsymbol{\xi} \cdot \boldsymbol{u})[c_3 \xi^2 + (\bar{c}_3 \xi^2 + c_3')(D+2)]
$$
$$
+ c_3^2 (\boldsymbol{\xi} \cdot \boldsymbol{u})^3 + 3c_3 u^2 (\bar{c}_3 \xi^2 + c_3')(\boldsymbol{\xi} \cdot \boldsymbol{u}) \big\}, \text{ and}
$$
$$
\begin{aligned}
\mathcal{A}_{i_1 i_2 i_3 i_4} \mathcal{P}_{i_1 i_2 i_3 i_4} = \rho \Big\{ &\big[c_4 \bar{\theta}_2 g + 2(c_4' + \bar{c}_4 u^2)\bar{\theta} + 2\bar{c}_4 \bar{\theta}_2 g(D+2) + d_4 + d_4'(D\bar{\theta} + u^2) \\
&+ \bar{d}_4 [\bar{\theta}_2 g D(D+2) + 2u^2 \bar{\theta} D + 4u^2 \bar{\theta} + u^4] \big] \cdot \big[3c_4 \xi^4 + 6(c_4' + \bar{c}_4 \xi^2)\xi^2(D+2) + 3(d_4 + d_4' \xi^2 \\
&+ \bar{d}_4 \xi^4)D(D+2) \big] + [c_4 \bar{\theta} + c_4' + \bar{c}_4 u^2 + \bar{c}_4 \bar{\theta} D + 4\bar{c}_4 \bar{\theta}] \big[6c_4 \xi^2 (\boldsymbol{\xi} \cdot \boldsymbol{u})^2 + 6(c_4' + \bar{c}_4 \xi^2)[\xi^2 u^2 \\
&+ (\boldsymbol{\xi} \cdot \boldsymbol{u})^2 (D+4)] + 6(d_4 + d_4' \xi^2 + \bar{d}_4 \xi^4)(D+2)u^2 \big] + c_4^2 (\boldsymbol{\xi} \cdot \boldsymbol{u})^4 + 6c_4 (c_4' + \bar{c}_4 \xi^2)(\boldsymbol{\xi} \cdot \boldsymbol{u})^2 u^2 \\
&+ 3(d_4 + d_4' \xi^2 + \bar{d}_4 \xi^4)u^4 c_4.
\end{aligned}
$$

The question concerning convergence boils down to know that the $u = 0$ limit $f^{(eq)}(\xi)$ has a reliable expression given by $\omega(\xi)$ times a polynomial of fourth order in ξ. Obviously the minimum condition is that $\omega(\xi)$ be sufficiently close to $f^{(eq)}(\xi)$ otherwise it will not be possible.

The numerical simulations of Sec. 4.8 are done with the EDF expanded to second

order, and for this reason, we write it below.

$$f^{(eq)}(\boldsymbol{\xi} - \boldsymbol{u}) = \rho\,\omega(\xi)\Big\{c_0^2 + c_1^2(\boldsymbol{\xi}\cdot\boldsymbol{u}) + \frac{1}{2}c_2(c_2\bar{\theta} + c_2')\xi^2 + \frac{c_2^2}{2}(\boldsymbol{\xi}\cdot\boldsymbol{u})^2$$
$$+ \frac{1}{2}c_2\bar{c}_2(D\bar{\theta} + u^2)\xi^2 + \frac{1}{2}(\bar{c}_2\xi^2 + c_2')[D(c_2\bar{\theta} + c_2') + c_2 u^2 + D\bar{c}_2(D\bar{\theta} + u^2)]\Big\}. \qquad (4.27)$$

4.4 Expansion in polynomials orthonormal for $\omega(\xi) = f^{eq}(\xi)$

In this section, we consider the series expansion in polynomials orthonormal under a weight equal to the EDF itself,

$$\omega(\xi) \equiv f^{(eq)}(\xi). \qquad (4.28)$$

All the results of the previous section still holds, nevertheless the above choice for the weight brings special properties to the projections, such as,

$$\sum_{N=0}^{\infty} \frac{1}{N!}\mathcal{A}_{i_1 i_2 \cdots i_N}(0)\mathcal{P}_{i_1 i_2 \cdots i_N}(\boldsymbol{\xi}) = 1, \qquad (4.29)$$

from where it follows that $\mathcal{A}_{i_1 i_2 \dots i_N}(0) = 0$ for $N \geq 1$ since $\mathcal{A}_0(0)\mathcal{P}_0(\boldsymbol{\xi}) = 1$. This has an important consequence for convergence, these projections are guaranteed to be small in case of a small macroscopic velocity $u \ll 1$. It holds that $\mathcal{A}_{i_1 i_2 \dots i_N}(\boldsymbol{u}) \approx u_{i_1}\delta_{i_2 \dots i_N}$ and $\mathcal{A}_{i_1 i_2 \dots i_N}(\boldsymbol{u}) \approx u^2\delta_{i_1 i_2 \dots i_N} + a.u_{i_1 i_2}\delta_{i_3 \dots i_N}$, where a is a coefficient. This holds for N odd and even, except in case of $\mathcal{A}_0$. Therefore the choice of Eq.(4.28) has important consequences, specially useful in case of the semiclassical statistics, given by the FD and BE EDFs [31]. We notice that the the macroscopic velocity $\boldsymbol{u}$ is a ratio normalized by a velocity appropriate to the bosons or fermions not necessarily equal to Mach's velocity.

The previously defined quantities ρ, $\bar{\theta}$ and g become integrals defined in Eq.(3.10),

$$\rho \equiv \int d^D\boldsymbol{\eta}\,\omega(\boldsymbol{\eta}) = I_0, \qquad (4.30)$$

$$\rho\bar{\theta}\delta_{i_1 i_2} \equiv \int d^D\boldsymbol{\eta}\,\omega(\boldsymbol{\eta})\eta^{i_1}\eta^{i_2} = I_2\delta_{i_1 i_2}, \qquad (4.31)$$

$$\rho\bar{\theta}^2 g\,\delta_{i_1 i_2 i_3 i_4} \equiv \int d^D\boldsymbol{\eta}\,\omega(\boldsymbol{\eta})\eta^{i_1}\eta^{i_2}\eta^{i_3}\eta^{i_4} = I_4\delta_{i_1 i_2 i_3 i_4}. \qquad (4.32)$$

New and interesting expressions for the projections emerge by considering that $\mathcal{P}_0(\boldsymbol{\eta})/c_0 = 1$ and the fact that the weight function is equal to the EDF.

$$\mathcal{A}_{i_1 i_2 \cdots i_N}(\boldsymbol{u}) = \frac{1}{c_0} \int d^D \boldsymbol{\eta} \, \omega(\boldsymbol{\eta}) \, \mathcal{P}_0(\boldsymbol{\eta}) \, \mathcal{P}_{i_1 i_2 \cdots i_N}(\boldsymbol{\eta} + \boldsymbol{u}), \qquad (4.33)$$

Hence the determination of the projections is reduced to the expansion $\mathcal{P}_{i_1 i_2 \cdots i_N}(\boldsymbol{\eta} + \boldsymbol{u})$ as a sum over polynomials $\mathcal{P}_{i_1 i_2 \cdots i_M}(\boldsymbol{\eta})$ of equal or lower order ($M \leq N$).

$$\mathcal{P}_{i_1 i_2 \ldots i_N}(\boldsymbol{\eta} + \boldsymbol{u}) = \mathcal{U}_0(\boldsymbol{u})\mathcal{P}_{i_1 i_2 \ldots i_N}(\boldsymbol{\eta}) + \ldots + \mathcal{U}_{i_1 i_2 \ldots i_N}(\boldsymbol{u})\mathcal{P}_0(\boldsymbol{\eta}).$$

The coefficients $\mathcal{U}_{i_1 i_2 \ldots i_{N-M}}(\boldsymbol{u})$ that multiplies the polynomial $\mathcal{P}_{i_1 i_2 \ldots i_M}(\boldsymbol{\eta})$ are tensors built from products of components u_i and the KroneckerÂ´s delta function δ_{ij} times coefficients which are themselves polynomials in u^2 without the constant term with the exception of $\mathcal{U}_0$ which is a constant itself. Indeed according to the above expression in the limit $\boldsymbol{u} \to 0$, it holds that $\mathcal{U}_0(0) = 1$ while for the higher order tensors $\mathcal{U}_{i_1 i_2 \ldots i_M}(0) = 0$. In summary the sought projections obtained from Eq.(4.33) become,

$$\mathcal{A}_{i_1 i_2 \ldots i_N}(\boldsymbol{u}) = \frac{1}{c_0}\mathcal{U}_{i_1 i_2 \ldots i_N}(\boldsymbol{u}).$$

Then it follows that $\mathcal{A}_{i_1 i_2 \ldots i_N}(\boldsymbol{u} = 0) = 0$ for $N \geq 1$, as previously stated. The obtainment of the projections in case the weight is the EDF itself is reduced to calculate the polynomial expansion, and we do it explicitly to order N=4.

• **Zeroth order** – The expansion in case of N=0 is $\mathcal{P}_0(\boldsymbol{\eta} + \boldsymbol{u}) = \mathcal{U}_0\mathcal{P}_0(\boldsymbol{\eta})$, hence $\mathcal{U}_0 = 1$.

• **First order** – The expansion in case of N=1 is $\mathcal{P}_{i_1}(\boldsymbol{\eta} + \boldsymbol{u}) = c_1(\eta_{i_1} + u_{i_1}) = \mathcal{U}_0(\boldsymbol{u})\mathcal{P}_{i_1}(\boldsymbol{\eta}) + \mathcal{U}_{i_1}(\boldsymbol{u})\mathcal{P}_0(\boldsymbol{\eta})$. Thus $\mathcal{U}_0(\boldsymbol{u}) = 1$ and

$$\mathcal{U}_{i_1}(\boldsymbol{u}) = \frac{c_1}{c_0}u_{i_1}.$$

• **Second order** – Expanding the N=2 polynomial, $\mathcal{P}_{i_1 i_2}(\boldsymbol{\eta} + \boldsymbol{u}) = c_2(\eta_{i_1} + u_{i_1})(\eta_{i_2} + u_{i_2}) + [\bar{c}_2(\boldsymbol{\eta} + \boldsymbol{u})^2 + c_2']\delta_{i_1 i_2}$, gives that,

$$\mathcal{P}_{i_1 i_2}(\boldsymbol{\eta} + \boldsymbol{u}) = \mathcal{P}_{i_1 i_2}(\boldsymbol{\eta}) + \frac{c_2}{c_1}[u_{i_1}\mathcal{P}_{i_2}(\boldsymbol{\eta}) + u_{i_2}\mathcal{P}_{i_1}(\boldsymbol{\eta})] + \frac{2\bar{c}_2}{c_1}u_{i_3}\mathcal{P}_{i_3}(\boldsymbol{\eta})\delta_{i_1 i_2}$$
$$+ \frac{1}{c_0}\mathcal{P}_0(\boldsymbol{\eta})\left[c_2 u_{i_1} u_{i_2} + \bar{c}_2 \boldsymbol{u}^2 \delta_{i_1 i_2}\right].$$

Therefore one obtains that,

$$\mathcal{U}_{i_1 i_2}(\boldsymbol{u}) = \frac{1}{c_0}(c_2 u_{i_1} u_{i_2} + \bar{c}_2 \boldsymbol{u}^2 \delta_{i_1 i_2}).$$

• **Third order** –Similarly the expansion of the N=3 polynomial, $\mathcal{P}_{i_1 i_2 i_3}(\boldsymbol{\eta} + \boldsymbol{u})$, contains the N=0 polynomial plus higher order ones that are omitted for simplicity.

$$\mathcal{P}_{i_1 i_2 i_3}(\boldsymbol{\eta} + \boldsymbol{u}) = \frac{\mathcal{P}_0(\boldsymbol{\eta})}{c_0}\left\{\left[\frac{c_3 \bar{c}_2 D c_2'}{c_2(c_2 + D\bar{c}_2)} - \frac{c_3 c_2'}{c_2} - \frac{\bar{c}_3 D c_2'}{(c_2 + D\bar{c}_2)} + c_3' + \bar{c}_3 \boldsymbol{u}^2 + \frac{2\bar{c}_3 \bar{c}_2 D c_2'}{c_2(c_2 + D\bar{c}_2)}\right.\right.$$
$$\left.\left. - \frac{2\bar{c}_3 c_2'}{c_2}\right] u_{i_4} \delta_{i_1 i_2 i_3 i_4} + c_3 u_{i_1} u_{i_2} u_{i_3}\right\} + \mathcal{O}(\boldsymbol{\eta})$$

The above equation can be simplified using the expressions of the coefficients.

$$\mathcal{P}_{i_1 i_2 i_3}(\boldsymbol{\eta} + \boldsymbol{u}) = \mathcal{P}_0(\boldsymbol{\eta})\mathcal{U}_{i_1 i_2 i_3}(\boldsymbol{u}) + \mathcal{O}(\boldsymbol{\eta}),$$
$$\mathcal{U}_{i_1 i_2 i_3}(\boldsymbol{u}) = \frac{1}{c_0}\left\{\left[\frac{I_2}{I_0}[c_3 + \bar{c}_3(D+2)] + \bar{c}_3 \boldsymbol{u}^2 + c_3'\right] u_{i_4} \delta_{i_1 i_2 i_3 i_4} + c_3 u_{i_1} u_{i_2} u_{i_3}\right\}$$

• **Fourth order** – The N=4 polynomial $\mathcal{P}_{i_1 i_2 i_3 i_4}(\boldsymbol{\eta} + \boldsymbol{u})$ can be expanded in powers of $\boldsymbol{\eta}$ and such powers rearranged as a sum over the polynomials $\mathcal{P}_{i_1 \cdots i_M}(\boldsymbol{\eta})$, M=0 to 4, must be . Nevertheless we only seek the N=0 term and some considerations can be applied to simplify this task. For instance, the odd terms (η_{i_1}, $\eta_{i_1}\boldsymbol{\eta}^2$, $\eta_{i_1}\eta_{i_2}\eta_{i_3}$) do not contribute to the calculation of $\mathcal{A}_{i_1 i_2 i_3 i_4}$ and one can take that $\boldsymbol{\eta}^2 = DI_2/I_0 + \mathcal{O}(\boldsymbol{\eta})$. After some algebra, we have that:

$$\mathcal{P}_{i_1 i_2 i_3 i_4}(\boldsymbol{\eta} + \boldsymbol{u}) = \mathcal{P}_0(\boldsymbol{\eta})\mathcal{U}_{i_1 i_2 i_3 i_4}(\boldsymbol{u}) + \mathcal{O}(\boldsymbol{\eta}), \mathcal{U}_{i_1 i_2 i_3 i_4}(\boldsymbol{u}) = \frac{1}{c_0}\left\{c_4 u_{i_1} u_{i_2} u_{i_3} u_{i_4} + \left[\frac{I_2}{I_0}[c_4\right.\right.$$
$$\left. + \bar{c}_4(D+4)] + c_4' + \bar{c}_4 \boldsymbol{u}^2\right](\delta_{i_1 i_2} u_{i_3} u_{i_4} + \delta_{i_1 i_3} u_{i_2} u_{i_4} + \delta_{i_1 i_4} u_{i_2} u_{i_3} + \delta_{i_2 i_3} u_{i_1} u_{i_4} + \delta_{i_2 i_4} u_{i_1} u_{i_3} +$$
$$\delta_{i_3 i_4} u_{i_1} u_{i_2}) + \left[2\bar{c}_4 \frac{I_2}{I_0}\boldsymbol{u}^2 + d_4' \boldsymbol{u}^2 + 2D\frac{I_2}{I_0}\bar{d}_4 \boldsymbol{u}^2 + 4\frac{I_2}{I_0}\bar{d}_4 \boldsymbol{u}^2 + \boldsymbol{u}^4 \bar{d}_4\right]\delta_{i_1 i_2 i_3 i_4}\right\}.$$

Further simplification gives that,

$$\mathcal{U}_{i_1 i_2 i_3 i_4}(\boldsymbol{u}) = \frac{1}{c_0}\left\{c_4 u_{i_1} u_{i_2} u_{i_3} u_{i_4} + \left[\frac{I_2}{I_0}[c_4 + \bar{c}_4(D+4)] + c_4' + \bar{c}_4 \boldsymbol{u}^2\right](\delta_{i_1 i_2} u_{i_3} u_{i_4}\right.$$
$$+ \delta_{i_1 i_3} u_{i_2} u_{i_4} + \delta_{i_1 i_4} u_{i_2} u_{i_3} + \delta_{i_2 i_3} u_{i_1} u_{i_4} + \delta_{i_2 i_4} u_{i_1} u_{i_3} + \delta_{i_3 i_4} u_{i_1} u_{i_2}) + \left[2\bar{c}_4 \frac{I_2}{I_0}\boldsymbol{u}^2\right.$$
$$\left.\left. + d_4' \boldsymbol{u}^2 + 2D\frac{I_2}{I_0}\bar{d}_4 \boldsymbol{u}^2 + 4\frac{I_2}{I_0}\bar{d}_4 \boldsymbol{u}^2 + \boldsymbol{u}^4 \bar{d}_4\right]\delta_{i_1 i_2 i_3 i_4}\right\}$$

We summarize the projections below, obtained after some additional algebraic manipulation. Notice that they are functions of the integrals I_{2N} previously defined.

$$\mathcal{A}_0(\boldsymbol{u}) = I_0 c_0, \quad \mathcal{A}_{i_1}(\boldsymbol{u}) = I_0 c_1 \, u_{i_1}, \quad \mathcal{A}_{i_1 i_2}(\boldsymbol{u}) = I_0 \big(c_2 u_{i_1} u_{i_2} + \bar{c}_2 \boldsymbol{u}^2 \, \delta_{i_1 i_2} \big),$$

$$\mathcal{A}_{i_1 i_2 i_3}(\boldsymbol{u}) = I_0 \big\{ c_3 \, u_{i_1} u_{i_2} u_{i_3} + \big[c'_3 \big(1 - J_2 \big) + \bar{c}_3 \boldsymbol{u}^2 \big] \big(u_{i_1} \delta_{i_2 i_3} + u_{i_2} \delta_{i_1 i_3} + u_{i_3} \delta_{i_1 i_2} \big) \big\},$$

$$\mathcal{A}_{i_1 i_2 i_3 i_4}(\boldsymbol{u}) = I_0 \Big\{ c_4 \, u_{i_1} u_{i_2} u_{i_3} u_{i_4} + \big[\big(1 - J_2 J_4 \big) c'_4 + \bar{c}_4 \boldsymbol{u}^2 \big] \big) \big(u_{i_1} u_{i_2} \delta_{i_3 i_4} + u_{i_1} u_{i_3} \delta_{i_2 i_4}$$

$$+ u_{i_1} u_{i_4} \delta_{i_2 i_3} + u_{i_2} u_{i_3} \delta_{i_1 i_4} + u_{i_2} u_{i_4} \delta_{i_2 i_3} + u_{i_3} u_{i_4} \delta_{i_1 i_2} \big) + \big[\big(2 \frac{I_2}{I_0} \big(\bar{c}_4 + (D+2) \bar{d}_4 \big) + d'_4 \big) \boldsymbol{u}^2$$

$$+ \bar{d}_4 \boldsymbol{u}^4 \big] \delta_{i_1 i_2 i_3 i_4} \Big\}.$$

Using the definitions of the coefficients, one obtains that,

$$\mathcal{A}_0 \mathcal{P}_0 = 1, \quad \mathcal{A}_{i_1} \mathcal{P}_{i_1} = \frac{I_0}{I_2} (\boldsymbol{\xi} \cdot \boldsymbol{u})$$

$$\mathcal{A}_{i_1 i_2} \mathcal{P}_{i_1 i_2} = I_0 \Big[\frac{1}{I_4} (\boldsymbol{\xi} \cdot \boldsymbol{u})^2 - \frac{(\Delta_2^2 - 1)}{I_4 D} \boldsymbol{u}^2 \boldsymbol{\xi}^2 - \frac{I_2}{I_0 I_4} \Delta_2^2 \boldsymbol{u}^2 \Big]$$

$$\mathcal{A}_{i_1 i_2 i_3} \mathcal{P}_{i_1 i_2 i_3} = I_0 (\boldsymbol{\xi} \cdot \boldsymbol{u}) \Big[3(1 - J_2) \frac{J_4}{I_2} (D+2) \Delta_4^2$$

$$- 3 \frac{J_4}{I_4} \Delta_4^2 \boldsymbol{u}^2 - 3(1 - J_2) \frac{J_4}{I_4} \Delta_4^2 \boldsymbol{\xi}^2 + 3 \frac{\Delta_4^2 - 1}{I_6 (D+2)} \boldsymbol{\xi}^2 \boldsymbol{u}^2 + \frac{1}{I_6} (\boldsymbol{\xi} \cdot \boldsymbol{u})^2 \Big]$$

$$\mathcal{A}_{i_1 i_2 i_3 i_4} \mathcal{P}_{i_1 i_2 i_3 i_4} = I_0 \Big\{ c_4^2 (\boldsymbol{\xi} \cdot \boldsymbol{u})^4 + 6 c_4 (c'_4 + \bar{c}_4 \boldsymbol{\xi}^2) \boldsymbol{u}^2 (\boldsymbol{\xi} \cdot \boldsymbol{u})^2$$

$$+ 3 c_4 \boldsymbol{u}^4 (d_4 + d'_4 \boldsymbol{\xi}^2 + \bar{d}_4 \boldsymbol{\xi}^4) + 6 \Big[\frac{I_2}{I_0} (c_4 + \bar{c}_4 (D+4))$$

$$+ c'_4 + \bar{c}_4 \boldsymbol{u}^2 \Big] \big[c_4 \boldsymbol{\xi}^2 (\boldsymbol{\xi} \cdot \boldsymbol{u})^2 + (c'_4 + \bar{c}_4 \boldsymbol{\xi}^2) [\boldsymbol{\xi}^2 \boldsymbol{u}^2$$

$$+ (\boldsymbol{\xi} \cdot \boldsymbol{u})^2 (D+4)] + (d_4 + d'_4 \boldsymbol{\xi}^2 + \bar{d}_4 \boldsymbol{\xi}^4) \boldsymbol{u}^2 (D+2) \big]$$

$$+ 3 \big[\boldsymbol{u}^2 \frac{I_2}{I_0} 2 (\bar{c}_4 + D \bar{d}_4 + 2 \bar{d}_4) + d'_4 \boldsymbol{u}^2 + \bar{d}_4 \boldsymbol{u}^4 \big] [c_4 \boldsymbol{\xi}^4$$

$$+ 2 (c'_4 + \bar{c}_4 \boldsymbol{\xi}^2) \boldsymbol{\xi}^2 (D+2) + (d_4 + d'_4 \boldsymbol{\xi}^2 + \bar{d}_4 \boldsymbol{\xi}^4) D(D+2)] \Big\}$$

Notice that the macroscopic velocity controls the smallness of the coefficients $\mathcal{A}_{i_1 i_2 \cdots i_N}$, which to the lowest order are linear and quadratic in $\boldsymbol{u}$ for the odd and even $(N > 0)$ coefficients, respectively.

4.4.1 Direct derivation of the equilibrium distribution function to order N=2

The EDF expanded to N=2 in case that $\omega(\xi) \equiv f^{(eq)}(\xi)$ is readily obtained from the sum of the first three above coefficients. Here we derive this N=2 EDF assuming that it is a sum over all possible terms until the second power in the macroscopic velocity, namely, $\boldsymbol{\xi} \cdot \boldsymbol{u}$, $(\boldsymbol{\xi} \cdot \boldsymbol{u})^2$, $\boldsymbol{u}^2$, $\boldsymbol{\xi}^2 \boldsymbol{u}^2$.

$$f^{(eq)} = \omega(\xi) \left[f_0 + f_1 \, \boldsymbol{\xi} \cdot \boldsymbol{u} + \frac{f_2}{2} \, (\boldsymbol{\xi} \cdot \boldsymbol{u})^2 + \frac{f_3}{2} \, \boldsymbol{u}^2 + \frac{f_4}{2} \, \boldsymbol{\xi}^2 \boldsymbol{u}^2 \right]$$

We find the coefficients f_0, f_1, f_2, f_3 and f_4 in the EDF given below, without invoking the orthonormal polynomials and just derive them from the given physical parameters, namely, the density, the macroscopic velocity and the temperature (Eqs.(4.2), (4.3) and (4.4)). Notice that only integrals up to order ξ^4 are used in this derivation. Therefore the following relations are employed in the determination of the coefficients.

$$\int d^D \boldsymbol{\xi} \, \omega(\xi) = I_0,$$

$$\int d^D \boldsymbol{\xi} \, \omega(\xi) \, \xi_{i_1} = 0,$$

$$\int d^D \boldsymbol{\xi} \, \omega(\xi) \, \xi_{i_1} \, \xi_{i_2} = I_2 \, \delta_{i_1 i_2},$$

$$\int d^D \boldsymbol{\xi} \, \omega(\xi) \, \xi_{i_1} \, \xi_{i_2} \, \xi_{i_3} = 0,$$

$$\int d^D \boldsymbol{\xi} \, \omega(\xi) \, \xi_{i_1} \, \xi_{i_2} \, \xi_{i_3} \, \xi_{i_4} = I_4 \, \delta_{i_1 i_2 i_3 i_4}.$$

We start by imposing that Eq.(4.2) holds to find that $\rho = I_0 f_0 + (f_2 I_2 + f_3 I_0 + f_4 D I_2) \boldsymbol{u}^2 / 2$. Similarly from Eq.(4.3) it follows that $\rho \boldsymbol{u} = f_1 I_2 \boldsymbol{u}$. Finally from Eq.(4.4) one obtains that $\rho(u_{i_1} u_{i_2} + \bar{\theta} \delta_{i_1 i_2}) = f_0 I_2 \delta_{i_1 i_2} + f_2 I_4 u_{i_1} u_{i_2} + (\boldsymbol{u}^2 / 2) \delta_{i_1 i_2} [f_2 I_4 + f_3 I_2 + (D+2) I_4 f_4]$. Therefore

$$\rho = I_0 f_0, \quad f_2 I_2 + f_3 I_0 + f_4 D I_2 = 0, \quad \rho = f_1 I_2, \quad \rho \bar{\theta} = f_0 I_2, \quad \rho = f_2 I_4,$$

$$f_2 I_4 + f_3 I_2 + f_4 (D+2) I_4 = 0.$$

Solving these equations one obtains that $f_0 = \rho/I_0$, $f_1 = \rho/I_2$, $f_2 = \rho/I_4$ and $\bar{\theta} = I_2/I_0$. Then one is left with the a system of equations to solve for the remaining two

coefficients whose solution is $f_3 = -(\rho I_2 / I_4 I_0)\Delta_2^2$ and $f_4 = (\rho / I_4)(\Delta_2^2 - 1)/D$ where $\Delta_2^2 = 2/[(D+2) - J_2 D]$, $J_2 = I_2^2 / I_4 I_0$, as previously defined. Finally one obtains that,

$$f^{(eq)} = \frac{\rho}{I_0}\omega(\xi)\left\{1 + \frac{I_0}{I_2}\boldsymbol{\xi}\cdot\boldsymbol{u} + \frac{I_0}{I_4}\frac{1}{2}(\boldsymbol{\xi}\cdot\boldsymbol{u})^2 + \frac{1}{2}\boldsymbol{u}^2\left[\frac{I_0}{I_4}\left(\frac{\Delta_2^2 - 1}{D}\right)\boldsymbol{\xi}^2 - \frac{I_2}{I_4}\Delta_2^2\right]\right\} \tag{4.34}$$

This is equivalent to Eq.(4.27) by substitution of the polynomial coefficients for the case $\omega(\xi) = f^{eq}(\xi)$ and taking that $\rho = I_0$, as given by Eq.(4.30).

4.5 Macroscopic equations

In this section, we show the macroscopic equations followed by the semiclassical fluids, i.e., continuity, momentum conservation and energy conservation equations, and generalize their derivation, done in Ref. [30], for a generic EDF. We also discuss the minimum order that the EDF should be expanded in order to fully recover each macroscopic equation though the Chapman-Enskog expansion, developed below.

4.5.1 General equations

Here we list the general moments of the EDF needed to calculate the macroscopic equations. To recover the mass conservation (continuity equation):

$$\frac{\partial \rho}{\partial t} + \frac{\partial}{\partial x_{i_1}}(\rho u_{i_1}) = 0 \tag{4.35}$$

the zeroth and first order moments of the EDF are needed:

$$\rho = \int d^D \xi f^{eq}, \quad \rho u_{i_1} = \int d^D \xi \xi_{i_1} f^{eq} \tag{4.36}$$

To obtain the momentum equation, one needs to calculate the following second and third order moments:

$$\pi_{i_1 i_2} = \int d^D \xi f^{eq} \xi_{i_1} \xi_{i_2}, \tag{4.37}$$

$$\pi_{i_1 i_2 i_3} = \int d^D \xi f^{eq} \xi_{i_1} \xi_{i_2} \xi_{i_3}, \tag{4.38}$$

which are subsequently introduced into the generic momentum equation:

$$\frac{\partial}{\partial t}(\rho u_{i_1}) + \frac{\partial}{\partial x_{i_2}}\pi_{i_1 i_2} - \left(\tau - \frac{\Delta t}{2}\right)\frac{\partial}{\partial x_{i_2}}\frac{\partial}{\partial x_{i_3}}\pi_{i_1 i_2 i_3} - \left(\tau - \frac{\Delta t}{2}\right)\frac{\partial}{\partial x_{i_2}}\frac{\partial}{\partial t}\pi_{i_1 i_2} = 0 \quad (4.39)$$

And for energy conservation equation, the moments needed are the second, third and fourth order ones:

$$\phi = \frac{1}{2}d^D\xi f^{eq}\xi^2, \tag{4.40}$$

$$\phi_{i_1} = \frac{1}{2}d^D\xi f^{eq}\xi^2\xi_{i_1}, \tag{4.41}$$

$$\phi_{i_1 i_2} = \frac{1}{2}d^D\xi f^{eq}\xi^2\xi_{i_1}\xi_{i_2}. \tag{4.42}$$

which are introduced into the generic energy equation:

$$\frac{\partial}{\partial t}\phi + \frac{\partial}{\partial x_{i_1}}\phi_{i_1} - \left(\tau - \frac{\Delta t}{2}\right)\frac{\partial}{\partial x_{i_1}}\frac{\partial}{\partial x_{i_2}}\phi_{i_1 i_2} - \left(\tau - \frac{\Delta t}{2}\right)\frac{\partial}{\partial x_{i_1}}\frac{\partial}{\partial t}\phi_{i_1} = 0. \tag{4.43}$$

The Eqs. (4.35), (4.39) and (4.43) give the macroscopic equations after calculating the moments above for a specific EDF and after some algebraic manipulations [30, 34].

4.5.2 Macroscopic equations obtained with original function

In Ref. [30] the moments are calculated using the FD and BE EDFs expanded in Hermite polynomials up to fourth order. We generalize here this derivation for a generic non-expanded EDF. Using the definitions of ρ, $\boldsymbol{u}$, $\bar{\theta}$ and g (Eqs. (4.2), (4.3), (4.4) and (4.5) respectively), the moments can be straightforwardly calculated giving that:

$$
\begin{aligned}
\pi_{i_1 i_2} &= \rho\left[\bar{\theta}\delta_{i_1 i_2} + u_{i_1}u_{i_2}\right], \\
\pi_{i_1 i_2 i_3} &= \rho\left[\bar{\theta}(u_{i_1}\delta_{i_2 i_3} + u_{i_2}\delta_{i_1 i_3} + u_{i_3}\delta_{i_1 i_2}) + u_{i_1}u_{i_2}u_{i_3}\right], \\
\phi &= \rho\left(\bar{\theta}\frac{D}{2} + \boldsymbol{u}^2\right), \\
\phi_{i_1} &= \frac{\rho}{2}u_{i_1}\left[\bar{\theta}(D+2) + \boldsymbol{u}^2\right], \\
\phi_{i_1 i_2} &= \frac{\rho}{2}\left[(D+2)\delta_{i_1 i_2}\bar{\theta}^2 g + \bar{\theta}(D+4)u_{i_1}u_{i_2} + \bar{\theta}\boldsymbol{u}^2\delta_{i_1 i_2} + \boldsymbol{u}^2 u_{i_1}u_{i_2}\right],
\end{aligned}
\tag{4.44}
$$

which are the same ones found using the truncated fourth order expansion of EDF in Hermite polynomials [30]. As we will show in the next section, terms from expansion orders higher than the monomial order in the integrand (that is, $\xi_{i_1} \ldots \xi_{i_N}$, where N is the monomial order) do not contribute to the moment because of the orthogonality of the polynomials. In addition, the results above would be the same if the EDF were expanded up to fourth order in any set of orthogonal polynomials.

Therefore, when the moments given in Eq.(4.44) are substituted into Eqs.(4.39) and (4.43), they give the same macroscopic equations obtained in Ref. [30]. The momentum conservation equation or *semiclassical Navier-Stokes* reads:

$$\frac{\partial}{\partial t}(\rho u_{i_1}) + \frac{\partial}{\partial x_{i_2}}[\rho(\bar{\theta}\delta_{i_1 i_2} + u_{i_1}u_{i_2})] - \frac{\partial\bar{\sigma}_{i_1 i_2}}{\partial x_{i_2}} = 0. \tag{4.45}$$

And the energy conservation equation is given by:

$$\frac{\partial}{\partial t}\left[\frac{\rho}{2}(u^2 + D\bar{\theta})\right] + \frac{\partial}{\partial x_{i_1}}\left[\frac{\rho}{2}\left(u^2 + \bar{\theta}(D+2)\right)u_{i_1} + \tilde{Q}_{i_1} - u_{i_2}\bar{\sigma}_{i_1 i_2}\right] = 0, \tag{4.46}$$

where

$$\bar{\sigma}_{i_1 i_2} = \bar{\eta}\left(\frac{\partial u_{i_1}}{\partial x_{i_2}} + \frac{\partial u_{i_2}}{\partial x_{i_1}} - \frac{2}{D}\delta_{i_1 i_2}\frac{\partial u_{i_3}}{\partial x_{i_3}}\right)$$

is the viscosity stress tensor and

$$\tilde{Q}_{i_1} = -\bar{\kappa}\frac{\partial\bar{\theta}}{\partial x_{i_1}} - \frac{\partial}{\partial x_{i_1}}\left[\bar{\kappa}\bar{\theta}(g-1)\right] \tag{4.47}$$

is the heat flux vector (note that the second term disappears for the classical case, since $g = 1$). Here the shear viscosity stands for $\bar{\eta} = \rho\bar{\theta}\left(\tau - \frac{\Delta t}{2}\right)$ and the thermal conductivity for $\bar{\kappa} = \frac{D+2}{2}\rho\bar{\theta}\left(\tau - \frac{\Delta t}{2}\right)$. When the EDF is the BE or the FD distribution, the Eq.(4.47) can be written as a function of the physical temperature and chemical potential gradients. In this case, the quantities $\bar{\theta}$ and $g(z)$ are given by Eqs.(4.19) and (4.20) and Eq.(4.47) becomes:

$$\tilde{Q}_{i_1} = -\kappa_\theta\frac{\partial\theta}{\partial x_{i_1}} - \kappa_\mu\frac{\partial\mu}{\partial x_{i_1}},$$

giving the following transport coefficient:

$$\kappa_\theta = \kappa \left[\left(\frac{D}{2} + 2 \right) \frac{g_{\frac{D}{2}+2}(z)}{g_{\frac{D}{2}}(z)} - \left(\frac{D}{2} + 1 \right) \left(\frac{g_{\frac{D}{2}+1}(z)}{g_{\frac{D}{2}}(z)} \right)^2 \right], \quad \kappa_\mu = 0,$$

as obtained in Ref. [34].

4.5.3 Macroscopic equations obtained with expanded EDF

Here we analyze the minimum number of terms in the series expansion of the EDF that must be kept to obtain the macroscopic equations. This amounts to determine K in the series expansion defined in Sec. 6.2.2. According to Sec. 4.5.1 the moments of the EDF, expressed by Eqs.(4.37), (4.38), (4.40), (4.41) and (4.42) must be obtained. They are integrals of the EDF multiplied by monomials of ξ. For this reason we carry the following general discussion about a monomial tensor of order N, formed by the product of N velocity components. It can be written as a sum over the generalized polynomials that ranges from order zero to order N, that is,

$$\xi_{i_1}\xi_{i_2}\ldots\xi_{i_N} = C_0 \mathcal{P}_{i_1\ldots i_N} + \ldots + C_{i_1\ldots i_N}\mathcal{P}_0,$$

where $C_{i_1\ldots i_N}$ are tensors constructed from the Kronecker's delta function and polynomials coefficients. Thus, a moment of order N of the expanded EDF gives:

$$\pi_{i_1\ldots i_N} = \int d^D\xi f^{eq}\xi_{i_1}\ldots\xi_{i_N}$$

$$= \int d^D\xi \left[\rho\omega(\boldsymbol{\xi}) \sum_{M=0}^{K} \frac{1}{M!}\mathcal{A}_{i_1\cdots i_M}(\boldsymbol{u})\mathcal{P}_{i_1\cdots i_M}(\boldsymbol{\xi}) \right] \left[C_0 \mathcal{P}_{i_1\ldots i_N} + \ldots + C_{i_1\ldots i_N}\mathcal{P}_0 \right].$$

The importance of the orthogonality of the polynomials, Eq. (3.1), can be appreciated at this point. The integrals of the terms in the series expansion which are of order $N + 1$ and above simply vanish. This means that, a moment of order N can be equally obtained either using the full non expanded EDF or the expanded EDF to order N.

For instance, to recover the continuity equation, Eq.(4.35), we need the zero and first

order moments (Eq.(4.36)). Using that $1 = \mathcal{P}_0/c_0$ and $\xi_{i_1} = \mathcal{P}_{i_1}/c_1$, they become:

$$\int d^D \xi \frac{\mathcal{P}_0}{c_0} f^{eq} = \frac{\mathcal{A}_0}{c_0} = \rho, \quad \int d^D \xi \frac{\mathcal{P}_{i_1}}{c_1} f^{eq} = \frac{\mathcal{A}_{i_1}}{c_1} = \rho u_{i_1}.$$

Therefore, the *first order* $(K = 1)$ expansion of the EDF is enough to recover the continuity equation and terms higher than this $(K \geq 2)$ do not contribute.

For the momentum conservation equation, Eq.(4.45), we need the second and third moments $(K = 3)$ given in Eqs.(4.37) and (4.38). The monomials that are being integrated with the EDF can be written in terms of the polynomials as following:

$$\xi_{i_1} \xi_{i_2} = \frac{1}{c_2} \mathcal{P}_{i_1 i_2} - \frac{\bar{c}_2 \delta_{i_1 i_2}}{c_2(c_2 + D\bar{c}_2)} \mathcal{P}_{i_3 i_3} + \frac{c_2' \delta_{i_1 i_2}}{c_2 c_0} \left(\frac{\bar{c}_2 D}{c_2 + D\bar{c}_2} - 1 \right) \mathcal{P}_0,$$

$$\xi_{i_1} \xi_{i_2} \xi_{i_3} = \frac{1}{c_3} \mathcal{P}_{i_1 i_2 i_3} - \frac{\bar{c}_3}{c_3[c_3 + \bar{c}_3(D+2)]} \cdot (\mathcal{P}_{i_1 i_4 i_4} \delta_{i_2 i_3} + \mathcal{P}_{i_2 i_4 i_4} \delta_{i_1 i_3} + \mathcal{P}_{i_3 i_4 i_4} \delta_{i_1 i_2})$$
$$- \frac{c_3'}{c_3 c_1} \left[\frac{\bar{c}_3(D+2)}{c_3 + \bar{c}_3(D+2)} + 1 \right] (\mathcal{P}_{i_1} \delta_{i_2 i_3} + \mathcal{P}_{i_2} \delta_{i_1 i_3} + \mathcal{P}_{i_3} \delta_{i_1 i_2}).$$

Thus, to recover the full momentum conservation equation we need to expand the EDF until *third order* $(K = 3)$ in generalized polynomials, because this is the highest polynomial order that appear. For the calculation of $\pi_{i_1 i_2}$ only the zeroth and second order expansion terms are non-zero and for $\pi_{i_1 i_2 i_3}$ only the first and third order terms are relevant.

Analogously, we find out that to recover the energy conservation equation, we need the *fourth order* $(K = 4)$ expansion, since $\phi_{i_1 i_2}$ in Eq.(4.42) has a fourth order monomial. Hence we have shown that the macroscopic equations given in Sec. 4.5.2 stem from general arguments and so, are equations that govern the semiclassical fluids obtained with the original EDF since higher order terms in the series expansion do not contribute at all although they are there. In the LBM one takes advantage of this fact by eliminating the higher order terms. For this reason it is usual for practical purposes, to retain terms in the series expansion of the EDF only up to second order. This simplifies the computational models, applicable to a small Mach numbers in case of classical particles. We exploit a similar model for the semiclassical particles.

4.6   Forcing term

In this section we treat the presence of a forcing field in the Boltzmann-BGK equation describing a semiclassical fluid. The forcing term in the Boltzmann equation is given by $\boldsymbol{a} \cdot \nabla_\xi f$ (see Eq.(4.1)) and must satisfy the following moment constraints [90]:

$$\int d^D\xi \boldsymbol{a} \cdot \nabla_\xi f = 0 \tag{4.48}$$

$$\int d^D\xi \boldsymbol{\xi a} \cdot \nabla_\xi f = \int d^D\xi \boldsymbol{a} f \tag{4.49}$$

$$\int d^D\xi \xi_{i_1}\xi_{i_2}\boldsymbol{a} \cdot \nabla_\xi f = \int d^D\xi(\xi_{i_1}a_{i_2} + \xi_{i_2}a_{i_1})f. \tag{4.50}$$

The moments of the forcing term up to second order (equations above) are the same for f and f^{eq} according to the Chapmann-Enskog assumption. If the force does not depend on ξ, we have the usual moments

$$\int d^D\xi \boldsymbol{a} f = -\rho\boldsymbol{a} \quad \text{and} \tag{4.51}$$

$$\int d^D\xi(\xi_{i_1}a_{i_2} + \xi_{i_2}a_{i_1})f = -\rho(u_{i_1}a_{i_2} + u_{i_2}a_{i_1}). \tag{4.52}$$

However for semiclassical fluids the particles can be charged, such as in case of electrons in metals, a feature not commonly found in classical fluids. Therefore the Lorentz force must be included in its full account and so, there are two types of accelerations, one due to an electrical field $\boldsymbol{a_E} = \boldsymbol{E}$, which does not depend on the microscopic velocity, and another one, due to a magnetic field $\boldsymbol{a_B} = \boldsymbol{\xi} \times \boldsymbol{B}$, which does depend on the microscopic velocity. Recall that we have adopted natural units: $e = m_e = 1$.

In practice, the forcing term can be easily implemented in LBM simulations by updating the macroscopic velocity in the EDF [91, 137] as follows:

$$\boldsymbol{u}_{t+\Delta t} = \boldsymbol{u}_t + \tau\boldsymbol{a}, \tag{4.53}$$

where $\boldsymbol{a}$ is the acceleration. This approach is equivalent to the previous one up to order $\mathcal{O}(\tau^2)$.

Therefore our goal in this section is to verify that these moment constraints are respected by the forcing term built with the semiclassical EDF, as similarly done in Ref. [90] for the classical EDF. For the sake of simplicity, we verify explicitly the moment constraints only until second order, which means that we are considering the expanded EDF given by Eq.(4.27). Nevertheless we recall that such relations must hold to any expansion order. Since the EDF is a function of $(\boldsymbol{\xi} - \boldsymbol{u})$, we have that $\boldsymbol{a} \cdot \nabla_{\xi} f^{eq} = -\boldsymbol{a} \cdot \nabla_{u} f^{eq}$. Therefore,

$$- \boldsymbol{a} \cdot \nabla_{u} f^{eq} = -\rho \omega(\xi) \Big[c_1^2 \boldsymbol{\xi} + c_2^2 (\boldsymbol{\xi} \cdot \boldsymbol{u}) \boldsymbol{\xi} + (2 c_2 \bar{c}_2 + D \bar{c}_2^2) \xi^2 \boldsymbol{u} + (c_2 c_2' + D \bar{c}_2 c_2') \boldsymbol{u} \Big] \cdot \boldsymbol{a},$$

or, using the coefficient definitions, we can write it in terms of the integrals:

$$- \boldsymbol{a} \cdot \nabla_{u} f^{eq} = -\rho \omega(\xi) \Big[\frac{1}{I_2} \boldsymbol{\xi} + \frac{1}{I_4} (\boldsymbol{\xi} \cdot \boldsymbol{u}) \boldsymbol{\xi} + \frac{(\Delta_2^2 - 1)}{I_4 D} \xi^2 \boldsymbol{u} - \frac{I_2}{I_0 I_4} \Delta_2^2 \boldsymbol{u} \Big] \cdot \boldsymbol{a}, \qquad (4.54)$$

We proceed with the demonstration that Eqs. (4.48), (4.49) and (4.50) hold for the EDF given in Eq.(4.27).

- **Eq.**(4.48) – Considering $\boldsymbol{a_E}$ first, the Eq.(4.54) replaced in Eq.(4.48) gives:

$$\int d^D \xi (-\boldsymbol{a_E} \cdot \nabla_u f^{eq}) = - \int d^D \xi \rho \omega(\xi) \Big[\frac{1}{I_2} \xi_{i_1} E_{i_1} + \frac{1}{I_4} \xi_{i_3} u_{i_3} \xi_{i_1} E_{i_1} + \frac{(\Delta_2^2 - 1)}{I_4 D} \xi_{i_3} \xi_{i_3} u_{i_1} E_{i_1}$$

$$- \frac{I_2}{I_0 I_4} \Delta_2^2 u_{i_1} E_{i_1} \Big] = -\rho \Big[\frac{1}{I_4} u_{i_3} E_{i_1} I_2 \delta_{i_3 i_1} + \frac{(\Delta_2^2 - 1)}{I_4 D} u_{i_1} E_{i_1} I_2 D - \frac{I_2}{I_4 I_0} \Delta_2^2 u_{i_1} E_{i_1} I_0 \Big] = 0,$$

where we have used the definitions of the integrals, Eq.(3.10), and the fact that odd powers of ξ give null integrals. Thus, for a force that does not depend on ξ, the Eq. (4.48) is demonstrated. Now, for a magnetic acceleration $\boldsymbol{a_B} = \boldsymbol{\xi} \times \boldsymbol{B} \Rightarrow (a_B)_{i_1} = \epsilon_{i_1 i_2 i_3} \xi_{i_2} B_{i_3}$, where $\epsilon_{i_1 i_2 i_3}$ is the Levi-Civita tensor, we have:

$$\int d^D \xi (-\boldsymbol{a_B} \cdot \nabla_u f^{eq}) = - \int d^D \xi \omega(\xi) \rho \Big[\frac{1}{I_2} \xi_{i_1} \xi_{i_2} B_{i_3} \epsilon_{i_1 i_2 i_3}$$

$$+ \frac{1}{I_4} \xi_{i_4} u_{i_4} \xi_{i_1} \xi_{i_2} B_{i_3} \epsilon_{i_1 i_2 i_3} + \frac{(\Delta_2^2 - 1)}{I_4 D} \xi_{i_4} \xi_{i_4} u_{i_1} \xi_{i_2} B_{i_3} \epsilon_{i_1 i_2 i_3} - \frac{I_2}{I_0 I_4} \Delta_2^2 u_{i_1} \xi_{i_2} B_{i_3} \epsilon_{i_1 i_2 i_3} \Big]$$

$$= - \frac{\rho}{I_2} B_{i_3} I_2 \delta_{i_1 i_2} \epsilon_{i_1 i_2 i_3} = 0$$

So, Eq. (4.48) is demonstrated for the two cases.

- **Eq.**(4.49) – For $\boldsymbol{a_E}$:

$$
\int d^D\xi \xi_{i_4}(-\boldsymbol{a_E} \cdot \nabla_u f^{eq}) = -\int d^D\xi \omega(\xi)\rho \cdot \Big[\frac{1}{I_2}\xi_{i_1}\xi_{i_4}E_{i_1} + \frac{1}{I_4}\xi_{i_3}u_{i_3}\xi_{i_1}E_{i_1}\xi_{i_4}
$$
$$
+ \frac{(\Delta_2^2-1)}{I_4 D}\xi_{i_3}\xi_{i_3}u_{i_1}E_{i_1}\xi_{i_4} - \frac{I_2}{I_4}\Delta_2^2 u_{i_1}E_{i_1}\xi_{i_4}\Big] = \frac{\rho}{I_2}E_{i_1}I_2\delta_{i_1 i_4} = -\rho(a_E)_{i_4}.
$$

For $\boldsymbol{a_B}$:

$$
\int d^D\xi \xi_{i_5}(-\boldsymbol{a_B} \cdot \nabla_u f^{eq}) = -\int d^D\xi \omega(\xi)\rho \cdot \Big[\frac{1}{I_2}\xi_{i_1}\xi_{i_2}\xi_{i_5}B_{i_3}\epsilon_{i_1 i_2 i_3} + \frac{1}{I_4}\xi_{i_4}u_{i_4}\xi_{i_1}\xi_{i_2}\xi_{i_5}B_{i_3}\epsilon_{i_1 i_2 i_3}
$$
$$
- \frac{I_2}{I_0 I_4}\Delta_2^2 u_{i_1}\xi_{i_2}\xi_{i_5}B_{i_3}\epsilon_{i_1 i_2 i_3} + \frac{(\Delta_2^2-1)}{I_4 D}\xi_{i_4}\xi_{i_4}u_{i_1}\xi_{i_2}B_{i_3}\xi_{i_5}\epsilon_{i_1 i_2 i_3}\Big]
$$
$$
= -\rho\Big[\frac{1}{I_4}u_{i_4}B_{i_3}\epsilon_{i_1 i_2 i_3}I_4\delta_{i_1 i_2 i_4 i_5} - \frac{I_2}{I_4}\Delta_2^2 B_{i_3}u_{i_1}\epsilon_{i_1 i_2 i_3} \cdot I_2\delta_{i_2 i_5} + \frac{(\Delta_2^2-1)}{I_4 D}u_{i_1}B_{i_3}I_4\delta_{i_4 i_4 i_2 i_5}\epsilon_{i_1 i_2 i_3}\Big]
$$

but $\epsilon_{i_1 i_2 i_3}\delta_{i_1 i_2 i_4 i_5} = 0$ and $\epsilon_{i_1 i_2 i_3}\delta_{i_4 i_4 i_2 i_5} = -(D+2)\epsilon_{i_1 i_3 i_5}$, so:

$$
\int d^D\xi \xi_{i_5}(-\boldsymbol{a_B} \cdot \nabla_u f^{eq}) = \rho\Big[-\frac{I_2^2}{I_0 I_4}\Delta_2^2 B_{i_3}u_{i_1}\epsilon_{i_1 i_3 i_5} + \frac{1}{D}(\Delta_2^2-1)(D+2)u_{i_1}B_{i_3}\epsilon_{i_1 i_3 i_5}\Big]
$$
$$
= -\rho\Big[J_2\Delta_2^2 - \frac{D+2}{D}(\Delta_2^2-1)\Big](\boldsymbol{u} \times \boldsymbol{B})_{i_5} = -\rho(a_B)_{i_5},
$$

where we used the identity $J_2\Delta_2^2 - (D+2)/D(\Delta_2^2-1) = 1$ that can be shown with the expressions for J_2 and Δ_2 in terms of the integrals. Thus, the Eq.(4.49), which was equivalent to Eq.(4.51), is also verified.

- **Eq.**(4.50) – For $\boldsymbol{a_E}$,

$$
\int d^D\xi \xi_{i_5}\xi_{i_6}(-\boldsymbol{a_E} \cdot \nabla_u f) = -\int d^D\xi \omega(\xi)\rho \cdot \Big[\frac{1}{I_2}\xi_{i_1}\xi_{i_5}\xi_{i_6}E_{i_1} + \frac{1}{I_4}\xi_{i_3}u_{i_3}\xi_{i_1}E_{i_1}\xi_{i_5}\xi_{i_6}
$$
$$
+ \frac{(\Delta_2^2-1)}{I_4 D}\xi_{i_3}\xi_{i_3}u_{i_1}E_{i_1}\xi_{i_5}\xi_{i_6} - \frac{I_2}{I_0 I_4}\Delta_2^2 u_{i_1}E_{i_1}\xi_{i_5}\xi_{i_6}\Big] = -\rho\Big[\frac{1}{I_4}u_{i_3}E_{i_1}I_4\delta_{i_3 i_1 i_5 i_6}
$$
$$
+ \frac{I_4(\Delta_2^2-1)}{I_4 D}u_{i_1}E_{i_1}\delta_{i_3 i_3 i_5 i_6} - \frac{I_2}{I_0 I_4}\Delta_2^2 u_{i_1}E_{i_1}I_2\delta_{i_6 i_5}\Big] = -\rho(u_{i_5}E_{i_6} + u_{i_6}E_{i_5})
$$
$$
- \rho u_{i_1}E_{i_1}\delta_{i_5 i_6}\Big[1 + \frac{(\Delta_2^2-1)}{D}(D+2) - J_2\Delta_2^2\Big] = -\rho(u_{i_5}E_{i_6} + u_{i_6}E_{i_5}),
$$

giving the Eq.(4.52) as expected. For $\boldsymbol{a_B}$:

$$\int d^D\xi\xi_{i_5}\xi_{i_6}(-\boldsymbol{a_B}\cdot\nabla_u f^{eq}) = -\int d^D\xi\omega(\xi)\rho\cdot\Big[\frac{1}{I_2}\xi_{i_1}\xi_{i_2}\xi_{i_5}\xi_{i_6}B_{i_3}\epsilon_{i_1i_2i_3}$$

$$+\frac{1}{I_4}\xi_{i_4}u_{i_4}\xi_{i_1}\xi_{i_2}\xi_{i_5}\xi_{i_6}B_{i_3}\epsilon_{i_1i_2i_3} - \frac{I_2}{I_0I_4}\Delta_2^2 u_{i_1}\xi_{i_2}\xi_{i_5}\xi_{i_6}B_{i_3}\epsilon_{i_1i_2i_3} - \frac{I_2}{I_0I_4}\Delta_2^2 u_{i_1}\xi_{i_2}\xi_{i_5}\xi_{i_6}\cdot B_{i_3}\epsilon_{i_1i_2i_3}$$

$$+\frac{(\Delta_2^2-1)}{I_4D}\xi_{i_4}\xi_{i_4}u_{i_1}\xi_{i_2}B_{i_3}\xi_{i_5}\xi_{i_6}\epsilon_{i_1i_2i_3}\Big] = -\rho\frac{I_4}{I_2}\delta_{i_1i_2i_5i_6}B_{i_3}\epsilon_{i_1i_2i_3} = 0$$

which is the expected result since

$$\int d^D\xi(\xi_{i_5}(a_B)_{i_6} + \xi_{i_6}(a_B)_{i_5})f^{eq} = \int d^D\xi(\xi_{i_5}\epsilon_{i_6i_7i_8}\xi_{i_7}B_{i_8} + \xi_{i_6}\epsilon_{i_5i_7i_8}\xi_{i_7}B_{i_8})f^{eq}$$

$$= B_{i_8}\epsilon_{i_6i_7i_8}\frac{1}{D}\int d^D\xi\xi^2 f^{eq}\delta_{i_5i_7} + B_{i_8}\epsilon_{i_5i_7i_8}\frac{1}{D}\int d^D\xi\xi^2 f^{eq}\delta_{i_6i_7} = 0$$

Note that, for $\boldsymbol{a_B}$, the equations (4.50) and (4.52) are not equivalent.

4.7 Quadrature beyond Gauss-Hermite

In this section, we extend the concept of quadrature beyond the Gauss-Hermite concept [1], which means that the weight function $\omega(\xi)$ is not necessarily the gaussian function well suited for the D-dimensional Hermite polynomials (Eq.(4.13)). Here we are interested in the generalized polynomials applicable to the semiclassical LBM. The basic assumption is that there is a discrete space of microscopic velocities ξ_α where integrals can be replaced by sums where a discrete set of weights w_α play the role of the weight function $\omega(\xi)$. The following equations should be satisfied where I_M are known before hand from Eq.(3.10):

$$\sum_\alpha w_\alpha\xi_{\alpha i_1}\xi_{\alpha i_2}\ldots\xi_{\alpha i_M} = \int d^D\xi\omega(\xi)\xi_{i_1}\xi_{i_2}\ldots\xi_{i_M}, \qquad (4.55)$$

Hence we demand that the integral of Eq.(4.55) be equal to $I_M\delta_{i_1i_2\ldots i_M}$, according to Eq.(3.10), to obtain that,

$$\sum_\alpha w_\alpha\xi_{\alpha i_1}\xi_{\alpha i_2}\ldots\xi_{\alpha i_M} = I_M\delta_{i_1i_2\ldots i_M}. \qquad (4.56)$$

Notice that for the Gauss-Hermite quadrature $I_M = 1$ and $J_M = 1$ but not for a general weight function. One of the key and well-known features of the LBM is that it takes advantage that only a few of such conditions have to be implemented in order to reach the conservation of mass, momentum and energy. This gives rise to the discrete lattices where only a finite set of discrete weights w_α is obtained that solve the above relations up to a maximal M. Next we determine some of these sets to be used with the semi-classical Boltzmann-BGK equation. We use the standard nomenclature "DdVv", where "d" denotes the dimension and "v" the number of lattice vectors. We have defined the lattice vectors e_α proportional to the discrete velocities ξ_α, such that $\boldsymbol{\xi_\alpha} = \boldsymbol{e_\alpha}/c_s$, where c_s is the reference speed to be found by solving the quadrature equations. By introducing the reference speed one can choose to define one of the lattice vectors, usually the one oriented along the positive x axis, to be equal to one. Below we see the first six quadrature equations:

$$\sum_\alpha w_\alpha = I_0,$$

$$\sum_\alpha w_\alpha e_{\alpha i_1} = 0,$$

$$\sum_\alpha w_\alpha e_{\alpha i_1} e_{\alpha i_2} = I_2 c_s^2 \delta_{i_1 i_2},$$

$$\sum_\alpha w_\alpha e_{\alpha i_1} e_{\alpha i_2} e_{\alpha i_3} = 0,$$

$$\sum_\alpha w_\alpha e_{\alpha i_1} e_{\alpha i_2} e_{\alpha i_3} e_{\alpha i_4} = I_4 c_s^4 \delta_{i_1 i_2 i_3 i_4},$$

$$\sum_\alpha w_\alpha e_{\alpha i_1} e_{\alpha i_2} e_{\alpha i_3} e_{\alpha i_4} e_{\alpha i_5} = 0, \quad (\ldots).$$

The order M (see Eq.(4.55)) is an important characteristic of the quadrature, since it gives the maximum moment of the weight function for which the quadrature provides equivalence between sums and integrals. Notice that the quadrature equations with M odd are automatically satisfied due to the symmetry among vectors e_α, and so, give trivial expressions. In table B.1 we see the order M of some quadratures. It should be noticed that all w_α and c_s must be positive quantities in order to have stable simulations. Next, we

explicitly calculate one quadrature for each dimension: D1V3, D2V9 and D3V15. More quadratures can be found in B.

4.7.1 D1V3

The lattice vectors for this lattice are $e_\alpha = -1, 0, +1$ and there are two different weight: w_0 for $e_0 = 0$ and w_1 for $e_\pm = \pm 1$. So we have three variables to be determined: the two weights and the reference speed c_s. We need to solve three quadrature equations:

$$\sum_\alpha w_\alpha = I_0 \Rightarrow w_0 + 2w_1 = I_0,$$

$$\sum_\alpha w_\alpha e_\alpha^2 = I_2 c_s^2 \Rightarrow 2w_1 = I_2 c_s^2,$$

$$\sum_\alpha w_\alpha e_\alpha^4 = 3I_4 c_s^4 \Rightarrow 2w_1 = 3I_4 c_s^4.$$

The solution for this system is:

$$c_s = \sqrt{\frac{I_2}{3I_4}}, \quad w_0 = I_0\left(1 - \frac{J_2}{3}\right), \quad w_1 = \frac{I_0 J_2}{6}.$$

For the Hermite weight function, this solution becomes the standard D1V3 lattice: $w_0 = 2/3$, $w_1 = 1/6$ and $c_s = 1/\sqrt{3}$. For the D1V3 lattice, $M = 5$, meaning that moments up to order five in Eq.(4.55) are exactly calculated by the sums.

4.7.2 D2V9

The lattice vectors are $e_s = [(\pm 1, 0), (0, \pm 1)]$, $e_l = [(\pm 1, \pm 1)]$ and $e_0 = (0, 0)$, with weights w_s, w_l and w_0 respectively. As we have four unknowns (three weights and c_s), we need four equations, which are:

$$\sum_\alpha w_\alpha = I_0 \Rightarrow w_0 + 4w_s + 4w_l = I_0$$

$$\sum_\alpha w_\alpha e_{\alpha i_1} e_{\alpha i_2} = I_2 c_s^2 \delta_{i_1 i_2} \Rightarrow 2w_s + 4w_l = I_2 c_s^2$$

$$\sum_\alpha w_\alpha e_{\alpha i_1} e_{\alpha i_2} e_{\alpha i_3} e_{\alpha i_4} = I_4 c_s^4 \delta_{i_1 i_2 i_3 i_4} \Rightarrow \begin{cases} 2w_s + 4w_l = 3I_4 c_s^4 \\ 4w_l = I_4 c_s^4 \end{cases}$$

where the last quadrature equation split in two equations because there are two possible choices for the indexes that give non-trivial equations: one for $i_1 = i_2 = i_3 = i_4$ and other for $(i_1 = i_2) \neq (i_3 = i_4)$. The solution is:

$$w_0 = I_0 \left(1 - \frac{5J_2}{9}\right), \quad w_s = \frac{I_0 J_2}{9}, \quad w_l = \frac{I_0 J_2}{36}, \quad c_s = \sqrt{\frac{I_2}{3I_4}}.$$

It gives the standard D2V9 for the Hermite weight: $w_0 = 4/9$, $w_s = 1/9$, $w_l = 1/36$ and $c_s = 1/\sqrt{3}$.

4.7.3 D3V15

The lattice vectors are $e_0 = (0,0,0)$, $e_s = [(\pm 1, 0, 0), (0, \pm 1, 0), (0, 0, \pm 1)]$, $e_l = [(\pm 1, \pm 1, \pm 1)]$ with respective weights w_0, w_s and w_l. Quadrature equations:

$$\sum_\alpha w_\alpha = I_0 \Rightarrow w_0 + 6w_s + 8w_l = I_0$$

$$\sum_\alpha w_\alpha e_{\alpha i_1} e_{\alpha i_2} = I_2 c_s^2 \delta_{i_1 i_2} \Rightarrow 2w_s + 8w_l = I_2 c_s^2$$

$$\sum_\alpha w_\alpha e_{\alpha i_1} e_{\alpha i_2} e_{\alpha i_3} e_{\alpha i_4} = I_4 c_s^4 \delta_{i_1 i_2 i_3 i_4} \Rightarrow \begin{cases} 2w_s + 8w_l = 3I_4 c_s^4 \\ 8w_l = I_4 c_s^4 \end{cases}$$

Solutions:

$$w_0 = I_0 \left(1 - \frac{7J_2}{9}\right), \quad w_s = \frac{I_0 J_2}{9}, \quad w_l = \frac{I_0 J_2}{72}, \quad c_s = \sqrt{\frac{I_2}{3I_4}}.$$

It gives the standard D3V15 for the Hermite weight: $w_0 = 2/9$, $w_s = 1/9$, $w_l = 1/72$ and $c_s = 1/\sqrt{3}$

4.8 The isothermal LBM for electrons in metals

4.8.1 Model description

In this section, we build a simple and efficient model for electrons in metals in 2D and 3D dimensions and test it with the Riemann problem, the Poiseuille flow and the Ohm's law. The model complies with the condition $\omega(\xi) \approx f^{eq}(\xi)$, thus the weight is not equal to

the EDF itself. The electrons inside the metal are governed by the FD distribution [65],

$$f_{FD}^{eq} = \left\{ \exp\left[\frac{m_e(\boldsymbol{\chi} - \boldsymbol{v})^2}{2k_BT} - \frac{\mu'}{k_BT} \right] + 1 \right\}^{-1},$$

where χ and v are the microscopic and macroscopic velocities respectively, m_e is the electron mass, k_B is the Boltzmann constant, T is the temperature and μ' is the chemical potential. The Fermi energy can be expressed as a function of the Fermi temperature T_F and the Fermi speed v_F as

$$E_F = k_B T_F = \frac{1}{2} m_e v_F^2.$$

Considering the Fermi speed, $v_F = \sqrt{2k_B T_F/m_e}$, as the reference speed for our model, we can define non-dimensional variables:

$$\mu \equiv \frac{\mu'}{k_B T_F}, \quad \theta \equiv \frac{T}{T_F}, \quad \boldsymbol{\xi} \equiv \frac{\boldsymbol{\chi}}{v_F} \quad \text{and} \quad \boldsymbol{u} \equiv \frac{\boldsymbol{v}}{v_F}$$

leading to

$$f_{FD}^{eq} = \left\{ \exp\left[\frac{(\boldsymbol{\xi} - \boldsymbol{u})^2}{\theta} - \frac{\mu}{\theta} \right] + 1 \right\}^{-1}. \tag{4.57}$$

We consider in our model the physical parameters of cooper at room temperature ($T = 300$ K), which has Fermi temperature $T_F^{Cu} = 8.16 \times 10^4\, K$, giving $\theta \approx 1/270$, $\mu = 1$ and $z = e^{270}$ [7]. We expand the FD distribution in Eq.(4.57) up to second order in generalized polynomials, where the coefficients are calculated by orthogonalizing the polynomials with respect to the weight function below:

$$\omega(\xi) = \frac{1}{e^{-270}e^{270\xi^2} + 1}, \tag{4.58}$$

which, initially, is the Eq.(4.57) for $\boldsymbol{u} = 0$ and constant θ and μ. Hence the condition $\omega(\xi) = f^{eq}(\xi)$ discussed along this chapter is not being implemented here otherwise the weights would have to be updated at each time step since the chemical potential changes in $f^{eq}(\xi)$ while here $\omega(\xi)$ remains constant. The integrals I_N, Eq.(3.11), are different for

2D and 3D, which implies that the polynomial coefficients are also different for the two cases (see Sec. 3.4). The discrete version of the second order expansion in Eq.(4.27) becomes:

$$f_\alpha^{eq} = \rho\, w_\alpha \Big\{ c_0^2 + c_1^2(\boldsymbol{\xi_\alpha} \cdot \boldsymbol{u}) + \frac{1}{2}c_2(c_2\bar{\theta} + c_2')\xi_\alpha^2 + \frac{c_2^2}{2}(\boldsymbol{\xi_\alpha} \cdot \boldsymbol{u})^2 + \frac{1}{2}c_2\bar{c}_2(D\bar{\theta} + u^2)\xi_\alpha^2$$
$$+ \frac{1}{2}(\bar{c}_2\xi_\alpha^2 + c_2') \cdot [D(c_2\bar{\theta} + c_2') + c_2 u^2 + D\bar{c}_2(D\bar{\theta} + u^2)] \Big\}, \tag{4.59}$$

where $\bar{\theta}$ have different values for 2D and 3D and $\boldsymbol{\xi_\alpha} = \boldsymbol{e}_\alpha/c_s$ are the discrete velocities given in Sec. 4.7. Besides having constant temperature $\theta = 1/270$ we use another approximation for the semiclassical model in order to simplify the numerical implementation, which is $\bar{\theta} = I_2/I_0 = \theta g_{\frac{D}{2}+1}(z)/(2g_{\frac{D}{2}}(z)) = $ constant. For the classical LBM, $\bar{\theta}$ is automatically constant for the isothermal case, since $\bar{\theta}_{cl} = \theta$. Therefore, this extra approximation is not needed. With this approximations and using the expressions for the coefficients, we verify the identity $c_2\bar{\theta} + c_2' + D\bar{c}_2\bar{\theta} = 0$, which leads to:

$$f_\alpha^{eq} = \rho\, w_\alpha \Big\{ c_0^2 + c_1^2(\boldsymbol{\xi_\alpha} \cdot \boldsymbol{u}) + \frac{c_2^2}{2}(\boldsymbol{\xi_\alpha} \cdot \boldsymbol{u})^2 + \frac{1}{2}c_2\bar{c}_2 u^2 \xi_\alpha^2 + \frac{1}{2}(\bar{c}_2\xi_\alpha^2 + c_2')(c_2 + D\bar{c}_2)u^2 \Big\}. \tag{4.60}$$

The above EDF is the one used in our numerical algorithm together added to the values for the coefficients and $\bar{\theta}$ given in the next sections for $D = 2$ or 3 dimensions, respectively. The quadratures are given in the next sections and the time evolution is governed by the Boltzmann equation in its discrete form (see Eq.(4.8)) and in terms of the lattice vectors e_α.

$$f_\alpha(\mathbf{x} + \mathbf{e}_\alpha \Delta t, t + \Delta t) - f_\alpha(\mathbf{x}, t) = -\frac{\Delta t}{\tau}[f_\alpha(\mathbf{x}, t) - f_\alpha^{eq}(\mathbf{x}, t)],$$

The macroscopic quantities are calculated by:

$$\rho = \sum_\alpha w_\alpha f_\alpha, \quad \mathbf{u} = \frac{1}{\rho}\sum_\alpha w_\alpha f_\alpha \frac{\boldsymbol{e}_\alpha}{c_s}. \tag{4.61}$$

We can convert the density into the chemical potential and vice-versa by means of the relation (see Eq.(4.2))

$$\rho = (\pi\theta)^{D/2} g_{\frac{D}{2}}(e^{\frac{\mu}{\theta}}).$$

For $\mu/\theta \gg 1$, one can use the Sommerfeld expansion to approximate the FD integral:

$$g_\nu(e^{\frac{\mu}{\theta}}) = \frac{(\mu/\theta)^\nu}{\Gamma(\nu+1)}\left[1 + \nu(\nu-1)\frac{\pi^2}{6}\left(\frac{\theta}{\mu}\right)^2 + \nu(\nu-1)(\nu-2)(\nu-3)\frac{7\pi^4}{360}\left(\frac{\theta}{\mu}\right)^4 + \dots\right]$$

(4.62)

2D model

To build our model in 2D, we first calculate the polynomial coefficients using the weight function, Eq.(4.58), through their expressions given in Sec. 3.4.

c_0	0.564189583547756286948079
c_1	1.128353706923879405456370
c_2	2.763766115146273701436833
$\bar{c}_2$	0.572262450908341120084001
c_2'	-0.977116848075011682697851
$\bar{\theta}$	0.250011282126658766985161

where the pseudo-temperature was calculated by $\bar{\theta} = I_2/I_0 = \theta g_2(z)/(2g_1(z))$. The discrete weights are also calculated using the weight function in Eq.(4.58) to calculate the expressions in Table B.1. For a D2V9 lattice, we have:

w_0	0.523716900428241365084608
w_s	0.523575150632310374675607
w_l	0.130893787658077593668902
c_s	1.414149748226522446289974

Note that, although we are keeping the standard notation for the reference speed, c_s, it denotes the Fermi speed and not the sound speed as for the classical models.

To obtain the chemical potential from the density, we use the Sommerfeld's expansion, Eq.(4.62), leading to $\rho = \pi\theta g_1(z) \approx \pi\mu$. This is an excellent approximation for the 2D case with accuracy much beyond the double precision (10^{-16}).

3D model

Following the same procedure as for the 2D model, we calculate the polynomial coefficients and $\bar{\theta} = \theta g_{\frac{5}{2}}(z)/(2g_{\frac{3}{2}}(z))$:
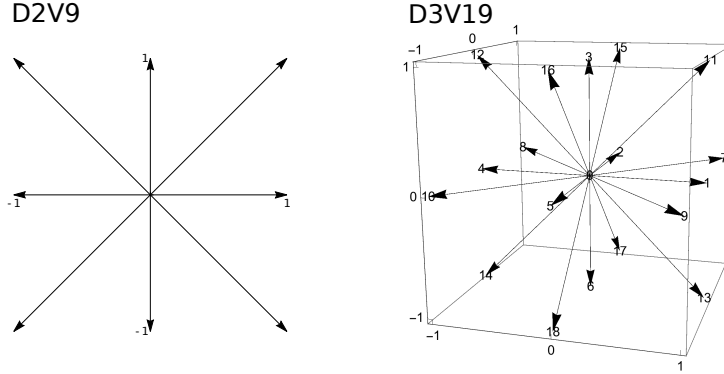
Figure 4.1: Quadratures used in the models.

c_0	0.488598377549843819982207
c_1	1.092502210196163024710861
c_2	2.890326124370599833053459
$\bar{c}_2$	0.559713196101887209686884
c_2'	-0.913955004948841398767998
$\bar{\theta}$	0.200013538215948856423209

The discrete weights can be seem below:

w_0	0.279433800596370971795231
w_s	0.325785607726861097214977
w_l	0.162892803863430548607489
c_s	1.527439075525116330156203

The density can be calculated as $\rho = (\pi\theta)^{3/2} g_{\frac{3}{2}}(e^{\frac{\mu}{\theta}})$, where $\theta = 1/270$ in our problem or, to extract the chemical potential from the density,

$$\mu = \theta \log \left[g_{\frac{3}{2}}^{-1} \left(\frac{\rho}{(\pi\theta)^{3/2}} \right) \right].$$

Note that these relations between ρ and μ are used just to set the initial conditions and to calculate the fields in the output. During the simulations just the density field is used. The Sommerfeld expansion can also be used but the accuracy is not as good as for the 2D case. The approximation with Eq.(4.62) is reliable just up to 10^{-8}, which is bellow the double precision. For this reason, we use numerical methods [122] to calculate the FD integral and its inverse in order to obtain better accuracy.

4.8.2 Riemann problem

The Riemann problem (or shock tube test) is a benchmark validation for computational fluid dynamic models and it consists in analyzing the shock waves formed when a discontinuity in the initial conditions evolves. This problem has analytical solutions for the inviscid case [144]. We simulate the Riemann problem using the two numerical methods (2D and 3D) in a effectively one-dimensional system: $L_X \times L_Y = 3000 \times 2$ for the 2D model and $L_X \times L_Y \times L_Z = 3000 \times 2 \times 2$ for the 3D model. Initially, the density and velocity fields are the same for both models: $\rho = 1.0$ inside the domain $L_X/4 < x < 3L_X/4$ and $\rho = 0.6$ outside and $\boldsymbol{u} = 0$ everywhere. The relaxation time has the constant value $\tau = 0.8$. The boundary conditions are periodic for all directions. In Fig. 4.2 we see the solutions given by our models and the analytical solutions for the classical case [144]. There is a good agreement for the densities field. For a sake of comparison, we correct the velocities given by the classical case by multiplying then by $\sqrt{\bar{\bar{\theta}}}$, since $c_s \propto \sqrt{T}$ and $\bar{\theta}$ plays a role of an "effective temperature" for the semiclassical models. After this correction, the velocities also matches.
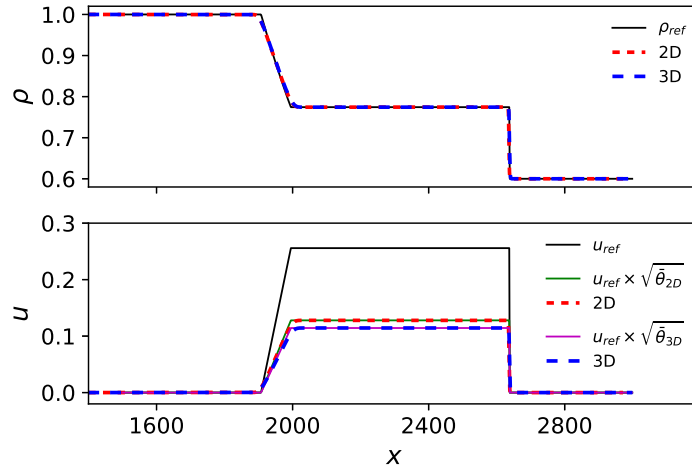
Figure 4.2: Solutions for the density and velocity fields in the Riemann problem obtained with our two models (2D and 3D) and with the analytical solution for the classical case. The classical solution for the velocity is corrected by $\sqrt{\bar{\bar{\theta}}}$ in order to compare with the semiclassical results.

4.8.3 Poiseuille flow

We simulate the viscous fluid of electrons in metals passing through a channel of constant cross section (parallel plates) and analyze the velocity profile for the steady state. Assuming an incompressible fluid submitted to an external force with acceleration $\mathbf{a} = a\mathbf{i}$ in the x direction, the Navier-Stokes equation for semiclassical fluids, Eq.(4.45), has the following solution for the stationary state:

$$u_x(y) = \frac{\rho a}{2\bar{\eta}}(y^2 - yL_y).$$

(4.63)

Thus, we use this equation to calculate the numerical shear viscosity $\bar{\eta}$ of our models, which is needed to convert to physical units. The system size for the 2D model is $L_X \times L_Y = 256 \times 256$ with periodic boundary conditions in the x direction and bounce-back in the y direction and for the 3D model is $L_X \times L_Y \times L_Z = 256 \times 256 \times 1$ with periodic boundaries in the x and z directions and bounce back in the y direction. An external electrical field of magnitude $E = 10^{-8}$ in lattice units is is implemented as in Eq.(4.53) ($a = E$ in natural units). Initially, we set $\mu = 1.0$ and $\boldsymbol{u} = 0$ everywhere for the two models. Note that the initial densities are different because we set equal μ. In Fig. 4.3 we see the velocity profiles for five different relaxation times after 10^6 time steps. A curve fit using Eq.(4.63) is made in the points given by the simulation, which provides the shear viscosity. As we can see in Fig. 4.3, $\bar{\eta}$ the relation below is followed with good agreement by the two models:

$$\bar{\eta} = \frac{1}{3}\left(\tau - \frac{\Delta t}{2}\right).$$

(4.64)

4.8.4 Ohm's law

When an electrical current passes through an ohmic material (e.g, metals) they offer a resistance produced by the collisions between the electrons and a background of impurities
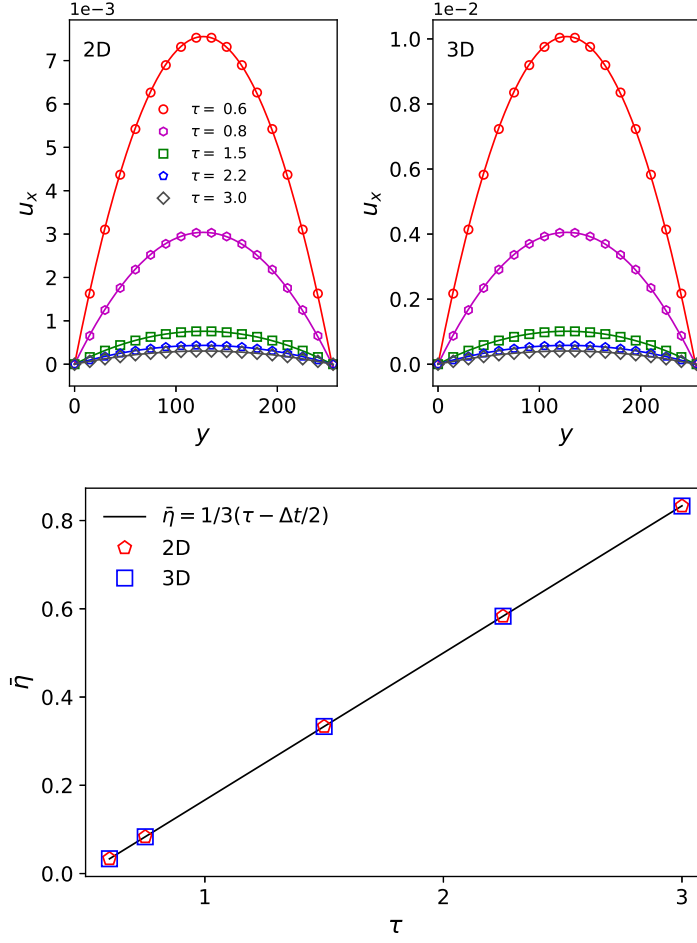
Figure 4.3: Velocity profiles for the Poiseuille flow obtained with the two models for five different relaxation times and the viscosity measurement for the two models.

and defects on the crystal lattice [65]. The relation between the current I and the applied electrical potential difference V is linear: $V = RI$, where R is the resistance. Here we model the electrical resistance with randomly placed obstacles through which the electrons flow. For the 2D sample with system size $L_X \times L_Y = 512 \times 256$, we sort 64 circles of radius 3 forming a porous medium with porosity $\phi_{2D} = 0.986$ while for the 3D sample, with system size $L_X \times L_Y \times L_Z = 128 \times 128 \times 128$, we sort 450 spheres of radius 3 forming a medium with porosity $\phi_{3D} = 0.974$ (see Fig. 4.4). The relaxation time is set $\tau = 0.9$. Initially, $\mu = 1.0$ and $\boldsymbol{u} = 0$ in the whole domain for the two models. We set periodic boundary conditions in the x direction, slip-free conditions in the y direction

(also in the z direction for the 3D model) and bounce-back conditions on the obstacle's surface. To measure the convergence with time, we calculate the relative error as the spatial average of $||\boldsymbol{u}_{new}| - |\boldsymbol{u}_{old}||/|\boldsymbol{u}_{new}|$ considering all fluid point with non-zero $\boldsymbol{u}_{new}$ and we stop the simulations when the error is smaller than 10^{-7}. In Fig. 4.5 we see that the average speed in the x direction (considering all fluid points) have a linear relation with external electrical field E. This relation straightforwardly leads to the Ohm's law ($V = RI \Rightarrow I = \frac{L_X}{R}E$) since the current can be written as $I_{2D} = \rho L_Y \phi \langle u_x \rangle$ for 2D and $I_{3D} = \rho L_Y L_Z \phi \langle u_x \rangle$ for 3D (the densities are essentially constant in the whole domain for the steady state: $\rho_{2D} = 3.142$ and $\rho_{3D} = 4.189$).
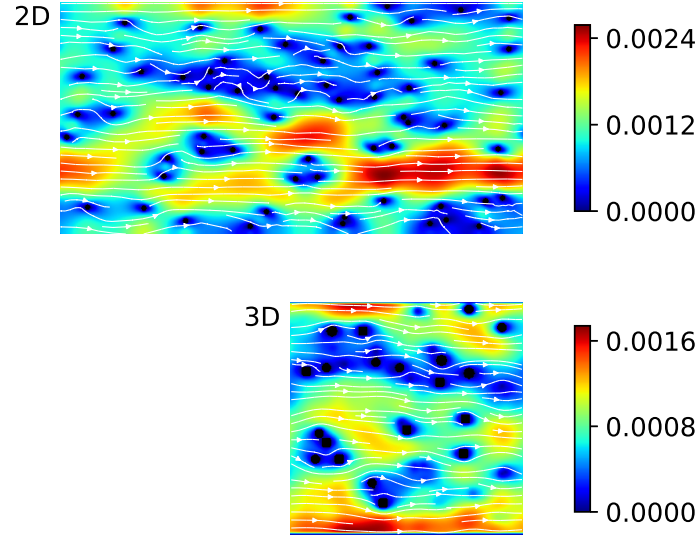
Figure 4.4: Steady state of the velocity field for the electrons passing through randomly placed obstacles to obtain the Ohm's law. The black objects are the obstacles, the colors represent the magnitude of the velocity field and the streamlines show its directions. The entire sample used in the 2D model is shown on the top while a cross section at $z = L_Z/2$ of the 3D sample can bee seem on the bottom. The electrical filed used was $E = 10^{-7}$ in lattice units.

4.9   Conclusion

The two main goals of the present chapter are the construction of the theoretical basis of the semiclassical LBM and the test of an isothermal LBM that simulates electrons in
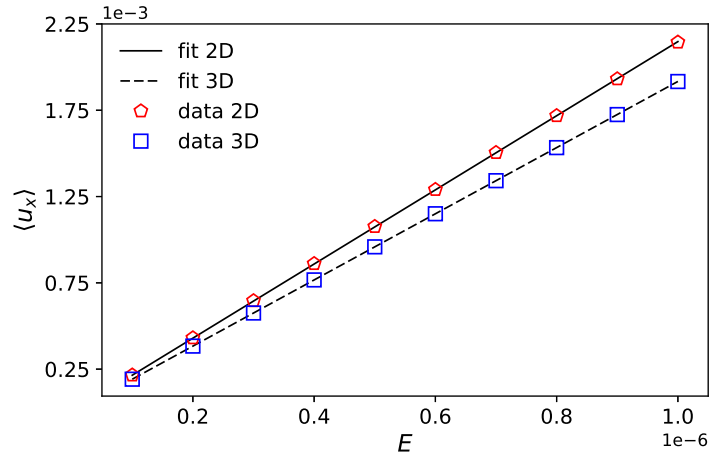
Figure 4.5: Linear relation between the average velocity in the x direction and the external electrical field. This linear relation leads to the Ohm's law.

metals in the hydrodynamic regime.

We have obtained an expansion of the EDF up to fourth order in generalized D-dimensional polynomials, orthonormal under a generic weight. The Hermite polynomials are just a particular case of these generalized polynomials where the weight is given by the gaussian function. The choice of a weight function close to the EDF renders convergence attainable within a few terms in the truncated expansion. We extend here the concept of quadrature to the generic weight function of the polynomials thus beyond the Gauss-Hermite quadrature which is restricted to the Gauss-Hermite weight. In this way we generalize the standard lattices used in the LBM of classical fluids to the semiclassical ones. The macroscopic equations for semiclassical fluids are obtained here through the Chapman-Enskog expansion. The notorious advantageous feature of the LBM is that the mass, momentum and energy conservation equations stem from a Chapman-Enskog expansion where the distribution function is expanded only up to first, third and fourth order [30] in the orthonormal polynomials, respectively. This renders the same results as obtained using the non-expanded distribution function. We show here that the forcing term for the semiclassical distribution satisfies the moment constraints up to second order even for the Lorentz force, which depends on the microscopic velocity in case of the

magnetic force.

An isothermal LBM for electrons in metals for two and three dimensions was developed using a weight near to the FD EDF. It is based on the expansion of the FD distribution up to second order in generalized polynomials and uses the new D2V9 and D3V19 quadratures. We validate our model with the Riemann problem by comparing the density and velocity profiles of the shock waves with the analytical solution for the classical inviscid case. We also perform the Poiseuille flow, obtaining the expected parabolic profiles for the velocity. Lastly, we retrieved the Ohm's law by forcing the electrons to pass through a medium with randomly placed impurities (obstacles) analogously as a classical porous medium. We verified a linear relation between the applied external electrical field and the average velocity of the fluid in the steady state flow which leads to the Ohm's law.

Chapter 5

Relativistic lattice Boltzmann method for semiclassical fluids

In this chapter, we develop and characterize the fully dissipative Lattice Boltzmann method for ultra-relativistic fluids in two dimensions using three equilibrium distribution functions: Maxwell-Jüttner, Fermi-Dirac and Bose-Einstein. Our results stem from the expansion of these distribution functions up to fifth order in relativistic polynomials. We also obtain new Gaussian quadratures for square lattices that preserve the spatial resolution. Our models are validated with the Riemann problem and the limitations of lower order expansions to calculate higher order moments are shown. The kinematic viscosity and the thermal conductivity are numerically obtained using the Taylor-Green vortex and the Fourier flow respectively and these transport coefficients are compared with the theoretical prediction from Grad's theory. In order to compare different expansion orders, we analyze the temperature and heat flux fields on the time evolution of a hot spot.

5.1   Introduction

Relativistic fluid dynamics and kinetic theory [23] for relativistic gases play an important role in the study of many physical systems, ranging from the big scale of cosmology and astrophysics [12,29,131] to the microscopic scale of particle physics [77] and condensed

matter physics [106]. Since the discovery of the flow of the quark-gluon plasma formed during ultra-relativistic nuclear collisions [2], several models based on relativistic fluid dynamics have appeared to describe the experimental results [19,63,140]. Two-dimensional models have been used to describe galaxy formation [69], cosmological models [79] and quark-gluon plasma [114,126], but they have gained special importance after the discovery of graphene [111,112] and Dirac materials [150], in which the charge carriers, governed by the FD distribution, behave effectively as massless ultra-relativistic quasi-particles moving at Fermi speed. Relativistic models based on BE statistics have also applicability to explain fluid dynamics effects, as the collective behavior of the matter formed shortly after nuclear collisions [16], gravitational analogy with BE condensates [43] and even attempts to explain dark matter [18].

The LBM [136] is a numerical technique based on the Boltzmann equation and on the Gaussian quadrature, which have been successfully applied to model classical fluids [33,82], governed by the MB distribution, and also to semi-classical [30,31,157] and relativistic fluids. In 2010, the first RLBM was proposed by Mendoza et. al. [96] and subsequently improved in numerical stability [63]. The theoretical background for the RLBM and the extension to ultra-relativistic gases was done by Romatschke et. al. [125], where the authors used a model with interpolated streaming since the velocity vectors disposed along a sphere do not match with the square lattice. In Ref. [99], an improved dissipation model based on a third order expansion of the MJ distribution was proposed, which does not recover the dissipation completely because a fifth order expansion is required. This model relies on a new Gaussian quadrature with exact streaming on a square lattice, recovering one of the main advantages of LBM, but costing a loss of resolution. Very recently, a new RLBM, also based on a third order expansion of the MJ distribution, can implement exact streaming on a square lattice without loosing spatial resolution allowing also to treat the regime of massive particles [49]. Meanwhile, other RLBMs with exact streaming have been used for graphene, where the grid points are disposed on a hexagonal lattice [47,113]

such as in the molecular structure of graphene. Nevertheless, for these quadratures, the polynomial expansion of the EDF is limited to second order, which might be enough for practical purposes, but gives a poor description if the velocities and/or the temperature fluctuations are moderately high, as shown here. In Ref. [32], the first model based on a fifth order expansion of the FD distribution was used to study the Kelvin-Helmholtz instability on graphene. Since this is a viscous fluid dynamical effect, a fully dissipative method is desirable to achieve better accuracy of the results.

The Grad [54] and Chapman-Enskog [26] (CE) methods are the most common ones to calculate, from the Boltzmann equation, the transport coefficients and the hydrodynamic equations, i.e, the Navier-Stokes equation and the Fourier law. Both methods give the same results in the non-relativistic case [81]. For relativistic fluids, these two methods give the same conservation equations, but different transport coefficients [23], which is still a controversial topic nowadays [13]. Other methods have been proposed to obtain the transport coefficients in relativistic fluids, as the renormalization group method, which gives the same results obtained with the CE method [72, 147, 148]. Numerical methods based on a bottom-up construction are important tools to gain insight about the correct form of the transport coefficients and recent simulations with three dimensional relativistic methods have consistently confirmed the prediction of the CE method [13, 45, 48]. Surprisingly, few have calculated the transport coefficients in two dimensions, despite the increasing importance that the two-dimensional relativistic systems have gained during the last years. In Ref. [100] the Grad method was done in two dimensions, obtaining the correspondent bulk and shear viscosities and the thermal conductivity, which have been used to calculate the relaxation time in RLBM simulations [99, 102, 113]. However, in Ref. [47], the shear viscosity and the thermal conductivity, numerically measured using a RLBM for graphene, disagree with the ones obtained with Grad's expansion. Furthermore, the bulk viscosity was also calculated in Ref. [79] for a two-dimensional relativistic gas, but they did not investigate the other transport coefficients. So far, the CE method

for relativistic gases in two dimensions has never been used to derive the full set of transport coefficients, remaining this an important open task to achieve a better understanding of the two-dimensional relativistic gases.

In this chapter, we build two-dimensional RLBMs with full dissipation using the MJ and BE distributions and compare them with the model for the FD distribution described in Ref. [32]. To do so, we expand the EDFs up to fifth order and develop new Gaussian quadratures able to calculate tensors up to fifth order and that preserve the spatial resolution. To test and characterize our models, we perform four numerical simulations. The models are validated using the Riemann problem though the comparison of the results with a reference model (Ref. [99]). At this point, we calculate tensors from second to fifth order and show that different expansion orders give different results. We numerically measure, with high precision, the kinematic viscosity, with the Taylor-Green vortex, and the thermal conductivity, through Fourier flow and compare the results with the reference model. As will be shown, these measurements do not agree with the coefficients obtained with Grad's expansion, but they agree with previous measurements using RLBM [32, 47]. In addition, we simulate the hot-spot relaxation in order to observe the differences between different expansion orders for the temperature and heat flux fields.

This chapter is organized as follows. In Secs. 5.2.1 and 5.2.2 we review the relativistic Boltzmann equation and the relativistic orthogonal polynomials. In Sec. 5.2.3, we describe the expansion of the three distribution functions (MJ, FD and BE) in orthogonal polynomials, with more details given in the Appendix C, and in Sec. 5.2.4 we calculate the Gaussian quadratures. The full EDF expansion of the distribution functions as well as the quadratures with high precision can be found in the Supplemental Material[1] (see also in the Appendix D the explicit expansion for the FD distribution). In Sec. 5.3 we describe and show the results for the four numerical tests used to validate and characterize

---

[1] Download the Supplemental Material together with the source files at arXiv: `https://arxiv.org/e-print/1709.09073`

the models. In Sec. 5.4 we summarize the main results and conclude.

5.2 Model description

5.2.1 Relativistic Boltzmann Equation

The temporal evolution in our model is given by the relativistic Boltzmann equation [23] with the Anderson-Witting collision operator, which assumes a single relaxation time for the problem, τ, and allows us to treat massless ultra-relativistic particles:

$$\bar{p}^\mu \partial_\mu f = -\frac{\bar{p}_\mu U^\mu}{c^2 \tau}(f - f^{eq}), \tag{5.1}$$

where c is the speed of light. Repeated indexes represent a sum (Einstein's notation). For two-dimensional systems, the greek indexes range from 0 to 2 (0 is the temporal component) while the latin indexes range from 1 to 2. The relativistic (2+1)-momentum stands for $\bar{p}^\mu = (E/c, \bar{\mathbf{p}})$, the (2+1)-velocity for $U^\mu = \gamma(u)(c, \mathbf{u})$ and the space-time coordinates for $x^\mu = (ct, \mathbf{x})$, where $\gamma(u) = 1/\sqrt{1 - u^2/c^2}$ is the Lorentz factor. Note that Eq. (5.1) becomes the non-relativistic Boltzmann equation in the classical limit, $u/c \ll 1$. The EDF, f^{eq}, can be either FD, MJ or BE distributions, as described in section 5.2.3.

In the ultra-relativistic limit, i.e., when the kinetic energy is much larger than the rest mass energy, $\bar{p}^\mu \bar{p}_\mu = (\bar{p}^0)^2 - \bar{\mathbf{p}}^2 = 0 \;\Rightarrow\; \bar{p}^0 = |\bar{\mathbf{p}}|$, and Eq. (5.1) becomes

$$\frac{\partial f}{\partial t} + \mathbf{v} \cdot \nabla f = -\gamma(1 - \mathbf{v} \cdot \mathbf{u})\frac{(f - f^{eq})}{\tau}, \tag{5.2}$$

where $\mathbf{v} = \hat{\mathbf{p}} = \bar{\mathbf{p}}/|\bar{\mathbf{p}}|$ is the microscopic velocity with norm c, and we adopt from now on natural units: $c = k_B = \hbar = 1$. In the numerical algorithm, the discrete form of Eq.(5.2) is used:

$$f_\alpha(t + \delta t, \mathbf{r} + \mathbf{v}_\alpha \delta t) - f_\alpha(t, \mathbf{r}) = -\gamma(1 - \mathbf{v}_\alpha \cdot \mathbf{u})\frac{\delta t(f_\alpha - f_\alpha^{eq})}{\tau}, \tag{5.3}$$

where δt is the time step of the simulations. Because all particles move at (or nearly) the speed of light, the microscopic velocity is always unitary in natural units, $\mathbf{v}_\alpha = \bar{\mathbf{p}}_\alpha/|\bar{\mathbf{p}}_\alpha| =$

1, what must be considered in the Gaussian quadrature calculation, as done in section 5.2.4.

5.2.2 Relativistic Polynomials

In the LBM, the EDF is expanded in orthogonal polynomials up to a finite order N in order to use the Gaussian quadrature [1] for the exact equivalence between the sums and integrals. In this procedure, the information contained in the terms of order above N is lost. Thus, to have a faster convergence in the expansion and, therefore, minimize the loss of accuracy due to the truncation, the weight function used in the orthogonalization of the polynomials should be close to the EDF. With this purpose, we calculate relativistic generalized polynomials following the procedure developed in Ref. [31] for non-relativistic polynomials. The polynomials below allow us to find orthogonal polynomials for generic weight functions, $\omega(p)$.

$$P = A_1, \quad P^{i_1} = B_1 p^{i_1}, \quad P^0 = C_1 p^0 + C_2$$

$$P^{i_1 i_2} = D_1 p^{i_1} p^{i_2} + [D_2 (p^0)^2 + D_3 p^0 + D_4] \delta^{i_1 i_2}, \quad P^{i_1 0} = [E_1 p^0 + E_2] p^{i_1},$$

$$P^{i_1 i_2 i_3} = F_1 p^{i_1} p^{i_2} p^{i_3} + [F_2 (p^0)^2 + F_3 p^0 + F_4] \cdot [p^{i_1} \delta^{i_2 i_3} + p^{i_2} \delta^{i_1 i_3} + p^{i_3} \delta^{i_1 i_2}],$$

$$P^{i_1 i_2 0} = [G_1 p^0 + G_2] p^{i_1} p^{i_2} + \delta^{i_1 i_2} [G_3 (p^0)^3 + G_4 (p^0)^2 + G_5 p^0 + G_6]$$

$$P^{i_1 i_2 i_3 i_4} = H_1 p^{i_1} p^{i_2} p^{i_3} p^{i_4} + [H_2 (p^0)^2 + H_3 p^0 + H_4] \cdot [p^{i_1} p^{i_2} \delta^{i_3 i_4} + p^{i_1} p^{i_3} \delta^{i_2 i_4} + p^{i_1} p^{i_4} \delta^{i_2 i_3}$$

$$+ p^{i_2} p^{i_3} \delta^{i_1 i_4} + p^{i_2} p^{i_4} \delta^{i_1 i_3} + p^{i_3} p^{i_4} \delta^{i_1 i_2}] + [H_5 (p^0)^4 + H_6 (p^0)^3 + H_7 (p^0)^2 + H_8 p^0 + H_9] \delta^{i_1 i_2 i_3 i_4}$$

$$P^{i_1 i_2 i_3 0} = [I_1 p^0 + I_2] p^{i_1} p^{i_2} p^{i_3} + [I_3 (p^0)^3 + I_4 (p^0)^2 + I_5 p^0 + I_6] [p^{i_1} \delta^{i_2 i_3} + p^{i_2} \delta^{i_1 i_3} + p^{i_3} \delta^{i_1 i_2}]$$

$$P^{i_1 i_2 i_3 i_4 i_5} = J_1 p^{i_1} p^{i_2} p^{i_3} p^{i_4} p^{i_5} + [J_2 (p^0)^2 + J_3 p^0 + J_4] \cdot [p^{i_3} p^{i_4} p^{i_5} \delta^{i_1 i_2} + p^{i_2} p^{i_4} p^{i_5} \delta^{i_1 i_3} + p^{i_2} p^{i_3} p^{i_5} \delta^{i_1 i_4}$$

$$+ p^{i_2} p^{i_3} p^{i_4} \delta^{i_1 i_5} + p^{i_1} p^{i_4} p^{i_5} \delta^{i_2 i_3} + p^{i_1} p^{i_3} p^{i_5} \delta^{i_2 i_4} + p^{i_1} p^{i_3} p^{i_4} \delta^{i_2 i_5} + p^{i_1} p^{i_2} p^{i_5} \delta^{i_3 i_4} + p^{i_1} p^{i_2} p^{i_4} \delta^{i_3 i_5}$$

$$+ p^{i_1} p^{i_2} p^{i_3} \delta^{i_4 i_5}] + [J_5 (p^0)^4 + J_6 (p^0)^3 + J_7 (p^0)^2 + J_8 p + J_9] [p^{i_1} \delta^{i_2 i_3 i_4 i_5} + p^{i_2} \delta^{i_1 i_3 i_4 i_5} + p^{i_3} \delta^{i_1 i_2 i_4 i_5}$$

$$+ p^{i_4} \delta^{i_1 i_2 i_3 i_5} + p^{i_5} \delta^{i_1 i_2 i_3 i_4}]$$

$$P^{i_1 i_2 i_3 i_4 0} = [K_1 p^0 + K_2] p^{i_1} p^{i_2} p^{i_3} p^{i_4} + [K_3 (p^0)^3 + K_4 (p^0)^2 + K_5 p^0 + K_6][p^{i_3} p^{i_4} \delta^{i_1 i_2} + p^{i_2} p^{i_4} \delta^{i_1 i_3}$$

$$+ p^{i_2} p^{i_3} \delta^{i_1 i_4} + p^{i_1} p^{i_4} \delta^{i_2 i_3} + p^{i_1} p^{i_3} \delta^{i_2 i_4} + p^{i_1} p^{i_2} \delta^{i_3 i_4}] + [K_7 (p^0)^5 + K_8 (p^0)^4 + K_9 (p^0)^3 + K_{10} (p^0)^2$$

$$+ K_{11} p^0 + K_{12}] \delta^{i_1 i_2 i_3 i_4}.$$

For each order N of the polynomials, there are two groups of components: $P^{i_1 \ldots i_N}$ and $P^{i_1 \ldots i_{N-1} 0}$. This structure assures that all possible monomials are considered for a generic spatial dimension D. The coefficients (A's, B's, C's, ...) are calculated through the orthonormality relations:

$$\int \frac{d^D p}{p^0} \omega(p) P^{i_1 \ldots i_N} P^{j_1 \ldots j_M} = \delta_{NM} \delta^{i_1 \ldots i_N | j_1 \ldots j_N},$$

$$\int \frac{d^D p}{p^0} \omega(p) P^{i_1 \ldots i_N 0} P^{j_1 \ldots j_M 0} = \delta_{NM} \delta^{i_1 \ldots i_N | j_1 \ldots j_N},$$

$$\int \frac{d^D p}{p^0} \omega(p) P^{i_1 \ldots i_N 0} P^{j_1 \ldots j_M} = 0. \tag{5.4}$$

Here, the normalization factor is the same as for the Hermite polynomials in D-dimensions [30, 42], where we define $\delta_{i_1 \ldots i_N | j_1 \ldots j_N} \equiv \delta_{i_1 j_1} \cdots \delta_{i_N j_N} +$ all permutations of j's and δ^{ij} is the Kronecker's delta. The weight functions used to build the models in this chapter will be discussed in the next section (Eqs. (5.7), (5.8) and (5.9)) and the polynomial coefficients can be found in the Supplemental Material.

5.2.3 Expansion

In this section, we describe the fifth order expansion in relativistic polynomials of the MJ, BE and FD using a different set of polynomials for each distribution. Lets write the three EDFs in a general form:

$$f^{eq} = \frac{A}{z^{-1} \exp\left(\frac{\bar{p}_\alpha U^\alpha}{k_B T}\right) + \xi} \tag{5.5}$$

where A is a normalization factor, $z = e^{\frac{\bar{\mu}}{k_B T}}$ is the fugacity, $\bar{\mu}$ is the chemical potential and ξ distinguishes the EDFs: $\xi = 0$ for MJ (also $z = 1$), $\xi = 1$ for FD and $\xi = -1$ for BE. To expand the EDFs, we introduce non-dimensional quantities: $\theta = T/T_0$, $\mathbf{p} = \bar{\mathbf{p}}/T_0$ and

$\mu = \bar{\mu}/T_0$, where T_0 is the reference temperature, e.g, the initial one. Thus, considering the ultra-relativistic regime, Eq. (5.5) becomes

$$f^{eq} = \frac{A}{z^{-1}\exp\left[p^0\gamma(1 - \mathbf{v}\cdot\mathbf{u})/\theta\right] + \xi}. \tag{5.6}$$

As discussed in the previous section, the weight function must be close to the EDF. The expansion is done around $U = 0$ (small Mach numbers) and around $\theta = 1$, leading to the general weight function $\omega(p) = A/[z_r^{-1}\exp(p) + \xi]$. The reference fugacity z_r is a constant parameter with numerical value close to the physical one. Therefore, for the MJ distribution the weight function reads

$$\omega(p) = \frac{1}{2\pi}e^{-p}. \tag{5.7}$$

For the FD distribution, we use $z = 1$, which is appropriate, for instance, to model the Dirac fluid on graphene close to the charge neutrality point ($\mu = 0$) [32,47]. So the weight function becomes

$$\omega(p) = \frac{1}{e^p + 1}. \tag{5.8}$$

The weight function for the BE distribution is chosen to describe a system close to the BE condensation (ideally, $z = 1$). Because some integrals diverge for $z_r = 1$, we set $z_r \equiv z_c = 1 - \epsilon$, where $\epsilon = 10^{-7}$ denotes a small number compared to unity, leading to

$$\omega(p) = \frac{1}{z_c^{-1}e^p - 1}. \tag{5.9}$$

The general expansion up to fifth order is given by

$$f^{eq} = \omega(\xi)\left[\sum_{N=0}^{5}\frac{1}{N!}A^{i_1...i_N}P^{i_1...i_N} + \sum_{M=0}^{4}\frac{1}{M!}A^{i_1...i_M0}P^{i_1...i_M0}\right], \tag{5.10}$$

where $A^{\mu_1\mu_2\cdots\mu_N}$ are the projections of the EDF on the polynomials:

$$A^{\mu_1\mu_2\cdots\mu_N} = \int\frac{d^2\mathbf{p}}{p^0}f^{eq}P^{\mu_1\mu_2\cdots\mu_N}. \tag{5.11}$$

More details about the calculation of the integrals used for the expansion can be found in the Appendix C and the explicit expansion can be found in the Supplemental Material. It was used in Ref. [32] for FD distribution, but can be straightforwardly generalized to MJ and BE if one changes the polynomial coefficients and the FD integral by the generalized EDF integral defined as:

$$g_\nu(z) = \frac{1}{\Gamma(\nu)} \int_0^\infty \frac{x^{\nu-1}dx}{z^{-1}e^x + \xi}, \tag{5.12}$$

with ξ defined as in Eq.(5.5). Note that for MJ, $\xi = 0$ and $g_\nu(1) = 1$ for any ν. In Fig. 5.1, we see the comparison between the original (non-expanded) EDFs and the expanded ones around the origin of the expansion ($\theta = 1$ and $u = 0$). The distributions are multiplied by a normalization factor $A = \left(\int d^2\mathbf{p}/p^0 \, f^{eq}\right)^{-1}$. The second order expansion is the first to deviate from the original EDF when it moves away from $\theta = 1$ and $u = 0$, followed by the third, fourth and fifth order expansions respectively. We can clearly see that the fifth order expansion gives more accurate results for higher temperature deviations and higher velocities when compared to the previous orders. For instance, considering the MJ distribution at $\beta = 0.6$, the second order expansion gives a relative error when compared with the original EDF of 18.5% while the fifth order gives only 1.8%. At the extremes of Fig. 5.1 ($\theta = 0$ and 2 and $\beta = 0.8$) we see large deviations for all expansion orders, but one should not expect high accuracy for parameters very far from the expansion origin. Therefore, the models based on the fifth order expansion are more reliable and can be used as a reference to test other simpler models and also to simulate flows with high Mach numbers and temperature deviations. In Sec. 5.3.4, we will analyze the different results in numerical simulations based on expansions from second to fifth order.

5.2.4 Gaussian Quadrature

The Gaussian quadrature [1] offers an efficient way to calculate integrals in LBM, used to obtain the macroscopic quantities (e.g, density, macroscopic velocity and temperature),
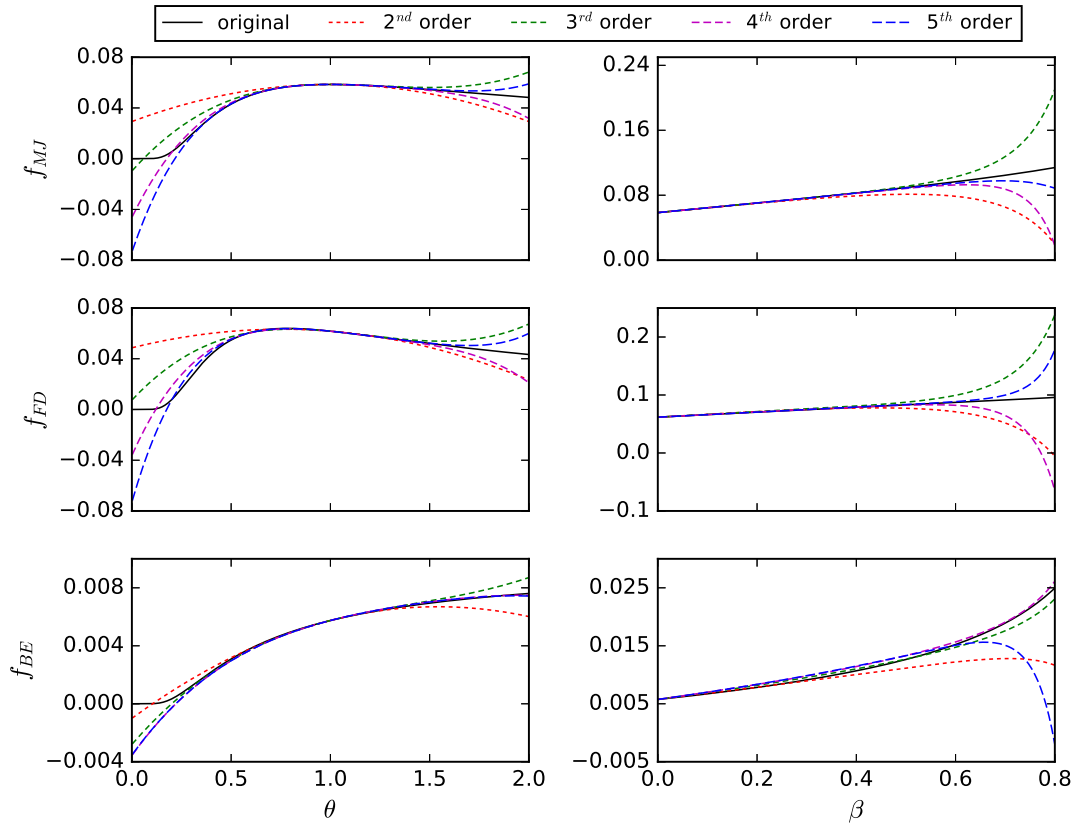
Figure 5.1: Comparison between the original and expanded MJ, FD and BE distributions around the expansion origin: $\theta = 1$ and $u = 0$. The momentum vector is the same for all distributions: $\mathbf{p} = (1.0, 0.0)$. For FD, $z = 1$ and for BE, $z = 1 - 10^{-7}$. On the left side, the distributions are shown as functions of the relative temperature, $\theta = T/T_0$ (where T and T_0 are the physical and the reference temperature respectively) with $\mathbf{u} = 0$. On the right side, the EDFs are shown for different velocities, $\mathbf{u}/c = (\beta, 0.0)$, with $\theta = 1$.

by transforming them into sums. In general, the method provides an approximation for the integrals, but it can be exact if the integrated function is expanded in orthogonal polynomials up to a maximum order determined by the quadrature. Here, we calculate quadratures that allow us to calculate tensors up to fifth order $(M = 5)$,

$$T^{\mu_1 \cdots \mu_M} = \int \frac{d^2 p}{p^0} f^{eq} p^{\mu_1} \ldots p^{\mu_M} = \sum_{i=1}^{Q} f_i^{eq} p_i^{\mu_1} \ldots p_i^{\mu_M}.$$
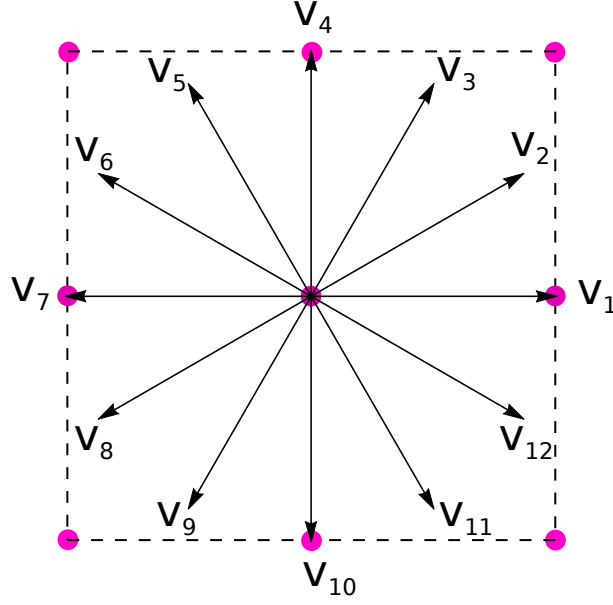
Figure 5.2: Velocity vectors for the d2v72 quadrature.

Since we have a fifth order expansion for our EDFs, we need to find the discrete weights and momentum vectors that satisfy the quadrature equations,

$$\int \frac{d^2p}{p^0}\omega(p)p^{\mu_1}\ldots p^{\mu_N} = \sum_{i=1}^{Q} w_i p_i^{\mu_1}\ldots p_i^{\mu_N}, \tag{5.13}$$

for $N = 0, 1, \ldots, 10$ and for all combinations of indexes ($\mu = 0, 1, 2$). The weight function, $\omega(p)$, used to calculate the quadrature and the polynomials must be the same for each model (Eqs. (5.7), (5.8), (5.9)). As a consequence of the quadrature theorem, we can find the momentum vectors for our quadrature (with $N = 10$) by calculating the roots of the sixth order polynomial, which can be separated in angular and radial parts. For the angular part, there are two orthogonal polynomials,

$$L_6^{(1)}(\phi) = \cos(6\phi), \ L_6^{(2)}(\phi) = \sin(2\phi)[2\cos(4\phi) + 1],$$

which give the same set of solutions, but rotated by $\pi/12$. The roots of $L_6^{(2)}(\phi) = 0$, are $\phi_n = n\pi/6$ for $n = 0, \ldots, 11$, which are the directions of the momentum vectors (see Fig. 5.2). The sixth order polynomial for the radial part,

$$R_6(p) = p^6 + ap^5 + bp^4 + cp^3 + dp^2 + ep + f,$$

is calculated by Gram-Schmidt procedure, where the coefficients, $a, \ldots, f$, are different for each weight function. The solutions of $R_6(p) = 0$ give six momentum vectors, which are the same for each of the 12 directions obtained with the angular polynomial. To calculate the discrete weights, we apply Eq.(5.13). The solutions for MJ, using Eq.(5.7), are

$$p_1 = 0.222847 \qquad w_1 = 3.824706 \times 10^{-2}$$

$$p_2 = 1.188932 \qquad w_2 = 3.475007 \times 10^{-2}$$

$$p_3 = 2.992736 \qquad w_3 = 9.447782 \times 10^{-3}$$

$$p_4 = 5.775144 \qquad w_4 = 8.665998 \times 10^{-4}$$

$$p_5 = 9.837467 \qquad w_5 = 2.175143 \times 10^{-5}$$

$$p_6 = 15.982874 \qquad w_6 = 7.487899 \times 10^{-8},$$

for BE, using Eq.(5.9),

$$p_1 = 0.015771 \qquad w_1 = 7.785968$$

$$p_2 = 0.811549 \qquad w_2 = 5.510286 \times 10^{-1}$$

$$p_3 = 2.617676 \qquad w_3 = 9.444240 \times 10^{-2}$$

$$p_4 = 5.428098 \qquad w_4 = 7.784734 \times 10^{-3}$$

$$p_5 = 9.503366 \qquad w_5 = 1.911972 \times 10^{-4}$$

$$p_6 = 15.65413 \qquad w_6 = 6.539175 \times 10^{-7},$$

and for FD using Eq.(5.8),

$$p_1 = 0.252017 \qquad w_1 = 1.465430 \times 10^{-1}$$

$$p_2 = 1.284314 \qquad w_2 = 1.606581 \times 10^{-1}$$

$$p_3 = 3.102998 \qquad w_3 = 5.069991 \times 10^{-2}$$

$$p_4 = 5.873790 \qquad w_4 = 4.904943 \times 10^{-3}$$

$$p_5 = 9.929605 \qquad w_5 = 1.245349 \times 10^{-4}$$

$$p_6 = 16.072385 \qquad w_6 = 4.300942 \times 10^{-7}.$$

The three quadratures can be found with higher precision in the Supplemental Material.

To calculate the macroscopic fields, we use the Landau-Lifshitz decomposition [23]. We first calculate the energy-momentum tensor

$$T^{\mu\nu} = \sum_{i=1}^{Q} f_i p_i^{\mu} p_i^{\nu}, \tag{5.14}$$

and, then, solve the following eigenvalue problem using the power method [61]:

$$T_{E\ \beta}^{\alpha} U^{\beta} = T^{\alpha}_{\ \beta} U^{\beta} = \varepsilon U^{\alpha} \tag{5.15}$$

to find the energy density ε and the macroscopic velocity U^{μ}, where the letter E indicates that the tensor was calculated with the EDF. The hydrostatic pressure P can be obtained using the equation of state, $\varepsilon = 2P$. The density of particles, n, is calculated as the contraction of the macroscopic velocity with the particles flux N^{μ},

$$n = U_{\mu} N_E^{\mu} = U_{\mu} N^{\mu} = U_{\mu} \sum_{i=1}^{Q} f_i p_i^{\mu}. \tag{5.16}$$

Lastly, the temperature is calculated with

$$\theta = \frac{1}{2} \frac{g_2(z)}{g_3(z)} \left(\frac{\varepsilon}{n} \right), \tag{5.17}$$

where the EDF integral, $g_{\nu}(z)$, is defined in Eq.(5.12).

The density of particles and the internal energy can be calculated with the EDF, since, by Eqs.(5.15) and (5.16), they give the same result as for the non-equilibrium distribution:

$$n = 2\pi\theta^2 g_2(z), \ \text{ and } \ \varepsilon = 2P = 4\pi\theta^3 g_3(z). \tag{5.18}$$

The Eq.(5.17) was calculated using Eq.(5.18). The validity of Eqs.(5.15) and (5.16) is a consequence of the conservation of particles flow and the conservation of the energy-momentum tensor,

$$\partial_{\mu} N^{\mu} = 0, \quad \partial_{\mu} T^{\mu\nu} = 0. \tag{5.19}$$

To calculate the transport coefficients using the Grad's expansion, one also needs an equation for the third order non-equilibrium tensor [99], which requires the fifth order equilibrium tensor,

$$T_E^{\alpha\beta\gamma\delta\epsilon} = \int f^{eq} p^\alpha p^\beta p^\gamma p^\delta p^\epsilon \frac{d^2p}{p^0}, \tag{5.20}$$

so, the fifth order expansion is clearly need to recover the full dissipation. Another way to see the required expansion order of the EDF, is to observe that the pressure deviator, Eq.(5.24), has terms with five velocities, which can be recovered just with a fifth order expansion. In the Landau-Lifshitz decomposition, the particle flow reads [23]

$$N^\mu = nU^\mu - \frac{q^\mu}{h_E}, \tag{5.21}$$

where q^μ is the heat flux,

$$q^\mu = \kappa \left(\nabla^\mu T - \frac{T}{c^2} DU^\mu \right), \tag{5.22}$$

κ is the thermal conductivity, $D = U^\alpha \partial_\alpha$ and $h_E = (\varepsilon + P)/n = 3\,T\,g_3(z)/g_2(z)$ is the enthalpy per particle, and the energy-momentum tensor is written as

$$T^{\mu\nu} = p^{\langle\mu\nu\rangle} - (P + \varpi)\Delta^{\mu\nu} + \frac{\varepsilon}{c} U^\mu U^\nu, \tag{5.23}$$

where

$$p^{\langle\mu\nu\rangle} = 2\eta \left[\frac{1}{2}(\Delta_\gamma^\mu \Delta_\delta^\nu + \Delta_\delta^\mu \Delta_\gamma^\nu) - \frac{1}{3}\Delta^{\mu\nu}\Delta_{\gamma\delta} \right] \nabla^\gamma U^\delta \tag{5.24}$$

is the pressure deviator, $\varpi = -\mu_b \nabla_\alpha U^\alpha$ is the dynamic pressure, η is the shear viscosity and μ_b is the bulk viscosity. Here, $\Delta^{\mu\nu} = \eta^{\mu\nu} - U^\mu U^\nu/c^2$ stands for the projector into the space perpendicular to U^μ and $\nabla^\mu = \Delta^{\mu\nu}\partial_\nu$ for the gradient operator.

In the next section, we adopt a reference model (denoted as "ref." in the figures) to validate our new models and compare our results with the two-dimensional version of the LBM described in Ref. [99]. This model is based on a third order expansion, and

therefore less accurate than the models presented here, but it has the advantage to have a quadrature with exact streaming, which allows us to analyze the effects of our interpolated streaming. Because all ultra-relativistic particles move essentially with the same speed, to find a quadrature with exact streaming on a square lattice, one has to find velocity vectors belonging, simultaneously, to the lattice nodes and to a circle of radius R:

$$n_x^2 + n_y^2 = R^2,$$

where n_x and n_y are integers. The simplest lattice that satisfies the above equation and the quadrature equations, Eq. (5.13), up to $N = 6$ (third order model) has radius $R = 5$ and 36 momentum vectors, where the velocity vectors are:

$$v_x = \{-5, -4, -4, -3, -3, 0, 0, 3, 3, 4, 4, 5\}$$
$$v_y = \{0, -3, 3, -4, 4, -5, 5, -4, 4, -3, 3, 0\}$$

The main disadvantage of this quadrature is a loss of resolution. As a consequence, to simulate the same system size one needs $5 \times 5 = 25$ times more lattice points. In addition, this quadrature can not be used to simulate models based on expansions of orders higher than three, like our fifth order model. This would require a much bigger radius R, making the resolution so small that the model would have little practical utility. So, the interpolated streaming arises as an alternative to keep the resolution and to have higher order expansions.

5.3   Numerical validation and characterization

5.3.1   Riemann Problem

The Riemann problem consists of a discontinuity in the initial conditions of the macroscopic quantities (e.g., density or velocity) which generates shock waves when the system evolves. This is a benchmark validation for fluid dynamics models which has analytic

solution for the inviscid hydrodynamic equations [144] but needs to be solved numerically for viscous fluids [19]. In order to validate our models, we compare solutions for the pressure, velocity and density fields with a reference model described in Ref. [99]. Initially, we set the density $n_0 = 1.0$ in the domain $L_X/4 < x < 3L_X/4$ and 0.1 elsewhere, with temperature $\theta_0 = 1.0$ and velocity $\mathbf{u_0} = 0.0$ on the whole domain. The effectively one-dimensional system has dimensions $L_X \times L_Y = 1000 \times 2$ with periodic boundary conditions in both directions. Just half of the system is shown because the other half is an exact mirror image. The reference model, as well as the previous relativistic LBMs, uses the viscosity given by Grad's expansion, but, as we will see in Sec. 5.3.2, the measured viscosity differs from this theoretical prediction. Because of this discrepancy, instead of using constant η/s as usual, we perform our simulation using a constant relaxation time of $\tau = 10.0$. In Fig. 5.3, we see that the three models agree very well with the reference model for those fields. Notice that the pressure differs for the three EDFs due to the EDF integrals (see Eq.(5.18)), but, since it is divided by the initial pressure at $x = 500$, the curves coincide in Fig. 5.3.
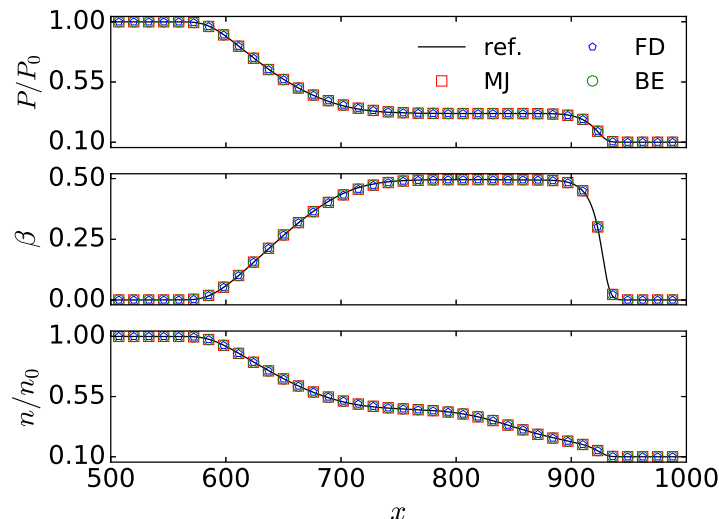
Figure 5.3: Solution of the Riemann problem after $t = 200$ time steps for the pressure, velocity and density fields using our three models and the reference model. The pressure and the density fields are divided by their initial value at the center ($x = 500$).

In order to show the differences between different expansion orders of the EDF, we calculate the diagonal components of the tensorial fields, from second to fifth order, in the Riemann problem:

$$\pi^{xx} = \sum_i (f - f^{eq})p^x p^x, \tag{5.25}$$

$$\pi^{xxx} = \sum_i (f - f^{eq})p^x p^x p^x,$$

$$\pi^{xxxx} = \sum_i (f - f^{eq})p^x p^x p^x p^x,$$

$$\pi^{xxxxx} = \sum_i (f - f^{eq})p^x p^x p^x p^x p^x.$$

The results can be seen in Fig. 5.4 for the three EDFs expanded up to fifth order on the left and for the MJ distribution expanded from second to fifth order on the right. The numerical values of the tensors are divided by the initial density and temperature at the center ($x = 500$) in order to make them non-dimensional. The differences between the three EDFs clearly appear for these tensors. Considering the MJ distribution with different expansion order (on the right), we see that all models give similar results for the second order tensor, but the differences increase with the order of the tensors, becoming large for the fifth order tensor. As in Fig. 5.1, the results seem to converge when the expansion order increases. This shows the importance of using higher order expansions when higher order tensors are considered.

5.3.2   Viscosity measurement

We measure the kinematic viscosity in our models through the Taylor-Green vortex experiment. This is a initial value problem consisting of initial vortexes rotating in determined directions, which kinetic energy dissipates with time due to the viscosity. The conservation equations, Eq.(5.19), can be solved exactly for this problem if one considers low velocities compared to the speed of light, giving exponential decay with time for the
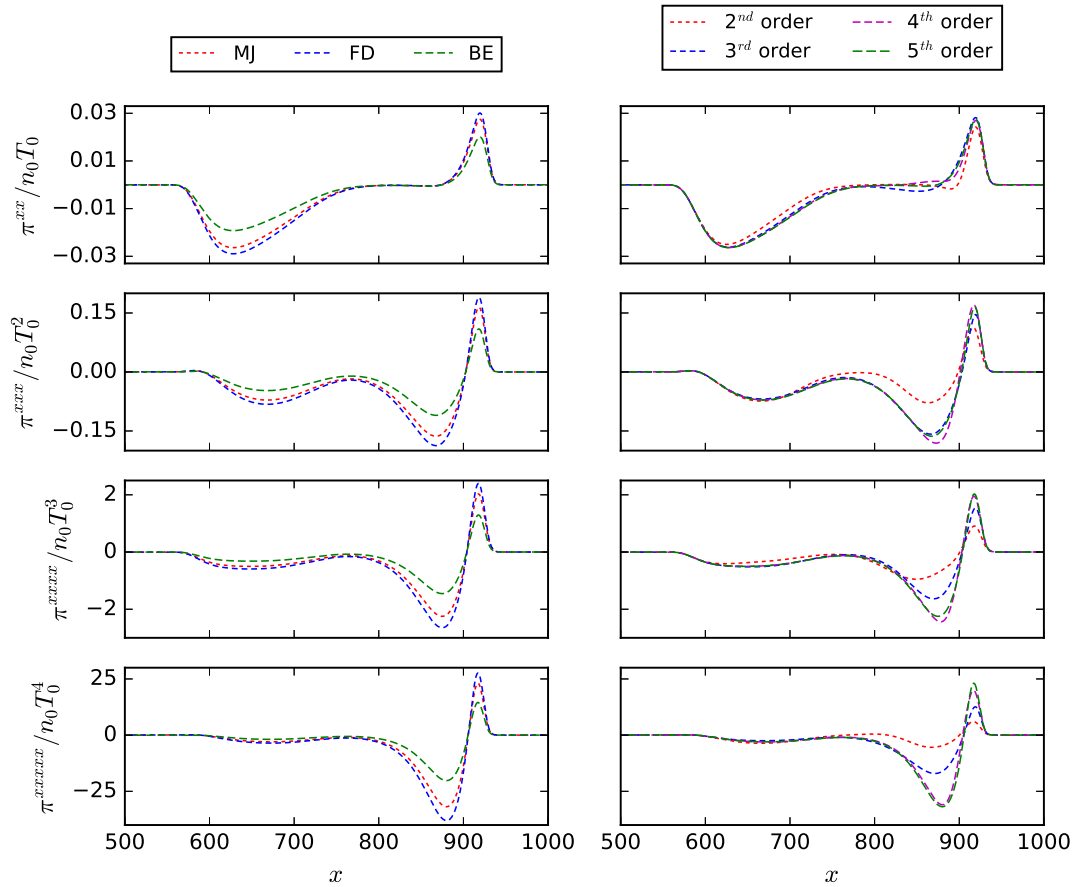
Figure 5.4: The diagonal components of the second to fifth order tensors (see Eq.(5.25)) calculated using the three EDFs expanded up to fifth order (left side) and with the MJ distribution expanded from second to fifth order in orthogonal polynomials (right side). The tensors are divided by the initial density at the center ($x = 500$), n_0, and by the initial temperature T_0 to remove the units.

velocity field depending on the kinematic viscosity ν [48, 95]:

$$\mathbf{u}(x, y, t) = \mathbf{u}_0(x, y) e^{-2\nu t(2\pi/L)^2}, \tag{5.26}$$

where $\mathbf{u}_0$ is the initial velocity and L the length of the squared domain. We simulate a system with dimensions $L \equiv L_X = L_Y = 512$ and with periodic boundary conditions for five different relaxation times, ranging from 0.8 to 5.0 for 45000 time steps. The initial

conditions are $n_0 = 1.0$ and $\theta_0 = 1.0$ in the whole domain and the initial velocities are:

$$u_{0x}(x, y) = -u_0 \cos\left(\frac{2\pi x}{L}\right) \sin\left(\frac{2\pi y}{L}\right) \tag{5.27}$$

$$u_{0y}(x, y) = u_0 \sin\left(\frac{2\pi x}{L}\right) \cos\left(\frac{2\pi y}{L}\right), \tag{5.28}$$

where $u_0 = 0.1$. The initial non-equilibrium distribution is set as described in Ref. [95] in order to reduce the oscillations in the fields. So the average squared velocity writes

$$\langle u^2 \rangle = \int_0^L \int_0^L \frac{dxdy}{L^2}(u_x^2 + u_y^2) = \frac{u_0^2}{2}e^{-16\pi^2\nu t/L^2}, \tag{5.29}$$

and the standard deviation for u^2 is given by

$$\sigma_{u^2} = \sqrt{\int_0^L \int_0^L \frac{dxdy}{L^2}(u^2 - \langle u^2 \rangle)^2} = \frac{u_0^2}{4}e^{-16\pi^2\nu t/L^2} \tag{5.30}$$

In Fig. 5.5A we see σ_{u^2} as a function of time in semi-log scale for the three models. From the slope of $\sigma_{u^2}(t)$, we can measure the kinematic viscosity ν. Note that ν does not depend on the distribution, but the shear viscosity, $\eta = (\varepsilon + P)\nu$, does. Fig. 5.5C shows the measured kinematic viscosity as a function of the relaxation time. The relation

$$\nu(\tau) = \frac{1}{4}\left(\tau - \frac{\delta t}{2}\right), \tag{5.31}$$

shows good agreement for ultra-relativistic models based on exact streaming [47], but the interpolated streaming introduces a numerical diffusivity which increases the effective viscosity of the fluid [84, 152, 159], i.e.,

$$\nu_{eff} = \frac{1}{4}\left[\tau - \delta t\left(\frac{1}{2} + \delta_\nu\right)\right]. \tag{5.32}$$

With a linear fit, we measure the increment δ_ν in the viscosity for the three EDFs:

$$\delta_\nu^{MJ} = -0.2454 \pm 0.0001$$

$$\delta_\nu^{FD} = -0.2454 \pm 0.0002$$

$$\delta_\nu^{BE} = -0.2449 \pm 0.0005.$$

These results can be summarized as $\nu_{eff} = \frac{1}{4}\left(\tau - 0.2546\,\delta t\right)$; see in Fig. 5.5C this function compared to the data from the simulations. In order to have a more realistic thermodynamic behavior, the shear viscosity-entropy ratio (η/s) is set constant and the relaxation time is calculated with $\tau = 4\eta/(s\theta) + 0.2546\,\delta t$, which will be used in Sec. 5.3.4.

In order to compare our results with the viscosity from a model with exact streaming, we perform the same numerical experiment with the reference model, but with different system dimensions, $L_X \times L_Y = 320 \times 320$, due to the differences in the resolution described in Sec. 5.2.4. Notice that this system size would be equivalent to $L_X \times L_Y = 64 \times 64$ for the models described in this chapter. A linear fit $\nu(\tau) = a(\tau + b)$ gives:

$$a = 0.2502 \pm 0.0003$$

$$b = 0.4996 \pm 0.0005$$

confirming Eq.(5.31), see Fig. 5.5C. Note that, although this result was obtained directly from the Boltzmann equation, it is not compatible with the prediction from Grad's expansion [100], $\nu_{Grad} = k_B\tau/5$, what underlines the need for a better understanding about the transport coefficients of relativistic fluids in two dimensions.

5.3.3 Thermal Conductivity Measurement

From the correspondence between the Eckart and Landau-Lifshitz decompositions [23], one can calculate the heat flux directly by the macroscopic fields (see Eq.(5.21)):

$$q^\alpha = \frac{3T g_3(z)}{g_2(z)}(nU^\alpha - N^\alpha). \tag{5.33}$$

Thus, combining Eq.(5.22) with Eq.(5.33), we can calculate the thermal conductivity of the fluid. Considering a one dimensional gradient in temperature in x-direction, Eq.(5.22) becomes

$$q^x = \kappa F(\Delta T) \tag{5.34}$$

where

$$F(\Delta T) \equiv - \left\{ \left(1 + \frac{(u^x)^2 \gamma^2}{c^2}\right) \frac{\partial T}{\partial x} + \frac{T\gamma}{c^2} \left[c\frac{\partial}{\partial t}(\gamma u^x) + u^x \frac{\partial}{\partial x}(\gamma u^x) \right] \right\}. \qquad (5.35)$$

In the non-relativistic limit, Eq.(5.34) becomes Fourier's law, while $F(\Delta T) \to -\partial T/\partial x$.

In order to measure the thermal conductivity we simulate an effectively one dimensional system with dimensions $L_x \times L_y = 2048 \times 2$ for 5 different gradients in temperature in the x direction. We calculate the spatial average of F, $\langle F(\Delta T) \rangle$, with Eq.(5.35) and the average heat flux, $\langle q^x \rangle$ with Eq.(5.33), where both are essentially constant in space. For each simulation, the temperatures on the left and right boundaries are constant and set as $\theta_L = 1 - \Delta T/2$ on the left and $\theta_R = 1 + \Delta T/2$ on the right, while the differences in temperature are $\Delta T = \{5.0, 7.5, 10.0, 12.5, 15.0\} \times 10^{-4}$. A zeroth order extrapolation using the first fluid neighbors is performed to find the density and velocity on left and right borders and periodic boundary condition are used on top and bottom. The initial conditions are $n_0 = 1.0$ and $\mathbf{u_0} = 0$ everywhere and we set an initial temperature gradient as $\theta_0(x) = \theta_L + x(\theta_R - \theta_L)/L_x$ to have a faster convergence to the solution. Fig. 5.5B shows the average heat flux as a function of $\langle F(\Delta T) \rangle$ for 5 relaxation times and for the three EDFs, and their respective linear fits (overlap for the three distributions) after 2000 time steps. The slope of each line gives the thermal conductivity, which can be seen in Fig. 5.5D as a function of the relaxation time. The linear fits, $[\kappa g_2(z)/g_3(z)](\tau) = a\tau$, for the three EDFs give:

$$a_{MJ} = 1.4999998 \pm 0.0000002$$

$$a_{FD} = 1.4999998 \pm 0.0000002$$

$$a_{BE} = 1.4999997 \pm 0.0000004,$$

suggesting that the thermal conductivity-relaxation time relation is

$$\kappa(\tau) = \frac{3\,\tau\,g_3(z)}{2\,g_2(z)}. \qquad (5.36)$$

This relation also agrees with the thermal conductivity obtained using the reference model (with system dimensions $L_X \times L_Y = 2560 \times 5$), as shown in Fig. 5.5D, for which we find

$$a_{ref} = 1.4999994 \pm 0.0000008,$$

with the linear fit. Interestingly, this results shows that the interpolated streaming changes the viscosity but not the thermal conductivity. A similar relation was found in Ref. [47], where the authors obtained $\kappa(\tau) = 1.525\tau$, with a relative error of 7.2% compared to our result, possibly due to the small resolution of the numerical experiment ($L_x \times L_Y = 32 \times 32$). Similarly for the viscosity in Sec. 5.3.2, the thermal conductivity obtained with relativistic LBM differs from the one predicted by Grad's expansion [100], which is $\kappa_{Grad} = 3c^2 k_B n\tau/8$. It shows the importance to perform a careful Chapman-Enskog expansion in two dimensions, since other works in three dimensions have shown very good agreement between LBM and Chapmann-Enskog [48].

5.3.4 Hot spot relaxation

In the hot spot relaxation experiment [20,44,127] a homogeneous fluid is heated within a limited region (e.g., with a laser), and then let to relax to equilibrium. Here, we perform this numerical experiment using our model based on the MJ distribution expanded from second to fifth order in the relativistic polynomials. The relaxation time is calculated following the measurements done in Sec. 5.3.2: $\tau = 4\eta/(s\theta) + 0.2546\delta t$, where $\eta/s = 0.5$ and θ is the local temperature. In a system with dimensions $L_X \times L_Y = 512 \times 512$, we have initially $n_0 = 1.0$ and $\mathbf{u_0} = 0.0$ everywhere and the temperature is $\theta = 1.5$ inside the region $(x - L_X/2)^2 + (y - L_Y/2)^2 \leq 32^2$, and $\theta = 0.5$ elsewhere. Open boundary conditions are used in both directions. In Fig. 5.6, we see the time evolution of the temperature and density along the line $y = L_Y/2$ (due to the circular symmetry, this region contains all important information). Fig. 5.7 shows temperature and the x-component of the heat flux (Eq.(5.33)) profiles at time $t = 100$ and at $y = L_Y/2$. In the insets, we can see the

deviations between different expansion orders. In order to quantify the differences, we calculate the average deviation of θ and q^x with respect to the results obtained with the fifth order model:

$$\epsilon_\theta^{(N)} = \frac{\sum_{x=x_1}^{x_2} |\theta^{(N)} - \theta^{(5)}|}{\sum_{x=x_1}^{x_2} \theta^{(5)}}, \quad \epsilon_q^{(N)} = \frac{\sum_{x=x_1}^{x_2} |(q^x)^{(N)} - (q^x)^{(5)}|}{\sum_{x=x_1}^{x_2} (q^x)^{(5)}},$$

where N denotes the order of the model used to calculate the field and x_1 and x_2 delimit the interval considered to calculate the average. Adopting $x_1 = 256$ and $x_2 = 388$, where x_2 here was chosen as the limit from where the fields remain constant ($q^x = 0$ and $\theta = 0.5$), we have the following average deviations:

$$\epsilon_\theta^{(2)} = 0.224\% \quad \epsilon_q^{(2)} = 5.195\%$$

$$\epsilon_\theta^{(3)} = 0.114\% \quad \epsilon_q^{(3)} = 1.781\%$$

$$\epsilon_\theta^{(4)} = 0.059\% \quad \epsilon_q^{(4)} = 0.744\%$$

These deviations are due to the different values that the truncated expansions give for the same set of parameters (temperature, velocity, chemical potential), as can be seem in Fig. 5.1 for the EDF. This result reinforces that higher expansion order provides a more accurate description, specially in problems with high velocity and/or high temperature deviations.

5.4   Conclusion

We presented new RLBMs for semiclassical fluids in two dimensions governed by the BE, FD and MJ distributions expanded up to fifth order. New polynomials and quadratures were developed using appropriate weight functions, which are the distributions themselves with zero macroscopic velocity. We analyzed the differences between different expansion orders concluding that, as expected, higher order expansions give more accurate results for higher velocities and temperature deviations. Since the fifth order expansion is,

so far, the highest used in relativistic LBMs, the models presented here are recommended for simulations where accuracy is important.

The transport coefficients were numerically measured for our models. The previous models used the viscosity given by Grad's theory, but, as verified with the measurements, this theoretical value is not reproduced by the relativistic fluids. We also measured the kinematic viscosity and thermal conductivity using a reference model, which uses exact streaming and, therefore, gives results without numerical difusivity. The measurement suggests that

$$\eta = \frac{(\varepsilon + P)}{4} \left(\tau - \frac{\delta t}{2} \right), \quad \text{and} \quad \kappa = \frac{3\,\tau\,g_3(z)}{2\,g_2(z)}.$$

These coefficients should be confirmed in future analytical calculations using Chapman-Enskog expansion. As demonstrated recently [48], relativistic hydrodynamics is better described by Chapman-Enskog rather than by Grad method, which, to the best of our knowledge, has not been done yet for two-dimensional ultra-relativistic fluids.

The present study opens the way to develop a fully dissipative model with multi-relaxation time collision operator, similarly as done in Ref. [87], in order to independently adjust the transport coefficients and enhance the numerical stability. The presented models can also be extended to three dimensions following similar procedures. The relativistic polynomials can straightforwardly be calculated for three dimensions, since they are written in a tensorial form, and the quadratures can be calculated by finding the roots of the radial and angular polynomials as done here. The EDF expansion becomes significantly more complicated, but one can use the ansatz described in Ref. [125].
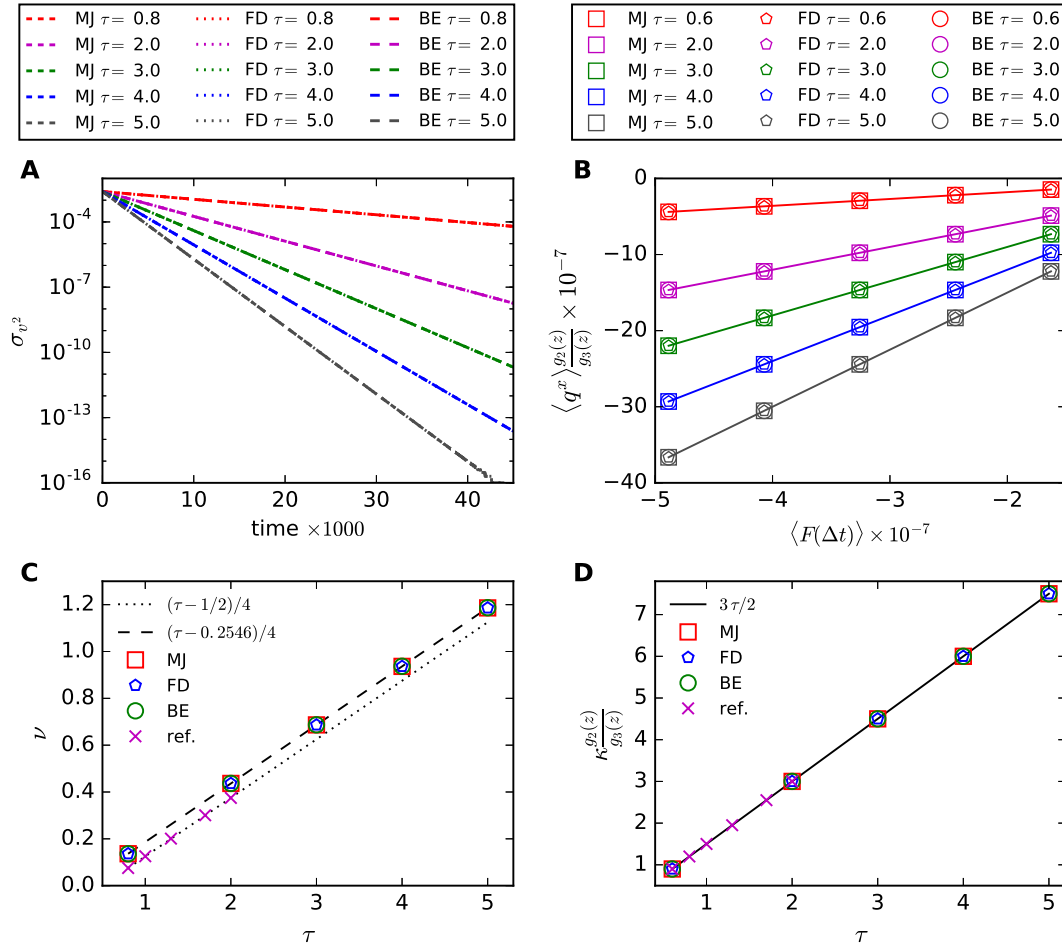
Figure 5.5: Measurement of transport coefficients. A) Decay with time of σ_{u^2} for the three distributions and five different relaxation times τ in the Taylor-Green vortex. The curves for the same τ fall on top of each other. B) Average heat flux as a function of $\langle F(\Delta T) \rangle$ (Eq.(5.35)) for the three distributions and five relaxation times. The solid lines represent linear fits, which fall on top of each other for the three distributions. C) Kinematic viscosity – relaxation time relation for the three distributions obtained with the Taylor-Green vortex and comparison with the results from the reference model. D) Thermal conductivity– relaxation time relation for the three distributions and comparison with the reference model.
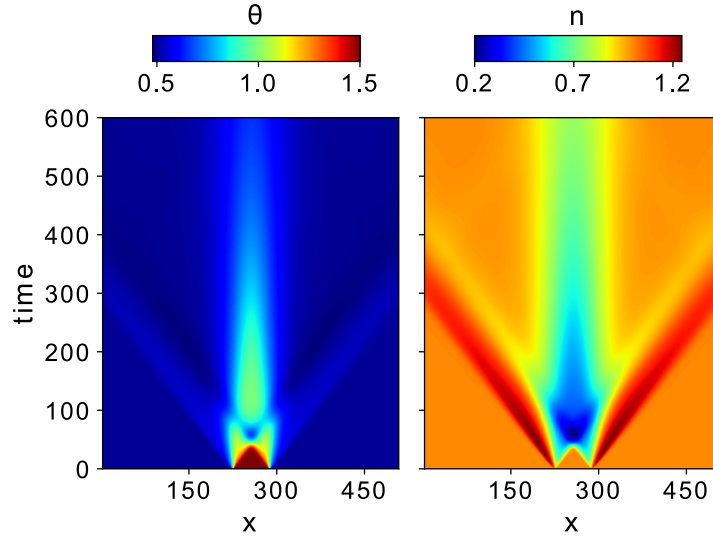
Figure 5.6: Time evolution of the temperature (left), where $\theta = T/T_r$, with $T_r = 1.0$, and density (right) at $y = L_Y/2$. The model used is based in a fifth order expansion of MJ distribution.
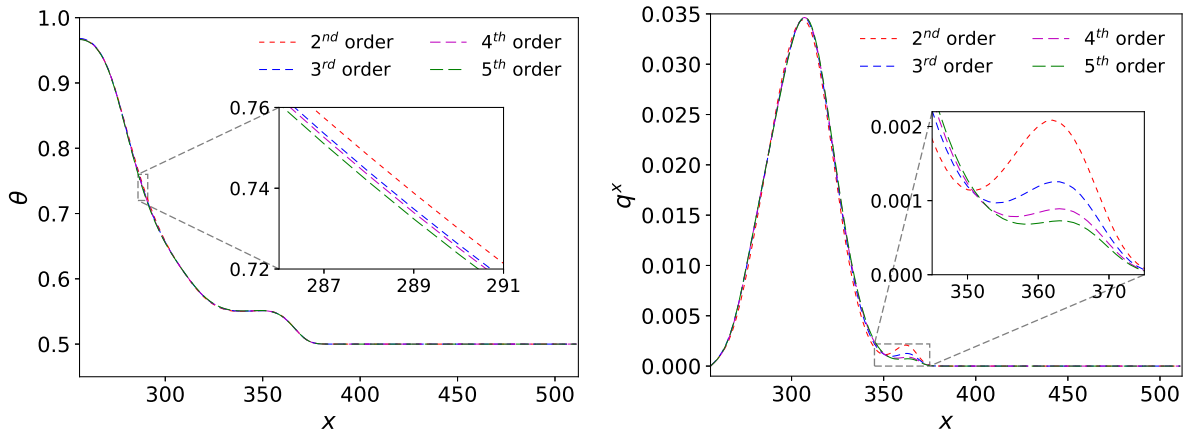
Figure 5.7: Temperature and heat flux profiles at $t = 100$ at $y = L_Y/2$ and $256 \leq x < 512$ for MJ distribution. Due to the symmetry, this region in space contains all relevant information about the problem. The inset shows the differences between different expansion orders.

Chapter 6

Kelvin-Helmholtz instability on graphene

In this chapter, we provide numerical evidence that a Kelvin-Helmholtz instability occurs in the Dirac fluid of charge carriers in graphene and can be detected in current experiments. This instability appears for electrons in the viscous regime passing though a micrometer scale obstacle and affects measurements on the time scale of nanoseconds. A possible realization with a needle shaped obstacle is proposed to produce and detect this instability by measuring the electric potential difference between contact points located before and after the obstacle. We also show that, for our setup, the Kelvin-Helmholtz instability leads to the formation of whirlpools similar to the ones reported by Bandurin, D. A., et al. [9] (see Figs. 1.1 and 1.2). To perform the simulations, we use the lattice Boltzmann method developed in Chap. 5, which is able to recover the full dissipation in a fluid of massless particles.

6.1 Introduction

The Kelvin-Helmholtz instability (KHI) is one of the most famous instabilities in fluid dynamics and it is an important mechanism for the formation of vortices and precursor of turbulence [134, 141, 155]. It appears when two fluids, or two parts of the same fluid, are sheared against each other with a small perturbation at the interface [25]. It occurs

in many situations in nature, as with fluctus clouds in the sky, the waves on the beach or the red spot of Jupiter and it plays an important role to understand phenomena in magnetohydrodynamics [102] as the interaction between the solar wind and the Earth's magnetosphere [60]. It was also observed experimentally [15] in superfluid ^{3}He. The KHI does not appear for supersonic relative speeds between the two fluids [17], which explains the stable flow for relativistic planar jets in astrophysical systems as galactic nuclei and gamma-ray bursts [29, 120].

In this chapter, we provide numerical evidence that the KHI can be produced and detected, with current technology, on the Dirac fluid in graphene. Since most of the recent studies are on the steady states of the flow (e.g., whirlpools), our proposal to observe the KHI should make it possible to explore also transient states, complementing our understanding about the hydrodynamic regime of electrons. We first simulate an idealized system (Sec. 6.4) to observe the appearance of the so-called cat-eyes pattern in the charge density field when we have shear between two regions of the fluid. Next, in Sec. 6.5,we simulate the fluid of electrons passing by an obstacle of micrometric scale, which creates a shear in the fluid, and analyze the impact of the KHI on the electric potential difference (EPD) between two contact points before and after the obstacle. According to our simulations, the duration of the instability is on the time scale of nanoseconds. Since this is challenging to observe experimentally, we suggest to produce it many times by using an alternating squared current of few hundreds of megahertz, and later take the statistical average of the signal. As we will see, the KHI leads to the formation of whirlpool-like regions similar to the ones in Ref. [9].

To perform the simulations in this chapter, we use the new RLBM developed in chapter 5 for the Dirac fluid in graphene based on the expansion of the FD distribution up to fifth order in orthogonal polynomials. According to the 14-moment Grad's theory, the fifth order expansion of the EDF is needed to recover the full dissipation in the fluid, i.e., the Navier-Stokes equation and Fourier's law [23, 99, 100], which is necessary to have an

accurate description for instabilities and other viscous effects. The previous models for graphene using a similar approach were limited to a second order expansion [97, 113].

This chapter is organized as follows. In Sec. 6.2 we review the RLBM developed in Chap. 5 adapting it for the physics of graphene. In Sec. 6.3, we review the theory for KHI and discuss the conditions for which it happens in graphene. In Sec. 6.4, we study the formation of the KHI in a idealized setup with shear between two parts of the electronic fluid. In Sec. 6.5, we propose a realistic setup to produce the KHI and show how to detect it though the electric current and electric potential difference (EPD).

6.2   Model description

In this section, we review and adapt the model of Chap. 5 to simulate the hydrodynamics of the Dirac fluid of charge carriers in graphene. We use the relativistic formalism to describe the relativistic dispersion relation and the equation of states of graphene. In this relativistic approach the speed of light (c) is played by the Fermi speed (v_F). Nevertheless, the fluid moves with velocity much smaller than the Fermi speed in our setup to study the KHI. Because of this, relativistic corrections of our formalism are negligible giving, therefore, the same results as standard (non-relativistic) hydrodynamics [85].

6.2.1   Lattice Boltzmann equation

We use in our model the relativistic Boltzmann equation with the Anderson-Witting collision operator [23] (the same used in Chap. 5, Eq. (6.1)), which is appropriate to treat massless particles, to describe the time evolution for the Dirac fluid:

$$\bar{p}^{\mu}\partial_{\mu}f = -\frac{\bar{p}_{\mu}U^{\mu}}{v_F^2\tau}(f - f^{eq}), \tag{6.1}$$

where τ is the relaxation time, which is a numerical parameter of our model used to tune the shear viscosity. We assume the Einstein's notation, where repeated indexes represent a sum. The greek indexes range from 0 to 2 while the latin ones range from 1 to 2. The

relativistic momentum is denoted by $\bar{p}^\mu = (E/v_F, \bar{\mathbf{p}})$, the velocity is $U^\mu = \gamma(v_F, \mathbf{u})$ and the time-space coordinates are $x^\mu = (v_F t, \mathbf{x})$, where $\gamma(u) = 1/\sqrt{1 - u^2/v_F^2}$ is the Lorentz factor. We use here the relativistic FD distribution,

$$f_{FD}^{eq} = \frac{1}{z^{-1} \exp\left[\frac{\bar{p}_\alpha U^\alpha}{k_B T}\right] + 1}, \tag{6.2}$$

where $z = e^{\bar{\mu}/k_B T}$ is the fugacity. The charge carries are modeled as ultra-relativistic particles, for which the kinetic energy is much larger than the rest mass energy. Thus $\bar{p}^\mu \bar{p}_\mu = (\bar{p}^0)^2 - \bar{\mathbf{p}}^2 = 0 \Rightarrow \bar{p}^0 = |\bar{\mathbf{p}}|$, and Eq. (6.1) becomes

$$\frac{\partial f}{\partial t} + \mathbf{v} \cdot \nabla f = -\gamma(1 - \mathbf{v} \cdot \mathbf{u}) \frac{(f - f^{eq})}{\tau}. \tag{6.3}$$

Here $\mathbf{v} = \hat{\mathbf{p}} = \bar{\mathbf{p}}/|\bar{\mathbf{p}}|$ is the microscopic velocity with norm v_F and we adopt from now on natural units $v_F = k_B = \hbar = e = 1$. Note that $u/v_F \to u$ in natural units. To implement the above equation numerically, the phase space is discretized as described in section 4.7 and we use the discrete version of Eq. (6.1):

$$f_\alpha(t + \delta t, \mathbf{r} + \mathbf{v}_\alpha \delta t) - f_\alpha(t, \mathbf{r}) = -\gamma(1 - \mathbf{v}_\alpha \cdot \mathbf{u}) \frac{\delta t (f_\alpha - f_\alpha^{eq})}{\tau}, \tag{6.4}$$

where δt is the time step of the simulations.

In the above formalism for ultra-relativistic particles the linear dispersion relation of charge carriers in graphene was naturally included. Nevertheless, the electronic fluid moves with a small velocity as compared to the Fermi speed ($\mathbf{u} \ll v_F \Rightarrow \gamma \approx 1$) and the relativistic corrections from our model are negligible.

6.2.2 Expansion of the equilibrium distribution function

To expand the FD distribution, we first introduce non-dimensional quantities: $\theta = T/T_0$, $\mathbf{p} = \bar{\mathbf{p}}/T_0$ and $\mu = \bar{\mu}/T_0$, where T_0 is the initial temperature. So, considering the ultra-reativistic regime, Eq. (6.2) becomes

$$f_{FD}^{eq} = \frac{1}{z^{-1} \exp\left[p^0 \gamma (1 - \mathbf{v} \cdot \mathbf{u})/\theta\right] + 1}. \tag{6.5}$$

We find the relativistic polynomials by a Gram-Schmidt procedure, with the weight functions for graphene with zero chemical potential reads:

$$\omega(p) = \frac{1}{e^p + 1}.$$

(6.6)

The details can be found in Sec. 5.2.2 while the explicit expansion is given in the Appendix D and in the Supplemental Material[1]

The expansion of the EDF up to fifth order can be expressed as following,

$$f^{eq} = \omega(\xi)\left[\sum_{N=0}^{5} \frac{1}{N!} A^{i_1 \ldots i_N} P^{i_1 \ldots i_N} + \sum_{M=0}^{4} \frac{1}{M!} A^{i_1 \ldots i_M 0} P^{i_1 \ldots i_M 0}\right],$$

(6.7)

where A are the projections of the EDF on the polynomials

$$A^{\mu_1 \mu_2 \cdots \mu_N} = \int \frac{d^2\mathbf{p}}{p^0} f^{eq} P^{\mu_1 \mu_2 \cdots \mu_N}.$$

(6.8)

Notice that the denominators $N!$ and $M!$ in the expansion stem from the normalization, Eq.(5.4), as derived in Ref. [31] and for the Hermite polynomials. The explicit expansion can be found in the Supplemental Material. This expansion allows us to calculate the full set of conservation equations for a viscous fluid and the transport coefficients, since it is required to expand up to fifth order to recover the fifth order moment of the EDF [23,99,100]:

$$T_E^{\alpha\beta\gamma\delta\epsilon} = \int f^{eq} p^\alpha p^\beta p^\gamma p^\delta p^\epsilon \frac{d^2 p}{p^0}.$$

(6.9)

The Gaussian quadrature used in this model to calculate the moments of the EDF is given in Sec. 5.2.4. It uses the weight function of Eq. 6.6 to calculate the discrete weights and the momentum vectors.

6.3 Kelvin-Helmholtz instability

When two fluid or two regions of the same fluid shear against each other with different tangential velocities and a perturbation is introduced on the interface, the KHI takes

---

place. To understand the critical values for which the instability occurs, lets consider two fluids, separated by a flat interface in the middle, under an external force perpendicular to the velocities, e.g, an electrical force [47]. The fluid in the upper part has smaller energy density ε_2 and is moving with velocity $\mathbf{U_2}$ while the fluid in the bottom has energy density ε_1 and velocity $\mathbf{U_1}$. If a perturbation in the fields (charge density, velocity or pressure),

$$\delta q \propto \exp[i(kx + ly - \omega t)], \tag{6.10}$$

is introduced at the interface, a linear stability analysis [25] provides that the minimum wave number in the parallel direction (transverse modes do not affect the instability) of the shear flow to have the KHI is

$$k_{min} = \frac{E\, g_2(z)|\varepsilon_1^2 - \varepsilon_2^2|}{3\,\varepsilon_1\,\varepsilon_2\,T\,g_3(z)(U_1 - U_2)^2}, \tag{6.11}$$

where we considered an external electrical field E perpendicular to the flow causing an acceleration $\frac{nE}{\varepsilon+P} = \frac{Eg_2(z)}{3Tg_3(z)}$. The KHI occurs for any $k > k_{min}$. Note that here the external force has a stabilizing role. Another way to stabilize the shear flow is with a gradient of charge density and/or velocity [50]. Defining the relativistic Richardson number for this problem as

$$Ri = -\frac{E\, g_2(z)}{3\,\varepsilon\,T\,g_3(z)} \frac{d\varepsilon/dy}{(dU^x/dy)^2}, \tag{6.12}$$

the linear stability analysis gives that the necessary condition to have a stable flow is $Ri > 1/4$ everywhere [25, 107]. The flow can be stable for $Ri < 1/4$ only in the absence of perturbations. The flow can also be stable for supersonic shear velocities [17]. For instance, for the simple case with $l = \omega = 0$, the flow is stable when $\mathcal{M} > 1$, where the relativistic Mach number is defined as

$$\mathcal{M} = \frac{u^x \gamma(u^x)}{c_s \gamma(c_s)}. \tag{6.13}$$

For the conditions we consider in the simulations for graphene, the flow is unstable for every perturbation because we do not have any external force perpendicular to the flow neither supersonic velocities.
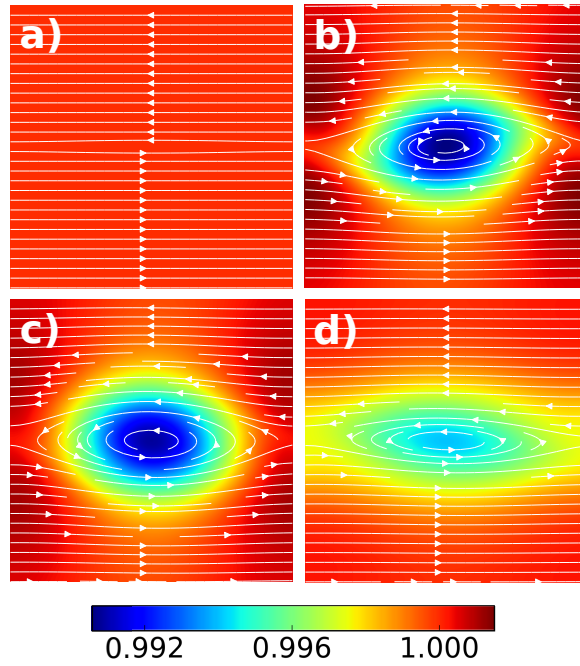
Figure 6.1: Formation of the KHI in graphene at a) $t = 0$ ns, b) $t = 0.72$ ns, c) $t = 1.00$ ns, d) $t = 1.43$ ns. The streamlines shows the velocity field and the colors represents the charge density fluctuations relative to the initial charge density, n/n_0.
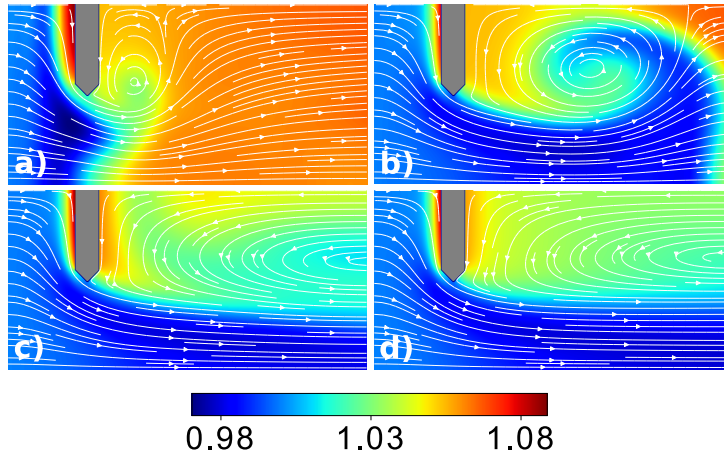
Figure 6.2: Realistic setup to observe the KHI at $Re = 53$. By using a constant current $0.05\,v_F$ in the source (left side), we see the snapshots for a) $t = 0.14$ ns, b) $t = 0.43$ ns, c) $t = 0.85$ ns, d) $t = 1.42$ ns. The colors represent the density fluctuations relative to the initial density, n/n_0, and the gray object represents a needle shaped obstacle. The streamlines show the directions of the velocity field.

In the following simulations, we consider that the charge carriers are in the hydrodynamic regime, which implies that the mean free path for carrier-carrier collisions gives the

smallest spatial scale for the system. See Ref. [83] for measurements of mean free paths and for the transition between ballistic and hydrodynamic regime in graphene. In order to reduce the scattering with impurities and phonon, we consider ultra-clean samples at appropriate temperature. The sample is on a substrate, e.g., SiO_2, with finite carrier density controlled by an external gate voltage. In addition, all simulations are performed for small velocities.

6.4 Ideal setup

As an idealized setup to observe the KHI, we model a system with size $L_x \times L_y = 512 \times 512$ grid points, representing a 37μm $\times 37\mu$m physical system, where the fluid has opposite velocities in the two halves, that is,

$$u_x^0 = -U_0 \tanh\left(\frac{y - L_y/2}{a}\right), \tag{6.14}$$

where we set $U_0 = 0.1v_F$ and $a = 1$. We introduce a small perturbation to trigger the instability as

$$u_y^0 = u_{pert} \sin\left[\frac{2\pi(x - L_x/2)}{L_x}\right] \exp\left[-\frac{(y - L_y/2)^2}{b^2}\right], \tag{6.15}$$

where $u_{pert} = 0.005v_F$ and $b = 10$. Initially, the charge density [98] and the temperature are the same everywhere, $n_0 = 2.26 \times 10^{-5}$ C/m^2 and $T_0 = 100$ K. For this temperature, the electron-phonon interactions are negligible [10]. The numerical shear viscosity-entropy ratio for the simulations of the KHI is $\eta/s = 0.12$. By using the Gibbs-Duhem relation for zero chemical potential, $\varepsilon + p = sT$, we calculate the kinematic viscosity $\nu = (\eta/s)/T_0 = 0.12$ and the Reynolds number for this simulation, $Re = L_0 v_0/\nu = 427$, where we use the size of the sample as the characteristic length L_0 and the velocity in each half as the characteristic velocity v_0. For a graphene sample with $T = 100K$ the kinematic viscosity [97] is $\nu = 8.57 \times 10^{-3} \, m^2/s$. The boundary conditions are periodic in left and right direction and, at top and bottom, the boundary is open except for the horizontal

velocity $u_x(t) = u_x^0$ that is set constant. In Fig. 6.1 we see the formation and evolution of the KHI for different times ($\delta t = 71$ fs). At $t = 0$ ns, we have the two regions of the fluid moving in opposite directions and a small perturbation in the velocity field at the middle. Since there is no external force perpendicular to the flow, Eq.(6.11) gives that $k_{min} = 0$, i.e., any perturbation makes the flow be unstable. Therefore the KHI appears as we can see in Fig. 6.1 for $t = 0.72$ ns and $t = 1.00$ ns, where we can recognize the pattern of the cat-eyes in the charge density field. After some time, the flow stabilizes due to the generation of a gradient in the velocity and charge density fields and to the absence of perturbations (Fig.6.1 d).

6.5 Realistic setup

In order to detect the KHI in experiments we propose a more realistic setup that could be performed nowadays, where we force the Dirac fluid to flow through an obstacle (see Fig. 6.2). We simulate a system with $L_x \times L_y = 512 \times 256$ with a needle shaped obstacle measuring 16×128 nodes, which represents $1.1\,\mu$m $\times\,9.1\,\mu$m, positioned 96 nodes ($6.8\,\mu$m) away from the source. Initially, all fields are homogeneous: $n_0 = 2.26 \times 10^{-5}$ C/m^2, $T_0 = 100$ K, $\mathbf{u_0} = 0$. We use bounce-back boundary conditions at the obstacle's surface ($\mathbf{u} = 0$), open boundary at the right side (drain), slide-free boundaries at top and bottom ($u_y = 0$) and, at the left side, the source, we set a current in the horizontal direction: $n^{in} = n_0$, $u_x^{in}(t)$, $u_y^{in} = 0$, and we obtain the temperature at the boundaries by a zero-order extrapolation from the first fluid neighbors.

Now we analyze the fields when a constant current is applied at the source. In Fig. 6.2, we see the evolution of the charge density field and the formation of the KHI for a velocity $u_x^{in} = 0.05 v_F$ at the source, which corresponds to an electrical current of $I_0 = j_0\,L_y = 20.6\,\mu$A. Considering u_x^{in} as the characteristic velocity and the length of the obstacle as the characteristic length, we have $Re = 53$ for this simulation. When the current reaches the obstacle ($t = 0.14$ ns), we see that the fluid at the bottom region
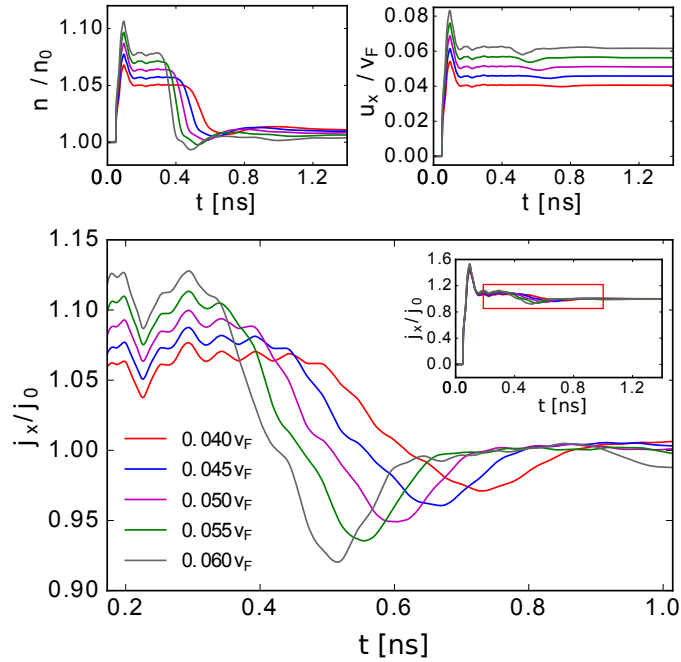
Figure 6.3: Average charge density, average x-component of the velocity and current as functions of time for different source velocities measured close to the drain. The inset show the current for a longer time and the red rectangle indicates the region that is being amplified.
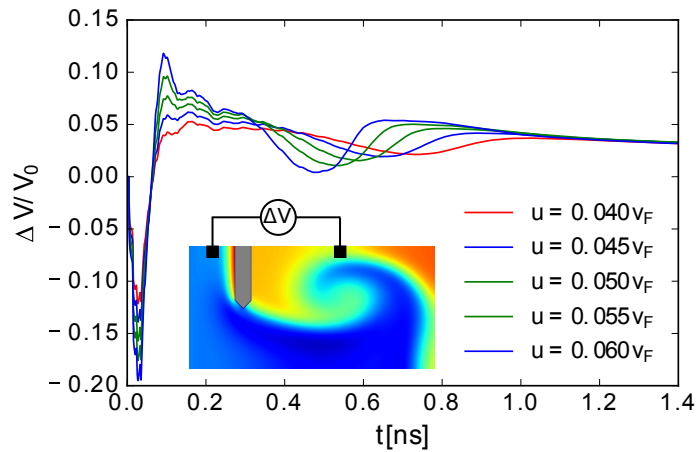
Figure 6.4: EPD between the two points indicated by the black squares in the inset divided by a reference voltage V_0.

has velocity $> u_x^{in}$, while the fluid at the upper region has $u_x = 0$ generating a shear flow. Since we have no external force in the vertical direction, Eq.(6.11) says that the flow is unstable for every perturbation, which, in our case, is generated by the initial
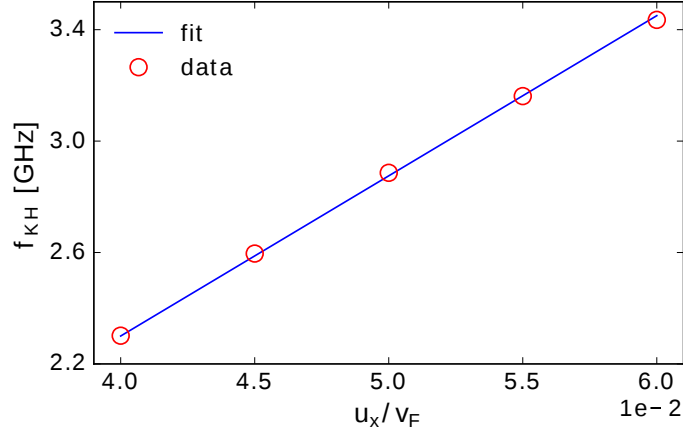
Figure 6.5: Frequency of the signal due to the KHI as a function of the source velocity and a linear fit.

passage of the fluid and, therefore, the KHI appears (Fig. 6.2b). At $t = 0.85$ ns the flow begins to stabilize due to the formation of gradients and the absence of perturbations and, at $t = 1.42$ ns, we can not see signs of the instability anymore. The streamlines in Fig. 6.2 show that, after the passage of the KHI, we have the formation of permanent (steady state) whirlpool-like regions between the obstacle and the drain similarly to the ones reported in Refs. [9, 86, 119, 145]. It suggests that the KHI drives the formation of these experimentally observed whirlpools in graphene analogously to many other vortex formation in nature [134, 141, 155]. The KHI can be identified in the electrical current signal, because there are fluctuations in charge density and velocity when the instability passes by the measurement points. In Fig. 6.3, we see the time evolution for the current , $j_x(t) = \int dy\, n\, u_x$, the average charge density, $n(t) = \int dy\, n/L_y$, and the average x-component of the velocity, $u_x(t) = \int dy\, u_x/L_y$, measured close to the drain (10 nodes before) for 5 source velocities, where $\delta t = 71$ fs. For the velocity $0.05 v_F$, we can observe fluctuations in the fields due to the instability starting approximately from 0.36 ns to 0.71 ns, which agrees with, respectively, the times when the instability reaches the right border and disappears in Fig. 6.2. In the inset of Fig. 6.3 one can observe the first big oscillation in the electrical current that is due to the waves generated by the initial

passage of the fluid through the obstacle. Since these waves depend only of the sound speed, they reach the drain at the same time, independently of the source velocity u_x^{in}. After this, one can observe oscillations, of few microamperes, due to the KHI that have a smaller period for higher source velocities. This is expected as the instabilities have approximately the same dimensions, but travel faster for higher velocities. To estimate the period of each oscillation of the instability, T_{KH}, we consider the charge density curves, since they are smoother and the instability's sign can be identified more easily. In order to numerically measure the beginning of the oscillation, we define it as the point at which the derivative is smaller than a reference value, which we choose as being half of the derivative at the decreasing region in the fields (for instance, between 0.4 ns and 0.6 ns for $u_0 = 0.05 v_F$). We find the end of the oscillation in a analogous way but considering the derivative in the increasing region. Thus, we calculate the frequency of the instability defined by $f_{KH} = 1/T_{KH}$ and plot it as a function of the source velocity, Fig. 6.5. We can identify a linear relation, which is expected from the wave equation $v = \lambda \times f$. By a linear fit we find $\lambda \approx 17.4\,\mu$m, that approximately corresponds to the length of the instability. In Fig. 6.2, we see that the length of the instability does correspond to roughly half of the system size ($18.2 \mu m$), what confirms that this oscillation in the current measurement is due to the KHI.

One can detect the instability in experiments by measuring the electric potential difference (EPD). We consider the simplification adopted in Ref. [146], which considers that the EPD is caused by fluctuations in the charge density field, leading to:

$$\Delta V \approx \frac{\Delta n}{C}, \tag{6.16}$$

where $C = \epsilon_0 \epsilon_r / d$ is the capacitance per unit area, ϵ_0 is the vacuum permeability, ϵ_r is the relative permeability of the substrate and d is the thickness of the substrate. Fig. 6.4 shows the EPD between the two points indicated by black squares in the inset (upper boundary and in the middle of each domain) divided by a reference potential, $V_0 = n_0/C$,

with n_0 being the initial density. Here, $\Delta n = n_R - n_L$ is the difference between the charge density at the right and left contacts. Initially, the EPD is zero, due to the homogeneous initial condition in charge density. The first oscillations occur when the moving fluid reaches the contacts and they do not depend on the fluid velocity as discussed before. Between 0.3 ns and 1 ns, we can see the oscilations due to the KHI, which depend on the fluid velocity likewise with the electrical current. Considering, for instance, a substrate of SiO_2, which has $\epsilon_r = 3.9$, and typical experimental parameters [41] ($d = 3 \times 10^{-7}$ m, $n_0 = 2.26 \times 10^{-5}$ C/m^2), we can estimate that the oscillations due to the KHI are on the scale of ~ 10 mV, which could be measured in current experiments. The oscillations in the electrical current, on the scale of microamperes, are much harder to detect.

Since the duration of the KHI is on the scale of nanoseconds, it would be challenging to observe it with a constant current, but one could generate it with a high frequency and observe its influence on the electrical current and EPD. We simulate a squared current (on-off) with a frequency of 470 MHz for three source velocities and the time dependence of the electrical current and the EPD can be seen in Fig. 6.6 for three cycles starting from 4 ns to avoid the initial stabilization of the system. The behavior that we observed for a constant current (Figs. 6.3 and 6.4) can be reproduced indefinitely and we can clearly identify the oscillations that are due to the KHI, since they change with the source velocity. As can be seen in Fig. 6.6, the cycles are basically identical and, therefore, one could distinguish the oscillations due to the KHI from the experimental noise by taking the statistical average of many cycles. Note that the current at the drain becomes negative when the source current is interrupted, which is due to the whirlpools (see Fig. 6.2) that cause a back flow.

6.6   Conclusion

The Kelvin-Helmholtz instability was analyzed in an idealized setup, with a shear flow between two regions of the Dirac fluid moving in opposite directions. We also simulated a
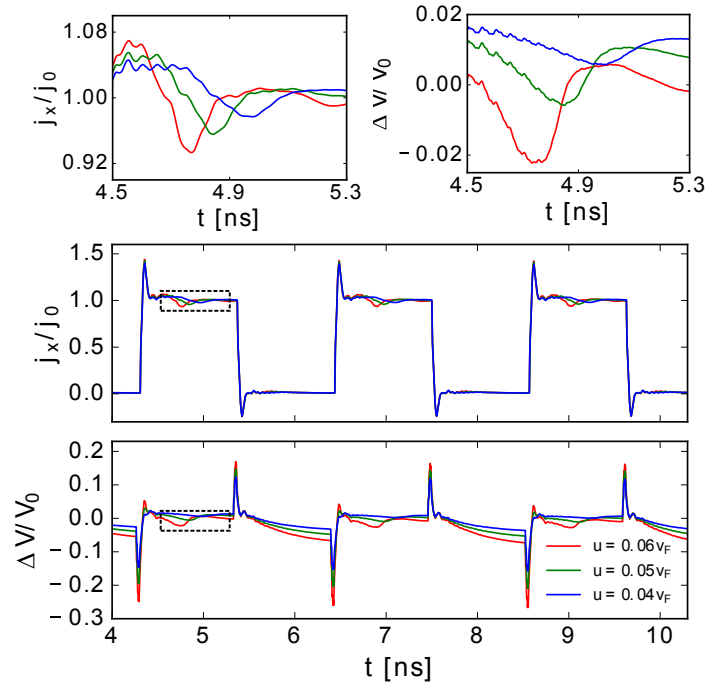
Figure 6.6: Electrical current at the drain and EPD between the two contacts indicated in Fig. 6.4 when an alternated squared current of 470 MHz is applied at the source for three different source velocities. The dashed rectangles indicate where the oscillations due to the KHI can be identified, which are amplified in the figures on the top.

flow through a needle shaped obstacle, which would be a possible experimental realization to observe this instability, and we analyzed its impact on the electrical potential difference measurements. The Kelvin-Helmholtz instability can be identified by changing the current at the source. An alternating squared current can be used to produce the instability many times, such that one can later take the statistical average over the different cycles and differentiate the instability from noise. Since this instability always occur in the presence of an obstacle, it can even be produced and measured accidentally in experiments and be confused with experimental noise. Therefore, it should be considered in experiments performing measurements on the scale of nanoseconds. As illustrated here, the Kelvin-Helmholtz instability leads to the formation of whirlpools similar to the ones reported in Ref. [9] (see Fig. 6.2).

Chapter 7

Conclusion

Here we summarize the main results and give future perspectives for the work developed in this thesis.

One of the main advantages of the LBM is the ease of simulating flows in complex geometries without the need to draw sophisticated meshes as occur for the finite element methods for instance. This was illustrated in Chap. 2 with the simulation of a fluid passing though many different samples of porous media. These samples were artificially built by placing spheres in random positions until the desired porosity is reached. The use of artificial samples instead of the digitalization of real rocks offers the possibility to control the characteristics of the samples such as the porosity and the size of the grains and, besides, we have more statistics. Using LBM, we were able to calculate fluid dynamic properties of the samples (permeability and tortuosity) and relate them with geometrical properties (porosity, size of the grains and specific surface area). We found out that the Kozeny-Carman equation applies to our artificial samples.

In previous attempts to build a LBM for semiclassical fluids, including my master thesis (Refs. [30, 34, 67, 130, 157]), regimes far from the classical one can not be achieved. Therefore, one could not treat electrons in metals for instance. This occur because, in these previous models, the expansion of the BE and FD distributions is made in Hermite polynomials, which are appropriate only for the MB distribution (classical fluids). This problem was solved with the discovery of the generalized polynomials described in Chap.

3. These polynomials are orthogonal for a generic weight function and are particularly interesting for the expansion of semiclassical distributions (BE and FD) using appropriate weights. We calculate analytically the polynomial coefficients up to fourth order and, as expected, we are able to recover well known polynomials (Hermite, Chebyshev and Legendre) using their respective weights to calculate the coefficients.

The non-relativistic semiclassical LBM, based on the generalized polynomials, is described in details in Chap. 4. We expand a generic distribution function, which can be the BE and the FD, up to fourth order in generalized polynomials. The obtainment of the macroscopic equations for semiclassical fluids is done using a non-expanded generic distribution function by means of the Chapman-Enskog method, which generalizes the work done in my master thesis [30, 34]. Also, the forcing therm is studied for the new model in order to see if it satisfies the first three moment constraints and new Gaussian quadratures are calculated to be used in the semiclassical models. A simple model for electrons in metals is constructed and tested by using the Riemann problem and the Poiseuille flow. As expected for electrons in metals, the Ohm's law is recovered when the electronic fluid pass through a medium with randomly placed obstacles, which exemplifies the use of the LBM for electrons in complex geometries.

It is known that to recover the macroscopic equations and the transport coefficients for a fluid made of ultrarelativistic particles we need, at least, a fifth order expansion of the EDF [100]. In 2013, Mendoza et. al. [99] developed a model with improved dissipation, which is based on a third order expansion of the MJ EDF. The first model with full dissipation is developed in the Chap. 5 for ultrarelativistic semiclassical particles. We expand the three relativistic distributions (MJ, FD and BE) up to fifth order in relativistic polynomials, which are a relativistic version of the polynomials given in Chap. 3. Besides, new quadratures able to calculate high order moments of the EDF are developed. These quadratures require interpolations to find the distributions at the grid points, but they have the advantage to preserve the spatial resolution in a squared lattice. We validate

and characterize the models using four numerical tests: the Riemann problem, the Taylor-Green vortex, the Fourier flow and the hot-spot relaxation. In these tests, we analyze qualitatively and quantitatively the differences between the models based in different expansion order of the EDF. Furthermore, we numerically measure, with high precision, the kinematic viscosity and the thermal conductivity for ultrarelativistic fluids in two dimensions. As discussed, these transport coefficients do not agree with the predictions from the Grad method, but should serve for future comparisons with results from the Chapman-Enskog method, which was gives correct results for three dimensional systems.

In Chap. 6, we use the fully dissipative relativistic LBM developed in Chap. 5 to simulate the Dirac fluid of charge carriers in graphene. The relativistic LBMs was used many times in literature for graphene because it naturally includes its linear dispersion relation, but the low velocity regime is adopted. We investigate the Kelvin-Helmholtz instability of electrons in graphene and we propose an experiment to detect it through the electric potential difference and the electric current. As we observed, this instability occur very easily in the presence of an obstacle, which should be considered in measurement on the time scales of nanoseconds. This application illustrates the use of LBM to study transient states of the flow in electron hydrodynamics, what would be challenging to perform analytically with the macroscopic equations (Navier-Stokes).

In this thesis, we have two specific materials: metals and graphene. Nevertheless, our methodology is general and these models could be straightforwardly extended to other systems just changing the physical parameters (e.g., chemical potential, density). The hydrodynamic regime can be achieved in a wide range of novel materials as the Dirac materials [150], topological insulators [24], which has carriers on the surface that may behave like a fluid, Weyl systems [89] and 2D metal Palladium cobaltate [103].

Besides, the models here presented can be improved to account other effects. For instance, thermal effects can be treaded if more relaxation times are included in the collision term as done in Ref. [87] for relativistic models or in Ref. [128] for non-relativistic

models. In addition, one could study electron-phonon interaction if the spatial curvature is included in the forcing term as in Refs. [40, 52].

Bibliography

[1] M. Abramowitz and I.A. Stegun. *Handbook of Mathematical Functions: With Formulas, Graphs, and Mathematical Tables*. Applied mathematics series. Dover Publications, 1964. 8, 83, 102, 105

[2] K. H. et. al. Ackermann. Elliptic flow in $au + au$ collisions at $\sqrt{s}_{\mathrm{nn}} = 130\mathrm{GeV}$. *Phys. Rev. Lett.*, 86:402–407, Jan 2001. 98

[3] Heiko Andrä, Nicolas Combaret, Jack Dvorkin, Erik Glatt, Junehee Han, Matthias Kabel, Youngseuk Keehm, Fabian Krzikalla, Minhui Lee, Claudio Madonna, et al. Digital rock physics benchmarksâpart i: Imaging and segmentation. *Computers & Geosciences*, 50:25–32, 2013. 24

[4] Heiko Andrä, Nicolas Combaret, Jack Dvorkin, Erik Glatt, Junehee Han, Matthias Kabel, Youngseuk Keehm, Fabian Krzikalla, Minhui Lee, Claudio Madonna, et al. Digital rock physics benchmarksâpart ii: computing effective properties. *Computers & Geosciences*, 50:33–43, 2013. 24

[5] Kin Chung Fong Andrew Lucas. Hydrodynamics of electrons in graphene. *arXiv preprint arXiv:1710.08425*, 2017. 3

[6] Saeid Jamshidi Arash Rabbani and Saeed Salehi. Determination of specific surface of rock grains by 2d imaging. *Journal of Geological Research*, 2014(945387), 2014. xviii, 20, 24

[7] N.W. Ashcroft and N.D. Mermin. *Solid State Physics*. Science: Physics. Saunders College, 1976. 1, 60, 65, 87

[8] Alexander A. Balandin, Suchismita Ghosh, Wenzhong Bao, Irene Calizo, Desalegne Teweldebrhan, Feng Miao, and Chun Ning Lau. Superior thermal conductivity of single-layer graphene. *Nano Letters*, 8(3):902–907, 2008. PMID: 18284217. 3

[9] D. A. Bandurin, I. Torre, R. Krishna Kumar, M. Ben Shalom, A. Tomadin, A. Principi, G. H. Auton, E. Khestanova, K. S. Novoselov, I. V. Grigorieva, L. A. Ponomarenko, A. K. Geim, and M. Polini. Negative local resistance caused by viscous electron backflow in graphene. *Science*, 351(6277):1055–1058, 2016. xvii, 4, 5, 59, 123, 124, 133, 136

[10] Amelia Barreiro, Michele Lazzeri, Joel Moser, Francesco Mauri, and Adrian Bachtold. Transport properties of graphene in the high-current limit. *Phys. Rev. Lett.*, 103:076601, Aug 2009. 130

[11] S. Berkowitz and F. J. Garner. The calculation of multidimensional Hermite polynomials and Gram–Charlier coefficients. 24(111):537–545, July 1970. 30

[12] Jeremy Bernstein. *Kinetic Theory in the Expanding Universe*. Cambridge Monographs on Mathematical Physics. Cambridge University Press, 1988. 97

[13] Rajeev S. Bhalerao, Amaresh Jaiswal, Subrata Pal, and V. Sreekanth. Relativistic viscous hydrodynamics for heavy-ion collisions: A comparison between the chapman-enskog and grad methods. *Phys. Rev. C*, 89:054903, May 2014. 99

[14] Prabhu Lal Bhatnagar, Eugene P Gross, and Max Krook. A model for collision processes in gases. i. small amplitude processes in charged and neutral one-component systems. *Physical review*, 94(3):511, 1954. 6

[15] R. Blaauwgeers, V. B. Eltsov, G. Eska, A. P. Finne, R. P. Haley, M. Krusius, J. J. Ruohio, L. Skrbek, and G. E. Volovik. Shear flow and kelvin-helmholtz instability in superfluids. *Phys. Rev. Lett.*, 89:155301, Sep 2002. 124

[16] Jean-Paul Blaizot, François Gelis, Jinfeng Liao, Larry McLerran, and Raju Venugopalan. Bose–einstein condensation and thermalization of the quark–gluon plasma. *Nuclear Physics A*, 873:68–80, 2012. 98

[17] G. Bodo, A. Mignone, and R. Rosner. Kelvin-helmholtz instability for relativistic fluids. *Phys. Rev. E*, 70:036304, Sep 2004. 124, 128

[18] CG Böhmer and T Harko. Can dark matter be a bose–einstein condensate? *Journal of Cosmology and Astroparticle Physics*, 2007(06):025, 2007. 98

[19] I. Bouras, E. Molnár, H. Niemi, Z. Xu, A. El, O. Fochler, C. Greiner, and D. H. Rischke. Relativistic shock waves in viscous gluon matter. *Phys. Rev. Lett.*, 103:032301, Jul 2009. 98, 112

[20] U. Briskot, M. Schütt, I. V. Gornyi, M. Titov, B. N. Narozhny, and A. D. Mirlin. Collision-dominated nonlinear hydrodynamics in graphene. *Phys. Rev. B*, 92:115426, Sep 2015. 5, 118

[21] PC Carman. Fluid flow through granular beds. *Chemical Engineering Research and Design*, 75:S32–S48, 1997. 14

[22] A. H. Castro Neto, F. Guinea, N. M. R. Peres, K. S. Novoselov, and A. K. Geim. The electronic properties of graphene. *Rev. Mod. Phys.*, 81:109–162, Jan 2009. 3, 5

[23] Carlo Cercignani and Gilberto Medeiros Kremer. *Relativistic Boltzmann Equation*. Birkhäuser Basel, Basel, 2002. 5, 97, 99, 101, 109, 110, 116, 124, 125, 127

[24] AtMa P. O. Chan, Thomas Kvorning, Shinsei Ryu, and Eduardo Fradkin. Effective hydrodynamic field theory and condensation picture of topological insulators. *Phys. Rev. B*, 93:155122, Apr 2016. 59, 139

[25] S. Chandrasekhar. *Hydrodynamic and hydromagnetic stability.* 1961. 123, 128

[26] Sydney Chapman and Thomas George Cowling. *The mathematical theory of non-uniform gases: an account of the kinetic theory of viscosity, thermal conduction and diffusion in gases.* Cambridge university press, 1970. 5, 63, 99

[27] T.S. Chihara. 45 years of orthogonal polynomials: a view from the wings. *Journal of Computational and Applied Mathematics*, 133(1â2):13 – 21, 2001. 5th Int. Symp. on Orthogonal Polynomials, Special Functions and t heir Applications. 29

[28] M. Ben Clennell. Tortuosity: a guide through the maze. *Geological Society, London, Special Publications*, 122(1):299–344, 1997. 17

[29] Rodrigo C V Coelho, MaurÃcio O CalvÃ£o, Ribamar R R Reis, and Beatriz B Siffert. Standardization of type ia supernovae. *European Journal of Physics*, 36(1):015007, 2015. 97, 124

[30] Rodrigo C. V. Coelho, Anderson Ilha, Mauro M. Doria, R. M. Pereira, and Valter Yoshihiko Aibe. Lattice boltzmann method for bosons and fermions and the fourth-order hermite polynomial expansion. *Phys. Rev. E*, 89:043302, Apr 2014. 2, 6, 14, 30, 31, 57, 59, 75, 76, 77, 95, 98, 103, 137, 138

[31] Rodrigo C. V. Coelho, Anderson S. Ilha, and Mauro M. Doria. A lattice boltzmann method based on generalized polynomials and its application for electrons in metals. *EPL (Europhysics Letters)*, 116(2):20001, 2016. 3, 6, 30, 31, 57, 59, 64, 70, 98, 102, 127

[32] Rodrigo C. V. Coelho, Miller Mendoza, Mauro M. Doria, and Hans J. Herrmann. Kelvin-helmholtz instability on graphene. *arXiv:1706.00801v1*, Jul 2017. 10, 32, 59, 99, 100, 104, 105

[33] Rodrigo C V Coelho and Rodrigo F Neumann. Fluid dynamics in porous media with sailfish. *European Journal of Physics*, 37(5):055102, 2016. xvii, 7, 9, 31, 57, 98

[34] Rodrigo Carlos Viana Coelho. Lattice boltzmann method for bosons and fermions. Master's thesis, 2014. 2, 76, 78, 137, 138

[35] Rodrigo CV Coelho, Miller Mendoza, Mauro M Doria, and Hans J Herrmann. Fully dissipative relativistic lattice boltzmann method in two dimensions. *arXiv preprint arXiv:1709.09073*, 2017. 10, 32

[36] Jesse Crossno, Jing K. Shi, Ke Wang, Xiaomeng Liu, Achim Harzheim, Andrew Lucas, Subir Sachdev, Philip Kim, Takashi Taniguchi, Kenji Watanabe, Thomas A. Ohki, and Kin Chung Fong. Observation of the dirac fluid and the breakdown of the wiedemann-franz law in graphene. *Science*, 351:1058, 2016. 5

[37] Henry Philibert Gaspard Darcy. *Dètermination des lois d'ècoulement de l'eau à travers le sable*. 1856. 18

[38] M. J. M. de Jong and L. W. Molenkamp. Hydrodynamic electron flow in high-mobility wires. *Phys. Rev. B*, 51:13389–13402, May 1995. 4

[39] Anil Deane, Gunther Brenner, David R Emerson, James McDonough, Damien Tromeur-Dervout, N Satofuka, A Ecer, and Jacques Periaux. *Parallel Computational Fluid Dynamics 2005: Theory and Applications*. Elsevier, 2006. 14

[40] Jens-Daniel Debus. *Flow though curved spaces*. PhD thesis, ETH Zürich, 2016. xvii, 8, 140

[41] Vincent E. Dorgan, Myung-Ho Bae, and Eric Pop. Mobility and saturation velocity in graphene on sio2. *Applied Physics Letters*, 97(8):082112, 2010. 3, 135

[42] Mauro M Doria and Rodrigo CV Coelho. Chebyshev, legendre, hermite and other orthonormal polynomials in d-dimensions. *arXiv preprint arXiv:1703.08670*, 2017. 62, 103

[43] Serena Fagnocchi, Stefano Finazzi, Stefano Liberati, Marton Kormos, and Andrea Trombettoni. Relativistic bose–einstein condensates: a new system for analogue models of gravity. *New Journal of Physics*, 12(9):095012, 2010. 98

[44] J.-L. Feugeas, Ph. NicolaÃ⁻, X. Ribeyre, G. Schurtz, V. Tikhonchuk, and M. Grech. Modeling of two-dimensional effects in hot spot relaxation in laser-produced plasmas. *Physics of Plasmas*, 15(6):062701, 2008. 118

[45] Wojciech Florkowski, Radoslaw Ryblewski, and Michael Strickland. Testing viscous and anisotropic hydrodynamics in an exactly solvable case. *Phys. Rev. C*, 88:024903, Aug 2013. 99

[46] Lars Fritz, Jörg Schmalian, Markus Müller, and Subir Sachdev. Quantum critical transport in clean graphene. *Phys. Rev. B*, 78:085416, Aug 2008. 5

[47] O. Furtmaier, M. Mendoza, I. Karlin, S. Succi, and H. J. Herrmann. Rayleigh-bénard instability in graphene. *Phys. Rev. B*, 91:085401, Feb 2015. 10, 59, 98, 99, 100, 104, 115, 118, 128

[48] A. Gabbana, M. Mendoza, S. Succi, and R. Tripiccione. Kinetic approach to relativistic dissipation. *Phys. Rev. E*, 96:023305, Aug 2017. 99, 114, 118, 120

[49] A. Gabbana, M. Mendoza, S. Succi, and R. Tripiccione. Towards a unified lattice kinetic scheme for relativistic hydrodynamics. *Phys. Rev. E*, 95:053304, May 2017. 10, 98

[50] Yanbiao Gan, Aiguo Xu, Guangcai Zhang, and Yingjun Li. Lattice boltzmann study on kelvin-helmholtz instability: Roles of velocity and density gradients. *Phys. Rev. E*, 83:056704, May 2011. 128

[51] Sebastian Geller, Manfred Krafczyk, Jonas Tölke, Stefan Turek, and Jaroslav Hron. Benchmark computations based on lattice-boltzmann, finite element and finite volume methods for laminar flows. *Computers & Fluids*, 35(8):888–897, 2006. 14

[52] Ilario Giordanelli, Miller Mendoza, and Hans Herrmann. Modelling electron-phonon interactions in graphene with curved space hydrodynamics. *arXiv preprint arXiv:1702.04156*, 2017. 10, 59, 140

[53] Alexander O. Govorov and Jean J. Heremans. Hydrodynamic effects in interacting fermi electron jets. *Phys. Rev. Lett.*, 92:026803, Jan 2004. 5

[54] Harold Grad. Note on n-dimensional hermite polynomials. *Communications on Pure and Applied Mathematics*, 2(4):325–330, 1949. 30, 31, 33, 62, 99

[55] Harold Grad. On the kinetic theory of rarefied gases. *Communications on Pure and Applied Mathematics*, 2(4):331–407, 1949. 31

[56] I.S. Gradshteyn and I.M. Ryzhik. *Table of Integrals, Series, and Products*. Academic Press, Elsevier, 2014. 29, 52, 53, 54

[57] Haoyu Guo, Ekin Ilseven, Gregory Falkovich, and Leonid S Levitov. Higher-than-ballistic conduction of viscous electron flows. *Proceedings of the National Academy of Sciences*, page 201612181, 2017. 4

[58] RN Gurzhi. Hydrodynamic effects in solids at low temperature. *Physics-Uspekhi*, 11(2):255–270, 1968. 4

[59] Johannes Habich, Christian Feichtinger, Harald Köstler, Georg Hager, and Gerhard Wellein. Performance engineering for the lattice boltzmann method on gpgpus:

Architectural requirements and performance results. *Computers & Fluids*, 80:276–282, 2013. 14, 15

[60] H Hasegawa, M Fujimoto, T-D Phan, H Reme, A Balogh, MW Dunlop, C Hashimoto, and R TanDokoro. Transport of solar wind into earth's magnetosphere through rolled-up kelvin–helmholtz vortices. *Nature*, 430(7001):755–758, 2004. 124

[61] Joe D Hoffman and Steven Frankel. *Numerical methods for engineers and scientists.* CRC press, 2001. 109

[62] Haibo Huang, Lei Wang, and Xi yun Lu. Evaluation of three lattice boltzmann models for multiphase flows in porous media. *Computers & Mathematics with Applications*, 61(12):3606 – 3617, 2011. Mesoscopic Methods for Engineering and Science â Proceedings of ICMMES-09Mesoscopic Methods for Engineering and Science. 28

[63] D. Hupp, M. Mendoza, I. Bouras, S. Succi, and H. J. Herrmann. Relativistic lattice boltzmann method for quark-gluon plasma simulations. *Phys. Rev. D*, 84:125015, Dec 2011. 9, 10, 98

[64] Rudolph C Hwa and Xin-Nian Wang. *Quark-gluon plasma 4.* World Scientific, 2010. 10

[65] Harald Ibach and Hans Lüth. Solid-state physics: an introduction to principles of material science. *Advanced Texts in Physics, Springer-Verlag berlin Heidelberg New York*, 2003. 1, 2, 87, 93

[66] M. Januszewski and M. Kostur. Sailfish: A flexible multi-gpu implementation of the lattice boltzmann method. *Computer Physics Communications*, 185(9):2350 – 2368, 2014. 14, 15, 16

[67] Yao-Tien Kuo Jaw-Yen Yang, Li-Hsin Hung. Semiclassical axisymmetric lattice boltzmann method. *Adv. Appl. Math. Mech.*, 2:626–639, 2010. 2, 59, 137

[68] D. R. Jenkins. Specific surface area of overlapping spheres in the presence of obstructions. *The Journal of Chemical Physics*, 138(7), 2013. 24

[69] Bernard J. T. Jones. The origin of galaxies: A review of recent theoretical developments and their confrontation with observation. *Rev. Mod. Phys.*, 48:107–149, Jan 1976. 98

[70] M. Kaviany. *Principles of Heat Transfer in Porous Media*. Springer, Verlag New York, 2n edition, 1995. 18

[71] A. Ebrahimi Khabbazi, J.S. Ellis, and A. Bazylak. Developing a new form of the kozenyâcarman parameter for structured porous media through lattice-boltzmann modeling. *Computers & Fluids*, 75:35 – 41, 2013. 14, 15

[72] Yuta Kikuchi, Kyosuke Tsumura, and Teiji Kunihiro. Mesoscopic dynamics of fermionic cold atoms â quantitative analysis of transport coefficients and relaxation times. *Physics Letters A*, 380(24):2075 – 2080, 2016. 99

[73] Andreas Klöckner, Nicolas Pinto, Yunsup Lee, B. Catanzaro, Paul Ivanov, and Ahmed Fasih. PyCUDA and PyOpenCL: A Scripting-Based Approach to GPU Run-Time Code Generation. *Parallel Computing*, 38(3):157–174, 2012. 14

[74] Pieter Kok and Samuel L Braunstein. Multi-dimensional hermite polynomials in quantum optics. *Journal of Physics A: Mathematical and General*, 34(31):6185, 2001. 31

[75] A. Koponen, M. Kataja, and J. Timonen. Tortuous flow in porous media. *Phys. Rev. E*, 54:406–410, Jul 1996. 15, 26, 27

[76] A. Koponen, M. Kataja, and J. Timonen. Permeability and effective porosity of porous media. *Phys. Rev. E*, 56:3319–3325, Sep 1997. 15, 25, 27, 28

[77] Hiroaki Kouno, Masahiro Maruyama, Fujio Takagi, and Koichi Saito. Relativistic hydrodynamics of quark-gluon plasma and stability of scaling solutions. *Phys. Rev. D*, 41:2903–2911, May 1990. 97

[78] Josef Kozeny. *Über kapillare Leitung des Wassers im Boden:(Aufstieg, Versickerung und Anwendung auf die Bewässerung)*. Hölder-Pichler-Tempsky, 1927. 14

[79] G. M. Kremer and F. P. Devecchi. Thermodynamics and kinetic theory of relativistic gases in 2d cosmological models. *Phys. Rev. D*, 65:083515, Apr 2002. 98, 99

[80] Gilberto M. Kremer. *An Introduction to the Boltzmann Equation and Transport Processes in Gases*. Springer, Verlag Berlin Heidelberg, 2010. 6

[81] Gilberto Medeiros Kremer. *An Introduction to the Boltzmann Equation and Transport Processes in Gases*. Springer-Verlag Berlin Heidelberg, 2010. 5, 31, 57, 59, 63, 99

[82] T. Krüger, H. Kusumaatmaja, A. Kuzmin, O. Shardt, G. Silva, and E.M. Viggen. *The Lattice Boltzmann Method: Principles and Practice*. Graduate Texts in Physics. Springer International Publishing, 2016. 2, 6, 31, 59, 98

[83] R Krishna Kumar, DA Bandurin, FMD Pellegrino, Y Cao, A Principi, H Guo, GH Auton, M Ben Shalom, LA Ponomarenko, G Falkovich, et al. Super-ballistic flow of viscous electron fluid through graphene constrictions. *Nature Physics*, 2017. 4, 130

[84] Pierre Lallemand and Li-Shi Luo. Theory of the lattice boltzmann method: Dispersion, dissipation, isotropy, galilean invariance, and stability. *Phys. Rev. E*, 61:6546–6562, Jun 2000. 115

[85] L.D. Landau and E.M. Lifshitz. *Fluid Mechanics*. Robert Maxwell, M.C., 1986. 2, 11, 125

[86] Leonid Levitov and Gregory Falkovich. Electron viscosity, current vortices and negative nonlocal resistance in graphene. *Nature Physics*, 2016. xvii, 4, 59, 133

[87] Q. Li, K. H. Luo, and X. J. Li. Lattice boltzmann method for relativistic hydrodynamics: Issues on conservation law of particle number and discontinuities. *Phys. Rev. D*, 86:085044, Oct 2012. 120, 139

[88] S. Lowell, J.E. Shields, M.A. Thomas, and M. Thommes. *Characterization of Porous Solids and Powders: Surface Area, Pore Size and Density*. Particle Technology Series. Springer Netherlands, 2012. 24

[89] Andrew Lucas, Richard A. Davison, and Subir Sachdev. Hydrodynamic theory of thermoelectric transport and negative magnetoresistance in weyl semimetals. *Proceedings of the National Academy of Sciences*, 113(34):9463–9468, 2016. 59, 139

[90] Li-Shi Luo. Theory of the lattice boltzmann method: Lattice boltzmann models for nonideal gases. *Phys. Rev. E*, 62:4982–4996, Oct 2000. 80, 81

[91] Nicos S. Martys and Hudong Chen. Simulation of multicomponent fluids in complex three-dimensional geometries by the lattice boltzmann method. *Phys. Rev. E*, 53:743–750, Jan 1996. 80

[92] Federico Massaioli and Giorgio Amati. Achieving high performance in a lbm code using openmp. In *The Fourth European Workshop on OpenMP, Roma*, 2002. 14

[93] Maciej Matyka and Zbigniew Koza. How to calculate tortuosity easily? *AIP Conference Proceedings*, 1453(1), 2012. 26

[94] Guy R. McNamara and Gianluigi Zanetti. Use of the boltzmann equation to simulate lattice-gas automata. *Phys. Rev. Lett.*, 61:2332–2335, Nov 1988. 14

[95] Renwei Mei, Li-Shi Luo, Pierre Lallemand, and Dominique dâHumières. Consistent initial conditions for lattice boltzmann simulations. *Computers & Fluids*, 35(8):855–862, 2006. 114, 115

[96] M. Mendoza, B. M. Boghosian, H. J. Herrmann, and S. Succi. Fast lattice boltzmann solver for relativistic hydrodynamics. *Phys. Rev. Lett.*, 105:014502, Jun 2010. 9, 10, 14, 32, 98

[97] M. Mendoza, H. J. Herrmann, and S. Succi. Preturbulent regimes in graphene flow. *Phys. Rev. Lett.*, 106:156601, Apr 2011. 10, 59, 125, 130

[98] M Mendoza, HJ Herrmann, and S Succi. Hydrodynamic model for conductivity in graphene. *Scientific reports*, 3, 2013. 10, 130

[99] M. Mendoza, I. Karlin, S. Succi, and H. J. Herrmann. Relativistic lattice boltzmann model with improved dissipation. *Phys. Rev. D*, 87:065027, Mar 2013. 10, 59, 98, 99, 100, 110, 112, 124, 127, 138

[100] M Mendoza, I Karlin, S Succi, and H J Herrmann. Ultrarelativistic transport coefficients in two dimensions. *Journal of Statistical Mechanics: Theory and Experiment*, 2013(02):P02036, 2013. 99, 116, 118, 124, 127, 138

[101] A. A. Mohamad. *Lattice Boltzmann Method*. Springer-Verlag, 2011. 7

[102] F. Mohseni, M. Mendoza, S. Succi, and H. J. Herrmann. Lattice boltzmann model for resistive relativistic magnetohydrodynamics. *Phys. Rev. E*, 92:023309, Aug 2015. 99, 124

[103] Philip J. W. Moll, Pallavi Kushwaha, Nabhanila Nandi, Burkhard Schmidt, and Andrew P. Mackenzie. Evidence for hydrodynamic electron flow in pdcoo2. *Science*, 351(6277):1061–1064, 2016. 59, 139

[104] V. Mourzenko, J.-F. Thovert, O. Vizika, and P. M. Adler. Geometrical and transport properties of random packings of polydisperse spheres. *Phys. Rev. E*, 77:066306, Jun 2008. 23

[105] Markus Müller, Lars Fritz, and Subir Sachdev. Quantum-critical relativistic magnetotransport in graphene. *Phys. Rev. B*, 78:115406, Sep 2008. 5

[106] Markus Müller, Jörg Schmalian, and Lars Fritz. Graphene: A nearly perfect fluid. *Phys. Rev. Lett.*, 103:025301, Jul 2009. 3, 98

[107] Kunji Nakayama. The richardson criterion for relativistic swirling flows. *Publications of the Astronomical Society of Japan*, 42:331–339, 1990. 128

[108] B. N. Narozhny, I. V. Gornyi, M. Titov, M. Schütt, and A. D. Mirlin. Hydrodynamics in graphene: Linear-response transport. *Phys. Rev. B*, 91:035414, Jan 2015. 5

[109] B. N. Narozhny, M. Titov, I. V. Gornyi, and P. M. Ostrovsky. Coulomb drag in graphene: Perturbation theory. *Phys. Rev. B*, 85:195421, May 2012. 5

[110] Boris N Narozhny, Igor V Gornyi, Alexander D Mirlin, and Jörg Schmalian. Hydrodynamic approach to electronic transport in graphene. *Annalen der Physik*, 2017. 3, 5, 59

[111] K. S. Novoselov, A. K. Geim, S. V. Morozov, D. Jiang, Y. Zhang, S. V. Dubonos, I. V. Grigorieva, and A. A. Firsov. Electric field effect in atomically thin carbon films. *Science*, 306(5696):666–669, 2004. 3, 98

[112] Kostya S Novoselov, Andre K Geim, SVb Morozov, Da Jiang, MIc Katsnelson, IVa Grigorieva, SVb Dubonos, and AAb Firsov. Two-dimensional gas of massless dirac fermions in graphene. *nature*, 438(7065):197–200, 2005. 3, 98

[113] D. Oettinger, M. Mendoza, and H. J. Herrmann. Gaussian quadrature and lattice discretization of the fermi-dirac distribution for graphene. *Phys. Rev. E*, 88:013302, Jul 2013. 10, 56, 59, 98, 99, 125

[114] Jean-Yves Ollitrault. Anisotropy as a signature of transverse collective flow. *Phys. Rev. D*, 46:229–245, Jul 1992. 98

[115] S. Palpacelli, S. Succi, and R. Spigler. Ground-state computation of bose-einstein condensates by an imaginary-time quantum lattice boltzmann scheme. *Phys. Rev. E*, 76:036712, Sep 2007. 6

[116] Silvia Palpacelli and Sauro Succi. The quantum lattice boltzmann equation: recent developments. *Communications in Computational Physics*, 4(5):980–1007, 2008. 6

[117] Chongxun Pan, Li shi Luo, and Cass T. Miller. An evaluation of lattice boltzmann schemes for porous medium flow simulation, 2006. 15

[118] R.K. Pathria and P.D. Beale. *Statistical Mechanics*. Academic Press, Boston, third edition edition, 2011. 54

[119] Francesco M. D. Pellegrino, Iacopo Torre, Andre K. Geim, and Marco Polini. Electron hydrodynamics dilemma: Whirlpools or no whirlpools. *Phys. Rev. B*, 94:155414, Oct 2016. 4, 59, 133

[120] Manuel Perucho, Michał Hanasz, Jose-Maria Martí, and Helene Sol. Stability of hydrodynamical relativistic planar jets-i. linear evolution and saturation of kelvin-helmholtz modes. *Astronomy & Astrophysics*, 427(2):415–429, 2004. 124

[121] Paulo C. Philippi, Luiz A. Hegele, Luís O. E. dos Santos, and Rodrigo Surmas. From the continuous to the lattice boltzmann equation: The discretization problem and thermal models. *Phys. Rev. E*, 73:056702, May 2006. 7, 31, 57

[122] William H Press, Saul A Teukolsky, William T Vetterling, and Brian P Flannery. Numerical recipes in c++. *The art of scientific computing*, 2015. 90

[123] Alessandro Principi, Giovanni Vignale, Matteo Carrega, and Marco Polini. Bulk and shear viscosities of the two-dimensional electron liquid in a doped graphene sheet. *Phys. Rev. B*, 93:125410, Mar 2016. 5

[124] Bing Ren, Hongjie Wen, Ping Dong, and Yongxue Wang. Improved {SPH} simulation of wave motions and turbulent flows through porous media. *Coastal Engineering*, 107:14 – 27, 2016. 28

[125] P. Romatschke, M. Mendoza, and S. Succi. Fully relativistic lattice boltzmann algorithm. *Phys. Rev. C*, 84:034903, Sep 2011. 10, 98, 120

[126] JÃ¼rgen Schukraft, Anthony Timmins, and Sergei A. Voloshin. Ultra-relativistic nuclear collisions: Event shape engineering. *Physics Letters B*, 719(4):394 – 398, 2013. 98

[127] V. K. Senecha, A. V. Brantov, V. Yu. Bychenkov, and V. T. Tikhonchuk. Temperature relaxation in hot spots in a laser-produced plasma. *Phys. Rev. E*, 57:978–981, Jan 1998. 118

[128] Xiaowen Shan and Hudong Chen. A general multiple-relaxation-time boltzmann collision model. *International Journal of Modern Physics C*, 18(04):635–643, 2007. 139

[129] A. E SHEIDEGGER. *The Physics of Flow through Porous Media*. Univ.Toronto Press, 3 ed edition, 1974. 17

[130] Yu-Hsin Shi and J.Y. Yang. A gas-kinetic {BGK} scheme for semiclassical boltzmann hydrodynamic transport. *Journal of Computational Physics*, 227(22):9389 – 9407, 2008. 2, 59, 137

[131] Steven N Shore. *An introduction to astrophysical hydrodynamics.* Academic Press, 2012. 97

[132] Panayiotis D. Siafarikas. Preface. *Journal of Computational and Applied Mathematics*, 133(1â2):xiii – xiv, 2001. 5th Int. Symp. on Orthogonal Polynomials, Special Functions and their Applications. 29

[133] V. Skakalova and A.B. Kaiser. *Graphene: Properties, Preparation, Characterisation and Devices.* Woodhead Publishing Series in Electronic and Optical Materials. Elsevier Science, 2014. 4, 59

[134] William D. Smyth and James N. Moum. Ocean mixing by kelvin-helmholtz instability. *Oceanography*, 25:140–149, June 2012. 123, 133

[135] Sergio Solorzano, Miller Mendoza, Sauro Succi, and Hans Herrmann. Lattice wigner equation. *arXiv preprint arXiv:1709.05934*, 2017. 6

[136] S. Succi. *The Lattice Boltzmann Equation for Fluid Dynamics and Beyond.* Clarendon Press, 2001. 6, 31, 59, 98

[137] M. Sukop and D. Thorne. *Lattice Boltzmann Modeling.* Springer-Verlag, 2006. 80

[138] Sirikalaya Suvachittanont, Chikao Kanaoka, Akihiro Tsuchinari, and Wiwut Tanthapanichakoon. Measurement of the specific surface area of porous media through pressure drop. *Advanced Powder Technology*, 7(2):91 – 99, 1996. 24

[139] Gabor Szegö. *Orthonormal Polynomials.* American Mathematical Society, Fourth Edition, 1975. 29

[140] Derek A Teaney. Viscous hydrodynamics and the quark gluon plasma. *Quark-gluon plasma*, 4:207, 2009. 10, 98

[141] K. Theilhaber and C. K. Birdsall. Kelvin-helmholtz vortex formation and particle transport in a cross-field plasma sheath. *Phys. Rev. Lett.*, 62:772–775, Feb 1989. 123, 133

[142] F. V. Tikhonenko, A. A. Kozikov, A. K. Savchenko, and R. V. Gorbachev. Transition between electron localization and antilocalization in graphene. *Phys. Rev. Lett.*, 103:226801, Nov 2009. 4, 59

[143] Jonas Tölke and Manfred Krafczyk. Teraflop computing on a desktop pc with gpus for 3d cfd. *International Journal of Computational Fluid Dynamics*, 22(7):443–456, 2008. 15

[144] E.F. Toro. *Riemann Solvers and Numerical Methods for Fluid Dynamics: A Practical Introduction.* Springer Berlin Heidelberg, 2009. 91, 112

[145] Iacopo Torre, Andrea Tomadin, Andre K. Geim, and Marco Polini. Nonlocal transport and the hydrodynamic shear viscosity in graphene. *Phys. Rev. B*, 92:165433, Oct 2015. 4, 59, 133

[146] Iacopo Torre, Andrea Tomadin, Roman Krahne, Vittorio Pellegrini, and Marco Polini. Electrical plasmon detection in graphene waveguides. *Phys. Rev. B*, 91:081402, Feb 2015. 134

[147] Kyosuke Tsumura, Yuta Kikuchi, and Teiji Kunihiro. Relativistic causal hydrodynamics derived from boltzmann equation: A novel reduction theoretical approach. *Phys. Rev. D*, 92:085048, Oct 2015. 99

[148] Kyosuke Tsumura and Teiji Kunihiro. Derivation of relativistic hydrodynamic equations consistent with relativistic boltzmann equation by renormalization-group method. *The European Physical Journal A*, 48(11):162, Nov 2012. 99

[149] E. A. Uehling and G. E. Uhlenbeck. Transport phenomena in einstein-bose and fermi-dirac gases. i. *Phys. Rev.*, 43:552–561, Apr 1933. 2

[150] T.O. Wehling, A.M. Black-Schaffer, and A.V. Balatsky. Dirac materials. *Advances in Physics*, 63(1):1–76, 2014. 98, 139

[151] Stephen Whitaker. Flow in porous media i: A theoretical derivation of darcy's law. *Transport in porous media*, 1(1):3–25, 1986. 18

[152] J. Wu and C. Shu. A solution-adaptive lattice boltzmann method for two-dimensional incompressible viscous flows. *Journal of Computational Physics*, 230(6):2246 – 2269, 2011. 115

[153] A. Wünsche. Hermite and laguerre 2d polynomials. *Journal of Computational and Applied Mathematics*, 133(1):665–678, 2001. 31

[154] A. Wünsche. Generating functions for products of special laguerre 2d and hermite 2d polynomials. *Applied Mathematics*, 6(1):2142–2168, 2015. 31

[155] P. F. Wyper and D. I. Pontin. Kelvin-helmholtz instability in a current-vortex sheet at a 3d magnetic null. *Physics of Plasmas*, 20(3):032117, 2013. 123, 133

[156] Peng Xu and Boming Yu. Developing a new form of permeability and kozenyâcarman constant for homogeneous porous media by means of fractal geometry. *Advances in Water Resources*, 31(1):74 – 81, 2008. 14, 19, 23

[157] Jaw-Yen Yang and Li-Hsin Hung. Lattice uehling-uhlenbeck boltzmann-bhatnagar-gross-krook hydrodynamics of quantum gases. *Phys. Rev. E*, 79:056708, May 2009. 2, 6, 59, 98, 137

[158] K. Yazdchi, S. Srivastava, and S. Luding. *On the validity of the Carman-Kozeny equation in random fibrous media*. Eccomas, 2011. 23

[159] Dazhi Yu, Renwei Mei, Li-Shi Luo, and Wei Shyy. Viscous flow computations with the method of lattice boltzmann equation. *Progress in Aerospace Sciences*, 39(5):329 – 367, 2003. 115

Appendix A

Tensorial identities involving the I_N

Here we obtain especial formulas derived from the definition of the I_N's given in Eq.(3.10) and obtained from tensorial contractions of the tensor $\xi_{i_1} \cdots \xi_{i_N}$, and, consequently, from the $\delta_{i_1 \cdots i_N}$.

$$\int d^D \boldsymbol{\xi}\, \omega(\boldsymbol{\xi}) = I_0, \qquad\qquad \int d^D \boldsymbol{\xi}\, \omega(\boldsymbol{\xi})\, \xi_{i_1}\xi_{j_1} = I_2\, \delta_{i_1 j_1},$$

$$\int d^D \boldsymbol{\xi}\, \omega(\boldsymbol{\xi})\, \xi^2 = D\, I_2. \qquad\qquad \int d^D \boldsymbol{\xi}\, \omega(\boldsymbol{\xi})\, \xi_{i_1}\xi_{i_2}\xi_{j_1}\xi_{j_2} = I_4\, \delta_{i_1 j_1 i_2 j_2},$$

$$\int d^D \boldsymbol{\xi}\, \omega(\boldsymbol{\xi})\, \xi_{i_1}\xi_{i_2}\xi^2 = (D+2)I_4\, \delta_{i_1 j_1}, \quad \int d^D \boldsymbol{\xi}\, \omega(\boldsymbol{\xi})\, \xi^4 = (D+2)DI_4. \tag{A.1}$$

$$\int d^D \boldsymbol{\xi}\, \omega(\boldsymbol{\xi})\, \xi_{i_1}\xi_{i_2}\xi_{i_3}\xi_{j_1}\xi_{j_2}\xi_{j_3} = I_6\, \delta_{i_1 j_1 i_2 j_2 i_3 j_3},$$

$$\int d^D \boldsymbol{\xi}\, \omega(\boldsymbol{\xi})\, \xi_{i_1}\xi_{i_2}\xi_{j_1}\xi_{j_2}\xi^2 = (D+4)I_6\, \delta_{i_1 j_1 i_2 j_2}, \tag{A.2}$$

$$\int d^D \boldsymbol{\xi}\, \omega(\boldsymbol{\xi})\, \xi_{i_1}\xi_{i_2}\xi^4 = (D+4)(D+2)I_6\, \delta_{i_1 j_1}, \tag{A.3}$$

$$\int d^D \boldsymbol{\xi}\, \omega(\boldsymbol{\xi})\, \xi^4 = (D+4)(D+2)DI_6. \tag{A.4}$$

$$\int d^D \boldsymbol{\xi}\, \omega(\boldsymbol{\xi})\, \xi_{i_1}\xi_{i_2}\xi_{i_3}\xi_{i_4}\xi_{j_1}\xi_{j_2}\xi_{j_3}\xi_{j_4} = I_8\, \delta_{i_1 j_1 i_2 j_2 i_3 j_3 i_4 j_4},$$

$$\int d^D \boldsymbol{\xi}\, \omega(\boldsymbol{\xi})\, \xi_{i_1}\xi_{i_2}\xi_{i_3}\xi_{j_1}\xi_{j_2}\xi_{j_3}\xi^2 = (D+6)I_8\, \delta_{i_1 j_1 i_2 j_2 i_3 j_3},$$

$$\int d^D \boldsymbol{\xi}\, \omega(\boldsymbol{\xi})\, \xi_{i_1}\xi_{i_2}\xi_{j_1}\xi_{j_2}\xi^4 = (D+6)(D+4)I_8\, \delta_{i_1 j_1 i_2 j_2},$$

$$\int d^D \boldsymbol{\xi}\, \omega(\boldsymbol{\xi})\, \xi_{i_1}\xi_{j_1}\xi^6 = (D+6)(D+4)(D+2)I_8\, \delta_{i_1 j_1},$$

$$\int d^D \boldsymbol{\xi}\, \omega(\boldsymbol{\xi})\, \xi^8 = (D+6)(D+4)(D+2)DI_8. \tag{A.5}$$

Appendix B

Quadratures for the semiclassical LBM

In Table (B.1) we show more quadratures for the semiclassical LBM in 1D, 2D and 3D. The expressions for the D1V7 lattice can be found below.

The lattice D1V7 can be used in models with higher orders EDF expansions sin it has order $M = 9$. The geometrical velocities are $\{e_0, e_1, e_2, e_3, e_4, e_5, e_6\} = \{0, +1, -1, +2, -2, +3, -3\}$, and the weight are w_0 for α=0, w_1 for $\alpha = 1$ and 2, w_2 for $\alpha = 3$ and 4 and w_3 for $\alpha = 5$ and 6. Quadrature equations satisfied by the D1V7 lattice:

$$\sum_\alpha w_\alpha = I_0 \Rightarrow w_0 + 2w_1 + 2w_2 + 2w_3 = I_0$$

$$\sum_\alpha w_\alpha e_\alpha^2 = I_2 c_s^2 \Rightarrow 2w_1 + 8w_2 + 18w_3 = I_2 c_s^2$$

$$\sum_\alpha w_\alpha e_\alpha^4 = 3I_4 c_s^4$$

$$\Rightarrow 2w_1 + 32w_2 + 162w_3 = 3I_4 c_s^4$$

$$\sum_\alpha w_\alpha e_\alpha^6 = 15I_6 c_s^6$$

$$\Rightarrow 2w_1 + 128w_2 + 1458w_3 = 15I_6 c_s^6$$

$$\sum_{\alpha} w_{\alpha} e_{\alpha}^8 = 105 I_8 c_s^8$$

$$\Rightarrow 2w_1 + 512w_2 + 13122w_3 = 105 I_8 c_s^8$$

Solutions:

$$w_0 = \frac{1}{360}(360 I_0 - 150 I_6 c_s^6 + 420 I_4 c_s^4 - 490 I_2 c_s^2)$$

$$w_1 = \frac{1}{16}(-13 I_4 c_s^4 + 5 I_6 c_s^6 + 12 I_2 c_s^2)$$

$$w_2 = \frac{1}{120}(30 I_4 c_s^4 - 15 I_6 c_s^6 - 9 I_2 c_s^2)$$

$$w_3 = \frac{1}{720}(15 I_6 c_s^6 - 15 I_4 c_s^4 + 4 I_2 c_s^2)$$

There are six solutions for c_s, which can be found by solving the equation

$$12 I_2 - 49 I_4 c_s^2 + 70 I_6 c_s^4 - 35 I_8 c_s^6 = 0.$$

One of them is:

$$c_s = \left\{ \frac{2}{3} \frac{I_6}{I_8} - \frac{49 \, 2^{1/3} I_4}{(B + \sqrt{4A^3 + B^2})^{1/3}} \right.$$

$$\left. + \frac{140 \, 2^{1/3} I_6^2}{3 I_8 (B + \sqrt{4A^3 + B^2})^{1/3}} + \frac{(B + \sqrt{4A^3 + B^2})^{1/3}}{105 \, 2^{1/3} I_8} \right\}^{1/2}$$

where

$$A = -4900 I_6^2 + 5145 I_4 I_8$$

$$B = 686000 I_6^3 - 1080450 I_4 I_6 I_8 + 396900 I_2 I_8^2$$

Lattice	M	$\boldsymbol{e_\alpha}$	p	w_α	c_s
D1V3	5	0	1	$I_0(1 - J_2/3)$	$\sqrt{\dfrac{I_2}{3I_4}}$
		± 1	2	$I_0 J_2/6$	
D1V5	7	0	1	$I_0 - 10I_2 c_s^2/9 + I_4 c_s^4/3$	
(a and b)		± 1	2	$9I_2 c_s^2/16 - 3I_4 c_s^4/16$	$\sqrt{\dfrac{10I_4 \pm \sqrt{100I_4^2 - 60I_6 I_2}}{10I_6}}$
		± 3	2	$3I_4 c_s^4/144 - I_2 c_s^2/144$	
D2V6	3	$\left(\cos\frac{2\pi n}{6}, \sin\frac{2\pi n}{6}\right)$	6	$I_0/6$	$\sqrt{\dfrac{I_0}{2I_2}}$
D2V9	5	$(0,0)$	1	$I_0(1 - 5J_2/9)$	
		$(1,0)_{FS}$	4	$I_0 J_2/9$	$\sqrt{\dfrac{I_2}{3I_4}}$
		$(1,1)_{FS}$	4	$I_0 J_2/36$	
D3V15	5	$(0,0,0)$	1	$I_0(1 - 7J_2/9)$	
		$(1,0,0)_{FS}$	6	$I_0 J_2/9$	$\sqrt{\dfrac{I_2}{3I_4}}$
		$(1,1,1)_{FS}$	8	$I_0 J_2/72$	
D3V19	5	$(0,0,0)$	1	$I_0(1 - 2J_2/3)$	
		$(1,0,0)_{FS}$	6	$I_0 J_2/18$	$\sqrt{\dfrac{I_2}{3I_4}}$
		$(1,1,0)_{FS}$	12	$I_0 J_2/36$	
D3V27	5	$(0,0,0)$	1	$I_0 - 2I_2^2/(3I_4) - I_6 I_2^3/(27I_4^3)$	
		$(1,0,0)_{FS}$	6	$(3I_2^2 I_4^2 + I_6 I_2^3)/(54I_4^3)$	$\sqrt{\dfrac{I_2}{3I_4}}$
		$(1,1,0)_{FS}$	12	$(3I_4^2 I_2^2 - I_6 I_2^3)/(108I_4^3)$	
		$(1,1,1)_{FS}$	8	$I_2^3 I_6/(216I_4^3)$	

Table B.1: Generalized lattices and their weights. M is order of the quadrature (see Sec. 4.7) and p is the number of velocities with the same weight. The subscript FS denotes a fully symmetric set of points.

Appendix C

Integrals for the relativistic model

Here we show more details about the calculation of the integrals used in the EDF expansion, Eq.(5.10), which are laborious to solve analytically even using computer algorithms. Consider, for instance, the projection in the second order polynomial $P^{i_1 i_2}$,

$$A^{i_1 i_2} = \int \frac{d^2 p}{p^0} \frac{D_1 p^{i_1} p^{i_2} + [D_2 (p^0)^2 + D_3 p^0 + D_4]\delta^{i_1 i_2}}{z^{-1} e^{p^0 \gamma (1 - \mathbf{v} \cdot \mathbf{u})/\theta} + \xi}. \tag{C.1}$$

Because of the inner product $\mathbf{v} \cdot \mathbf{u}$ (where $\mathbf{v} = \mathbf{p}/|\mathbf{p}|$) in the exponential, the integration in separate spatial components is more complicated than in non-relativistic case. To solve this kind of integral we consider the integration of each monomial separately, which, in the example above, are $\{p^x p^x,\ p^x p^y,\ p^y p^y,\ (p^0)^2,\ p^0,\ 1\}$.

One can write $\mathbf{v} \cdot \mathbf{u} = u \cos(\phi - \alpha)$ where α is the angle between $\mathbf{u}$ and the x-axis and ϕ is the angle between $\mathbf{v}$ and the x-axis. Lets define a generic integral of f^{eq} as

$$I_1^{(mnq)} \equiv \int_0^{2\pi} \int_0^\infty dp d\beta \frac{p^m \sin^n(\beta) \cos^q(\beta)}{z^{-1} e^{p\gamma(1 - u\cos(\beta)/\theta)} + \xi},$$

where $\beta \equiv \phi - \alpha$. If n is odd, the integral is zero, but if n is even

$$I_1^{(mnq)} = 2 \int_0^\pi \int_0^\infty dp d\beta \frac{p^m \sin^n(\beta) \cos^q(\beta)}{z^{-1} e^{p\gamma(1 - u\cos(\beta)/\theta)} + \xi}.$$

Using the identity

$$\int_0^\infty dp \frac{p^m}{z^{-1} e^{py} + \xi} = y^{-(m+1)} \Gamma(m+1) g_{m+1}(z),$$

where $g_\nu(z)$ is defined in Eq.(5.12), and after some algebra, we find

$$I_1^{(mnq)} = \frac{2\theta^{m+1}}{\gamma^{m+1}u^{n+q}}\Gamma(m+1)g_{m+1}(z) \cdot \int_0^\pi dw[u^2 - (1-w)^2]^{(n-1)/2}\frac{(1-w)^q}{w^{m+1}}. \qquad (C.2)$$

The remaining integral can be solved exactly for given integers m, n and q. With this, we have separated the original integral of two variables in two non-dimensional integrals in one variable, including the EDF integral $g_\nu(z)$.

The Eq.(C.2) allows us to calculate projections of the EDFs in the monomials:

$$I_2^{mnq} \equiv \int \frac{d^2p}{p^0} \frac{p^m(p^x)^n(p^y)^q}{z^{-1}e^{p\gamma(1-\mathbf{v}\cdot\mathbf{u})/\theta} + \xi}.$$

As an example, lets consider the projection in the monomial $p^x p^x$,

$$I_2^{020} = \int \frac{d^2p}{p^0} \frac{(p^x)^2}{z^{-1}e^{p\gamma(1-\mathbf{v}\cdot\mathbf{u})/\theta} + \xi} = \int_0^{2\pi}\int_0^\infty dpd\phi \frac{(p\cos(\beta+\alpha))^2}{z^{-1}e^{p\gamma(1-u\cos(\beta))/\theta} + \xi}$$

Since

$$\cos^2(\alpha+\beta) = \frac{1}{2} + \frac{1}{2}\cos^2(\alpha)\cos^2(\beta)$$
$$-\frac{1}{2}\cos^2(\beta)\sin^2(\alpha) - 2\cos(\alpha)\sin(\alpha)\cos(\beta)\sin(\beta)$$
$$-\frac{1}{2}\cos^2(\alpha)\sin^2(\beta) + \frac{1}{2}\sin^2(\alpha)\sin^2(\beta),$$

and considering that the odd powers of $\sin(\beta)$ give null integrals, we write

$$I_2^{020} = \frac{1}{2}I_1^{(200)} + \frac{1}{2}(\cos^2(\alpha) - \sin^2(\alpha))(2I_1^{(202)} - I_1^{(200)}).$$

Thus, using Eq.(C.2), we have

$$I_2^{020} = 2\pi\theta^3 g_3(z)\gamma^2[(1-u^2) + 3u^x u^x].$$

And with the integrals I_2, one can calculate any projection of the EDF. Eq.(C.1), for instance, becomes for the A^{xx} component:

$$A^{xx} = D_1 I_2^{020} + D_2 I_2^{200} + D_3 I_2^{100} + D_4 I_2^{000}.$$

Below we see all the integrals needed to perform the fifth order expansion

$$I_2^{000} = 2\pi\theta g_1(z)$$

$$I_2^{100} = 2\pi\theta^2 g_2(z)\gamma$$

$$I_2^{200} = 2\pi\theta^3 g_3(z)(2 + u^2)\gamma^2$$

$$I_2^{300} = 6\pi\theta^4 g_4(z)(2 + 3u^2)\gamma^3$$

$$I_2^{400} = 6\pi(8 + 24u^2 + 3u^4)\theta^5 g_5(z)\gamma^4$$

$$I_2^{010} = 2\pi\theta^2 g_2(z)u^x\gamma$$

$$I_2^{020} = 2\pi\theta^3 g_3(z)(1 - u^2 + 3u^x u^x)\gamma^2$$

$$I_2^{030} = 6\pi\theta^4 g_4(z)(3(1 - u^2)u^x + 5(u^x)^3)\gamma^3$$

$$I_2^{040} = (6\pi(3 + 3u^4 + 30(u^x)^2 + 35(u^x)^4 - 6u^2(1 + 5(u^x)^2))\theta^5 g_5(z))\gamma^4$$

$$I_2^{001} = 2\pi\theta^2 g_2(z)u^y\gamma$$

$$I_2^{002} = 2\pi\theta^3 g_3(z)(1 - u^2 + 3u^y u^y)\gamma^2$$

$$I_2^{003} = 6\pi\theta^4 g_4(z)(3(1 - u^2)u^y + 5(u^y)^3)\gamma^3$$

$$I_2^{004} = ((6\pi(3 + 3u^4 + 30(u^y)^2 + 35(u^y)^4 - 6u^2(1 + 5(u^y)^2))\theta^5 g_5(z))\gamma^4)$$

$$I_2^{220} = 6\pi(4 - 3u^2 - u^4 + 5(u^x)^2(6 + u^2))\theta^5 g_5(z)\gamma^4$$

$$I_2^{120} = 6\pi\theta^4 g_4(z)((1 - u^2) + 5u^x u^x)\gamma^3$$

$$I_2^{202} = 6\pi(4 - 3u^2 - u^4 + 5(u^y)^2(6 + u^2))\theta^5 g_5(z)\gamma^4$$

$$I_2^{102} = 6\pi\theta^4 g_4(z)((1 - u^2) + 5u^y u^y)\gamma^3$$

$$I_2^{022} = (6\pi((1 - u^2) + 4(1 - u^2)u^2 + 35(u^x)^2(u^y)^2)\theta^5 g_5(z))\gamma^4$$

$$I_2^{031} = 30\pi\theta^5 g_5(z)(3(1 - u^2) + 7(u^x)^2)u^x u^y\gamma^4$$

$$I_2^{211} = 30\pi(6 + u^2)\theta^5 g_5(z)u^x u^y\gamma^4$$

$$I_2^{011} = 6\pi\theta^3 g_3(z)u^x u^y\gamma^2$$

$$I_2^{111} = 6\pi\theta^4 g_4(z)(5u^x u^y)\gamma^3$$

$$I_2^{130} = -30\pi u^x(-3 + 3u^2 - 7(u^x)^2)\theta^5 g_5(z)\gamma^4$$

$$I_2^{310} = 30\pi(4 + 3u^2)\theta^5 u^x g_5(z)\gamma^4$$

$$I_2^{110} = 6\pi\theta^3 g_3(z)u^x\gamma^2$$

$$I_2^{101} = 6\pi\theta^3 g_3(z)u^y\gamma^2$$

$$I_2^{013} = 30\pi\theta^5 g_5(z)(3(1 - u^2) + 7(u^y)^2)u^x u^y\gamma^4$$

$$I_2^{103} = -30\pi u^y(-3 + 3u^2 - 7(u^y)^2)\theta^5 g_5(z)\gamma^4$$

$$I_2^{121} = -30\pi(-1 + u^2 - 7(u^x)^2)u^y\theta^5 g_5(z)\gamma^4$$

$$I_2^{201} = 6\pi\theta^4 g_4(z)(4 + u^2)u^y\gamma^3$$

$$I_2^{301} = 30\pi(4 + 3u^2)\theta^5 u^y g_5(z)\gamma^4$$

$$I_2^{021} = 6\pi\theta^4 g_4(z)((1 - u^2) + 5u^x u^x)u^y\gamma^3$$

$$I_2^{112} = -30\pi(-1 + u^2 - 7(u^y)^2)u^x\theta^5 g_5(z)\gamma^4$$

$$I_2^{210} = 6\pi\theta^4 g_4(z)(4 + u^2)u^x\gamma^3$$

$$I_2^{012} = 6\pi\theta^4 g_4(z)((1 - u^2) + 5u^y u^y)u^x\gamma^3$$

$$I_2^{050} = 30\pi u^x(15(1 - u^2)^2 + 70(u^x)^2(1 - u^2) + 63(u^x)^4)\theta^6 g_6(z)\gamma^5$$

$$I_2^{005} = 30\pi u^y(15(1 - u^2)^2 + 70(u^y)^2(1 - u^2) + 63(u^y)^4)\theta^6 g_6(z)\gamma^5$$

$$I_2^{500} = 30\pi(8 + 40u^2 + 15u^4)\theta^6 g_6(z)\gamma^5$$

$$I_2^{230} = 30\pi u^x(18 - 3u^4 + 56(u^x)^2 + u^2(-15 + 7(u^x)^2))\theta^6 g_6(z)\gamma^5$$

$$I_2^{203} = 30\pi u^y(18 - 3u^4 + 56(u^y)^2 + u^2(-15 + 7(u^y)^2))\theta^6 g_6(z)\gamma^5$$

$$I_2^{041} = 90\pi((1 - u^2)^2 + 14(u^x)^2(1 - u^2) + 21(u^x)^4)u^y\theta^6 g_6(z)\gamma^5$$

$$I_2^{221} = -30\pi(-6(1 - u^2) - u^2(1 - u^2) - 56(u^x)^2 + u^2(-7(u^x)^2))u^y\theta^6 g_6(z)\gamma^5$$

$$I_2^{014} = 90\pi((1 - u^2)^2 + 14(u^y)^2(1 - u^2) + 21(u^y)^4)u^x\theta^6 g_6(z)\gamma^5$$

$$I_2^{032} = -30\pi u^x((u^x)^2(-1 + 4u^2 - 63(u^y)^2) + 3(-1 + (-5 + 6u^2)(u^y)^2))\theta^6 g_6(z)\gamma^5$$

$$I_2^{212} = -30\pi(-6(1 - u^2) - u^2(1 - u^2) - 56(u^y)^2 + u^2(-7(u^y)^2))u^x\theta^6 g_6(z)\gamma^5$$

$$I_2^{410} = 90\pi u^x(8 + 12u^2 + u^4)\theta^6 g_6(z)\gamma^5$$

$$I_2^{023} = -30\pi u^y((u^y)^2(-1 + 4u^2 - 63(u^x)^2) + 3(-1 + (-5 + 6u^2)(u^x)^2))\theta^6 g_6(z)\gamma^5$$

$$I_2^{401} = 90\pi u^y(8 + 12u^2 + u^4)\theta^6 g_6(z)\gamma^5$$

$$I_2^{140} = 90\pi((1 - u^2)^2 + 14(u^x)^2(1 - u^2) + 21(u^x)^4)\theta^6 g_6(z)\gamma^5$$

$$I_2^{320} = -30\pi(-4(1 - u^2) - 3u^2(1 - u^2) - 42(u^x)^2 + u^2(-21(u^x)^2))\theta^6 g_6(z)\gamma^5$$

$$I_2^{104} = 90\pi((1 - u^2)^2 + 14(u^y)^2(1 - u^2) + 21(u^y)^4)\theta^6 g_6(z)\gamma^5$$

$$I_2^{302} = -30\pi(-4(1 - u^2) - 3u^2(1 - u^2) - 42(u^y)^2 + u^2(-21(u^y)^2))\theta^6 g_6(z)\gamma^5$$

$$I_2^{122} = -30\pi(-1 + u^2 - 6u^2(1 - u^2) - 63(u^x)^2(u^y)^2)\theta^6 g_6(z)\gamma^5$$

$$I_2^{131} = -630\pi u^x(-1 + u^2 - 3(u^x)^2)u^y\theta^6 g_6(z)\gamma^5$$

$$I_2^{311} = 315\pi(2 + u^2)\theta^6 g_6(z)2u^x u^y\gamma^5$$

$$I_2^{113} = -630\pi u^y(-1 + u^2 - 3(u^y)^2)u^x\theta^6 g_6(z)\gamma^5$$

Appendix D

Fifth order expansion of the relativistic Fermi-Dirac distribution

In this appendix, we show the expansion of the relativistic Fermi-Dirac distribution up to fifth order in orthogonal polynomials, which was used in Chaps. 5 and 6. The expansions of the MJ and BE distributions is given in the Supplemental Material[1].. To perform the expansion, we introduce some non-dimensional variables: $\theta = T/T_0$, $\mathbf{p} = \bar{\mathbf{p}}/T_0$ and $\mu = \bar{\mu}/T_0$, where T_0 is the initial temperature, and the Fermi-Dirac distribution becomes:

$$f_{FD}^{eq} = \frac{1}{z^{-1} \exp\left[p^0\gamma(1 - \mathbf{v} \cdot \mathbf{u})/\theta\right] + 1}, \tag{D.1}$$

where $z = e^{\frac{\mu}{\theta}}$ is the fugacity. The expansion up to fifth order is given by:

$$f^{eq} = \frac{n}{2\pi g_2(z)\theta^2}\,\omega(\xi)\left[\sum_{N=0}^{5}\frac{1}{N!}A^{i_1\ldots i_N}P^{i_1\ldots i_N} + \sum_{M=0}^{4}\frac{1}{M!}A^{i_1\ldots i_M 0}P^{i_1\ldots i_M 0}\right], \tag{D.2}$$

where Fermi-Dirac integral is

$$g_\nu(z) = \frac{1}{\Gamma(\nu)}\int_0^\infty \frac{x^{\nu-1}\,dx}{z^{-1}e^x \pm 1}, \tag{D.3}$$

and the projections of the EDF on the polynomials are

$$A^{\mu_1\mu_2\cdots\mu_N} = \int \frac{d^2\mathbf{p}}{p^0}\,f^{eq}P^{\mu_1\mu_2\cdots\mu_N}. \tag{D.4}$$

---

[1]Download the Supplemental Material together with the source files at arXiv: `https://arxiv.org/e-print/1709.09073`

Note that we divide the density n by a normalization factor $2\pi\theta^2 g_2(z)$, since $\int \frac{d^2 p}{p^0} p^\alpha f_{FD}^{eq} = 2\pi\theta^2 g_2(z) U^\alpha = nU^\alpha$. See below the terms of the expansion.

$$AP = 2A_1^2 g_1(z)\pi\theta$$

$$A^{i_1} P^{i_1} = 2B_1^2 (p^x u^x + p^y u^y) g_2(z)\gamma\pi\theta^2$$

$$A^0 P^0 = 2\pi\theta (C_2 g_1(z) + C_1 g_2(z)\gamma\theta)(C_2 + C_1 p)$$

$$
\begin{aligned}
A^{i_1 i_2} P^{i_1 i_2} = {}& 2\pi\theta((D_4 g_1(z) + \gamma\theta(D_3 g_2(z) + g_3(z)\gamma(D_1 + 2D_2 \\
& + (2D_1 + D_2)(u^x)^2 + (-D_1 + D_2)(u^y)^2)\theta))(D_4 + D_3 p + D_2 p^2 \\
& + D_1(p^x)^2) + 6D_1^2 g_3(z)\gamma^2 u^x u^y \theta^2 p^x p^y + (D_4 g_1(z) + \gamma\theta(D_3 g_2(z) \\
& + g_3(z)\gamma(D_1 + 2D_2 + (-D_1 + D_2)(u^x)^2 + (2D_1 + D_2)(u^y)^2)\theta)) \\
& (D_4 + D_3 p + D_2 p^2 + D_1(p^y)^2))
\end{aligned}
$$

$$A^{i_1 0} P^{i_1 0} = 2(p^x u^x + p^y u^y)\gamma\pi\theta^2 (E_2 g_2(z) + 3E_1 g_3(z)\gamma\theta)(E_2 + E_1 p)$$

$$
\begin{aligned}
A^{i_1 i_2 i_3} P^{i_1 i_2 i_3} = {}& 6\gamma\pi\theta^2 (u^x (F_4 g_2(z) + \gamma\theta(3F_3 g_3(z) + g_4(z)\gamma(F_1(3 \\
& + 2(u^x)^2 - 3(u^y)^2) + 3F_2(4 + u^2))\theta))p^x (3F_4 + 3F_3 p + 3F_2 p^2 \\
& + F_1(p^x)^2) + u^y (F_4 g_2(z) + 3\gamma\theta(F_3 g_3(z) + g_4(z)\gamma(F_1 + 4F_2 + (4F_1 \\
& + F_2)(u^x)^2 + (-F_1 + F_2)(u^y)^2)\theta))(F_4 + F_3 p + F_2 p^2 + F_1(p^x)^2)p^y \\
& + u^x (F_4 g_2(z) + 3\gamma\theta(F_3 g_3(z) + g_4(z)\gamma(F_1 + 4F_2 + (-F_1 + F_2)(u^x)^2 \\
& + (4F_1 + F_2)(u^y)^2)\theta))p^x (F_4 + F_3 p + F_2 p^2 + F_1(p^y)^2) + u^y (F_4 g_2(z) \\
& + \gamma\theta(3F_3 g_3(z) + g_4(z)\gamma(3F_2(4 + u^2) + F_1(3 - 3(u^x)^2 \\
& + 2(u^y)^2))\theta))p^y (3F_4 + 3F_3 p + 3F_2 p^2 + F_1(p^y)^2))
\end{aligned}
$$

$$
\begin{aligned}
A^{i_1 i_2 0} P^{i_1 i_2 0} = {}& 2\pi\theta((g_1(z)G_6 + \gamma\theta(g_2(z)G_5 + \gamma\theta(G_2 g_3(z)(1 + 2(u^x)^2 \\
& - (u^y)^2) + g_3(z)G_4(2 + u^2) + 3g_4(z)\gamma(G_1 + 2G_3 + (4G_1 + 3G_3)(u^x)^2 \\
& + (-G_1 + 3G_3)(u^y)^2)\theta)))(G_6 + G_5 p + G_4 p^2 + G_3 p^3 + G_2(p^x)^2 \\
& + G_1 p(p^x)^2) + 6\gamma^2 u^y \theta^2 (G_2 g_3(z) + 5G_1 g_4(z)\gamma\theta)(G_2 + G_1 p)p^y((p^x u^x \\
& + p^y u^y) - u^y p^y) + (g_1(z)G_6 + g_2(z)G_5\gamma\theta + g_3(z)G_4\gamma^2(2 + u^2)\theta^2 \\
& + G_2 g_3(z)\gamma^2 (1 - (u^x)^2 + 2(u^y)^2)\theta^2 + 3G_3 g_4(z)\gamma^3(2 + 3u^2)\theta^3 \\
& - 3G_1 g_4(z)\gamma^3 (-1 + (u^x)^2 - 4(u^y)^2)\theta^3)(G_6 + G_5 p + G_4 p^2 + G_3 p^3 \\
& + G_2(p^y)^2 + G_1 p(p^y)^2))
\end{aligned}
$$

$$A^{i_1i_2i_3i_4}P^{i_1i_2i_3i_4} = 6\pi\theta((g_1(z)H_9 + g_2(z)\gamma H_8\theta + g_3(z)\gamma^2 H_7(2$$
$$+u^2)\theta^2 + 2g_3(z)\gamma^2 H_4(1 + 2(u^x)^2 - (u^y)^2)\theta^2 + 3g_4(z)\gamma^3 H_6(2$$
$$+3u^2)\theta^3 + 6g_4(z)\gamma^3 H_3(1 + 4(u^x)^2 - (u^y)^2)\theta^3 + 3g_5(z)\gamma^4 H_5(8$$
$$+24u^2 + 3u^4)\theta^4 + 6g_5(z)\gamma^4 H_2(4 - 3u^2 - u^4 + 5(6 + u^2)(u^x)^2)\theta^4$$
$$+g_5(z)\gamma^4 H_1(3 + 3u^4 + 30(u^x)^2 + 35(u^x)^4 - 6u^2(1 + 5(u^x)^2))\theta^4)$$
$$(3(H_9 + p(H_8 + p(H_7 + p(H_6 + H_5p)))) + 6(H_4 + p(H_3$$
$$+H_2p))(p^x)^2 + H_1(p^x)^4) + 4\gamma^2 u^x u^y\theta^2(3g_3(z)H_4 + 5\gamma\theta(3g_4(z)H_3$$
$$+g_5(z)\gamma(H_1(3 + 4(u^x)^2 - 3(u^y)^2) + 3H_2(6 + u^2))\theta))p^x(3H_4$$
$$+3H_3p + 3H_2p^2 + H_1(p^x)^2)p^y + 4\gamma^2 u^x u^y\theta^2(3g_3(z)H_4$$
$$+5\gamma\theta(3g_4(z)H_3 + g_5(z)\gamma(3H_2(6 + u^2) + H_1(3 - 3(u^x)^2$$
$$+4(u^y)^2))\theta))p^x p^y(3H_4 + 3H_3p + 3H_2p^2 + H_1(p^y)^2) + 2(g_1(z)H_9$$
$$+\gamma\theta(g_2(z)H_8 + \gamma\theta(g_3(z)(H_4 + H_7)(2 + u^2) + 3\gamma\theta(g_4(z)(H_3 + H_6)$$
$$(2 + 3(u^x)^2 + 3(u^y)^2) - g_5(z)\gamma(-(H_2 + H_5)(8 + 3(u^x)^4 + 24(u^y)^2$$
$$+3(u^y)^4 + 6(u^x)^2(4 + (u^y)^2)) + H_1(-1 + 4(u^x)^4 - 3(u^y)^2 + 4(u^y)^4$$
$$-3(u^x)^2(1 + 9(u^y)^2)))\theta)))(H_9 + H_8p + H_7p^2 + H_6p^3 + H_5p^4$$
$$+p^2(H_4 + p(H_3 + H_2p)) + H_1(p^x)^2(p^y)^2) + (g_1(z)H_9 + g_2(z)\gamma H_8\theta$$
$$+g_3(z)\gamma^2 H_7(2 + u^2)\theta^2 - 2g_3(z)\gamma^2 H_4(-1 + (u^x)^2 - 2(u^y)^2)\theta^2$$
$$+3g_4(z)\gamma^3 H_6(2 + 3u^2)\theta^3 - 6g_4(z)\gamma^3 H_3(-1 + (u^x)^2 - 4(u^y)^2)\theta^3$$
$$+3g_5(z)\gamma^4 H_5(8 + 24u^2 + 3u^4)\theta^4 + 6g_5(z)\gamma^4 H_2(4 - 3u^2 - u^4$$
$$+5(6 + u^2)(u^y)^2)\theta^4 + g_5(z)\gamma^4 H_1(3 + 3u^4 + 30(u^y)^2 + 35(u^y)^4$$
$$-6u^2(1 + 5(u^y)^2))\theta^4)(3(H_9 + p(H_8 + p(H_7 + p(H_6 + H_5p))))$$
$$+6(H_4 + p(H_3 + H_2p))(p^y)^2 + H_1(p^y)^4))$$

$$A^{i_1i_2i_30}P^{i_1i_2i_30} = 6\gamma\pi\theta^2(u^x(g_2(z)I_6 + \gamma\theta(3g_3(z)I_5 + \gamma\theta(g_4(z)(I_2(3$$
$$+2(u^x)^2 - 3(u^y)^2) + 3I_4(4 + u^2)) + 5g_5(z)\gamma(I_1(3 + 4(u^x)^2 - 3(u^y)^2)$$
$$+3I_3(4 + 3(u^x)^2 + 3(u^y)^2))\theta)))(3(I_6 + p(I_5 + p(I_4 + I_3p)))p^x$$
$$+(I_2 + I_1p)(p^x)^3) + u^y(g_2(z)I_6 + 3\gamma\theta(g_3(z)I_5 + \gamma\theta(g_4(z)(I_2 + 4I_4$$
$$+(4I_2 + I_4)(u^x)^2 + (-I_2 + I_4)(u^y)^2) + 5g_5(z)\gamma(I_1 + 4I_3 + 3(2I_1$$
$$+I_3)(u^x)^2 + (-I_1 + 3I_3)(u^y)^2)\theta)))(I_6 + I_5p + I_4p^2 + I_3p^3 + (I_2$$
$$+I_1p)(p^x)^2)p^y + u^x(g_2(z)I_6 + 3g_3(z)\gamma I_5\theta + 3g_4(z)\gamma^2 I_4(4 + u^2)\theta^2$$
$$-3g_4(z)\gamma^2 I_2(-1 + (u^x)^2 - 4(u^y)^2)\theta^2 + 15g_5(z)\gamma^3 I_3(4 + 3u^2)\theta^3$$
$$-15g_5(z)\gamma^3 I_1(-1 + (u^x)^2 - 6(u^y)^2)\theta^3)p^x(I_6 + I_5p + I_4p^2 + I_3p^3$$
$$+(I_2 + I_1p)(p^y)^2) + u^y(g_2(z)I_6 + \gamma\theta(3g_3(z)I_5 - \gamma\theta(g_4(z)(I_2(-3$$
$$+3(u^x)^2 - 2(u^y)^2) - 3I_4(4 + u^2)) - 5g_5(z)\gamma(3I_3(4 + 3(u^x)^2$$
$$+3(u^y)^2) + I_1(3 - 3(u^x)^2 + 4(u^y)^2))\theta)))(3(I_6 + p(I_5 + p(I_4$$
$$+I_3p)))p^y + (I_2 + I_1p)(p^y)^3))$$

$$A^{i_1i_2i_3i_4i_5}P_{i_1i_2i_3i_4i_5} = 30\gamma\pi\theta^2(u^x(g_2(z)J_9 + g_6(z)\gamma^4 J_1(15\gamma^{-4}$$

$$-70(-1+u^2)(u^x)^2 + 63(u^x)^4)\theta^4 + 2\gamma^2\theta^2(g_4(z)J_4(3 + 2(u^x)^2$$

$$-3(u^y)^2) + 5\gamma\theta(g_5(z)J_3(3 + 4(u^x)^2 - 3(u^y)^2) + g_6(z)\gamma J_2(4(u^x)^4$$

$$+(u^x)^2(41+(u^y)^2) - 3(-6 + 5(u^y)^2 + (u^y)^4))\theta)) + 3\gamma\theta(g_3(z)J_8$$

$$+\gamma\theta(g_4(z)J_7(4+u^2) + 5\gamma\theta(g_5(z)J_6(4+3u^2) + 3g_6(z)\gamma J_5(8$$

$$+12u^2 + u^4)\theta)))(15(J_9 + p(J_8 + p(J_7 + p(J_6 + J_5p))))p^x$$

$$+10(J_4 + p(J_3 + J_2p))(p^x)^3 + J_1(p^x)^5) + u^y(g_2(z)J_9 + 3g_3(z)\gamma J_8\theta$$

$$+3g_4(z)\gamma^2 J_7(4+u^2)\theta^2 + 6g_4(z)\gamma^2 J_4(1 + 4(u^x)^2 - (u^y)^2)\theta^2$$

$$+15g_5(z)\gamma^3 J_6(4+3u^2)\theta^3 + 30g_5(z)\gamma^3 J_3(1+6(u^x)^2 - (u^y)^2)\theta^3$$

$$+45g_6(z)\gamma^4 J_5(8+12u^2 + u^4)\theta^4 + 15g_6(z)\gamma^4 J_1(\gamma^{-4} - 14(-1$$

$$+u^2)(u^x)^2 + 21(u^x)^4)\theta^4 - 30g_6(z)\gamma^4 J_2(-6 + u^4 - 56(u^x)^2 + u^2(5$$

$$-7(u^x)^2))\theta^4)(3(J_9 + p(J_8 + p(J_7 + p(J_6 + J_5p)))) + 6(J_4 + p(J_3$$

$$+J_2p))(p^x)^2 + J_1(p^x)^4)p^y + u^x(g_2(z)J_9 + 3g_3(z)\gamma J_8\theta$$

$$+3g_4(z)\gamma^2 J_7(4+u^2)\theta^2 - 6g_4(z)\gamma^2 J_4(-1 + (u^x)^2 - 4(u^y)^2)\theta^2$$

$$+15g_5(z)\gamma^3 J_6(4+3u^2)\theta^3 - 30g_5(z)\gamma^3 J_3(-1+(u^x)^2 - 6(u^y)^2)\theta^3$$

$$+45g_6(z)\gamma^4 J_5(8+12u^2 + u^4)\theta^4 + 15g_6(z)\gamma^4 J_1(\gamma^{-4} - 14(-1$$

$$+u^2)(u^y)^2 + 21(u^y)^4)\theta^4 - 30g_6(z)\gamma^4 J_2(-6 + u^4 - 56(u^y)^2$$

$$+u^2(5 - 7(u^y)^2))\theta^4)p^x(3(J_9 + p(J_8 + p(J_7 + p(J_6 + J_5p))))$$

$$+6(J_4 + p(J_3 + J_2p))(p^y)^2 + J_1(p^y)^4) + 2u^x(g_2(z)J_9$$

$$+\gamma\theta(3g_3(z)J_8 + \gamma\theta(g_4(z)(3J_7(4+u^2) + J_4(6 - (u^x)^2 + 9(u^y)^2))$$

$$+5\gamma\theta(g_5(z)(3J_6(4+3(u^x)^2 + 3(u^y)^2) + J_3(6+(u^x)^2 + 15(u^y)^2))$$

$$-g_6(z)\gamma(-9J_5(8 + (u^x)^4 + 12(u^y)^2 + (u^y)^4 + 2(u^x)^2(6+(u^y)^2))$$

$$-J_2((u^x)^4 + 2(u^x)^2(13 + 8(u^y)^2) + 3(12 + 46(u^y)^2 + 5(u^y)^4))$$

$$+J_1(4(u^x)^4 - (u^x)^2(1 + 41(u^y)^2) + 3(-1 - 5(u^y)^2$$

$$+6(u^y)^4)))\theta))))p^x(3J_9 + 3J_8p + (J_4 + 3J_7)(p^x)^2 + (J_3$$

$$+3J_6)p(p^x)^2 + (J_2 + 3J_5)(p^x)^4 + 3(J_4 + J_7)(p^y)^2 + 3(J_3$$

$$+J_6)p(p^y)^2 + (J_1 + 4J_2 + 6J_5)(p^x)^2(p^y)^2 + 3(J_2 + J_5)(p^y)^4)$$

$$+2u^y(g_2(z)J_9 + \gamma\theta(3g_3(z)J_8 + \gamma\theta(g_4(z)(J_4(6+9(u^x)^2 - (u^y)^2)$$

$$+3J_7(4+u^2)) + 5\gamma\theta(g_5(z)(J_3(6 + 15u^2) + 3J_6(4 + 3(u^x)^2 + 3(u^y)^2))$$

$$-g_6(z)\gamma(-9J_5(8 + (u^x)^4 + 12(u^y)^2 + (u^y)^4 + 2(u^x)^2(6+(u^y)^2))$$

$$-J_2(36 + 15(u^x)^4 + 26(u^y)^2 + (u^y)^4 + 2(u^x)^2(69 + 8(u^y)^2))$$

$$+J_1(-3 + 18(u^x)^4 - (u^y)^2 + 4(u^y)^4 - (u^x)^2(15$$

$$+41(u^y)^2)))\theta))))p^y(3J_9 + 3J_8p + 3(J_4 + J_7)(p^x)^2 + 3(J_3 + J_6)p(p^x)^2$$

$$+3(J_2 + J_5)(p^x)^4 + (J_4 + 3J_7)(p^y)^2 + (J_3 + 3J_6)p(p^y)^2 + (J_1 + 4J_2$$

$$+6J_5)(p^x)^2(p^y)^2 + (J_2 + 3J_5)(p^y)^4) + u^y(g_2(z)J_9 + g_6(z)\gamma^4 J_1(15\gamma^{-4}$$

$$-70(-1+u^2)(u^y)^2 + 63(u^y)^4)\theta^4 + 2\gamma^2\theta^2(g_4(z)J_4(3 - 3(u^x)^2$$

$$+2(u^y)^2) + 5g_5(z)\gamma J_3(3 - 3(u^x)^2 + 4(u^y)^2)\theta + 5g_6(z)\gamma^2 J_2(18 - 3u^4$$

$$+56(u^y)^2 + u^2(-15 + 7(u^y)^2))\theta^2) + 3\gamma\theta(g_3(z)J_8 + \gamma\theta(g_4(z)J_7(4+u^2)$$

$$+5\gamma\theta(g_5(z)J_6(4+3u^2) + 3g_6(z)\gamma J_5(8+12u^2 + u^4)\theta))))(15(J_9$$

$$+p(J_8 + p(J_7 + p(J_6 + J_5p))))p^y + 10(J_4 + p(J_3 + J_2p))(p^y)^3 + J_1(p^y)^5))$$

$$A^{i_1 i_2 i_3 i_4 0} P^{i_1 i_2 i_3 i_4 0} = 6\pi\theta((g_1(z)K_{12} + g_2(z)\gamma K_{11}\theta + g_3(z)\gamma^2 K_{10}(2$$
$$+u^2)\theta^2 + 2g_3(z)\gamma^2 K_6(1 + 2(u^x)^2 - (u^y)^2)\theta^2 + 3g_4(z)\gamma^3 K_9(2 + 3u^2)\theta^3$$
$$+6g_4(z)\gamma^3 K_5(1 + 4(u^x)^2 - (u^y)^2)\theta^3 + 3g_5(z)\gamma^4 K_8(8 + 24u^2 + 3u^4)\theta^4$$
$$+6g_5(z)\gamma^4 K_4(4 - 3u^2 - u^4 + 5(6 + u^2)(u^x)^2)\theta^4 + g_5(z)\gamma^4 K_2(3 + 3u^4$$
$$+30(u^x)^2 + 35(u^x)^4 - 6u^2(1 + 5(u^x)^2))\theta^4 + 15g_6(z)\gamma^5 K_7(8 + 40u^2$$
$$+15u^4)\theta^5 + 15g_6(z)\gamma^5 K_1(\gamma^{-4} - 14(-1 + u^2)(u^x)^2 + 21(u^x)^4)\theta^5$$
$$-30g_6(z)\gamma^5 K_3(-4 + 3u^4 - 42(u^x)^2 + u^2(1 - 21(u^x)^2))\theta^5)(3(K_{12}$$
$$+p(K_{11} + p(K_{10} + p(K_9 + p(K_8 + K_7 p))))) + 6(K_6 + p(K_5 + p(K_4$$
$$+K_3 p)))(p^x)^2 + (K_2 + K_1 p)(p^x)^4) + 6\gamma^2 u^x u^y \theta^2 (3g_3(z)K_6$$
$$+5\gamma\theta(3g_4(z)K_5 + \gamma\theta(g_5(z)(K_2(3 + 4(u^x)^2 - 3(u^y)^2) + 3K_4(6 + u^2))$$
$$+21g_6(z)\gamma(K_1(1 + 2(u^x)^2 - (u^y)^2) + 3K_3(2 + (u^x)^2 + (u^y)^2))\theta)))$$
$$\cdot(3(K_6 + p(K_5 + p(K_4 + K_3 p)))p^x p^y + (K_2 + K_1 p)(p^x)^3 p^y)$$
$$+2(g_1(z)K_{12} + \gamma\theta(g_2(z)K_{11} + \gamma\theta(g_3(z)(K_{10} + K_6)(2 + u^2)$$
$$+3\gamma\theta(g_4(z)(K_5 + K_9)(2 + 3(u^x)^2 + 3(u^y)^2) + \gamma\theta(g_5(z)((K_4 + K_8)$$
$$\cdot(8 + 24u^2 + 3u^4) + K_2(1 + 3u^2 - 4u^4 + 35(u^x)^2(u^y)^2))$$
$$+5g_6(z)\gamma((K_3 + K_7)(8 + 40u^2 + 15u^4) + K_1(1 + 5u^2 - 6u^4$$
$$+63(u^x)^2(u^y)^2))\theta))))))(K_{12} + K_{11}p + K_{10}p^2 + K_9 p^3 + K_8 p^4 + K_7 p^5$$
$$+p^2(K_6 + p(K_5 + p(K_4 + K_3 p))) + (K_2 + K_1 p)(p^x)^2(p^y)^2)$$
$$+4\gamma^2 u^x u^y \theta^2 (3g_3(z)K_6 + 5\gamma\theta(3g_4(z)K_5 - \gamma\theta(g_5(z)(K_2(-3 + 3(u^x)^2$$
$$-4(u^y)^2) - 3K_4(6 + u^2)) - 21g_6(z)\gamma(3K_3(2 + u^2) + K_1(1 - (u^x)^2$$
$$+2(u^y)^2))\theta)))(3(K_6 + p(K_5 + p(K_4 + K_3 p)))p^x p^y + (K_2$$
$$+K_1 p)p^x(p^y)^3) + (g_1(z)K_{12} + g_2(z)\gamma K_{11}\theta + g_3(z)\gamma^2 K_{10}(2 + u^2)\theta^2$$
$$-2g_3(z)\gamma^2 K_6(-1 + (u^x)^2 - 2(u^y)^2)\theta^2 + 3g_4(z)\gamma^3 K_9(2 + 3u^2)\theta^3$$
$$-6g_4(z)\gamma^3 K_5(-1 + (u^x)^2 - 4(u^y)^2)\theta^3 + 3g_5(z)\gamma^4 K_8(8 + 24u^2$$
$$+3u^4)\theta^4 + 6g_5(z)\gamma^4 K_4(4 - 3u^2 - u^4 + 5(6 + u^2)(u^y)^2)\theta^4$$
$$+g_5(z)\gamma^4 K_2(3 + 3u^4 + 30(u^y)^2 + 35(u^y)^4 - 6u^2(1 + 5(u^y)^2))\theta^4$$
$$+15g_6(z)\gamma^5 K_7(8 + 40u^2 + 15u^4)\theta^5 + 15g_6(z)\gamma^5 K_1(\gamma^{-4} - 14(-1$$
$$+u^2)(u^y)^2 + 21(u^y)^4)\theta^5 - 30g_6(z)\gamma^5 K_3(-4 + 3u^4 - 42(u^y)^2$$
$$+u^2(1 - 21(u^y)^2))\theta^5)(3(K_{12} + p(K_{11} + p(K_{10} + p(K_9 + p(K_8$$
$$+K_7 p))))) + 6(K_6 + p(K_5 + p(K_4 + K_3 p)))(p^y)^2 + (K_2 + K_1 p)(p^y)^4))$$

For a discrete version of this distribution function, it is enough to change the momentum vectors by the discrete ones given in section 4.7, $p^\alpha \to p_i^\alpha$, and do the same for the weight function, $\omega(p) \to w_i$. We used constant Fermi-Dirac integrals $g_\nu(z)$, since $\mu = 0 \to z = 1$, but it could be straightforwardly generalized for other chemical potentials.

See bellow the values we used:

Fermi-Dirac integrals for $\mu = 0$	
$g_1(1)$	0.69314718055994530942
$g_2(1)$	0.82246703342411321824
$g_3(1)$	0.90154267736969571405
$g_4(1)$	0.94703282949724591758
$g_5(1)$	0.97211977044690930594
$g_6(1)$	0.98555109129743510409

Below, we see the coefficients of the polynomials to expand the FD EDF using the weight function

$$\omega(p) = \frac{1}{e^p + 1}.$$

For the coefficients to expand the MJ and BE distributions, see the Supplemental Material.

Coefficients for the polynomials			
A_1	0.47917851280252809359	B_1	0.42016214416311657591 9
C_1	-0.43864412446295202649 8	C_2	0.52048156855304587691 1
D_1	-0.23360898938910800640 7	D_2	-0.09744100441339842570 3
D_3	0.91759704557976980240 8	D_4	-0.53147500058897557884 0
E_1	-0.24224757363021607283 4	E_2	0.76341279515419700390 2
F_1	-0.10339002798014891069 5	F_2	-0.03448719425366195678 9
F_3	0.49767917686158088137 5	F_4	-0.78767750415616656219 3
G_1	-0.10514569297912171552 9	G_2	0.53299220739620711346 7
G_3	-0.01800288369668221803 5	G_4	0.39375048127660593551 6
G_5	-1.41242053679826841080 7	G_6	0.53699068843525548835 8
H_1	-0.03896993030837024211 5	H_2	-0.01108052439070375110 0
H_3	0.21339434814660128869 0	H_4	-0.54334333961138653712 5
H_5	-0.00156177551099272566 0	H_6	0.07409521577310983185 1
H_7	-0.80250188620872017671 8	H_8	1.91656080101502381845 2
H_9	-0.54043408109106244546 0	I_1	-0.03921704170267163326 2
I_2	0.27552577173600931741 7	I_3	-0.00572048382506251117 7
I_4	0.16901462807501485165 1	I_5	-0.98355703618410375826 9
I_6	1.03960296434741226658 8	J_1	-0.01298072764430431616 6
J_2	-0.00329312153037332471 6	J_3	0.07896936540989263923 3
J_4	-0.27800688713532635396 5	J_5	-0.00039251007274307892 9
J_6	0.02343051488423359556 4	J_7	-0.34376413064566294588 5
J_8	1.33263254744864224902 0	J_9	-1.05698406384243701698 2
K_1	-0.01300819261024218999 9	K_2	0.11718460404874018173 9
K_3	-0.00167221051139645284 1	K_4	0.06191583009575570842 2
K_5	-0.49567538148972002162 8	K_6	0.84421535509899800324 9
K_7	-0.00018629880599600773 8	K_8	0.01217961652428804765 6
K_9	-0.23331383063916282145 0	K_{10}	1.43176527017931500014 3
K_{11}	-2.42703580325886113204 6	K_{12}	0.54284027698790564469 1